2016

The Role of clusterin in motor neuron disease and the molecular mechanism of its action

Daniel R. Whiten
University of Wollongong

The Role of Clusterin in Motor Neuron Disease and the Molecular Mechanism of its Action

A thesis submitted in fulfilment of the requirements for the award of the degree

Doctor of Philosophy

from

University of Wollongong

by

Daniel R. Whiten

Bachelor of Biotechnology (Adv) (Hons)

Illawarra Health and Medical Research Institute

School of Biological Sciences

University of Wollongong

2016

Thesis Certification

I, Daniel R. Whiten, declare that this thesis, submitted in fulfilment of the requirements for the award of Doctor of Philosophy, in the Department of Biological Sciences, University of Wollongong, is wholly my own work unless otherwise referenced or acknowledged. The document has not been submitted for qualifications at any other academic institution.

Daniel R. Whiten

2016

In loving memory of Valda Rayner

Acknowledgements

The creation of this thesis was far from an individual effort. There are many people to whom I owe thanks and appreciation for their assistance throughout my time at UOW.

Firstly, to my supervisors, Snr. Prof. Mark Wilson and Dr. Justin Yerbury, your advice and enthusiasm has been a constant source of inspiration and motivation. I greatly admire your ability to plan and hypothesise; I one day hope to be able to emulate it myself. I am privileged to have learnt from you for the past five years and cannot thank you enough for all of the opportunities you have provided.

I also wish to thank my colleagues who each contributed, socially and professionally, to my time at IHMRI - only some of whom I can name here. Special mentions to Dez, Nat, Rebecca San Gil, Luke, Jen, Raf, Dzung, Mon, Pat, Rebecca Brown and Rebecca Dabbs, for all the ideas, help and good times. To my other lab- and office-mates, thanks for helping make my candidacy a great experience.

Thanks also to Prof. David Klenerman FRS for welcoming me into your lab and providing the advice and resources required to complete a large section of this work. To the Klenerfolk, particularly Mathew, Laura, Nadia, Chris, Joe, Fran and Rebecca, thank you for making my six months in Cambridge among the most enjoyable of my time at university. Dr. Janet Kumita, thank you greatly for your time and advice.

My most heartfelt appreciation must go to my family. Mum and Dad, your support has been limitless, for which I am extremely grateful. Clearly, none of this would have been possible without your influence. Brent, thanks for setting the goal posts. Kathryn, over the course of my PhD tenure you went from my girlfriend, to fiancée, to wife. I am eternally grateful for everything you are and everything you do.

Abstract

Amyotrophic lateral sclerosis (ALS) is a currently untreatable disease characterised by the progressive loss of motor neurons. Death typically occurs as a result of respiratory failure within just 3 years of diagnosis. Aberrant protein aggregation is a hallmark of ALS – in particular, the aggregation of transactive response DNA binding protein 43 kDa (TDP-43) to form cytosolic inclusions is observed in >95% of ALS cases. Mutations in the gene encoding TDP-43 itself are believed to underpin the pathology in approximately 5-10% of all cases. Clusterin (CLU) was the first secreted mammalian chaperone identified. In recent years, it has been established that under endoplasmic reticulum (ER) stress conditions the secretion of CLU is reduced, and instead the protein is retrotranslocated to the cytosol. Much of the work described in this thesis was directed towards testing the hypothesis that (under ER stress) CLU may interact with TDP-43 in the cytosol to influence its aggregation and/or the clearance of inclusions.

The first aim of this project was to develop a robust technique that could be used to quantify the effect of intracellular CLU (or any protein, drug or treatment) on the number of intracellular inclusions formed by a target protein, such as TDP-43. In Chapter 3, a flow cytometric method (termed flow cytometric characterisation of inclusions and trafficking; FloIT) is described that involves the analysis of detergent-lysates of cells. By measuring both fluorescent protein inclusions and fluorescently-stained nuclei, the number of inclusions originating from a known number of cells

can be measured. FloIT was shown to accurately measure inclusions formed by a variety of proteins and can be adapted for use in a variety of applications, such as measuring the co-aggregation of proteins into inclusion bodies and the nuclear trafficking of fluorescent molecules.

Chapter 4 describes applying FloIT to study the effect of intracellular CLU on the numbers of inclusions in cells overexpressing TDP-43-TurboGFP with the ALS-associated M337V mutation (TDP-43^{M337V}-tGFP). In Neuro-2a cells (a murine neuronal cell line), under ER stress conditions, CLU significantly reduced the number of TDP-43^{M337V}-tGFP inclusions. This effect was not dependent solely upon either the ubiquitin-proteasome system or autophagy, suggesting that CLU can influence the turnover of intracellular proteins through multiple pathways. This is supported by previous reports that intracellular CLU alone can be degraded by the proteasome and upregulates autophagy. Additionally, CLU co-localises with TDP-43^{M337V}-tGFP inclusions, co-immunoprecipitates with soluble TDP-43^{M337V}-tGFP, and potently inhibits the *in vitro* aggregation of TDP-43-tGFP. Taken together, these results strongly support a role for CLU in maintaining intracellular protein homeostasis. Further work is required to identify whether this could potentially be manipulated as part of a new therapy for diseases associated with aberrant intracellular protein aggregation.

Chapter 5 is a separate but thematically-related piece of work, with the aim to investigate the effects of CLU on the aggregation, structure and toxicity of protein aggregates. Additionally, the structure and dynamism of reversible CLU-CLU oligomers was investigated, but proved difficult due to rapid dissociation of the oligomers and a lack of instrument sensitivity. It was established that the interaction between CLU and the client protein is dependent on the identity of the individual client and also its conformation. Different CLU:client protein stoichiometries were determined for amyloid-β and α-synuclein (αS) (responsible for Alzheimer's and Parkinson's diseases respectively), and also for the two structurally distinct oligomeric forms of αS. The binding of CLU to αS oligomers resulted in a compaction of their conformation. In addition, it was shown that CLU readily binds mature αS fibrils, and that this binding can reduce the potentially toxic effects of the fibrils without influencing their formation. This suggests that the cytoprotective effect of CLU can be exerted at multiple points along protein aggregation pathways. These results not only elucidate a potential protective role for CLU in α-synucleinopathies such as Parkinson's disease, but also provide the most detailed characterisation of the interaction between CLU and amyloid-forming client proteins to date. Mechanistic details such as these may prove critical when developing therapies relating to the chaperone activity of CLU.

Contents

List of Figures

List of Tables

Abbreviations

3MA	3-methyladenine
α_2M	α_2-macroglobulin
αS	α-synuclein
Aβ	amyloid-β
AD	Alzheimer's disease
AF	Alexa Fluor
AFU	arbitrary fluorescence units
ALS	amyotrophic lateral sclerosis
APP	amyloid precursor protein
ATP	adenosine triphosphate
AU	arbitrary units
Az	azide
BCA	bicinchoninic acid
BiP	binding immunoglobulin protein
BSA	bovine serum albumin
CLU	clusterin
COMMD1	copper metabolism MURR1 domain-containing protein 1
CQ	chloroquine
CSF	cerebrospinal fluid
CTF	C-terminal fragment
DHE	dihydroethidium
DLB	dementia with Lewy bodies
DNA	deoxyribonucleic acid
DM	double mutant
DMEM	Dulbecco's modified Eagle's medium
DMSO	dimethyl sulfoxide
DTT	dithiothreitol
EDTA	ethylenediaminetetraacetic acid
eGFP	enhanced green fluorescent protein
ER	endoplasmic reticulum
ERAD	endoplasmic reticulum-associated degradation
fALS	familial amyotrophic lateral sclerosis
FBS	foetal bovine serum
FCS	fluorescence correlation spectroscopy
FloIT	flow cytometric characterisation of inclusions and trafficking
FLUC	firefly luciferase
FRET	Förster resonance energy transfer
FSC	forward scatter
FUS	fused in sarcoma
GFPU	ubiquitin-enhanced green fluorescence protein
HDC	heat-denatured casein
HF	HiLyte Fluor
HEK	human embryonic kidney

HG	high glucose
Hsp	heat shock protein
Htt	huntingtin
LB	Luria-Bertani
LC3	microtubule-associated protein 1A/1B-light chain 3
LRP	lipoprotein receptor-related protein
mRNA	messenger ribonucleic acid
MES	2-(N-morpholino)ethanesulfonic acid
miRNA	microribonucleic acid
MSA	multiple systems atrophy
MWCO	molecular weight cut-off
N2a	Neuro-2a
NFAT	nuclear factor of activated T-cells
p62	sequestosome 1
PAGE	polyacrylamide gel electrophoresis
PBS	phosphate buffered saline
PD	Parkinson's disease
PDD	protein deposition disorder
PDMS	poly(dimethyl)siloxane
PFA	paraformaldehyde
PI	propidium iodide
PulSA	pulse shape analysis
Rap	rapamycin
RFP	red fluorescent protein
RME	receptor-mediated endocytosis
RNA	ribonucleic acid
RRM	ribonucleic acid recognition motif
RT	room temperature
sALS	sporadic amyotrophic lateral sclerosis
SD	standard deviation
SDS	sodium dodecyl sulphate
SEC	size exclusion chromatography
SEM	standard error of the mean
sHsp	small heat shock proteins
SSC	side scatter
SOD	superoxide dismutase
TCCD	two colour coincidence detection
TDP	transactive response deoxyribonucleic acid binding protein
Tg	thapsigargin
tGFP	Turbo green fluorescence protein
ThT	thioflavin T
TIRFM	total internal reflection fluorescence microscopy
UPR	unfolded protein response
UPS	ubiquitin-proteasome system
UV	ultraviolet
WT	wild-type

Chapter 1:

Introduction

1. Introduction

1.1 Protein folding

Most polypeptide chains need to fold into a specific ('native') 3-dimensional conformation in order to become biologically active. There are countless possible structures that any one chain could assume. The fact that even large proteins fold correctly on most occasions indicates that biological systems are in place to ensure this occurs (Hartl and Hayer-Hartl 2002). However, failure or inefficiency within these systems means that misfolded proteins can accumulate in response to various stresses. Misfolded proteins are responsible for (or are associated with) a range of devastating pathologies, from cancer to amyotrophic lateral sclerosis (ALS) (Stefani and Dobson 2003).

1.1.1 Mechanics of protein folding

The folding of small polypeptide chains is believed to occur in a relatively simple manner. 'Two-state' proteins (single domain proteins consisting of up to 120 amino acids) fold from an unfolded state directly to the native structure (Weikl 2010). This occurs within seconds and has no observable transition state (Jackson and Fersht 1991, Jackson 1998). In direct contrast, the folding of larger proteins involves many possible transition states and folding intermediates. Proteins were originally hypothesised to follow a sequential, well defined pathway while folding toward the native state (Levinthal 1968). Since then the mechanics of protein folding have been actively debated within the field, with several opposing views. One contemporary

view of protein folding is known as the 'energy landscape theory' (visually represented as a 'folding funnel' (Figure 1.1)) where the native conformation is the lowest free energy state. In contrast to the classic view, this theory eliminates the idea of a single sequential folding pathway. Rather, non-native proteins may be able converge to a stable state via a number of parallel routes and intermediates (Dobson 2003). It is not currently known precisely how these intermediates may be formed, but the process has been suggested to be thermodynamically controlled and include process such as the internal collapse of hydrophobic residues and gradual restriction of rotational freedom of amino acid side-chains (Chaires 2008, Liu *et al.* 2014). It is possible that the folding of such intermediates is facilitated by 'foldons'. Foldons are local regions of a protein that fold independently of the chain as a whole, but cooperate with adjacent foldons to achieve the native state (Maity *et al.* 2005). Through this cooperative folding foldons in the correct native conformation are believed to guide and stabilise the correct folding of neighbouring foldons. It has been suggested that the non-specific random search through possible conformations occurs on a timescale similar to observed protein folding in small foldons and can lead to efficient folding when combined with the hydrophobic collapse of local regions (Englander and Mayne 2014). Thus, a single foldon reaching its native conformation may be sufficient to trigger the non-random search through possible conformations for the entire protein chain (Englander *et al.* 2007). It was recently shown that foldons allow at least some proteins to fold via well defined, reproducible pathways (Walters *et al.* 2013, Hu *et al.* 2016). This has caused some to

suggest revisions to the energy landscape theory of protein folding back in the direction of Levianthal's (1968) original work (Englander and Mayne 2014). It should be noted that not all proteins or peptides adopt a natively folded structure. 'Natively unfolded' or 'intrinsically disordered' proteins such as amyloid-β (Aβ) are a class of proteins that do not adopt a specific conformation in order to fulfil their biological role (Dyson and Wright 2005). The exact reason for the lack of folding in these cases is unknown, but may be due to a high net charge and/or a lack of hydrophobic residues that can collapse toward the centre of the protein (Uversky and Dunker 2010).

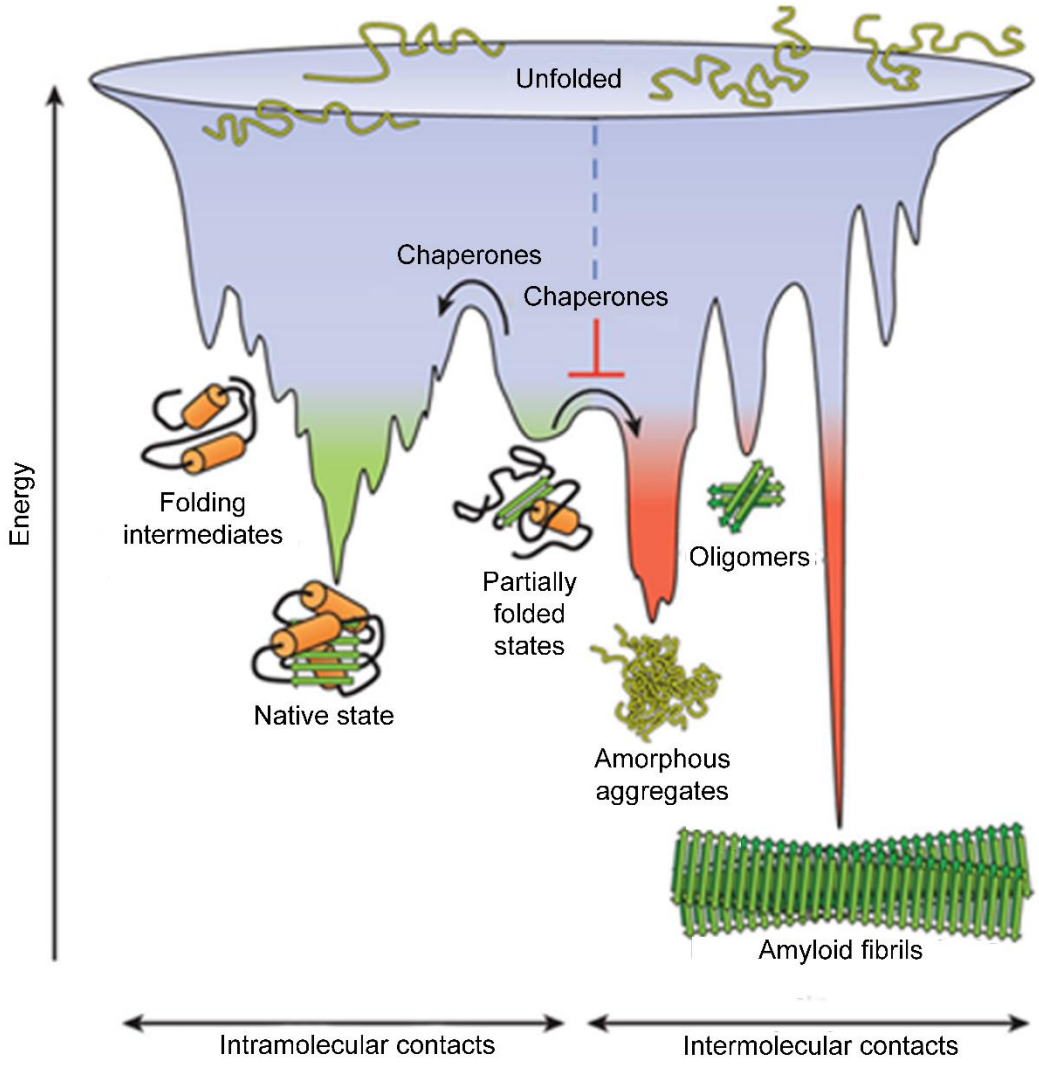

Figure 1.1: The protein folding funnel. A schematic two dimensional representation of the folding funnel. The wells on the side of the funnel are intermediates, partially folded states whose free energy is lower than that of the unfolded state yet higher than that of the native conformation (Plotkin and Onuchic 2002). Non-native intermediates that are close to the free energy minimum may become trapped on the off-folding pathway (red). Image adapted from (Hartl *et al.* 2011).

Proteins can become trapped in partially folded conformations with a free energy state between that of an unfolded and native protein. Interactions with molecular chaperones allow such proteins to overcome free-energy barriers and continue progress towards the native state (Hartl *et al.* 2011). Additionally, these chaperones can prevent illicit interactions with other partially folded proteins, preventing them

forming (or rescuing them from) very low-energy non-native conformations known as fibrillar or amorphous aggregates (Figure 1.1; discussed in more detail in the following sections).

1.1.2 Protein misfolding and aggregation

It is not uncommon for proteins to misfold or become unfolded. A wide variety of internal and external stresses can cause newly synthesised proteins to become trapped on the off-folding pathway (inevitably leading to aggregation), or induce the unfolding of a native protein. These factors include increased temperature, extremes of pH, molecular crowding and oxidative stress (Kelly 2003). Mutations may also result in the expression of a protein that is structurally destabilised, or in some cases incapable of assuming its native conformation (Stefani and Dobson 2003). Protein misfolding exposes the normally shielded hydrophobic interior to the environment. In a process similar to hydrophobic collapse in protein folding, multiple misfolded proteins can associate via hydrophobic interactions to form insoluble aggregates, which are either amorphous or fibrillar amyloid in structure (Rajan *et al.* 2002, Cheung and Truskett 2005). Amorphous aggregates (formed through disordered association) have no specific structure (Stranks *et al.* 2009), while amyloid fibrils are highly structured and contain a cross-β sheet arrangement (Blake and Serpell 1996). The aggregation pathway a protein takes (amorphous or amyloid) is affected by many variables, including protein concentration and composition, pH and temperature (Gorman *et al.* 2003, Vetri *et al.* 2007).

Otherwise unrelated proteins can produce amyloid via a strikingly similar mechanism, consisting of three macroscopic phases: nucleation, polymerisation and plateau. These phases are identified as such based on observations made from quantifying protein aggregation using bulk techniques, rather than discrete microscopic steps, and are believed to be shared by all amyloid-forming proteins (Arosio *et al.* 2015). The nucleation phase is the name ascribed to the period of time between initiation of aggregation and the formation of detectable protein aggregates. This phase is the start of amyloid formation, and (except in the case of natively unfolded proteins) necessarily begins with the misfolding or unfolding of the polypeptide chain to expose normally shielded hydrophobic residues. A small percentage of these unfolded proteins then associate to form soluble prefibrillar intermediates (termed 'nuclei'). These nuclei essentially act as catalytic surfaces for further aggregation and can grow into more complex structures known as protofibrils (Chiti and Dobson 2006). The polymerisation phase refers to the period of time where the detectable number of aggregates increases. On the microscopic level, along with continued nucleation, the protofibrils elongate and mature into protofilaments. Up to six of these can laterally associate (stabilised by hydrogen bonds) to form mature amyloid fibrils (Serpell *et al.* 2000, Stefani and Dobson 2003). The final plateau phase is characterised by the detectable aggregates (nuclei, protofibrils and fibrils) reaching an equilibrium with each other and the native proteins (Jarrett and Lansbury 1993). Historically, only a small number of proteins were thought to be capable of forming amyloid, however, it has since become clear

that rather than being an anomaly, the ability to form amyloid is an inherent property of polypeptide chains (Fandrich and Dobson 2002, Dobson 2003, Stefani 2010).

1.2 Protein quality control

Despite the inherently high aggregation propensity of polypeptide chains, only a minority of proteins aggregate *in vivo* to cause disease. This apparent paradox can be explained by the presence of effective intra- and extracellular protein folding quality control mechanisms (Figure 1.2) (Stefani 2010). Intracellular protein quality control systems function to i) degrade compromised polypeptide chains (e.g. the ubiquitin-proteasome system (UPS), autophagy and endoplasmic reticulum-associated degradation (ERAD)), ii) aid proteins in adopting their native structure ('foldase' chaperones), and iii) combat their propensity to aggregate during stress conditions (extracellular and intracellular 'holdase' chaperones) (summarised in Figure 1.2).

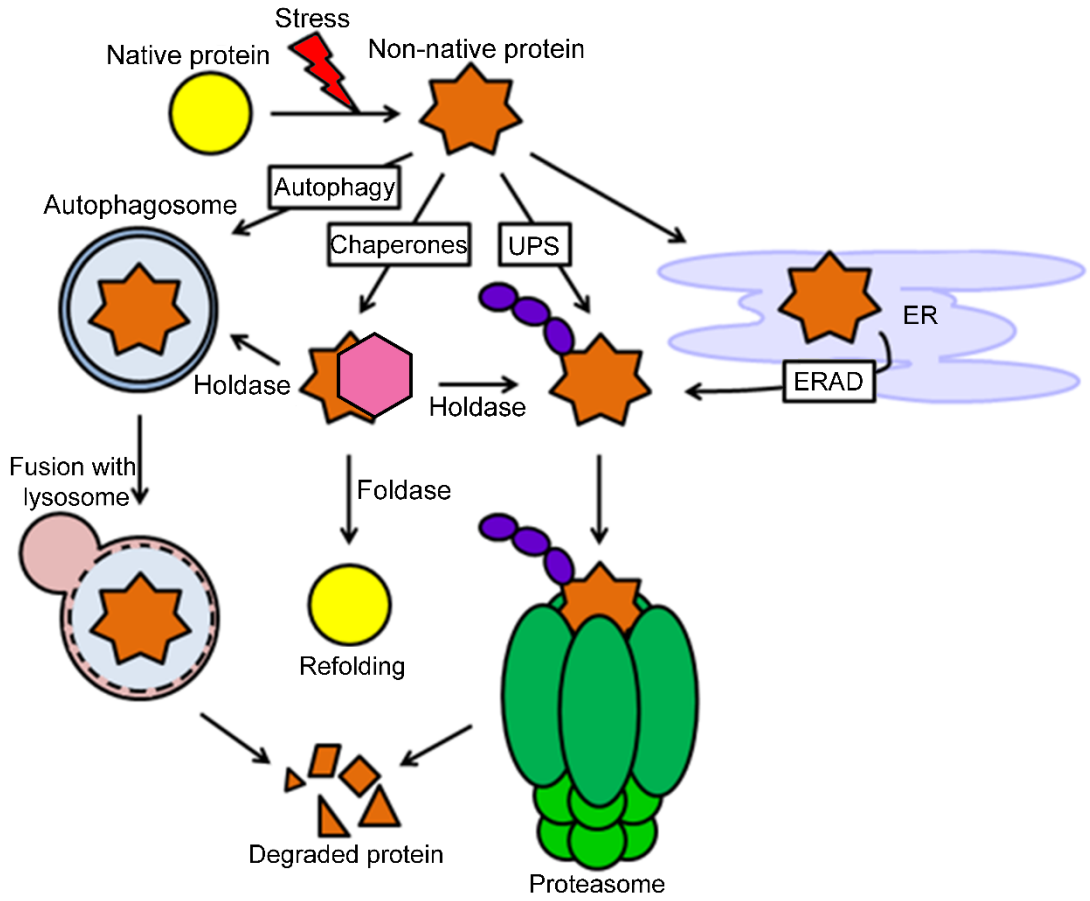

Figure 1.2: Intracellular protein degradation pathways. The degradation of intracellular non-native proteins is mediated by three processes: autophagy, the UPS and ERAD. Molecular chaperones aid by refolding non-native proteins or directing them to a degradative pathway. 'Holdase' refers to holdase chaperones that typically deliver client proteins for degradation; 'Foldase' refer to chaperones able to refold unfolded proteins. Abbreviations: ERAD, endoplasmic reticulum-associated degradation; UPS, ubiquitin-proteasome system. Structures not drawn to scale.

1.2.1 The ubiquitin-proteasome system and autophagy

The UPS is a complex, highly specific pathway that results in the degradation of targeted (usually misfolded or damaged) proteins (Ciechanover 1994). Thus, the UPS primarily functions to degrade proteins before they form aggregates or toxic intermediate structures. Degradation of a target protein by the UPS occurs in two steps: the covalent attachment of multiple ubiquitin molecules to the target protein

through the action of ubiquitin ligases, followed by the degradation of the tagged protein by the proteasome (Ciechanover 1994). Misfolded or unassembled proteins present in the endoplasmic reticulum (ER) can be degraded by the ERAD pathway. ERAD utilises either the UPS or autophagy following translocation of the protein from the ER membrane or lumen to the cytosol (Meusser *et al.* 2005, Fujita *et al.* 2007).

Autophagy utilises lysosomes to degrade various cellular constituents, including nucleic acids, lipids and proteins. Lysosomes are small acidic vesicles that contain many hydrolytic enzymes (Bohley and Seglen 1992) that mediate proteolysis as the end point of at least five processes: chaperone-mediated autophagy, receptor-mediated endocytosis (RME), pinocytosis, phagocytosis and autophagy (Ciechanover 2005). Both chaperone-mediated autophagy and RME are discussed in the upcoming sections.

1.2.2 Molecular chaperones

As described in section 1.1.2, proteins subjected to physical or chemical stress tend to become misfolded and aggregate as a result of interactions between exposed hydrophobic regions,. Molecular chaperones are a cornerstone of the protein quality control machinery; they are a group of functionally related but structurally diverse proteins which share the ability to recognise these regions of exposed

hydrophobicity and non-covalently bind to misfolded proteins (Lecker *et al.* 1989). In this fashion, molecular chaperones inhibit illicit interactions between stressed protein molecules (Ellis and van der Vies 1991, Bukau *et al.* 2006) and play an essential role in protein folding quality control systems (Melnikov and Rotanova, 2010).

Molecular chaperones can be divided into three primary classes:

i. 'Holdase' type chaperones that bind to misfolded proteins and prevent aggregation (e.g. small heat shock proteins (sHsps) and extracellular chaperones) (Ehrnsperger *et al.* 1997, Wilson and Easterbrook-Smith 2000). These chaperones stabilise the client protein either for subsequent degradation or refolding mediated by an adenosine triphosphate (ATP)-dependent folder chaperone (French *et al.* 2008, Wyatt *et al.* 2013b).

ii. 'Foldase' type chaperones that actively fold newly synthesised, partially unfolded and non-native proteins into their native conformation (e.g. Hsp60, Hsp70) (Forreiter 2006, Jansen *et al.* 2012).

iii. 'Unfoldase' type chaperones that hydrolyse ATP to drive the unfolding proteins for further processing, such as translocation across membranes, presentation to proteases or refolding (e.g. Hsp100) (Weber-Ban *et al.* 1999, Baneyx and Nannenga 2010).

As mentioned above chaperones play significant roles in the turnover of both intracellular and extracellular proteins. The roles of extracellular chaperones are discussed at length in section 1.3. The primary pathway that facilitates the clearance of chaperone-misfolded protein complexes from the cytosol is chaperone-mediated autophagy (Cuervo and Wong 2014). This process is dependent upon the binding of a chaperone (such as Hsp70) to a target protein, which functions to prevent illicit interactions until the complex binds to the lysosomal receptor LAMP2A. At this point the target protein is unfolded and is translocated into the lysosomal lumen (assisted by a luminal chaperone) where it is degraded (Bandyopadhyay *et al.* 2008, Bandyopadhyay *et al.* 2010). Additionally, chaperones are able to protect the cell from the effect of misfolded proteins in the ER through a process termed ERAD. Briefly, ER-resident chaperones are responsible for the recognition of misfolded proteins in the ER lumen, where they are transferred to an ER membrane receptor. As the target protein is translocated into the cytosol it is ubiquitinated by an E3-ubiquitin ligase and then degraded by a cytosolic proteasome (Meusser *et al.* 2005, Goder 2012).

Similarly to the unfolding of proteins for further processing, certain chaperones have been implicated in allowing the disassembly of protein aggregates. For example, CLU has been shown to bind oligomers that are naturally released from amyloid fibrils and prevent their re-association (Narayan *et al.* 2012). ATP-dependent chaperones such as Hsp100 and Hsp70 have also been shown to initiate

the dissagregation of protein complexes, often acting in conjunction with proteases to degrade the target protein (Saibil 2013).

Considering the important roles they perform, it is not surprising that molecular chaperones are heavily implicated in defence against disease. Normally, chaperones actively inhibit the formation of aggregates and toxic protein structures. Despite this, protein aggregation is known to occur in over 40 diseases (Chiti and Dobson 2006). Precisely why chaperones fail to prevent aggregation in these cases is not known. However, one possible explanation is that the capacity of the chaperones is exceeded when presented with numerous misfolded proteins; such an event is more likely to occur during aging (Csermely 2001). The increased production of non-native proteins is a part of normal aging and a result of several impaired processes. For example, proteasomes and lysosomes exhibit lower activity in aged organisms (Rubinztein *et al.* 2011, Saez and Vilchez 2014). Transcriptional and translational errors are also more common in the aged, resulting in protein folding defects and subsequent aggregation (Dukan *et al.* 2000). Similarly, genetic mutations accumulate slowly over time, potentially producing aggregation-prone proteins. Factors such as these can result in a large number of non-native proteins being presented to the chaperone machinery, which may become overloaded (Csermely 2001). This theory of chaperone overloading may explain the late onset, degenerative nature of a diverse range of diseases termed protein deposition

diseases (PDDs), such as ALS and Alzheimer's disease (AD) (Kaushik and Cuervo 2015).

1.3 Extracellular chaperones

All of the protein quality control mechanisms outlined thus far have been intracellular; however the accumulation of potentially toxic protein aggregates occurs extracellularly in many diseases (Table 1.1). Multiple steps in both the autophagic and proteasomal pathways are ATP-dependent (Plomp *et al.* 1987, Baumeister *et al.* 1998), and thus could not operate in the low ATP environment of extracellular fluids (compared to millimolar cytosolic levels, human blood plasma contains approximately 30 nM ATP (Gorman *et al.* 2007)). For the same reason, conventional foldase chaperones would also not be able to function. It is possible that intracellular holdase chaperones released from dying cells could chaperone extracellular proteins, but the level of these chaperones is too low to be physiologically relevant.

Table 1.1: Examples of PDDs and the major associated aggregate-forming proteins. Most of these diseases feature multiple aggregating proteins, many of which are omitted from this table. [Ex] Extracellular deposit.

Disease	Protein	Deposit structure
Alzheimer's disease	Amyloid-β Tau	Fibrillar[Ex] Fibrillar and amorphous
Amyotrophic lateral sclerosis	TDP-43	Fibrillar and amorphous
Corneal dystrophy	Keratoepithelin	Amorphous[Ex]
Creutzfeldt-Jakob disease	Prion protein	Fibrillar[Ex]
Dementia with Lewy bodies	αS	Fibrillar
Diabetes (Type 2)	Amylin	Fibrillar[Ex]
Down's syndrome	Aβ	Fibrillar
Familial British dementia	ABri peptide	Fibrillar[Ex]
Haemodialysis-related amyloidosis	β_2-Microglobulin	Fibrillar[Ex]
Hereditary non-neuropathic systemic amyloidosis	Lysozyme	Fibrillar[Ex]
Hereditary renal amyloidosis	Fibrinogen	Fibrillar[Ex]
Huntington's disease	Huntingtin	Fibrillar
Non-amyloidotic monoclonal IgG deposition disease	Immunoglobulin G	Amorphous[Ex]
Parkinson's disease	αS	Fibrillar
Primary systemic amyloidosis	Immunoglobulin light chain	Fibrillar[Ex]
Prion Diseases	PrP	Fibrillar[Ex]
Reactive amyloidosis	Amyloid-α	Fibrillar[Ex]
Renal disease	Tamm-Horsfall protein	Fibrillar[Ex]
Sickle cell anaemia	Haemoglobin	Fibrillar

References: (Thomas *et al.* 1995, Kelly 1996, Carrell and Lomas 1997, Hamidi Asl *et al.* 1997, Carrell and Gooptu 1998, Soto 2001, Crabb *et al.* 2002, Yerbury *et al.* 2005, Asea and Brown 2008, Da Cruz and Cleveland 2011).

Extracellular chaperones are believed to play a crucial role in maintaining proteostasis outside of cells. A model for an extracellular protein folding quality control system has been proposed, which consists of three key steps (Figure 1.3) (Yerbury *et al.* 2005):

i. Extracellular chaperones bind to a non-native client protein to stabilise it in solution.
ii. This facilitates uptake of the chaperone-client protein complex into cells such as macrophages and hepatocytes via RME.
iii. The internalised complex is degraded in lysosomes, destroying the misfolded protein.

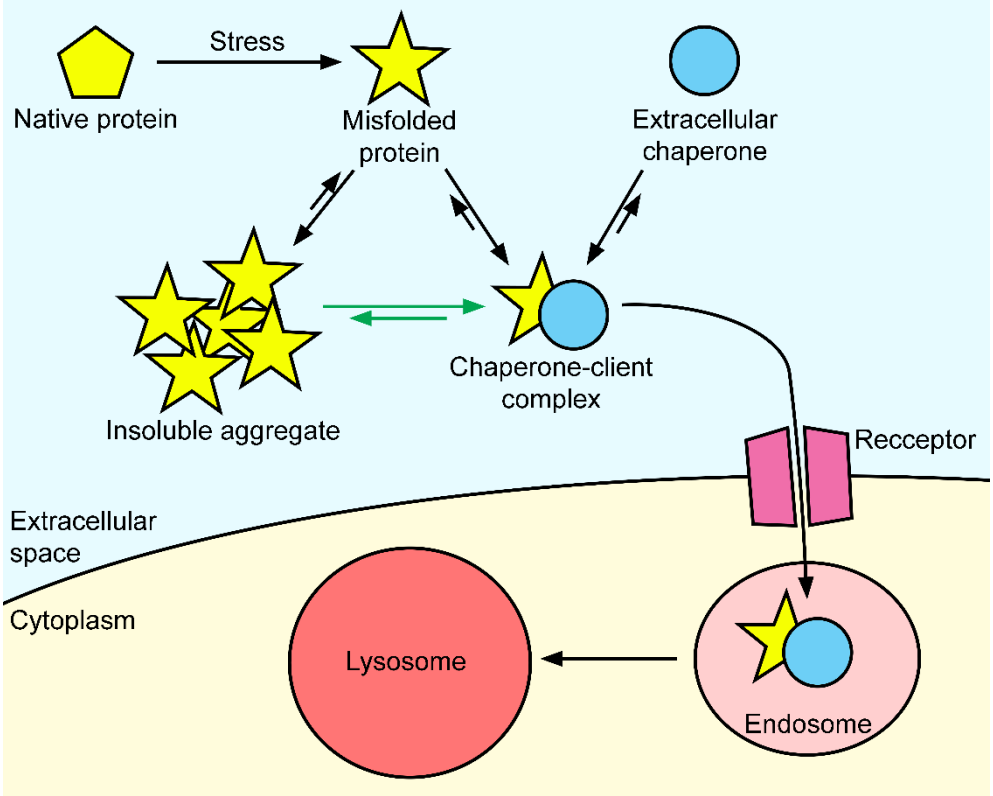

Figure 1.3: Extracellular chaperones mediate the disposal of misfolded proteins. Extracellular chaperones bind to non-native proteins and facilitate their destruction by RME and lysosomal degradation. Green arrows represent hypothetical pathways. Information from Wilson *et al*. (2008).

In the following sections, α_2-macroglobulin (α_2M) and clusterin (CLU) (prominent extracellular chaperones and of particular relevance to the work reported in this thesis) are discussed in more detail.

1.3.1 α_2-Macroglobulin

1.3.1.1 Synthesis

α_2M is synthesised by multiple cell types including astrocytes, hepatocytes and macrophages and is present in human serum at approximately 3 mg.ml^{-1} (Sottrup-

Jensen 1989). After stimulation with interleukin-6, neurons have also been shown to produce α_2M (Strauss *et al.* 1992). The protein is encoded by the *A2M* gene on chromosome 12p-12-13 (Matthijs *et al.* 1992b).

1.3.1.2 Structure and Function

α_2M is a 720 kDa tetramer comprised of two disulphide-bonded dimers. The α_2M subunits are arranged to create a large cage structure that can trap target proteases by steric interference and covalent bonding. α_2M is a potent inhibitor of many different proteases including plasmin, thrombin and trypsin (Borth 1992). The entrapment of proteases such as these occurs via a conformational change elicited by the cleavage of a 'bait region', a 39 amino-acid domain that contains specific cleavage sites for a range of different proteases (Barrett and Starkey 1973). The conformational change exposes a previously buried cysteine-glutamine thioester bond which is readily cleaved by the target protease, causing it to become covalently bound to α_2M (Sottrup-Jensen *et al.* 1989) (Figure 1.4). The structure of α_2M is such that there is space in the central cage for two proteases of 20 - 30 kDa, each covalently bound to one of the disulphide-bonded dimers. The cleavage of the bait region 'activates' α_2M, and the resulting conformational change also exposes a lipoprotein receptor recognition site that facilitates uptake into cells (Sottrup-Jensen 1989).

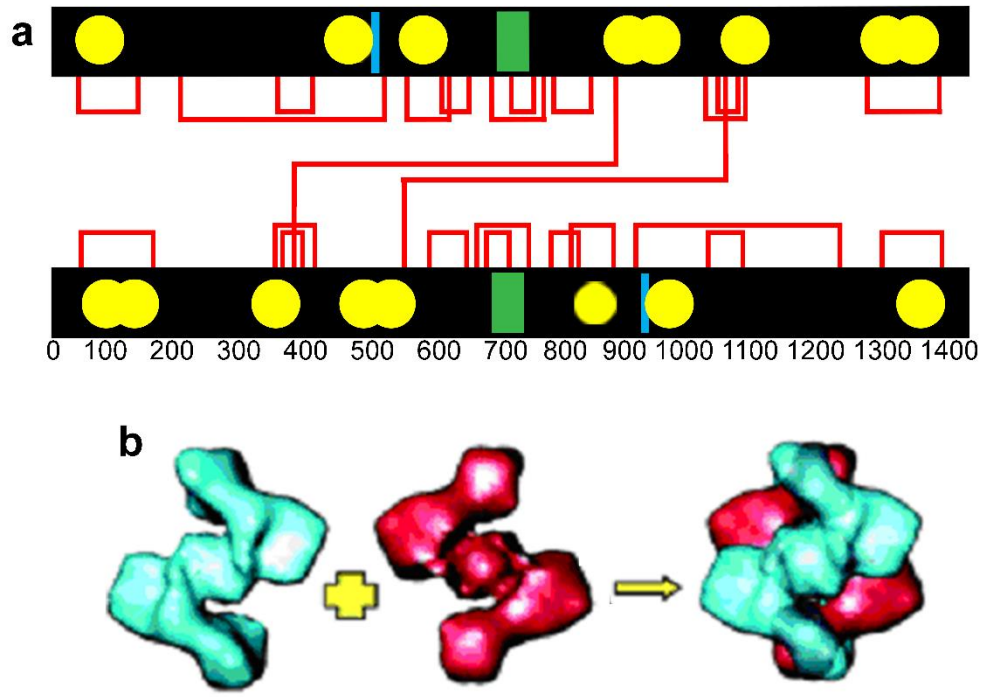

Figure 1.4: Schematic representation of the dimeric structure of α2M. a) Each monomer is glycosylated in 8 locations (yellow circles) and stabilised by 11 intramolecular disulfide bonds (red arches). The bait regions are indicated in green. The blue rectangles represent the thioester bond (Marrero *et al.* 2012).Two monomers are linked by two disulfide bonds to form the dimeric subunit. b) Two dimers (red and green) interact via non-covalent interactions to form mature tetrameric α_2M. Adapted from Kolodziej *et al.* (2002).

In addition to this protease inhibitory activity, α_2M was the third extracellular protein found to exhibit chaperone activity, following CLU and haptoglobin. Like the other well characterised extracellular chaperones, α_2M can bind to a variety of misfolded proteins and prevent aggregation in an ATP-independent manner (French *et al.* 2008, Yerbury *et al.* 2008, Wyatt *et al.* 2013a). α_2M was shown to protect neurons from the toxic effects of HypF-N and Aβ by preventing their non-specific binding to the cell surface (Mannini *et al.* 2012) and possibly delivering misfolded proteins specifically to cells for RME (Wu *et al.* 1997, Wyatt *et al.* 2014). The α_2M dimer, produced through oxidation of the native tetramer, is a more potent

chaperone than the native tetramer on a molar basis (Wyatt *et al.* 2014). Thus, it appears unlikely that the chaperone activity exhibited by α_2M is related to the trapping mechanism of protease inhibition. Rather, the mechanism of chaperone action appears to be similar to the other known extracellular chaperones: binding to regions of exposed hydrophobicity. Indeed, the oxidised dimer exhibits up to 4-fold greater exposed hydrophobicity than the native tetramer (Wyatt *et al.* 2014).

1.3.2 Clusterin

1.3.2.1 Synthesis and Structure

The human *CLU* gene contains nine exons and is located on chromosome 8p21-p12. Expression of this gene occurs constitutively in most tissues and is upregulated in response to a number of cellular stresses, including ER and oxidative stress. This upregulation may be controlled by the binding of certain transcription factors, such as heat shock factor 1, c-Fos and activator protein 1 (Michel *et al.* 1997, Jin and Howe 1999, Bayon *et al.* 2004).

Translation from the canonical start codon on a CLU mRNA transcript results in the production of a 449 amino acid chain which undergoes a variety of post-translational modifications. First, the peptide is co-translationally translocated to the ER where a 22 amino acid secretory signal peptide is removed and low-level glycosylation occurs. The remaining chain is then cleaved into α- (205 amino acid)

and β- (222 amino acid) chains which are assembled into an antiparallel heterodimer linked by five disulfide bonds between small cysteine-rich cores on each of the chains. Upon transfer to the Golgi complex the assembled dimer is then heavily glycosylated with branched, N-linked carbohydrates. This process accounts for approximately 30% of the mass of mature, secreted CLU. Unfortunately, due to the heavy glycosylation, large regions of structural disorder and self-oligomerisation, no crystal structure has yet been solved for CLU. Computational analyses suggest that except for the disordered regions, the secondary structure is largely α-helical (Figure 1.5).

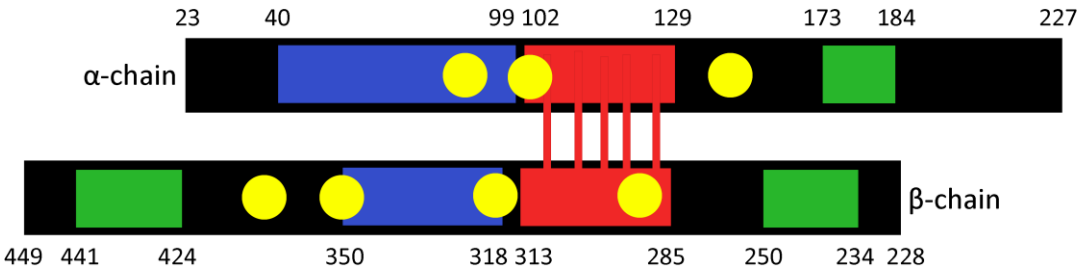

Figure 1.5: Schematic representation of the predicted secondary structure of secreted CLU. Secreted CLU is comprised of two chains connected by disulphide bonds between cysteine-rich cores (indicated in red). Coiled-coil alpha helices (blue) and amphipathic alpha helices (green) are predicted secondary structures. The seven known glycosylation sites are indicated by yellow circles (de Silva *et al.* 1990, Kirszbaum *et al.* 1992, Wilson and Easterbrook-Smith 2000, Zhang *et al.* 2003, Picariello *et al.* 2008).

1.3.2.2 Functions of clusterin

CLU is secreted by numerous mammalian cell types and is present at high levels in human cerebrospinal fluid (CSF), plasma, and seminal fluid (0.1 - 1.3, 35 - 105 and

2,000 – 15,000 μg.ml^{-1} respectively) (Murphy *et al.* 1988, O'Bryan *et al.* 1990, Polihronis *et al.* 1993). CLU was first described as mediating the 'clustering' of cultured cells (Blaschuk *et al.* 1983). Since then, a number of potential functions have been ascribed, including roles in lipid transport and regulation of apoptosis (Sansanwal *et al.* 2015). Additionally, CLU was the first secreted mammalian protein shown to have the ability to inhibit the aggregation of a broad range of misfolded proteins (Humphreys *et al.* 1999, Wilson and Easterbrook-Smith 2000). The extremely efficient chaperone action exhibited by CLU has led to general acceptance that the primary function of the protein is to act as an extracellular chaperone. This activity is believed to be similar to the sHsps, in that the chaperone holds the non-native protein in a state that prevents further aggregation (Humphreys *et al.* 1999, Poon *et al.* 2000). CLU binds to toxic prefibrillar species and slowly aggregating intermediates trapped on the off-folding pathway (Poon *et al.* 2002b), both preventing their precipitation and inhibiting the toxicity of protein aggregates on cultured cells (Yerbury *et al.* 2007b). As a result of these activities, CLU has been found co-localised with inclusions associated with a range of diseases, including age-related macular degeneration (Crabb *et al.* 2002), AD, and α-synucleinopathies CLU (Table 1.2).

Table 1.2: PDDs in which CLU has been found co-localised with insoluble protein deposits. Adapted from Yerbury *et al.* (2007a); additional references: Sasaki *et al.* (2002) and Zinkie *et al.* (2013).

Disease	Main constituent
α-synucleinopathies	αS
Age-related macular degeneration	Drusen
Alzheimer's disease	Aβ
Amyotrophic lateral sclerosis	SOD1
Atherosclerosis	LDL/ApoB100
Creutzfeldt-Jakob disease	PrP
Down's syndrome	Aβ
Familial British Dementia	ABri
Gelatinous drop-like corneal dystrophy	Keratoepithelin
Gerstmann-Straussler-Scheinker disease	PrP
HCHWA-Dutch type	Aβ
Lattice type 1 corneal dystrophy	M1S1
Pseudoexfoliation syndrome	PEX material

1.3.2.3 Biogenesis of intracellular clusterin

There is strong evidence that CLU accumulates intracellularly under stress conditions (Nizard *et al*. 2007). This usually coincides with a decreased level of CLU secretion. There are four proposed mechanisms which could account for the biogenesis of cytosolic CLU: (i) translation from mRNA transcripts lacking (or downstream of) the signal peptide, (ii) co-translational mistranslocation into the cytosol, (iii) retrotranslocation from the ER and/or Golgi, and (iv) uptake of extracellular CLU (summarised in Figure 1.6 and discussed below).

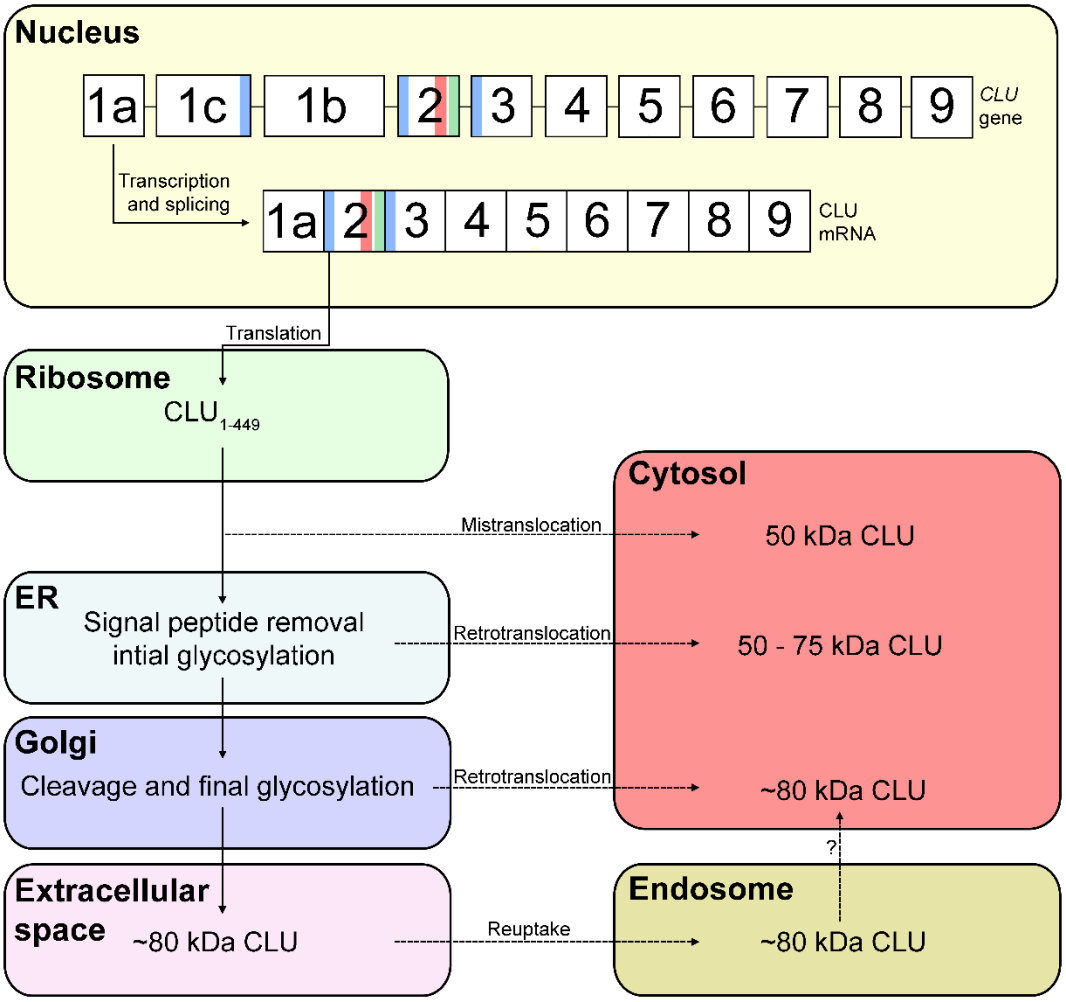

Figure 1.6: Biogenesis of intracellular CLU. Diagram showing the four proposed routes for the generation of intracellular CLU. Numbered boxes in the nucleus represent exons. The blue bars in the exons indicate start codons, the green bars indicates an unconventional start codon, and the red bar indicates the secretory signal sequence. Dashed lines show pathways thought or hypothesised to occur only primarily under stressed conditions.

At least three different CLU mRNA variants have been identified, which appear to be the products of transcription initiation at three distinct sites. Variant 1 is the canonical sequence that encodes secreted CLU and is overwhelmingly the most abundant CLU mRNA found in cells. Variants 2 and 3 each have large open reading frames upstream of the standard start codon which were shown to inhibit the

translation of these transcripts (Wong *et al.* 1994, Ota *et al.* 2004). Additionally, these transcripts have an extremely low abundance in comparison to variant 1, making up less than 0.35*%* of cellular CLU mRNA (even after stress-induced upregulation) (Prochnow *et al.* 2013) . Variant 3 contains a start codon upstream of the standard start codon, and it was originally suggested that translation from this position may impair the function of the secretory signal sequence, leading to the accumulation of an intracellular isoform of CLU (Rizzi *et al.* 2009b). However, this hypothesis was recently discredited, when the translation from this codon on variant 3 was shown to produce secreted CLU (Prochnow *et al.* 2013). Overall, the protein products from translation of variant 2 and 3 mRNA comprises an insignificant proportion of total CLU present within the cell, suggesting that the physiological impact of these forms is low.

An alternative splicing event (exon skipping) of variant 1 mRNA can produce a transcript with exon 2 removed (variant 1 Δex2) (Prochnow *et al.* 2013). As mentioned previously, exon 2 is the location of the secretory signal sequence. Therefore, translation from a start codon on exon 3 of variant 1 Δex2 mRNA results in aberrant translocation of the product into the cytosol, leading to an unglycosylated, uncleaved, 45 - 50 kDa intracellular isoform of CLU. This start codon is present on all transcripts so far identified and translation from any of these will result in the production of an identical isoform. A slightly larger variant can be generated by translation initiation from an unconventional CUG codon located on

exon 2 downstream of the secretory signal sequence. This is likely a functional homologue of the aforementioned isoform, due to the identical translocation into the cytosol and the subsequent lack of post-translational modifications. Often in the literature, any intracellular CLU is assumed to be the result of this alternative transcription. Recently however, Prochnow *et al*. (2013) have shown that this typically accounts for less than 5% of total cell-associated CLU, suggesting that this process does not account for the observation of large amounts of intracellular CLU.

Co-translational mistranslocation refers to protein products that fail to translocate into the ER despite the presence of a secretory signal peptide. Efficient co-translational translocation is dependent upon the binding of the secretory signal peptide to the signal recognition particle. This then facilitates the interaction between the nascent polypeptide chain and a receptor on the ER membrane (Akopian *et al.* 2013). In the case of CLU, failure of this process would result in the production of an unglycosylated, uncleaved isoform, consisting of all amino acids (1-449) localised in the cytosol. It was shown that unglycosylated CLU can accumulate in the cytosol of HeLa cells treated with a cotransin (Choi *et al.* 2013), a class of compounds which inhibit the translocation of proteins into the ER (Maifeld *et al.* 2011). A similar effect was reportedly caused by ER stress induced by thapsigargin (Tg), though the increase in unglycosylated CLU appears to be minor (Choi *et al.* 2013). Rohne *et al.* (2014) suggest that the intracellular presence of unglycosylated 55 kDa CLU may be accounted for by the mistranslocation of the

product into the cytosol. However, this possibility is raised without direct evidence of the subcellular location of this product. There is very limited evidence for the endogenous production of intracellular CLU through this pathway, likely due to the difficulties in establishing the exact structure and origin of the various similar isoforms.

As previously described, many newly synthesised proteins are translocated across the ER membrane, including proteins on the secretory pathway, membrane proteins, as well as ER and Golgi proteins. Retrotranslocation is the reversal of this process, that is, the retrieval of proteins from the secretory network back into the cytosol. Retrotranslocation was first characterised as a pathway for the removal of misfolded proteins from the ER (Tsai *et al.* 2002). However since then it has been shown that processed, native proteins can undergo retrotranslocation, including the ER chaperone calreticulin (Afshar *et al.* 2005). Both pre-secretory (unprocessed or partially processed CLU on the secretory pathway) and secretory (mature) CLU can be retrotranslocated under ER stress conditions (Nizard *et al.* 2007); it is possible that additional (e.g. oxidative, proteasomal) stress can also induce this pathway but it has not yet been described. CLU retrotranslocation is thought to be facilitated by an interaction with ER-resident chaperone binding immunoglobulin protein (BiP), which can both stabilise CLU and prevent secretion (Li *et al.* 2013).

Pre-secretory CLU retrotranslocated from the ER would be uncleaved and hypoglycosylated. As such, a 45-60 kDa band would be expected by sodium dodecyl sulphate-polyacrylamide gel electrophoresis (SDS-PAGE) (Nizard *et al.* 2007), which has made unambiguous identification challenging. Further complicating matters, Nizard *et al.* (2007) showed that proteolytically cleaved and fully glycosylated CLU can by subject to polyubiquitination and proteasomal degradation, suggesting that secretory CLU can also travel back from the Golgi to the ER for retrotranslocation. Other than subcellular localisation, this proteolytically cleaved and fully glycosylated CLU is indistinguishable from mature CLU secreted from cells or remaining on the pathway immediately prior to secretion.

The majority of the literature regarding the cellular uptake of extracellular CLU has focussed on the uptake of CLU complexed to misfolded client proteins. Megalin/glycoprotein 330 and lipoprotein receptor-regulated protein (LRP) have been shown to bind and internalise CLU-Aβ complexes (Zlokovic *et al.* 1996, Hammad *et al.* 1997); similarly, scavenger receptors appear likely to facilitate the internalisation of CLU-glutathione S-transferase and CLU–citrate synthase complexes (Wyatt *et al.* 2011). However, each of these authors also noted at least a small proportion of non-complexed CLU being endocytosed. Similarly, apolipoprotein E receptor 2 and very low density lipoprotein receptor have both been implicated in the uptake of free CLU (Kounnas *et al.* 1995, Bartl *et al.* 2001, Leeb *et al.* 2014). Following endocytosis by each of the aforementioned receptors,

CLU was found to go down the endocytic pathway, leading to degradation by lysosomes. It has been suggested by Debure *et al.* (2003) that CLU may escape this pathway in a manner similar to bacterial toxins, although this has yet to be established in the literature.

1.4 Proteostasis failure and disease

1.4.1 Toxic protein oligomers

Elaborate protein quality control systems (including extracellular chaperones) exist to maintain organismal proteostasis. However, the decline or failure of these systems can result in aberrant protein aggregation, leading to the pathology of PDDs. It was initially thought that the accumulation of insoluble amyloid deposits was the driving force behind PDD pathogenesis (the 'amyloid hypothesis') (Selkoe 1991). It was believed that mature amyloid fibrils were cytotoxic and would disrupt normal cellular activity when deposited (Selkoe 1991). However, in neurodegenerative diseases (such as AD) the degree of cognitive impairment a patient experiences is poorly correlated with the number of deposits in the brain (Coria *et al.* 1993, Dickson *et al.* 1995). This suggests that mature amyloid fibrils may not be the primary cause of pathologies in all cases (Zhu *et al.* 2000, Sousa *et al.* 2001). In fact, oligomeric intermediates generated along the amyloid-forming pathway appear to be more cytotoxic than mature fibrils (Dahlgren *et al.* 2002, Kayed *et al.* 2003) and may be the causative agent of pathology in many PDDs

(Stefani 2010). As discussed above, the formation of aggregates occurs independently of the specific amino acid sequence. In a similar fashion the toxicity of the aggregates is not dependent upon the specific amino acid sequence. Rather, it appears that toxicity arises from a common aspect of the supramolecular structure of the aggregate, such as exposed regions of hydrophobicity (Bucciantini *et al.* 2002). Understanding how oligomers cause toxicity is currently a very active field of research, and a number of hypotheses have been put forward to explain how toxicity arises. It has been demonstrated that Aβ protofibrils (Lasagna-Reeves *et al.* 2011) and oligomers (Jang *et al.* 2013) can insert into cell membranes and form pores, significantly disrupting the cell membrane permeability (Kayed and Lasagna-Reeves 2013). Similarly, oligomers appear to bind to certain cell surface receptors and disrupt their function (Um *et al.* 2012, Morkuniene *et al.* 2015). Like Aβ, α-synuclein (αS) oligomers are believed to cause cell death through membrane-interactions (Winner *et al.* 2011). Recently, Aβ oligomers were shown to directly interact with astrocytes and microglia to cause inflammation, something that was initially believed to be a byproduct of the disease (Minter *et al.* 2016, Sengupta *et al.* 2016). Thus, while it is widely accepted that protein aggregates can cause neurodegenerative disease, the exact mechanism(s)of toxicity remains unclear.

1.4.2 Amyotrophic lateral sclerosis

1.4.2.1 Overview

ALS is a currently untreatable adult-onset motor neuron disease that is characterised by aberrant protein aggregation within motor neurons. The disease features progressive death of motor neurons in both the brain and spinal cord. Death typically occurs as a result of respiratory failure, pneumonia or cardiac arrhythmias with a median survival of just 3 years after diagnosis. The disease has a prevalence of approximately 6 per 100,000 per year with incidence rates peaking between 65 – 74 years of age (McGuire *et al.* 1996). Three types of ALS have been identified based on epidemiologic and genetic factors: familial (~ 5 – 10% of cases, fALS), sporadic (90+% of cases, sALS) and Western Pacific forms (affects individuals in local geographical clusters) (Gajdusek and Salazar 1982, Kuzuhara *et al.* 2001). fALS cases usually show an autosomal dominant form of inheritance (Kurland and Mulder 1955, Siddique *et al.* 1991), but can also be autosomal recessive (Hentati *et al.* 1994) or X-linked (Deng *et al.* 2011). The most common cause of fALS is the hexanucleotide (GGGGCC) repeat expansion of *C9orf72* which is found in approximately one third of European cases (Renton *et al.* 2011). Other mutated genes known or believed to cause fALS include *SOD1* (Rosen *et al.* 1993), *TARDBP* (Gitcho *et al.* 2008) and *FUS* (Kwiatkowski Jr *et al.* 2009).

1.4.2.2 Proteostasis failure in ALS

There are a number of findings that support a role for UPS dysfunction in ALS disease pathology (Bendotti *et al.* 2012). Perhaps the most compelling is the motor neuron-specific Rpt3 (a critical proteasomal subunit) knock-out mouse that replicates ALS pathology, including motor neuron loss, gliosis and transactive response DNA binding protein-43 kDa (TDP-43), fused in sarcoma (FUS), optineurin and ubiquilin 2 mislocalisation (Tashiro *et al.* 2012). Furthermore, treating transgenic cell lines with proteasome inhibitors enhances aggregation and/or aggresome formation by mutant superoxide dismutase 1 (SOD1) and TDP-43 (Johnston *et al.* 2000, Lee *et al.* 2002, van Eersel *et al.* 2011).

Along with the UPS, autophagy is one of the two major intracellular proteolytic pathways and plays a crucial role in the degradation of non-native proteins, including those associated with ALS. Like the UPS, there is mounting evidence that dysfunction or dysregulation of autophagy may contribute to ALS pathology. Autophagy appears to be upregulated in motor neurons in both ALS patients (Sasaki 2011) and various ALS models, such as SOD1 G93A mice (Morimoto *et al.* 2007, Li *et al.* 2009, Zhang *et al.* 2011). Mice lacking expression of *Atg7* (responsible for inducing autophagy) in the central nervous system suffered neurodegeneration, motor deficits and ubiquitinated inclusion bodies (Komatsu *et al.* 2006). This suggests that autophagic failure alone can cause disease phenotypes. Rapamycin is a chemical inducer of autophagy through the mTOR pathway and has proven to

alleviate some effects of Huntington's and Parkinson's disease (PD) (Sarkar *et al.* 2008, Malagelada *et al.* 2010). In ALS, rapamycin induction of autophagy in a transgenic mouse model of frontotemporal lobar dementia with TDP-43 pathology partially rescued motor function and reduced the amount of TDP-43 immunoreactive inclusion bodies present in motor neurons (Wang *et al.* 2013). Similarly, rapamycin treatment was shown to reduce the cytosolic localisation of mutant TDP-43 in a transgenic cell line (Caccamo *et al.* 2009). Similarly to most of the results obtained with rapamycin, the level of TDP-43 and TDP-25 aggregates were decreased in transfected human cells when treated with trehalose, another inducer of autophagy (Wang *et al.* 2010).

Like the UPS and autophagy, defects within ERAD have been reported to occur in ALS (Nishitoh *et al.* 2008). The mechanism by which ERAD deficiency may cause or contribute to neurodegeneration remains unclear, although one possibility is through the induction of ER stress. ER stress is caused by the accumulation of non-native proteins within the ER lumen, and has been implicated in diseases such as ALS, Huntington's disease and AD (Rao and Bredesen 2004). In ALS specifically, both mutant SOD1 and mutant TDP-43 have been shown to cause ER stress by the specific inhibition of ERAD and an unknown mechanism, respectively (Nishitoh *et al.* 2008, Walker *et al.* 2013). ER stress may be responsible for the overload of the proteostasis machinery and therefore the cytosolic aggregation of these proteins (Yamagishi *et al.* 2007, Walker *et al.* 2013).

As mentioned previously, various subclasses of chaperones are responsible for the refolding or stabilisation of non-native proteins, as well as the unfolding of proteins for further processing. The age-related overloading of this chaperone machinery is commonly hypothesised to contribute to late-onset neurodegenerative diseases (Csermely 2001). As expected, there is significant evidence that molecular chaperones mediate the clearance of ALS-associated proteins. For example, HspB8 facilitates the autophagic degradation of mutant SOD1 and cytosolic TDP-43 (Crippa *et al.* 2010). Furthermore, the upregulation of the sHsp CG14207 provided complete and partial rescue of TDP-25 and TDP-43 pathology respectively in transgenic *Drosophila* (Gregory *et al.* 2012).

1.4.2.3 TDP-43 structure and function

TDP-43 is a highly conserved 414 amino acid member of the heterogeneous nuclear ribonucleoprotein family of proteins, which influence most gene expression pathways. TDP-43 is predominantly found in the nucleus of cells, however it is also actively shuttled to and from the cytosol (Buratti and Baralle 2008). Both structurally and functionally, the distinguishing features of TDP-43 are the two 60-amino acid long RNA recognition motifs (RRMs) and a C-terminal glycine-rich domain. RRM1 enables TDP-43 to bind preferentially (but not exclusively) to UG-rich single-stranded RNA and DNA sequences, as well as double stranded DNA with TG repeats (Buratti and Baralle 2001) (Polymenidou *et al.* 2011). The function of RRM2 remains unclear, it is not required for RNA binding but does interact with

single-stranded DNA (Kuo *et al.* 2009). The C-terminal glycine-rich region appears to be responsible for protein-protein interactions. The lack of secondary structures in this region suggests that conformational elasticity within this region can accommodate the large number of TDP-43 binding partners (Chen *et al.* 2010, Lagier-Tourenne *et al.* 2010).

Through the binding of RNA/DNA by the RRMs, TDP-43 plays a role in a wide variety of DNA and RNA processing systems. The most well characterised role of TDP-43 is the regulation of pre-mRNA splicing (Lagier-Tourenne *et al.* 2010). Binding of the protein to UG-rich regions of pre-mRNA has been shown to alter the splicing of various mRNAs, including cystic fibrosis transmembrane regulator exon 9, breast cancer 1 mutated substrate and polymerase δ interacting protein (Buratti *et al.* 2004, Shiga *et al.* 2012). TDP-43 also plays a role in the nuclear and cytosolic post-transcriptional regulation of microribonucleic acid (miRNA) expression. Through association with the nuclear Drosha complex (the proteins that mediate the early steps of miRNA maturation), TDP-43 facilitates the cleavage of a subset of precursor miRNA (Kim *et al.* 2009, Gregory *et al.* 2012).

Like nuclear TDP-43, cytosolic TDP-43 is involved in a number of RNA processing roles, although these are less well established. TDP-43 is found in RNA-transporting granules in neurons, suggesting that the protein has a role in the subcellular

translocation of RNA (Lagier-Tourenne *et al.* 2010). TDP-43 also interacts with many proteins that regulate translation, and acts as a translational repressor *in vitro* (Wang *et al.* 2008). TDP-43 is also a component in mRNA stress granules (Liu-Yesucevitz *et al.* 2010). These small complexes of mRNA and various proteins, including T-cell-restricted intracellular antigen-1, are formed under conditions of stress in order to protect and sequester mRNA not directly required for coping with stress. The stress granules can either dissipate when the cell has recovered (Anderson and Kedersha 2009) or progress to form inclusions (Parker *et al.* 2012).

Mutations in the TDP-43 gene (*TARDBP*) are believed to be sufficient to cause ALS, and TDP-43 inclusions are a pathological hallmark of the disease (discussed in depth in section 4.1.1) (Gitcho *et al.* 2008). As mentioned in section 1.3.2.2, CLU is able to reduce the toxic effects of misfolded proteins present in the extracellular space. Additionally, it was discussed how CLU can be rerouted from the secretory system to the cell cytosol. A detailed introduction to the known roles of intracellular CLU, and how it may affect intracellular protein aggregation (such as that by TDP-43) is provided in section 4.1.2.

1.5 Aims

The work presented in this thesis centres around the chaperone action of CLU. Given that CLU can be retrotranslocated under ER stress, and that ER stress

features in ALS pathology, it was hypothesised that CLU may affect the intracellular processing of the ALS-associated protein, TDP-43. To attest this hypothesis, a technique was developed to would allow the quantification of TDP-43 inclusions in cells. Thus, the aims of the work presented in Chapters 3 and 4 were to:

i. Develop a technique to allow the rapid and accurate enumeration of inclusions present in a population of cultured cells
ii. Investigate the potential of CLU to affect the *in vitro* aggregation and *in vivo* processing of TDP-43

In a distinct but thematically-related piece of work, Chapter 5 describes the use of single-molecule techniques to investigate the effects of CLU (and to a lesser extent, α_2M) on the aggregation, structure and toxicity of protein aggregates.

Chapter 2:

General Methods

2. General Methods

2.1 Protein quantification

Protein concentration was routinely measured using an appropriate extinction coefficient and absorbance at 280 nm (A_{280}) using either a Nanodrop 2000 UV-Vis Spectrophotometer (Thermo Fisher Scientific, USA) or a Spectra Max Plus 384 plate reader (Molecular Devices, USA). If the buffer absorbed ultraviolet (UV) light (e.g. contained imidazole) a bicinchoninic acid (BCA) assay was used instead. Briefly, 25 µl of protein was added to a well of a 96 well microtiter plate. BCA working reagent (50 parts 25 mM BCA, 190 mM sodium carbonate, 8 mM sodium tartrate, 112 mM sodium bicarbonate, pH 11.25 to 1 part 4% w/v copper sulphate pentahydrate) was then added to the plate (200 µl.well^{-1}) and incubated until sufficient colour had developed (up to 1 h at 37 °C or 15 min at 60 °C). Absorbance was measured at 562 nm using a Spectra Max Plus 384 plate reader and concentration was determined by comparison against bovine serum albumin (BSA) standards (0 – 1 mg.ml^{-1}).

2.2 SDS and native PAGE

The purity and molecular weight of protein samples were quantified by SDS-PAGE. A 10% v/v polyacrylamide resolving gel was overlayed with a 5% v/v stacking gel in a Hoefer^{TM} SE 250/260 SDS-PAGE apparatus (GE Healthcare Life Sciences, USA) at a thickness of either 0.75 or 1.5 mm. Samples were boiled in 60 mM Tris pH 6.8, 1% w/v SDS, 10% v/v glycerol, 0.01% w/v bromophenol blue for 5 min before being

loaded onto the gel, and gels were electrophoresed at 80 - 120 V in 96 mM glycine, 25 mM Tris, 0.1% w/v SDS, pH 8.25. The gels were then stained in Coomassie Blue R250 (0.2% w/v), methanol (40% v/v) and glacial acetic acid (10% v/v) and destained in the same buffer in the absence of Coomassie Blue.

Native PAGE analysis of α_2M was performed as above with slight modification. A 5% v/v resolving gel was overlayed with a 4% v/v stacking gel without the addition of SDS. Samples were loaded in 50 mM Tris, 400 mM glycine, pH 8.3 (without boiling) and the gels were electrophoresed in 40 mM Tris, 40 mM boric acid, pH 8.6 for 2 - 4 h at 100 V.

2.3 Western blotting

Proteins electrophoresed through an SDS-polyacrylamide gel were transferred onto a nitrocellulose membrane at 4 °C either overnight (20 V) or for 1 h (80 V) using a Western Transfer Unit (Bio-Rad, USA). The membrane was then blocked for 1 h at room temperature (RT) with blocking solution (1% w/v heat-denatured casein in phosphate buffered saline (PBS) containing 0.01% w/v thimerosal (HDC/PBS) or 5% w/v skim milk in PBS containing 0.1% v/v Triton X-100. The membrane was then incubated with an appropriate antibody (1 h at RT), which was first diluted in blocking solution according to the manufacturer's instructions. Unbound antibody was removed by washing the membrane three times with PBS containing 0.1% v/v Triton X-100 followed by three more washes with PBS. An appropriate secondary

antibody (conjugated to horseradish peroxidase (HRP)) was also diluted in blocking solution and incubated with the membrane for 1 h at RT. The membrane was then washed as described above. Depending on the sensitivity required, bound antibodies were detected using enhanced chemiluminescence with either Supersignal West Pico Chemiluminescent Substrate or Supersignal West Femto Chemiluminescent Substrate (both ThermoFisher Scientific, USA), according to the manufacturer's instructions. Bands were detected using either X-ray film (Amersham Hyperfilm; GE Life Sciences, USA) or a Gel Doc imaging system (Bio-Rad, USA). Band quantification was performed using ImageJ (version 1.48) (Schneider *et al.* 2012).

2.4 Tissue culture

2.4.1 Media

U251, Neuro-2a (N2a) and SH-SY5Y cells were cultured in Dulbecco's Modified Eagle's Medium/Ham's Nutrient Mixture F-12 (DMEM/F12); human embryonic kidney-293 (HEK-293) and HEK-TREX cells were cultured in high glucose (HG) DMEM/F12. All media was supplemented with 10% v/v foetal bovine serum (FBS), sterile filtered and warmed to 37 °C before use; cells were incubated at 37 °C and 5% v/v CO_2. Tissue culture was performed in a sterile laminar flow biosafety cabinet.

2.4.2 Passaging adherent cell lines

Media containing FBS was first removed from the cells to be passaged, which were then rinsed with either DMEM/F12 or HG DMEM/F12. Sufficient trypsin/ethylenediaminetetraacetic acid (EDTA; 0.05% w/v) was added to cover the cell monolayer, and then incubated at 37 °C for up to 5 min. If required the flask was gently tapped to promote the detachment of cells from the flask. The cells were then rinsed as above and centrifuged at 300 x *g* for 5 min at RT. After the supernatant was discarded the cells were resuspended in 1 ml of growth medium and reseeded at 10 – 50% of the original density, dependent on cell type and future use.

2.4.3 Transfection

Cells were transfected using either X-tremeGENE HP (Roche, Switzerland) or Lipofectamine 2000 (Invitrogen, USA) according to the manufacturer's instructions. Briefly, 1 µg plasmid DNA was used per ~3.5 cm^2 of cells to be transfected, present at approximately 70% (X-tremeGENE HP) or 90% (Lipofectamine 2000) confluency. Unless optimised, a ratio of transfection reagent (µl):DNA (µg) of 3:1 or 4:1 was used for X-tremeGENE HP and Lipofectamine 2000, respectively. Transfectants were analysed or treated further 24 - 48 h after transfection.

2.4.4 Cryogenic storage

Cells were first removed from flasks with trypsin/EDTA and pelleted as previously described. Following resuspension in DMEM/F12 supplemented with FBS (50% v/v) and dimethyl sulfoxide (DMSO; 10% v/v) the solution was aliquoted (1 ml) into sterile cryovials. These were then placed in a chilled Cryo 1 °C Freezing Container (Nalgene, Australia) containing isopropanol and stored in a -80 °C freezer overnight, before being transferred to liquid nitrogen for long-term storage.

2.5 Protein purification

2.5.1 Amyloid-β

Synthetic Aβ was synthesised by Bachem (Switzerland) with either Alexa Fluor (AF)-488 or HiLyte Fluor (HF)-647 conjugated to an N-terminal cysteine (hereafter referred to as $A\beta^{C}$):

$A\beta^{C}$-AF488

H-Cys(maleimido-C_5-AF488)-Asp-Ala-Glu-Phe-Arg-His-Asp-Ser-Gly-Tyr-Glu-Val-His-His-Gln-Lys-Leu-Val-Phe-Phe-Ala-Glu-Asp-Val-Gly-Ser-Asn-Lys-Gly-Ala-Ile-Ile-Gly-Leu-Met-Val-Gly-Gly-Val-Val-Ile-Ala-OH

Aβ^{C}-HF647

H-Cys(maleimido-C_2-HF647)-Asp-Ala-Glu-Phe-Arg-His-Asp-Ser-Gly-Tyr-Glu-Val-His-His-Gln-Lys-Leu-Val-Phe-Phe-Ala-Glu-Asp-Val-Gly-Ser-Asn-Lys-Gly-Ala-Ile-Ile-Gly-Leu-Met-Val-Gly-Gly-Val-Val-Ile-Ala-OH

To ensure the peptide stocks were free from pre-aggregated 'seeds', the Aβ^{C} was first dissolved in 10 mM NaOH to approximately 10 mg.ml^{-1}. The sample was loaded on to a BioSep-SEC-s2000 column (Phenomenex, USA) pre-equilibrated in SSPE buffer (10 mM sodium phosphate, 1 mM EDTA, 150 mM NaCl, pH 7.4) on a 1260 Infinity HPLC system (Agilent Technologies, USA). The elution was monitored by absorbance of each fluorophore (495 nm or 650 nm for AF488 and HF647 respectively) and the peak corresponding to monomeric Aβ^{C} was collected. The concentration of each fraction was determined spectrophotometrically using the absorbance of the fluorophores, as above. Monomeric Aβ^{C} was aliquoted into 50 µl samples, snap frozen in liquid nitrogen and stored at -80 °C.

2.5.2 α-Synuclein

Purified αS with the A90C mutation (αS^{A90C}) was initially a gift from Prof. Chris Dobson (University of Cambridge, UK) but was later purified from bacteria transformed with the pT7-7 vector containing αS^{A90C} cDNA (a gift from Dr. Laura Tosatto, University of Cambridge, UK).

Electrocompetent BL21*(DE3) and DH5α *E. coli* were produced by first inoculating 5 ml Luria-Bertani medium (LB; tryptone (1% w/v), yeast extract (0.5% w/v) and NaCl (1% w/v), pH 7), and incubating overnight at 37°C. This culture was then added to 95 ml of LB and incubated until the OD_{600nm} reached 1.0. The cells were then washed in 100 ml, 50 ml and then 20 ml of cold Milli-Q H_2O to reduce conductivity. All centrifugation steps were performed at 5,000 x *g* for 15 minutes, 4 °C in a Sorvall RC6+ Centrifuge (ThermoFisher Scientific, USA). The cells were resuspended in 0.5 ml chilled 10% v/v glycerol in dH_2O, aliquoted in 40 µl fractions and stored at -80 °C until use.

One aliquot of electrocompetent BL21*(DE3) (for protein expression) or DH5α (for plasmid storage) per transformation was slowly thawed on ice, and then gently mixed with ~ 40 ng of pT7-7 containing the mutant αS insert. The cells were transformed at 2.4 kV, 25 µFD, 200 Ω and time constant using a Gene Pulser II Electroporation System (Bio-Rad, USA). The bacteria were then transferred into 500 µl warm LB and shaken at 200 rpm at 37°C for 1 h, before various amounts (50 – 300 µl) were spread on LB agar plates containing 100 $\mu g.ml^{-1}$ ampicillin and incubated overnight at 37 °C to select for positive transformants. The plasmid was purified using a CompactPrep Plasmid MidiKit (Qiagen, Germany) and eluted into dH_2O for storage at -20 °C. The identity of the insert was confirmed by sequencing using a forward primer for the T7 promoter.

Both wild-type (WT) αS and αS^{A90C} were purified using the following procedure. Glycerol stocks of BL21*(DE3) *E. coli* containing WT αS in the pET-24a(+) expression vector were a gift from Dr. Heath Ecroyd (University of Wollongong, Australia). Protein expression in BL21*(DE3) containing plasmids encoding one of the above proteins was induced by incubation at 37 °C, 180 rpm for 4 h in the presence of 500 µM isopropyl β-D-1-thiogalactopyranoside. The bacteria were then pelleted at 5,000 x *g* for 30 min before being resuspended (3 $ml.g^{-1}$ bacteria) in 50 mM Tris, 100 mM NaCl, pH 8.0 supplemented with a Complete® protease inhibitor tablet (Roche, Switzerland). The solution was briefly vortexed before the addition of lysozyme (0.25 $mg.ml^{-1}$), and incubated on ice for 20 min with gentle rocking. Deoxycholic acid (Sigma Aldrich, USA) was added to a final concentration of 3.5 mM and the solution was incubated at 37 °C for 30 min. DNase I (Roche, Switzerland) was then added to 0.35 $\mu g.ml^{-1}$ before a further 20 min incubation at RT with rocking. Debris was then pelleted at 100,000 x *g* at 4 °C for 30 min. The supernatant was collected and dithiothreitol (DTT; 10 mM), polyethylenimine (0.3% v/v) and EDTA (1 mM) were added before being mixed at RT for 20 min. Any precipitate was then pelleted as above, and HCl was added dropwise to the supernatant until the pH reached 4 - 5. The exact pH varied slightly between purifications/variant and was chosen as the pH at which the precipitation of proteins was maximum. This precipitate was again pelleted as above and the pH of the supernatant was slowly raised back to 8.0 with NaOH. The bacterial extract was stored at -20 °C until further purification.

The thawed extract was buffer exchanged into 1 mM EDTA, 20 mM Tris pH 8.0 by dilution and concentration in a 3,000 molecular weight cut-off (MWCO) Vivaspin 20 (GE Healthcare Life Sciences, USA). The solution was centrifuged at 20,000 x *g* before being passed over a HiPrep DEAE FF 16/10 column (GE Healthcare Life Sciences, USA). Proteins were eluted using a 0 - 25% gradient of 20 mM Tris, 1 mM EDTA, 2 M NaCl pH 8.0. The sample was then concentrated and further purified by passage over a HiPrep 26/60 Sephacryl S-300 HR (GE Healthcare Life Sciences, USA) in 50 mM sodium phosphate pH 7.4. A Sephacryl S-300 was used as it was the only column available when the protocol was developed. A column designed for small proteins could be used for better separation from contaminants of similar molecular weights to αS. However, small contaminants were not found to be present in the αS samples purified using this protocol when assessed by SDS PAGE on a 12% gel (see section 5.3.2). The fractions containing pure αS were pooled, concentrated and aliquoted for storage at -20 °C.

2.5.3 Clusterin and α_2-macroglobulin

CLU and α_2M were purified from human blood as described below (University of Wollongong Human Ethics Approval H202/080).

2.5.3.1 Clusterin

CLU was purified from human blood (donated by Wollongong Hospital Pathology Unit; NSW, Australia) and supplemented with 10 mM sodium citrate. The plasma

was collected by centrifugation at 800 x *g* for 30 min at 4 °C and stored at -20 °C until required. Plasma (~ 500 ml) was thawed in a 37 °C water bath after the addition of a Complete® protease inhibitor tablet (Roche, Switzerland). The plasma was vacuum filtered through a GF/C glass microfibre filter (MicroAnalytic Products Inc., USA) followed by a 0.45 µm cellulose nitrate filter (Sartorius Stedim Biotech, Germany) to remove any particulates. Two Sepharose columns (Phenomenex, USA), each containing ~25 mg bound mouse monoclonal anti-CLU antibodies (G7 or 41D), were connected in tandem to an EP-1 Econo-Pump (Bio-Rad, USA). The columns were equilibrated into PBS/azide (PBS/Az), pH 7.4 and 400 - 500 ml of plasma was loaded. The columns were washed sequentially with PBS/Az and PBS + 0.5% Triton X-100 pH 7.4 to remove any bound lipids, before being re-equilibrated with PBS/Az. Weakly bound proteins were eluted with 200 mM sodium acetate and 500 mM NaCl, pH 5. Bound CLU was then removed with 2 M GdHCl pH 7.4 and dialysed into 20 mM 2-(N-morpholino)ethanesulfonic acid (MES), pH 6. The immunoaffinity columns were stored in PBS/Az at 4 °C.

A 5 ml HiTrap SP XL column (GE Healthcare Life Sciences, USA) attached to an Äkta Explorer (Amersham Pharmacia Biotech, UK) was equilibrated in 20 mM MES pH 6. The sample containing CLU was loaded and the flowthrough (containing CLU) was collected. Any bound contaminating proteins were eluted with 20 mM MES, 1 M NaCl, pH 6. The purity of the CLU was confirmed to be >95% (data not shown) by

SDS PAGE on a 10% gel and the protein was dialysed into PBS/Az for short-term storage (4 °C) or PBS for long-term storage (-20 °C).

2.5.3.2 α_2-Macroglobulin

α_2M was purified from human blood donated by myself or volunteers from the University of Wollongong, Australia. After collection, the blood (~100 ml) was immediately supplemented with heparin (0.4 $mg.ml^{-1}$ final) and centrifuged as previously described (section 2.5.3.1) to isolate the plasma. NaCl (1 M), HEPES (20 mM) and an EDTA-free Complete® protease inhibitor tablet (Roche, Switzerland) were added to the plasma. The plasma was filtered through a 0.45 µm nitrocellulose filter (Sartorius Stedim Biotech, Germany) and loaded onto a 5 ml HiTrap IMAC Sepharose column (GE Healthcare Life Sciences) freshly charged with Zn^{2+} and equilibrated in binding buffer (20 mM HEPES, 1 M NaCl, pH 7.4). The column was then washed with binding buffer until the A_{280} reached a steady baseline. Weakly bound proteins were removed with binding buffer containing 20 mM imidazole. Bound α_2M was then eluted with binding buffer containing 500 mM imidazole, pH 7.4. If required, any contaminants were removed by size exclusion chromatography (SEC) using a 320 ml column packed with Sephacryl S-300 HR (GE Healthcare Life Sciences, USA) equilibrated in PBS/Az. The protein was then concentrated using a Vivaspin 20 (30,000 MWCO) (GE Healthcare Life Sciences, USA) and stored at 4 °C in PBS/Az. The purity of α_2M was determined to

be >95% by 8% SDS-PAGE and the structure was determined by native PAGE analysis.

2.5.3.3 Shipping

Part of the work (Chapter 5) presented in this thesis was undertaken at the University of Cambridge, UK. For these experiments both CLU and α_2M was purified at UOW and shipped to the UK on dry ice. For α_2M, 100 mM sucrose was added to protect the native structure during freezing (Wyatt *et al.* 2015). Upon receiving the protein it was extensively dialysed against PBS/Az to remove the sucrose and the structure was once again assessed as above.

Chapter 3:

Quantification of Protein Inclusions in Mammalian Cells

3. Quantification of Protein Inclusions in Mammalian Cells

3.1 Introduction

3.1.1 Requirement for quantification of protein inclusions

As discussed at length in Chapter 1, the aberrant formation of inclusions both within and outside of cells is a hallmark of the pathology of many incurable diseases. Current methods of quantifying the number of inclusions in cell models of neurodegenerative diseases suffer from several drawbacks (see section below). Therefore, a truly high-throughput, unambiguous technique for the quantification of protein inclusions (large insoluble cytosolic protein aggregates) in mammalian cells would be of great use to the study of neurodegenerative diseases. Such a technique would be invaluable to evaluate the capacity of the proteostasis network to mitigate protein misfolding and to elucidate the effects of novel therapeutics on the quantity and relative sizes of inclusions in cells. In this chapter, a flow cytometric method for quantifying and characterising inclusions within cells is described, termed *flo*w cytometric characterisation of *i*nclusions and *t*rafficking (FloIT).

3.1.2 Existing methods for inclusion quantification

The quantification of inclusion bodies within cells is most commonly performed using images generated by fluorescence microscopy. Manually counting small inclusions is of questionable accuracy due to the limited resolution of confocal microscopes and capturing and analysing images is slow. Automation of this process with high-content image screening and self-learning algorithms has addressed some

of these issues but, in turn, has introduced new technical difficulties. Inaccurate treatment of clustered cells, poor performance on images with high background fluorescence, inclusions aligned in the z-axis (epifluorescence images) or away from the plane of focus (confocal images) all present challenges for image-based analysis (Daub *et al.* 2009, De Vos *et al.* 2010, Sommer and Gerlich 2013).

Recently, inclusions formed by the aggregation of polyglutamine-expanded huntingtin (Htt) were detected using a flow cytometric technique, called *pul*se *s*hape *a*nalysis (PulSA) (Ramdzan *et al.* 2012, Ramdzan *et al.* 2013). PulSA utilizes the differences in the height and width of the fluorescence peaks to differentiate between cells containing a fluorescently tagged protein having a diffuse cytosolic versus a punctate distribution (the latter is associated with protein inclusions). Thus, in theory, cells can be separated into two populations, those with and without inclusions, by setting gates on a plot of pulse height versus pulse width. However, while PulSA is a useful tool for some protein aggregation models, it lacks the resolution required to detect inclusions formed from a variety of proteins (see section 4.3) and thus a more broadly applicable technique is required.

3.1.3 FloIT

The work presented in this chapter extends upon the findings of Shiber *et al*. (2014), who showed that aggregates formed in heat shocked yeast cell cultures were quantifiable by flow cytometry of cell lysates, when used in conjunction with

strict timing and protein concentration assays (Shiber *et al.* 2014). Here, with FloIT, we extended and enhanced this concept to quantifying inclusions to mammalian cell-based models of neurodegeneration-associated protein aggregation. Using FloIT, the number of inclusions is normalised to the number of nuclei in each sample, which allows for rapid quantitative comparison across samples. This chapter describes the validation and potential uses of FloIT as a technique.

3.2 Methods

3.2.1 Plasmids and cloning

M337V TDP-43 cDNA was cloned by Genscript (USA) into pCMV6-AC-GFP (Origene, USA) to generate a mutant TDP-43 construct C terminally tagged with TurboGFP (tGFP). HA-NFAT1(1-460)-eGFP (nuclear factor of activated T-cells; a fluorescently-labelled transcription factor) was a gift from Anjana Rao (Addgene plasmid #11107) (Aramburu *et al.* 1999). Htt-mCherry encoding constructs, pT-Rex-Htt46Q-Tc1-mCherry and pT-Rex-Htt25Q-Tc1-mCherry, were gifts from Dr. Danny Hatters (University of Melbourne, Australia). peGFP-SOD1, peGFP-SOD1-A4V, peGFP-SOD1-G93A were gifts from Dr. Brad Turner (The Florey Institute of Neuroscience and Mental Health, Australia) (Turner *et al.* 2005). SOD1-tomato constructs were created by replacing the eGFP sequences in the SOD1-eGFP plasmids with tdTomato (Genscript, USA). The expression vector pCMV6-AC-GFP containing FUS cDNA was obtained from Origene and site directed mutagenesis was performed by Genscript (USA) to create the R495X mutant. Plasmids containing sequences encoding WT and temperature-sensitive double mutant (DM) firefly luciferase-eGFP ($FLUC^{WT}$-eGFP and $FLUC^{DM}$-eGFP) were a gift from Prof. Ulrich Hartl (Max Plank Institute, Germany) and were recloned by Genscript (USA) into pcDNA4/TO (Life Technologies, USA) for mammalian cell transfection. pCMV6-AC-FUS-GFP was originally obtained from Origene (USA); the mutant pCMV6-AC-FUS^{495X}-eGFP construct was cloned and validated by Genscript (USA). A plasmid encoding ubiquitin-RFP (pmRFP-Ub, cloned from peGFP-C1) was a gift from Nico Dantuma (Addgene plasmid #11935) (Bergink *et al.* 2006).

3.2.2 FloIT

Cells to be analysed were grown and transfected in 24 well plates. After the indicated treatments, the cells were harvested using 0.5% trypsin/EDTA. The trypsin containing the cell suspension was diluted with either DMEM/F12 containing 1% FBS or PBS. The cells were pelleted at 300 x*g* for 5 min at RT, washed once more in PBS and resuspended in 500 µl of PBS. To determine the transfection efficiency, an aliquot of the cell suspension (150 µl) and a non-transfected cell control were analysed by flow cytometry using an LSRFortessa X-20 (BD Bioscience, USA). GFP fluorescence was measured using 488 nm excitation and 525/50 nm emission; mCherry and tdTomato were excited at 561 nm and fluorescence was collected at 586/15 nm; RFP was excited at 561 nm and emission was collected at 610/20 nm. The remaining 350 µl of cells were pelleted as above and resuspended in lysis buffer (PBS with 0.5% Triton X-100 and Complete® protease inhibitor (Roche, Switzerland)). Except in control samples used to set gates, RedDot2 (Biotium, USA) was diluted 1:1,000 into the lysis buffer prior to addition to cells. After a 2 min incubation at RT the lysate was analysed by flow cytometry, measuring forward scatter (an indicator of particle size; FSC), side scatter (SSC, usually an indicator of cell "granularity"; see section 3.4), and fluorescence from RedDot2 (640 nm excitation, 670/30 nm collection), GFP, RFP, mCherry and/or tdTomato as above. All parameters were set to $\log_{10}$ during acquisition from cell lysates. The FSC threshold was set to the minimum value (200 AU) to minimise the exclusion of small protein inclusions. Nuclei were identified and enumerated based on RedDot2 fluorescence and FSC and then excluded from further analysis. The remaining particles were analysed for the presence of inclusions based on GFP/RFP/mCherry/tdTomato

fluorescence, FSC and comparison lysates prepared from cells expressing only the corresponding fluorescent protein. A schematic representation of FloIt is shown in Figure 3.1. The number of inclusions in the population can be normalised to the number of nuclei, and reported as inclusions/100 transfected cells (i_{FloIT}) according to the equation

Equation 3.1 $$i_{FloIT} = 100\left(\frac{n_i}{\gamma . n_{nuc}}\right)$$

where n_i is the number of inclusions acquired, n_{nuc} is the number of nuclei acquired, and γ is the transfection efficiency.

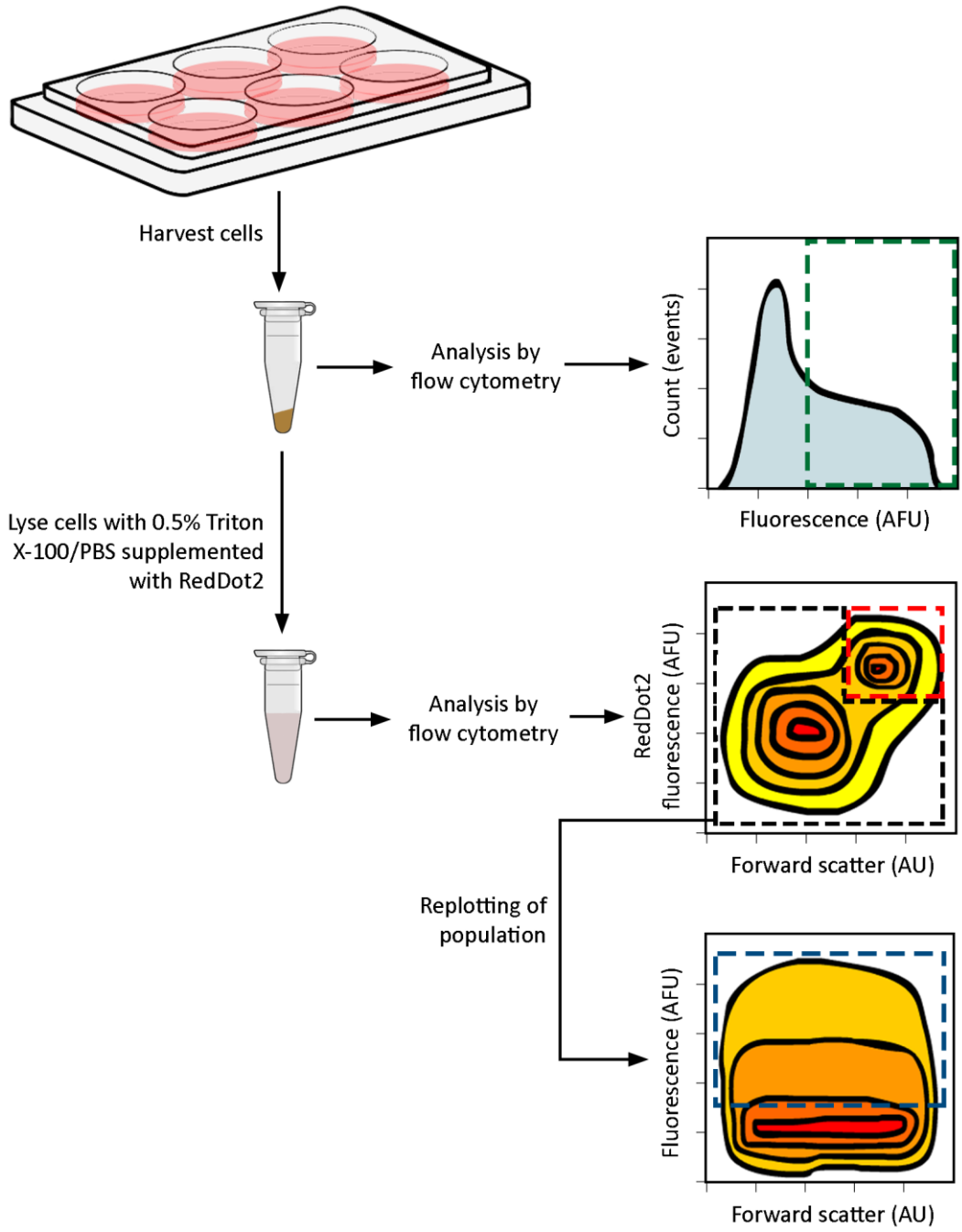

Figure 3.1: The FloIT workflow. Analysis by FloIT involves two flow cytometric measurements. The first measurement is performed on whole cells and is used to determine the proportion of transfected cells. On the upper histogram (right), the gate indicated by a dashed green line contains cells expressing a fluorescent fusion protein (the transfected cells). The second measurement is performed on cell lysates prepared using Triton X-100. In the middle panel (right), a cytogram plotting RedDot2 fluorescence (y-axis) versus FSC (x-axis) is used to discriminate between nuclei (contained within the gate drawn with a dashed red line) and non-nuclear particles (contained within the gate drawn with a dashed black line). The nuclei are enumerated and the non-nuclear population is replotted to allow enumeration of inclusions (dashed blue line). The middle and lower cytograms are shown as contour plots with red indicating the highest particle density, then orange, then yellow. Each of the gates shown are positioned on the basis of comparison with appropriate non-transfected or vector-only transfected cells.

Additionally, FloIT was used to quantify the extent of localisation of proteins in the nucleus. To achieve this, the nuclei (identified as above with RedDot2) were examined for the presence of the fluorescent protein conjugated to the protein of interest. The number of "positive" nuclei was then compared to the number of cells expressing the protein of interest to determine the proportion of cells expressing the protein in the nucleus. Analysis of all flow cytometry files was performed using FlowJo vX (FlowJo LLC, USA).

3.2.3 PulSA and manual counting

PulSA was performed as previously described (Ramdzan *et al.* 2012). Briefly, area, height and width parameters were collected for GFP/mCherry/tdTomato fluorescence using the excitation lasers and bandpass filters above. Plotting fluorescence height against width allows (in some cases) the identification of a population of cells with inclusions in the upper left portion of the cytogram. Manual counting of inclusions was performed by counting the number of fluorescent puncta present in three replicate image sets of 100 randomly selected transfected cells. Images were acquired using a Nikon epifluorescence microscope and a 63x air objective.

3.2.4 Sorting flow cytometry

N2a cells grown in 24-well microtiter plates were harvested and lysed as described above. The lysate was passed through a 40 µm nylon mesh and analysed on an S3e

Cell Sorter (Bio-Rad, USA) equipped with 488 and 561 nm lasers. The nuclei population was initially identified using propidium iodide (PI, 1 µg/ml, excitation 488 nm, emission 586/25 nm) instead of RedDot2 (due to the absence of a far-red 640 nm laser). Once identified, nuclei were collected based on FSC area (log_{10} axis) and SSC area (log_{10} axis) to eliminate the need for PI (and crosstalk into the GFP channel). Inclusions were collected based on FSC area and GFP-fluorescence area (excitation 488 nm, emission 525/30 nm). Particles were collected in 5 ml FACS tubes containing 50 µl of PBS for subsequent imaging by confocal microscopy.

3.2.5 TDP-43 experiments

N2a cells transfected to express TDP-43-tGFP were or were not stressed with MG132 (10 µM in DMSO; Cayman Chemicals, USA). After the indicated times, cells with inclusions were analysed by PULSA; inclusions were enumerated by manual counting and FloIT; and protein localisation (nuclear or otherwise) was measured using FloIT, as described above.

3.2.6 NFAT experiments

NFAT is a transcription factor that has been used extensively to study nuclear transport when conjugated to a fluorescent reporter (Scott 2001, Soderholm *et al.* 2011, Maguire *et al.* 2013). HEK-293 cells transfected to express with NFAT-eGFP were treated with ionomycin (dissolved in DMSO, Cayman Chemicals, USA) at the stated concentrations for 30 min. FloIT was performed after this period as

described above. For imaging of whole cells, the cells were grown directly in an 8 well µSlide (Ibidi, Germany), fixed with 4% paraformaldehyde (PFA) for 15 min at RT and incubated with RedDot2 before imaging using a Leica SP5 II microscope (Leica, Germany).

3.3 Results

To initially develop the FloIT technique, cultured N2a cells were transfected (or not) to overexpress SOD1^{G93A}-eGFP. The cells were subsequently lysed in 0.5% Triton X-100 in PBS and the nuclei stained with RedDot2 (Biotium, USA) before flow cytometric analysis. Incubation with Triton X-100 was found to rapidly lyse the cells and leave the inclusions intact (Figure 3.2).

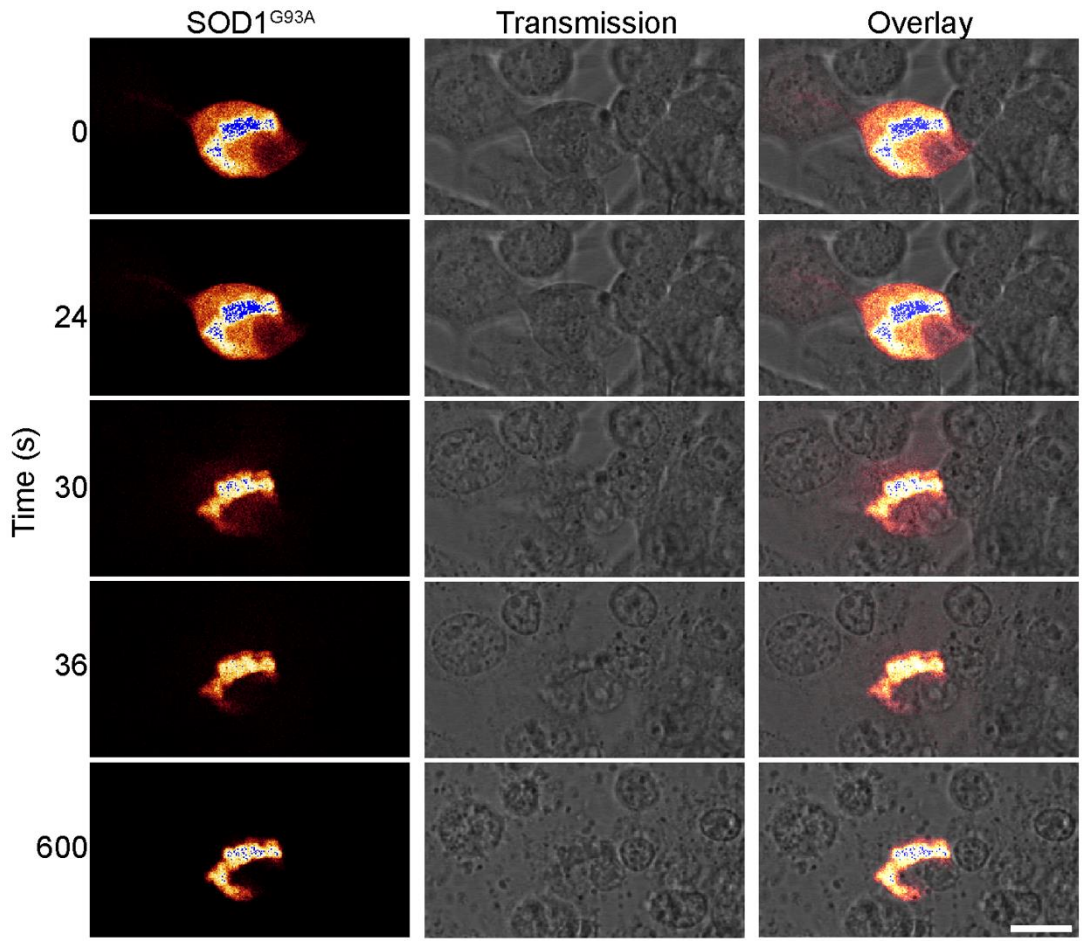

Figure 3.2: Triton X-100 lyses cells but does not disturb inclusions. Time series of confocal microscopy images showing cells expressing SOD1^{G93A}-eGFP imaged every 6 s following the addition of lysis buffer. The release of soluble SOD1^{G93A} from the newly lysed cell is visible at 30 s while the inclusions remain unchanged for at least 10 minutes. Scale bar is 10 µm. Result is representative of 20 cells across two experiments.

Nuclei were identified (and quantified) using FSC and RedDot2 fluorescence (Figure 3.3*a top*). By exploiting the tGFP tag on the aggregating TDP-43 protein, non-nuclear particles were then gated into inclusions and cellular debris (Figure 3.3*a bottom*). To calculate the average number of inclusions per transfected cell in the population analysed, the number of inclusions acquired is simply divided by the transfection efficiency multiplied by the corresponding number of cell nuclei enumerated (the fraction of cells transfected is separately estimated by flow cytometry). The identity of the nuclei and inclusions was confirmed by collecting these populations using sorting flow cytometry and then examining them by confocal microscopy (Figure 3.3*b*).

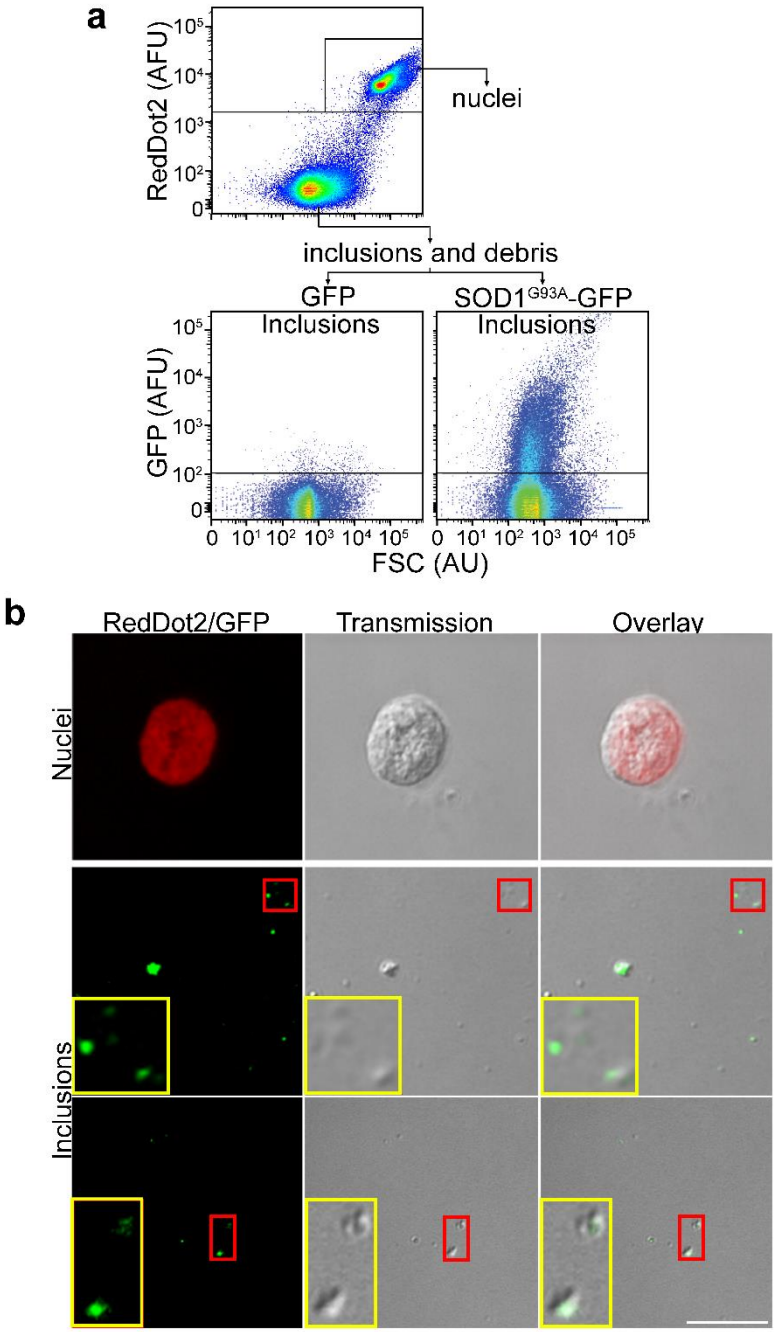

Figure 3.3: Gating inclusions in N2a lysate. a) Top: nuclei can be identified using a combination of FSC and RedDot2 fluorescence. Bottom: inclusions can be identified from the non-nuclei population by examining GFP fluorescence. b) Confocal images of sorted nuclei (top) and inclusions (bottom). Yellow boxes are 3X zoom of the regions identified by the red boxes. Scale is 10 µm.

To confirm that FloIT was accurately detecting and enumerating protein inclusions in cells, transfected N2a cells expressing TDP-43^{M337V}-tGFP were analysed by FloIT and the results directly compared with those obtained by manual counting of

inclusions by epifluorescence microscopy and PulSA. Quantification of TDP-43 inclusions by automated image analysis is difficult because of the normally nuclear localisation of the protein. To enhance the cytosolic translocation and aggregation of TDP-43^{M337V}-tGFP the cells were treated with the proteasome inhibitor MG132 over a 16 h time course. Over the full time course of the experiment, PulSA consistently detected inclusions in less than 6% of cells. In contrast, FloIT detected 26 inclusions/100 transfected cells at t = 0 h, and more than 90 inclusions/100 transfected cells after 16 h of MG132 treatment. FloIT tended to identify more inclusions in these cells than manual counting (Figure 3.4*a*; example gates are shown in figure 3.4*b*).

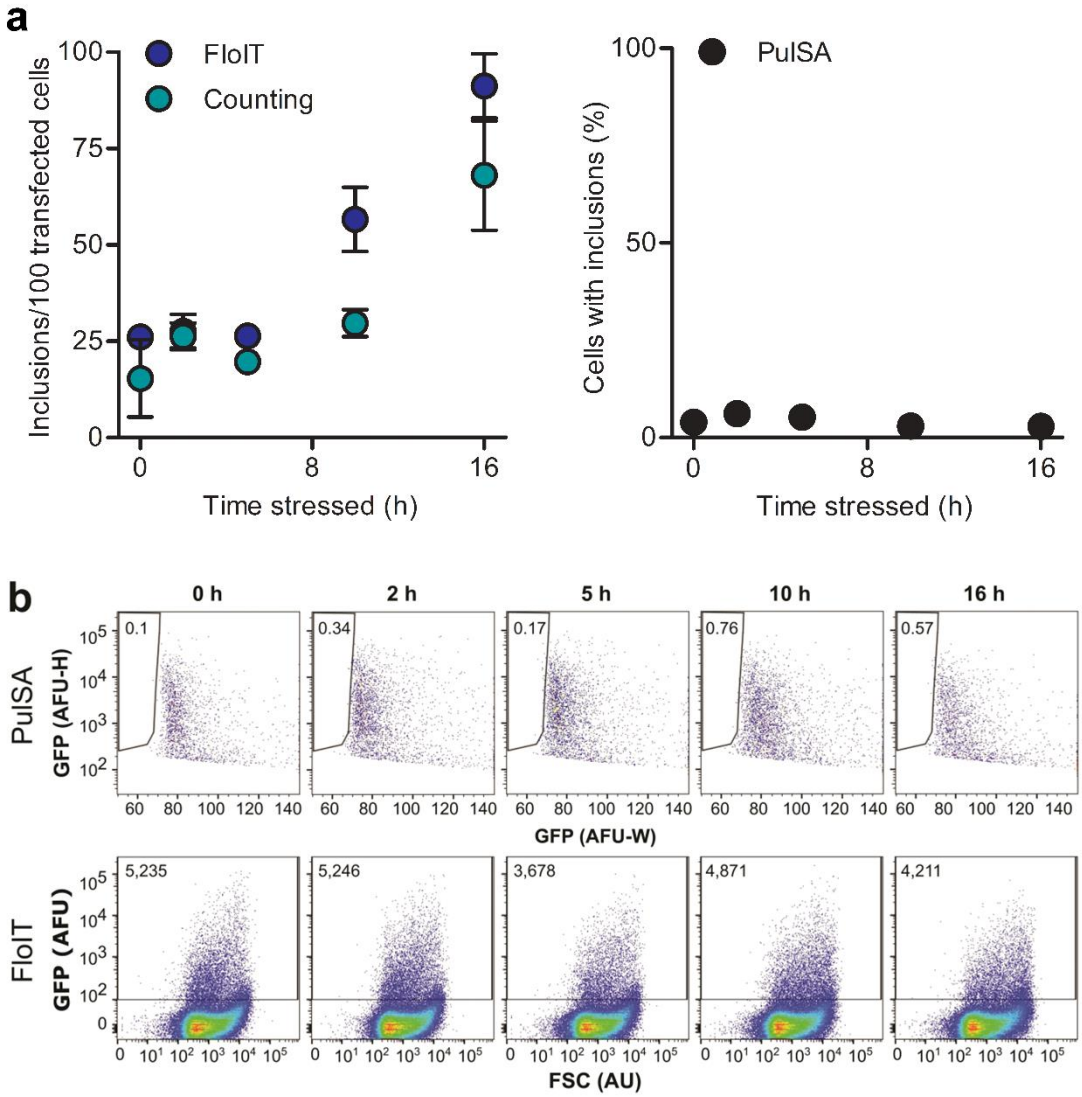

Figure 3.4: FloIT detects TDP-43-tGFP inclusions at least as efficiently as manual counting. a) N2a cells expressing TDP-43^{M337V} were treated with MG132 for up to 16 h. The number of inclusions was enumerated by FloIT or manual counting (left), and the number of cells with inclusions was determined by PulSA (right). Values are means, error bars are SEM, n = 3. b) Example gates for PulSA (cells with inclusions gated) and FloIT (inclusions from cell lysates gated) from data presented in **a**. The numbers within gates are the percentage of cells with inclusions (PulSA) and the number of inclusions measured (FloIT). Note that these values do not directly correlate with data shown in **a** due to differences between samples in nuclei enumerated and transfection efficiencies.

To confirm the general accuracy of FloIT, inclusions in N2a cells overexpressing Htt^{46Q}–mCherry and FLUC^{WT}–eGFP were also enumerated using FloIT and manual counting. In these cases FloIT tended to show slightly less inclusions than manual counting, but the differences were not significant (Figure 3.5). Manual counts of

inclusions formed by various other proteins (SOD1 variants and $FLUC^{DM}$) were attempted, but the inclusions proved too difficult to discriminate due to what appeared to be many overlapping but possibly individual puncta on the images.

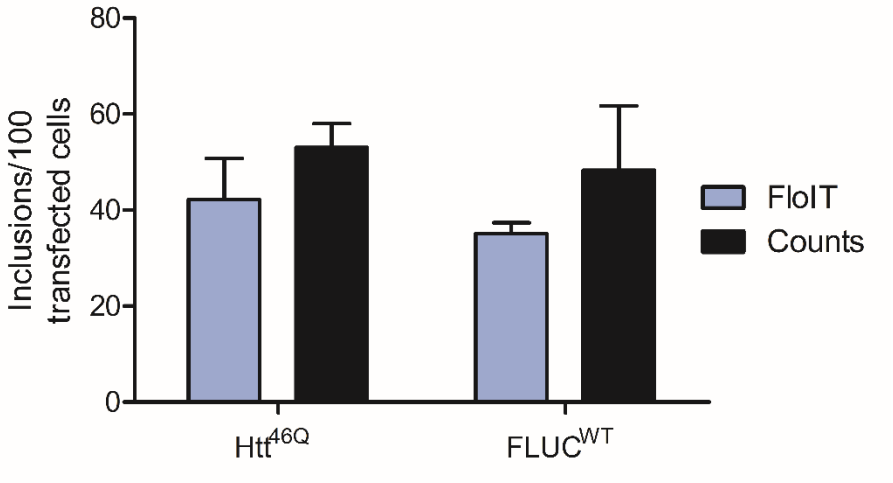

Figure 3.5: FloIT and manual counting provide similar estimates of Htt^{46Q}-mCherry and $FLUC^{WT}$-eGFP inclusions. The number of inclusions in N2a cells expressing Htt^{46Q}–mCherry or $FLUC^{WT}$–eGFP was enumerated by FloIT or manual counting. Values are means, error bars are SEM, n = 3. Differences were not significant, analysed by t-test.

The initial work was extended to show that FloIT can be used to enumerate inclusions formed by a variety of other protein aggregation models including Htt (Htt^{25Q} and Htt^{48Q})-mCherry, SOD1 ($SOD1^{WT}$, $SOD1^{A4V}$ and $SOD1^{G93A}$)-eGFP, and an aggregation prone mutant FLUC ($FLUC^{DM}$-eGFP) (Figure 3.6*a*). Thus, FloIT is a fast, sensitive method for the analysis of inclusions in mammalian cell lysates formed by a broad variety of proteins. In contrast, in our hands, PulSA (Ramdzan *et al.* 2012) was able to detect inclusions in transfected cells expressing Htt^{48Q}-mCherry and (to a lesser extent) $FLUC^{DM}$–eGFP but was unable to do so in any of the other models tested, including cells expressing Htt^{25Q}-mCherry, SOD1-eGFP variants (Figure 3.6*b*) or TDP-43-tGFP (shown above); example gates are shown in Figure 3.6*c*. In cells

expressing Htt^{46Q}–mCherry and $FLUC^{DM}$-eGFP, PulSA detected inclusions in approximately 25% and 8% of cells, respectively, but detected less than 1.5% of cells as containing inclusions when any of the other proteins were expressed.

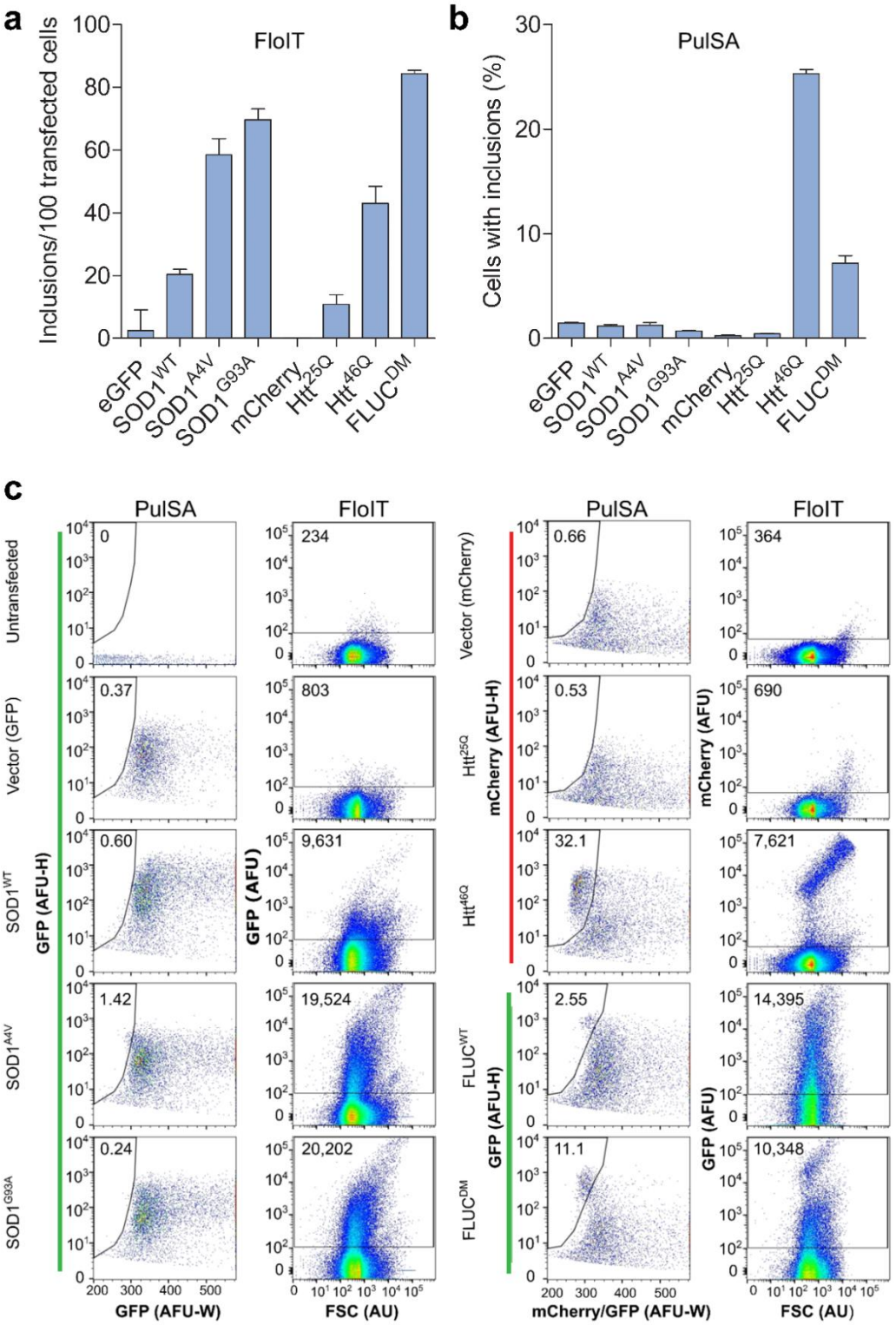

Figure 3.6: FLOIT identifies inclusions formed by many different proteins. N2a cells transfected to express the indicated protein fused to mCherry (Htt variants) or eGFP (all others) were analysed for the presence of inclusions by a) FloIT or b) PulSA. Values are mean +SEM, n = 3. c) Example gates for PulSA (percentage of cells with inclusions gated) and FloIT (number of inclusions from cell lysates gated) from data presented in **a** and **b**. Data shown is representative of at least two separate experiments. SOD1 and FLUC^{DM} data was collected with Ms. R. San Gil (University of Wollongong, Australia).

FloIT liberates the inclusions from cells and then enumerates and characterises the individual fluorescent particles. This ability is reflected in the relative sizes of the various inclusions measured by FloIT (based on the FSC signal), arranged in decreasing order: Htt^{46Q} (438.7 ± 26 AU), Htt^{25Q} (200 ± 44.2 AU), $SOD1^{WT}$ (72.1 ± 4 AU), $SOD1^{A4V}$ (61.6 ± 1.9 AU), $SOD1^{G93A}$ (57.7 ± 1.4 AU), $TDP\text{-}43^{WT}$ (39.8 ± 1.3 AU), $FLUC^{DM}$ (36.6 ± 3.6), $FLUC^{WT}$ (29.1 ± 0.3 AU), $TDP\text{-}43^{M337V}$ (25.6 ± 1.7 AU). Furthermore, with the exception of $SOD1^{A4V}$ and $SOD1^{G93A}$, FloIT was also able to clearly resolve populations of inclusions formed from different proteins using only the FSC and SSC signals (Figure 3.7).

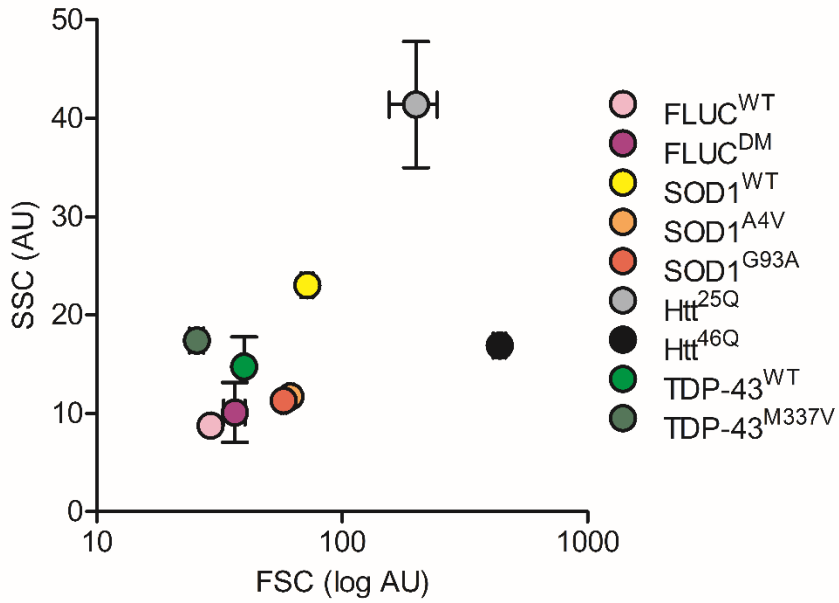

Figure 3.7: FloIT can resolve inclusions formed by different proteins. N2a cells overexpressing the indicated protein fused to mCherry (Htt variants) or eGFP (all others) were analysed for inclusions by FloIT. Values are mean ± SEM, n = 3. SOD1 and $FLUC^{DM}$ data was collected with Ms. R. San Gil (University of Wollongong, Australia).

Using a series of microspheres of known diameters (Figure 3.8*a*), it is possible to calibrate the FSC signal at the gain setting used for FloIT. FSC and bead diameter

display a near-linear relationship for bead sizes 0.56 – 14.3 µm (Figure 3.8*b*). This range of values encompasses the sizes of some inclusions detected, although many appeared to correspond to particles of < 500 nm in diameter (Figure 3.8*c*).

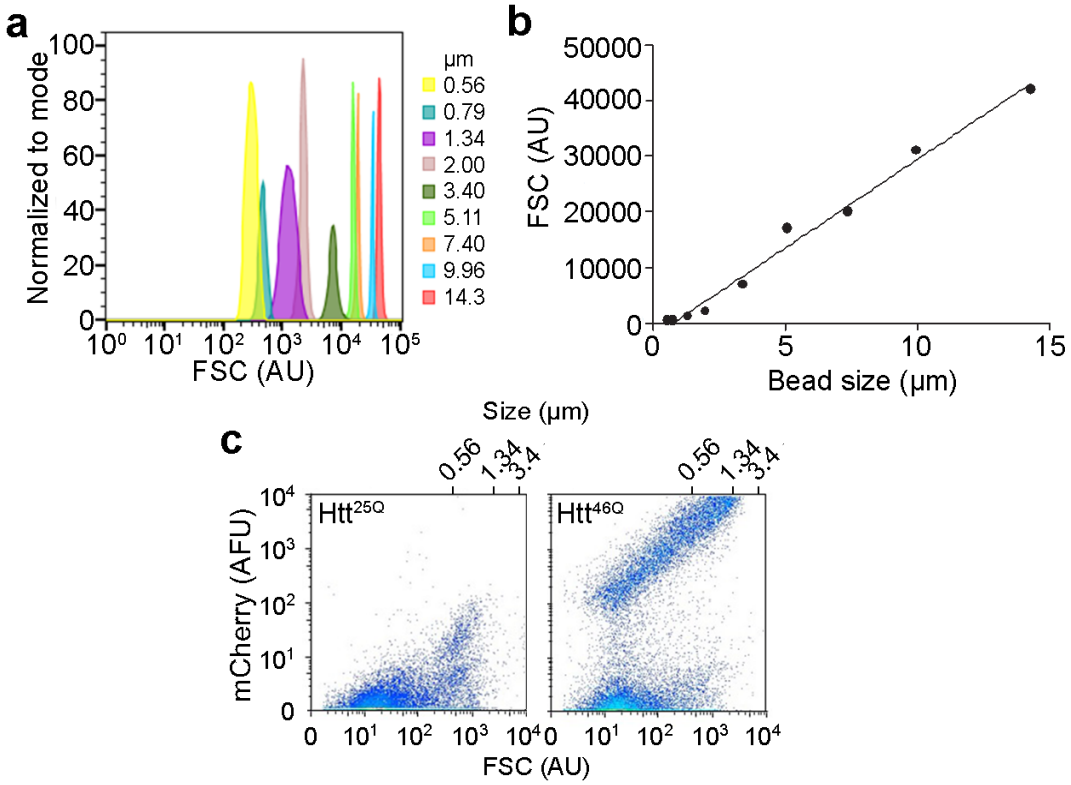

Figure 3.8: FSC can be used to determine the physical size of inclusions greater than 500 nm in diameter. FSC calibration microspheres were analysed by flow cytometry using a FSC voltage identical to that used for FloIT. A) FSC histograms of each of the beads. B) FSC is linearly dependent upon bead diameter. C) The sizes of some inclusions can be quantified, but many are smaller than the lower limits for quantification on standard flow cytometers.

To examine whether FloIT could be used to detect and quantify inclusions formed from more than one protein, N2a cells were co-transfected to express Htt^{46Q}-mCherry and FUS^{495X}-eGFP, Htt^{46Q}-mCherry and $SOD1^{G93A}$-eGFP or $SOD1^{G93A}$-tdTomato and $SOD1^{G93A}$-eGFP, and analysed by FloIT (Figure 3.9). Populations of inclusions were gated based on data collected for untransfected cells and singly-transfected cells. $SOD1^{G93A}$-tdTomato was manually compensated to

account for the spectral crosstalk into the GFP channel; no compensation was required for mCherry-tagged proteins. Approximately 45% of inclusions arising from cells co-transfected to express $SOD1^{G93A}$-eGFP and $SOD1^{G93A}$-tdTomato contained both proteins. In cells co-transfected to express FUS^{495X}–eGFP and Htt^{46Q}-mCherry, approximately 53% of inclusions exhibited both mCherry and GFP fluorescence. In contrast, only ~11% of inclusions in cells expressing Htt^{46Q}–mCherry and $SOD1^{G93A}$–eGFP contained both proteins.

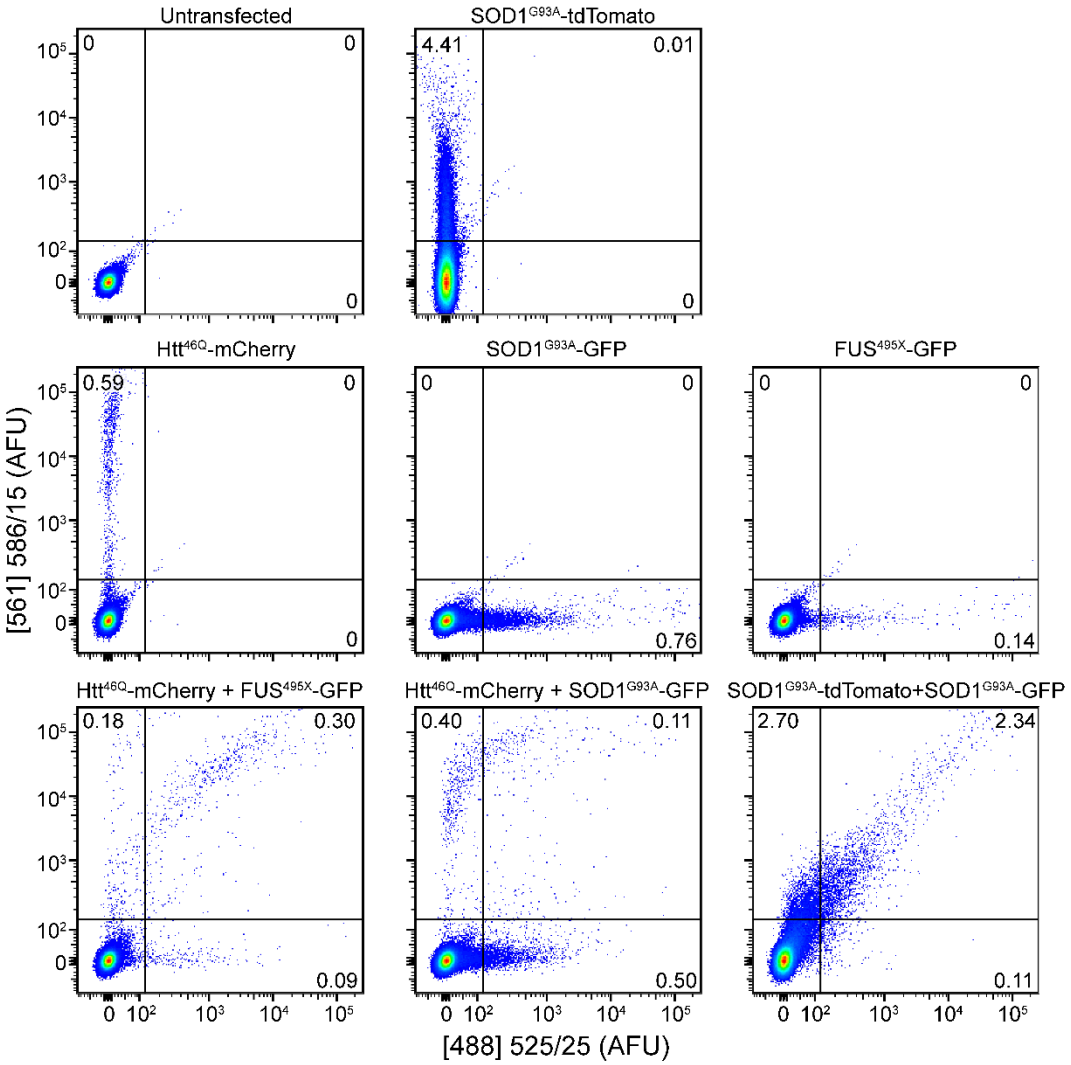

Figure 3.9: FloIT can quantify dual-colour inclusions. Flow cytograms of N2a cells overexpressing the indicated fusion proteins and analysed by FloIT. Numbers within the gates are percentages of total events. Axes are in the format '[excitation λ] emission band-pass filter'. The top-left quadrants show inclusions containing only mCherry or tdTomato (but not eGFP), the top-right quadrants show dual-colour inclusions and the lower-right quadrants show inclusions containing only eGFP (and not mCherry or tdTomato). AFU, arbitrary fluorescence units. Data shown is representative of three separate experiments.

In order to confirm that the particles detected by FloIT are extensively ubiquitinated (a hallmark of inclusion bodies), cells were co-transfected to express SOD1-eGFP variants and ubiquitin-RFP (Ub-RFP) and analysed by FloIT. Approximately 73% and 76% of SOD1 inclusions arising from cells expressing $SOD1^{A4V}$-eGFP and $SOD1^{G93A}$-eGFP respectively were ubiquitinated. In the case of

SOD1^{WT}-eGFP, 100% of inclusions containing GFP were also positive for RFP, although compared with the SOD1 mutants tested the inclusions identified had a higher ratio of Ub-RFP to SOD1-eGFP fluorescence (Figure 3.10).

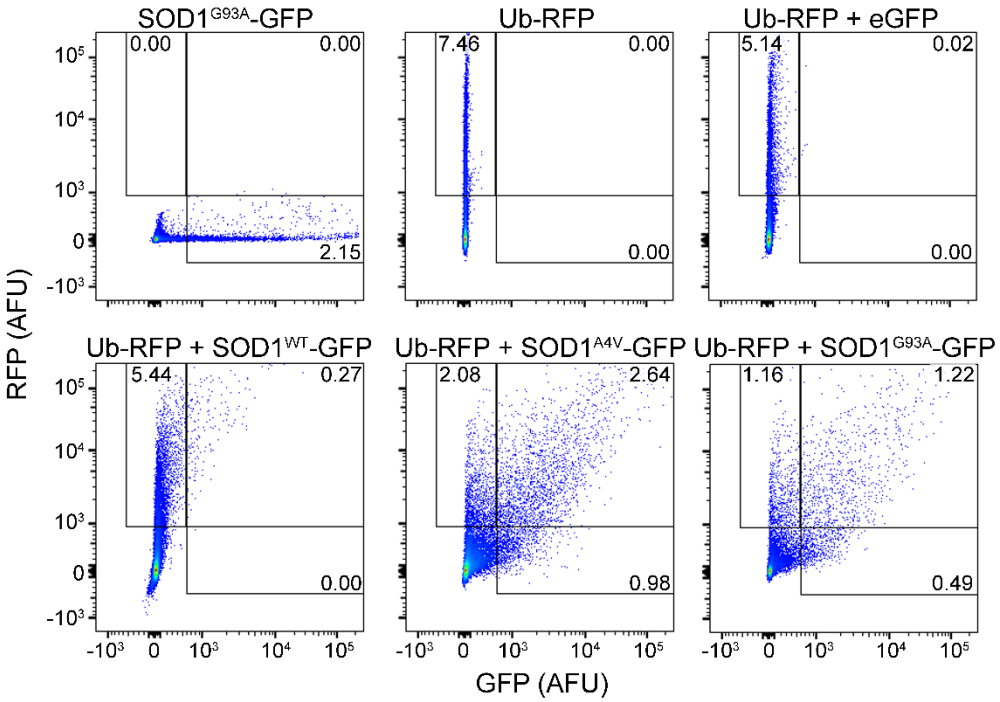

Figure 3.10: Most inclusions detected by FloIT are heavily ubiquitinated. Flow cytograms of N2a cells transfected to express the various protein(s) (indicated above the individual panels) and analysed by FloIT. Numbers within the gates are percentages. Data shown is representative of two separate experiments.

FloIT can also be used to measure the trafficking of a fluorescently tagged molecules into and out from the nucleus. To demonstrate this, N2a cells transfected to express TDP-43^{M337V}-tGFP were treated with MG132 (10 µM), the presence of GFP fluorescence in the nucleus was monitored using FloIT (see Figure 3.2*a*). Before treatment, approximately 51% of nuclei contained TDP-43^{M337V}-tGFP, with the positive nuclei averaging 14,331 arbitrary fluorescence units (AFU). Over the time course, less nuclei showed TDP-43^{M337V}-tGFP fluorescence (31% after 16 h) (Figure

3.11, *left*) and those that retained some TDP-43^{M337V}-tGFP were less strongly fluorescent (10,720 AFU) (Figure 3.11*, right*).

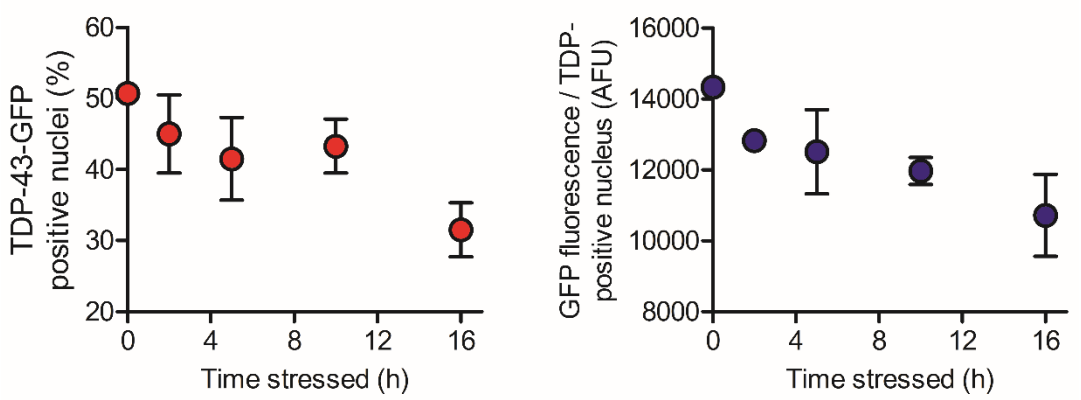

Figure 3.11: FloIT can quantify nuclear flux of fluorescent molecules. Time-dependent efflux of TDP-43^{M337V}-tGFP from the nuclei of MG132 treated N2a cells. Values are means, error bars are SD, n=3.

To further demonstrate the ability of FloIT to measure nuclear trafficking in a model independent of protein aggregation phenomena, NFAT-eGFP (a fluorescently tagged transcription factor) was transfected into HEK-293 cells, which were then treated with ionomycin (Aramburu *et al.* 1999, Soderholm *et al.* 2011). An influx of NFAT-eGFP was observed, with approximately 8% and 60% of nuclei containing the fusion protein before and after treatment with ionomycin (1 µM), respectively. Not only do more nuclei contain NFAT-eGFP with ionomycin treatment, but positive nuclei also contain a much higher amount of the protein (19-fold increase with 1 µM ionomycin) (Figure 3.12*a*). This influx was confirmed by confocal microscopy (Figure 3.12*b*).

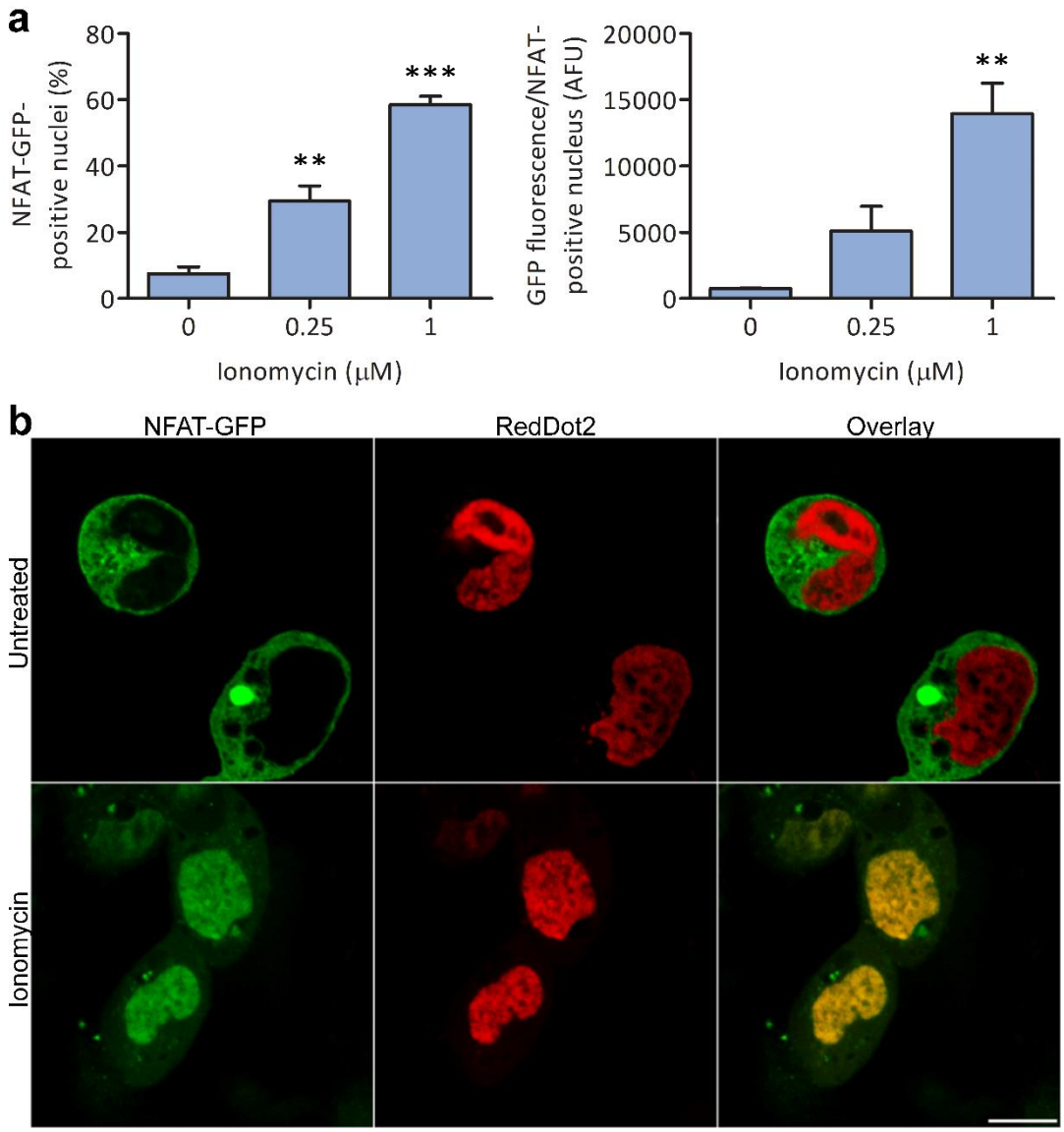

Figure 3.12: FloIT can quantify nuclear flux of fluorescently tagged proteins. a) Dose-dependent influx of NFAT-eGFP into the nuclei of ionomycin-treated HEK-293 cells, as quantified by FloIT. Values are means (n=3), error bars are SEM. ** $p < 0.01$, *** $p < 0.001$, analysed by a one-way ANOVA with a Bonferroni post-test. B) Confocal microscopy images of NFAT-eGFP-expressing HEK-293 cells with and without ionomycin treatment. Scale bar is 10 μm.

3.4 Discussion

The accuracy of FloIT was verified by analysing the same cell population by both manual counting and (subsequently) FloIT. While similar numbers of inclusions were detected using both methods, in some cases FloIT detected slightly more inclusions than manual counting. This is likely due to a number of factors: (i) FloIT detects very small inclusions that may not resolvable by fluorescence microscopy, (ii) multiple inclusions may have been aligned in the *Z*-axis such that they were not distinguishable when inspecting a two-dimensional image, and/or (iii) the low number of cells counted by fluorescence microscopy may not have been a representative sample (3x 100 cells at each time point compared to 3x ~30,000 cells with FloIT). Thus, the results of FloIT analyses are comparable to (but are obtained much faster than) counting inclusions from images.

In our hands, most protein inclusions could not be detected using PulSA. PulSA detects cells with inclusions by utilising differences in fluorescence pulse shapes. To be resolved by PulSA, cells with inclusions must show a reduced fluorescence pulse width and increased fluorescence pulse height, relative to cells without inclusions. However, except for Htt^{46Q}-mCherry and $FLUC^{DM}$-eGFP, none of the models tested met this requirement. The fluorescence pulse shape can be influenced by the numbers of inclusions within cells, the physical dimensions of the inclusions and their distribution within cells. For samples that can be analysed by PulSA, such as cells expressing Htt^{46Q}-mCherry, FloIT can be used together with PULSA to determine the: (i) percentage of cells with inclusions (PulSA), (ii) average number of

inclusions/transfected cells (FloIT), and therefore (iii) in those cells actually containing inclusions, the average number of these inclusions (combination of PulSA and FloIT). Thus, from the data presented in Figure 3.5*a* and *b*, it can be calculated that the average number of Htt^{46Q}-mCherry inclusions in those cells that contained these was 1.6. This additional metric may be of use when evaluating the effect of a protein or drug on the aggregation of a target protein. For example, FloIT may identify a decrease in the number of inclusions being formed, and the combination with PulSA could be used to identify whether this is representative of less cells containing inclusions, or cells with inclusions containing less of them.

As FloIT liberates inclusions from cells, relative to other approaches, it has the additional advantage of being able to quickly and easily collect data relating to the physical characteristics of individual inclusions. For example, the FSC parameter can be used to determine the relative and absolute size of the particles, although for absolute size determinations this is limited to the largest inclusions, due to the inherent limitations of standard flow cytometers (~500 nm diameter minimum). More specialised instruments promise more powerful quantification of small particles (less than 80 nm (Pospichalova et al. 2015)) and could potentially be used to more fully analyse the size distributions of inclusions. The SSC of the inclusion population can also be determined; for whole cells, SSC is generally used as an indicator of cell granularity. The SSC of inclusions varies depending on the aggregating protein and is independent of FSC, however, it is currently unclear

exactly what features of inclusions SSC is reporting (this might include density and/or morphological characteristics).

Other applications of FloIT include investigating the co-aggregation of proteins into inclusions. To demonstrate this, cells were co-transfected to express both $SOD1^{G93A}$-eGFP and $SOD1^{G93A}$-tdTomato, or Htt^{46Q}-mCherry with either FUS^{495X}-eGFP or $SOD1^{G93A}$-eGFP. These combinations were chosen as it was previously demonstrated that FUS^{495X}-eGFP was incorporated into insoluble protein deposits along with Htt, whereas $SOD1^{G93A}$ was shown to form separate inclusions not associated with Htt inclusions (Farrawell *et al.* 2015). Supporting this hypothesis, FloIT identified 53% co-localisation between FUS^{495X}-eGFP and Htt^{46Q}-mCherry and only 11% co-localisation between $SOD1^{G93A}$-eGFP and Htt^{46Q}-mCherry.

The majority of particles enumerated by FloIT are likely mature, ubiqutinated inclusions (see Figure 3.9), but due to the sensitivity of the technique smaller non-ubiquitinated aggregates appear to be quantifiable as well. If it was necessary to measure only *certain* inclusions, additional criteria could easily be incorporated into the analysis. For example, a fluorescent ubiquitin tag, such as Ub-RFP used here, could be used to resolve only ubiquitinated inclusions. Size constraints could also be utilised, for example measuring only particles greater than 1 µm. A combination of these could limit the count to that of certain well-defined inclusions, however, for

most cases this seems unnecessary as the technique as described provides a fast and accurate assessment of the total load of insoluble protein inclusions within the cell population.

One limitation of the FloIT technique is that the level of expression of the protein of interest cannot be accounted for. Unfortunately, the two possible methods that could be used to easily achieve this are both flawed. Quantification of the fluorescence level of a fluorophore conjugated to the protein of interest cannot be used, since the incorporation of the fluorophore into inclusion bodies may result in some quenching of the fluor. Thus, the measurement of fluorescence may not directly correlate with the amount of insoluble protein in the inclusion. Similarly, the samples cannot be reliably quantified by Western blot since inclusion bodies can be very difficult to solubilise (TDP-43 inclusions, for example, are resistant to SDS, urea and guanidine[1]). However, if one of these techniques is suitable in a specific case, or another technique to measure the amount of protein is developed, this factor could easily be incorporated into the analysis to provide an enumeration of inclusions while explicitly accounting for the expression level of the protein of interest. A possible strategy to achieve this would be to transfect the cells with a bicistronic plasmid encoding both the protein of interest and a soluble fluorescent protein as a reporter of expression level. If FloIT is further developed it seems that incorporating this currently unknown factor would be the ideal area of focus.

[1] Mark Wilson (2015) *Unpublished data*. University of Wollongong, Wollongong.

FloIT can be used to measure the trafficking and compartmental localisation of any fluorescent molecule, provided that the compartment of interest remains intact following lysis. As a technique, FloIT is dependent upon the release of undisturbed inclusions and nuclei from cells. This was accomplished by performing the lysis using a low concentration of the non-ionic detergent Triton X-100. After optimisation and validation, other methods of cell lysis could potentially be used, such as hypotonic lysis or mechanical disruption. These methods could present an opportunity to measure the trafficking between structures such as the ER and Golgi apparatus. Additionally, these methods of cell disruption could allow the quantification of detergent-soluble protein aggregates (if they are large enough). It is important to note that cytosolic protein inclusions are well known to be resistant to non-ionic detergents - their enrichment by treatment with Triton X-100 and centrifugation is a common practice (Beaulieu *et al.* 1999, Basso *et al.* 2009).

FloIT can be used to rapidly quantify cytosolic protein inclusions, one of the major hallmarks of neurodegenerative disease. Manual counting by microscopy and PulSA, previously described methods to enumerate inclusions, are respectively time-consuming or applicable to only a very few cell-based protein aggregation models. In contrast, FloIT is simple to perform and was successfully applied to all nine protein aggregation models tested.

Chapter 4:

Clusterin Influences Intracellular TDP-43 Processing

4. Clusterin Influences Intracellular TDP-43 Processing

4.1 Introduction

The prevalence of the various types of inclusions in both sALS and fALS cases suggests that motor neurons are unable to maintain effective mechanisms to prevent the misfolding of proteins and their subsequent aggregation. Indeed, dysfunctions in autophagy, the UPS and ERAD are implicated in ALS, and each may be sufficient to cause neurodegeneration. Additionally, as outlined in Chapter 1, various molecular chaperones have been shown to co-localise with ALS inclusions, and inefficiencies in chaperone activity are also implicated in the disease.

Intracellular inclusion-forming proteins that appear to avoid or overload the normal degradative pathways may present an interesting potential target for CLU, since CLU can be retained within the cell under stress conditions (see section 1.3.2.3). Whilst there are indications that CLU can affect intracellular proteostasis, this has never been examined in the context of neurodegenerative disease. The work presented in this chapter aimed to explore the role of intracellular CLU, and determine the effect the normally secreted chaperone has on TDP-43 aggregation and clearance (using FloIT, among other techniques). This builds upon the work of collaborators and lab members that show CLU can ameliorate the cytotoxicity of mutant TDP-43 in *Drosophila melanogaster*[2].

[2] Gregory, J.; Brown, R. A.; de Barros, T. P.; Kumita, J. R.; Meehan, S.; Yerbury, J. J.; Dobson, C. M.; Wilson, M. R.; Luheshi, L. M. (2014) *Unpublished data.*

4.1.1 TDP-43 in ALS

Ubiquitinated inclusions within surviving spinal neurons are a pathological hallmark of ALS. Neumann *et al.* (2006) showed that a consistent component of these inclusions is TDP-43. This lead to the genetic screening of a large number of ALS patients for mutations within the *TARDBP* gene, and the subsequent discovery of the first causal links between TDP-43 and ALS – the missense mutations G294A, Q331K and M337V (Sreedharan *et al.* 2008). Since this time, at least 39 mutations have been found on *TARDBP* in ALS patients (Abel *et al.* 2012). These mutations appear to be causal of approximately 5-10% of all ALS cases (both familial and sporadic) (Gitcho *et al.* 2008).

A distinguishing feature of ALS pathology (particularly sALS) is the disappearance of TDP-43 from the nucleus and its accumulation and aggregation within the cytosol of motor neurons. It is likely that cytosolic TDP-43 is the result of translocation of the protein out of the nucleus, as well as impairments in nuclear import (Barmada *et al.* 2010). Cytosolic TDP-43 is typically subjected to heavy post-translational modifications such as cleavage, hyperphosphorylation and ubiquitination before sequestration in inclusions (Neumann *et al.* 2009). Due to the varied nature of cellular processes that occur within a short time-frame in ALS pathology (such as the nuclear depletion of TDP-43 and the formation of toxic cytosolic inclusions) the exact reasons that TDP-43 mutations lead to ALS pathology has not yet been established (Veering *et al.* 1990, Da Cruz and Cleveland 2011).

4.1.2 Roles of intracellular clusterin

Intracellular CLU has had many different putative roles ascribed to it, often varying with the specific cellular context of the study. Many of the conflicting reports suffer from the same flaw: overexpression of extremely rare isoforms accompanied with sweeping claims as to the biological function. The transfection of mutated and/or cleaved versions of CLU, which might account for at most 5% of total cell-associated CLU (Prochnow *et al.* 2013), has been performed many times by many lab groups, e.g. Debure *et al.* (2003), Scaltriti *et al.* (2004), and Essabbani *et al*. (2013). It remains unclear whether results obtained using this type of approach have any physiological relevance. Regardless, there is significant evidence that intracellular CLU influences several different pathways:

i. Autophagy

CLU was shown to co-localise with autophagy proteins microtubule-associated protein 1A/1B-light chain 3 (LC3) and sequestosome 1 (p62) in nephropathic cystinosis (Sansanwal *et al.* 2015). p62 binds both ubiquitinated proteins destined for degradation and LC3 (a membrane component of autophagosomes), thus leading to the autophagic degradation of target proteins. As cytosolic CLU is usually ubiqutinated (Rizzi *et al.* 2009a), it is not known whether p62 interacts with CLU due to this ubiquitination, or another reason. However, the interaction between CLU and LC3 appears to be specific. In cancer cells, CLU was shown to bind LC3, facilitating LC3 lipidation and the stability of the LC3-Atg3 heterocomplex, enhancing autophagy (Zhang *et al.* 2014). Additionally, CLU binds the copper-ATPases ATP7A and ATP7B and facilitates the lyosomal degradation of the proteins

(Barrett and Starkey 1973, Materia *et al.* 2011b). The cause of the intracellular retention of CLU was not explored in these reports.

ii. Ubiquitin-proteasome system

Intracellular CLU is polyubiquitinated and degraded by proteasomes (Matthijs *et al.* 1992a, Nizard *et al.* 2007, Zoubeidi *et al.* 2010a). CLU was also shown to facilitate the proteasomal degradation of copper metabolism MURR1 domain-containing protein 1 (COMMD1) and IκB by interacting with an E3 ligase (Zoubeidi *et al.* 2010a). Unfortunately, like with the copper ATPases above, how CLU escaped from the secretory system into the cytosol in this case was not explored.

iii. Apoptosis

In some contexts, CLU localised to the nucleus or mitochondria may be pro-apoptotic (Chen *et al.* 2004). The overexpression of mutant nuclear-targeted CLU was found to sequester Bcl-XL, releasing Bax, and promoting apoptosis (Kim *et al.* 2012), however, as outlined above this approach may not be the most physiologically relevant. Conversely, secretory CLU was shown to inhibit apoptosis by supressing p53-activating stress signals (Trougakos *et al.* 2009) as well as binding and inhibiting Bax (Zhang *et al.* 2005a). CLU also promotes cell survival through the phosphatidylinositol 3-kinase/Akt pathway (Ammar and Closset 2008, Kim *et al.* 2010) and by indirectly enhancing NF-κB activity (Zoubeidi *et al.* 2010a).

4.1.3 Experimental aims

The work presented in this Chapter aimed to explore the impact of intracellular CLU on the processing of TDP-43. The ability of CLU to influence the turnover of intracellular proteins has been previously demonstrated, but never in neurons, and the reason for the intracellular retention in these cases has never been shown (Materia *et al.* 2011a, Materia *et al.* 2012). As mentioned above, TDP-43 aggregation is believed to be responsible for a large proportion of ALS cases (Gitcho *et al.* 2008), and it was hypothesised that, under ER stress, CLU would either inhibit this process by mediating the degradation of the protein and/or inhibiting aggregation through a chaperoning effect. Due to a limited ability to raise a heat shock response to counter proteotoxicity, motor neurons are particularly vulnerable to the effects of protein aggregation (Batulan *et al.* 2003). The identification of new defensive mechanisms that protect neurons from proteotoxicity is essential for broadening the scope of future therapeutic developments.

4.2 Methods

4.2.1 Inducing the aggregation of TDP-43

Despite its high propensity to aggregate, WT and mutant TDP-43 rarely spontaneously form inclusions within mammalian cell lines without additional treatment, even when overexpressed (Walker *et al.* 2013, Farrawell *et al.* 2015). In order to investigate the cytosolic aggregation of TDP-43 various drugs (and combinations of them) that target different cellular processes were tested (Table 4.1). Unless otherwise noted, these conditions were used in all subsequent experiments.

Table 4.1: Incubation conditions and mode of action of different chemicals used to treat cells. ER; endoplasmic reticulum.

Compound	Conc.	Time	Cellular effect
MG132	10 µM	8 – 16 h	Proteasome inhibition
Leptomycin	50 µM	16 h	Nuclear export (exportin 1) disruption
Ivermectin	25 µM	16 h	Nuclear import (importin α/β) disruption
Importazole	40 µM	16 h	Nuclear import (importin β) disruption
Thapsigargin	2.75 µM	8 – 16 h	ER stress (disrupts Ca^{2+} homeostasis)
A23187	2.5 µM	10 h	ER stress (disrupts Ca^{2+} homeostasis)
Brefeldin A	10 µM	10 h	ER stress (prevents protein transport between ER to Golgi)
Tunicamycin	3 µM	10 h	ER stress (prevents protein glycosylation)
dithiothreitol	100 µM	10 h	ER stress (prevents formation of disulfide bonds)
Chloroquine	50 µM	10 h	Autophagy disruption (inhibits fusion of lysosomes and autophagosomes)
Bafilomycin A1	100 nM	10 h	Autophagy disruption (inhibits vacuolar type H+-ATPases)
3-methyladenine	10 mM	10 h	Autophagy disruption (inhibits PI3K)
U0126	60 nM	10 h	Autophagy disruption (inhibits ERK)

References: Wagstaff *et al.* (2012), Sonderholm *et al.* (2011), Wu *et al.* (2014), Sungwook *et al.* (2015), (Frieboes *et al.* 2014).

4.2.2 Immunofluorescence detection of TDP-43

4.2.2.1 Detection of total cellular TDP-43

Cells were harvested using trypsin/EDTA as previously described. After being washed twice in cold PBS (300 x *g*, 5 min, RT), the supernatant was discarded and the cells resuspended in freshly made 4% w/v PFA in PBS, pH 7.4 and incubated for

15 min at RT. All subsequent wash steps were 700 x *g* for 10 min, 4 °C. Cells were washed three times to remove residual PFA, and incubated in blocking/permeabilisation solution (0.3% v/v Triton X-100, 3% w/v BSA, 5% v/v goat serum in PBS) for 1 h at RT. Following another wash, the cells were resuspended in blocking solution containing mouse monoclonal anti-TDP-43 (2E2-D3; 1:400 dilution; Abnova, Taiwan) and incubated at 4 °C overnight, with rocking. Cells were then resupended in a large volume (~15 ml) of 1% w/v BSA in PBS and placed on a rocker for 10 min at RT to thoroughly remove any unbound primary antibody. This was followed by centrifugation as above and washing as described three times. The cells were then incubated with goat anti-mouse IgG-AF488 (1 $\mu g.ml^{-1}$, Life Technologies, USA) in blocking/permeabilisation solution without goat serum for 2 h at RT. Unbound secondary antibodies were then removed by washing with PBS as above. The cells were analysed immediately or stored for future analysis for up to one week (4 °C in 1% w/v PFA in PBS, pH 7.4). All imaging was performed on a Leica TCS SP5 II confocal microscope using Leica Application Suite Advanced Fluorescence version 2.6.1-7314, and flow cytometry was performed on either an LSRII or LSRFortessa X-20 (both BD Biosciences, USA).

4.2.2.2 Specific detection of cytosolic TDP-43

A protocol was developed that allowed the immunofluorescence detection of only cytosolic TDP-43. This was based on the methods used for total cell detection with the following changes:

i. 10 min fixation

ii. 10 min permeabilisation on ice with 5 µM digitonin in PBS before blocking/permeabilisation solution was applied

iii. Blocking solution did not contain Triton X-100

4.2.3 Co-immunoprecipitation

N2a cells were transfected to express TDP-43^{M337V}-tGFP (Origene, USA) and human CLU using Lipofectamine 2000 transfection reagent according to the manufacturer's instructions (Life Technologies, USA). Some cells were only transfected to express TDP-43^{M337V}-tGFP. 48 h after transfection the cells were or were not stressed as described above in Table 4.1. The cells were harvested with trypsin/EDTA and washed twice with PBS (300 x g, 5 min) before being lysed on ice for 5 min in PBS containing 1% v/v Triton X-100 and Complete® Protease Inhibitor Cocktail (Roche, Switzerland). Any insoluble material was pelleted (21,000 x g, 15 min, 4 °C) and the cleared lysate gently mixed overnight at 4 °C with Sepharose beads coupled to mouse monoclonal G7 anti-CLU antibody. In some cases purified human CLU or BSA (100 nM) was added directly to the lysate immediately prior to the addition of the Sepharose beads. The beads were then washed 4 times in PBS (10 min, 2,000 x *g*, 4 °C) before eluting the bound proteins by boiling the beads for 5 min in SDS sample buffer. The beads were removed by centrifugation (2,000 x g, 10 min) and the proteins were separated by SDS-PAGE on a 10% gel. A Western blot was then performed and TDP-43^{M337V}-tGFP detected using either an HRP-conjugated mouse

monoclonal antibody against tGFP (Origene, USA) or a mouse monoclonal antibody against TDP-43 (Abnova, Taiwan) as previously described (Chapter 2).

4.2.4 *In vitro* translation of TDP-43

cDNA encoding a human TDP-43^{WT} -tGFP construct was cloned into pT7CFE1-CHis (Thermo Fisher Scientific, USA). Both the cloning and the verification of insertion by sequencing was performed by Genscript (USA). The fusion protein was expressed using the TnT® T7 Quick Coupled Transcription/Translation System (Promega) in a 96 well microtiter plate held in POLARstar Omega plate reader (BMG LabTech, Germany) at 30°C for 90 min. After the reaction was complete a final yield of 43 nM was estimated (the manufacturer's suggested yield) and the mixture was centrifuged to remove any aggregated material (16,600 x g, 10 min). The supernatant was incubated at either 4°C or 37°C for 4 h with shaking to induce aggregation with or without the addition of CLU or BSA (both at 43 nM). Following this incubation the samples were centrifuged again as above to pellet any aggregated protein. The supernatant containing any remaining soluble TDP-43-tGFP was collected and 5 µl was separated by electrophoresis through a reducing 10% SDS PAGE gel and analysed by Western blot for the presence of TDP-43 as previously described (section 2.3).

4.2.5 Plasmids

Transfections were performed using Lipofectamine 2000 (Invitrogen, USA) as previously described. A plasmid encoding a TDP-43 C-terminal fragment (amino acids 216-414; pEGFP-N1-TDP-CTF) was a gift from Zuoshang Xu (Addgene plasmid #28197) (Yang *et al.* 2010). This construct is hereafter referred to as 'TDP-CTF-eGFP'. pRc/CMV-HT7 (encoding human CLU) was originally cloned by Prof. Mark Wilson using the pRc/CMV parent plasmid (Invitrogen, USA) pmCherry-C1 (encoding unconjugated mCherry) was a gift from Dr. Ian Blair, Macquarie University, Australia)

4.2.6 Co-transfections

Transfections for FloIT experiments were performed on N2a cells grown to approximately 80 – 90% confluency in 24 well plates. Lipofectamine 2000 was used as previously described with the following change when using two plasmids: the total amount of DNA used was divided evenly between both plasmids. That is, for a single well in a 24 well plate, the 0.5 µg DNA used was comprised of 0.25 µg of each plasmid used in the co-transfection. In addition to these double transfections, the FloIT experiments typically involved a single transfection of cells to express only TDP-43^{M337V}-tGFP. For these transfections, 0.5 µg DNA was used for each well of a 24 well microtiter plate so singly and co-transfected cells were treated with an equivalent amount of DNA in order to keep total expression levels similar. This information is summarised in Table 4.2.

Table 4.2: Amounts of DNA used in transfections for FloIT experiments. The values shown indicate the amount of DNA used (μg) for the transfection of a single well on a 24 well microtiter plate.

	Plasmid encoding		
Transfection	TDP-43^{M337V}-tGFP	CLU	mCherry
TDP-43^{M337V} only	0.25	-	-
TDP-43^{M337V} + CLU	0.25	0.25	-
TDP-43^{M337V} + mCherry	0.25	-	0.25

4.2.7 Fluorescence correlation spectroscopy

Fluorescence correlation spectroscopy (FCS) was performed using U251 cell transfected to express TDP-43^{M337V}-tGFP. Cells were harvested with trypsin as previously described and lysed with 0.5% Triton X-100/PBS containing Complete® protease inhibitor (Roche, Switzerland). FCS was performed using Leica LAS AF FCS Wizard and SymPhoTime attached to a Leica SP5 II microscope (Leica, Germany).

4.2.8 Inclusion quantification

The number of inclusions present in a population of cells were quantified using FloIT as described in Chapter 3.

4.2.9 LC3 immunocytochemistry

N2a cells were immunostained for LC3 using a protocol supplied by the manufacturer of the primary antibody (Cell Signalling, USA). Cells were grown in 8 well glass bottom μ-Slides (Ibidi, Germany) and treated as indicated with Tg (2.75 μM), MG132 (10 μM) and/or chloroquine (CQ; 50 μM). Cells were rinsed twice

in PBS and then fixed and permeabilised with 100% methanol (15 min at -20°C). The cells were then rinsed in PBS three times before being blocked for 1 h at RT with 5% w/v BSA, 0.3% v/v Triton X-100 in PBS. The blocking solution was aspirated and rabbit anti-LC3B primary antibody (Cell Signalling #2775) was added (diluted in antibody dilution buffer (1% w/v BSA, 0.3% v/v Triton X-100 in PBS). In the case where cells were co-stained for CLU, purified G7 anti-CLU antibody was used at 1 µg/ml. After an overnight incubation at 4°C, the primary antibody was aspirated and cells were rinsed three times with PBS. Secondary antibodies in antibody dilution buffer were added (anti-rabbit IgG-AF647 for LC3 (2 µg/ml, ab150079, Abcam, USA) and anti-mouse IgG-AF555 for CLU (2 µg/ml, ab150114, Abcam, USA). The cells were then washed as above and analysed by confocal microscopy as described in section 4.2.2.1 or flow cytometry using an LSRFortessa X-20 (BD Biosciences, USA).

4.2.10 Image processing

Two methods of determining the co-localisation between proteins from confocal images were used: (i) line analysis and (ii) percent pixel co-localisation.

4.2.10.1 Line analysis

N2a cells transfected to express TDP-43^{M337V}-tGFP as above were treated (or not) with Tg and MG132. The cells were immunostained for CLU and LC3 as described above (section 4.2.9). Line intensity profiles were used to examine the possibility of

co-localisation between proteins following confocal microscopy (performed as described above). ImageJ (version 1.48) (Schneider *et al.* 2012) was used to draw a straight line through the centre of the cell. The relative amount of individual proteins at each point along the line was assessed by pixel fluorescence intensity. These values were normalised to the maximum value for each protein and plotted as a line graph such that coincident peaks represent likely regions of co-localisation.

4.2.10.2 Percent pixel co-localisation

To provide a more quantitative analysis of co-localisation, the percent co-localisation of fluorescent proteins imaged via confocal microscopy was calculated using a script written in Python v2.7 by myself (Appendix I; summarised in Figure 4.1). Firstly, images were taken so a small number of pixels were over-exposed. Pixels below an arbitrary threshold of 40% of the maximum possible brightness (i.e. the value of the over-exposed pixels) were then set to 0 (black). Pixels above the threshold were set to the maximum value (binarised) for ease of processing and then summed and averaged to provide the 'calculated coincidence' between the proteins.

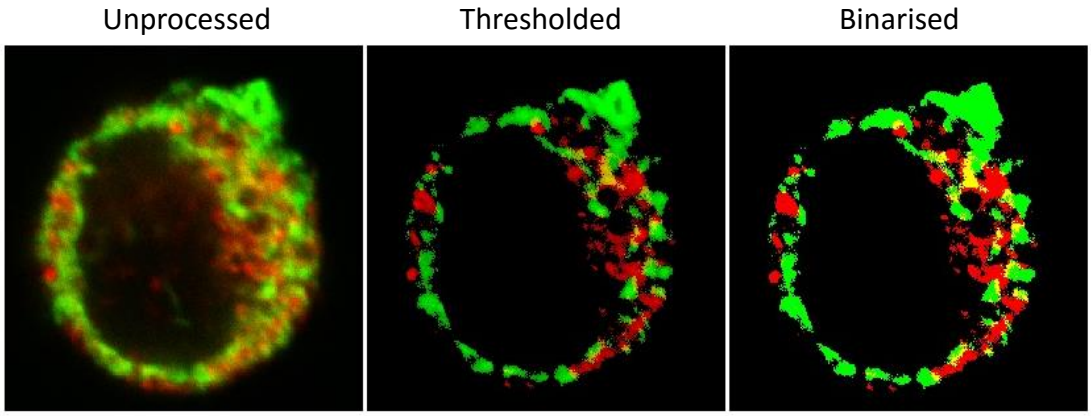

Figure 4.1: Example images of the process used to quantify protein co-localisation. The process can be used for two (in this case CLU, green and LC3, red) or more proteins.

Chance coincidence (the amount of overlapping pixels expected purely by chance, based on the percentage of positive pixels) was calculated by creating a new image with the positive pixels from the binarised images randomly spread over the image area. The shuffled pixels were packed into an area 79% the size of the original image to take into account the approximate packing efficiency of a roughly circular cell in a square image (Figure 4.2). The chance coincidence will always shows a smaller value than the calculated coincidence if the proteins are originally excluded from the nucleus (as in Figure 4.1), but due to the varying nuclear sizes, and protein expression pattern, this proved impossible to control for in the analysis.

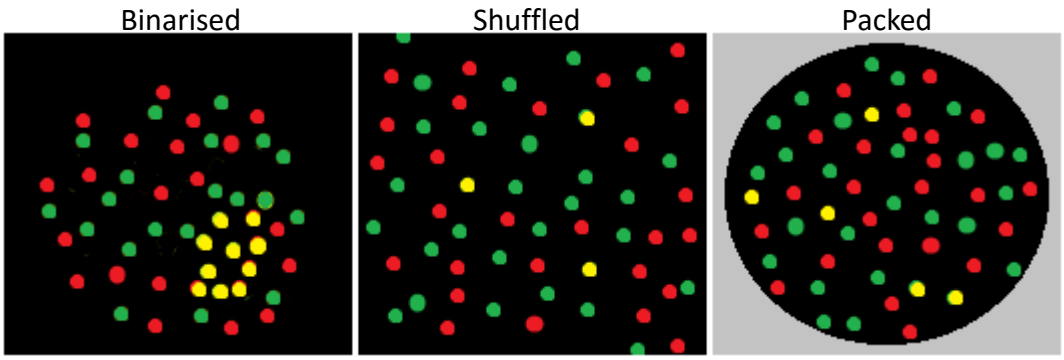

Figure 4.2: Diagram of the process of chance coincidence calculation. The red and green dots represent positive pixels from a binarised source image, yellow dots represent coincident pixels. In this case original coincident pixels = 10 whereas chance = 5, indicating that half of the coincidence in the original image was due to chance.

4.3 Results

A flow cytometric method was established that allowed the specific detection of cytosolic TDP-43. The method was based on the selective permeabilisation of the cell membrane by digitonin (Fiskum 1985). The exclusion of membrane-bound organelles from permeabilisation using this method was confirmed by immunostaining U251 cells with primary antibodies reactive against ER-resident chaperone BiP (Figure 4.3*a*) or histones (*data not shown*). Digitonin permeabilised cells immunostained for TDP-43 displayed a low level of fluorescence diffused throughout the cytosol, which is expected for TDP-43 due to its normal nuclear localisation (Figure 4.3*b*). This method was used on U251 cells that had been treated (or not) with MG132, leptomycin, ivermectin or importazole before being fixed and permeabilised. MG132, leptomycin and ivermectin each significantly increased the level of cytosolic TDP-43, by approximately 2.5, 1.5 and 1.25-fold respectively (Figure 4.3*c*).

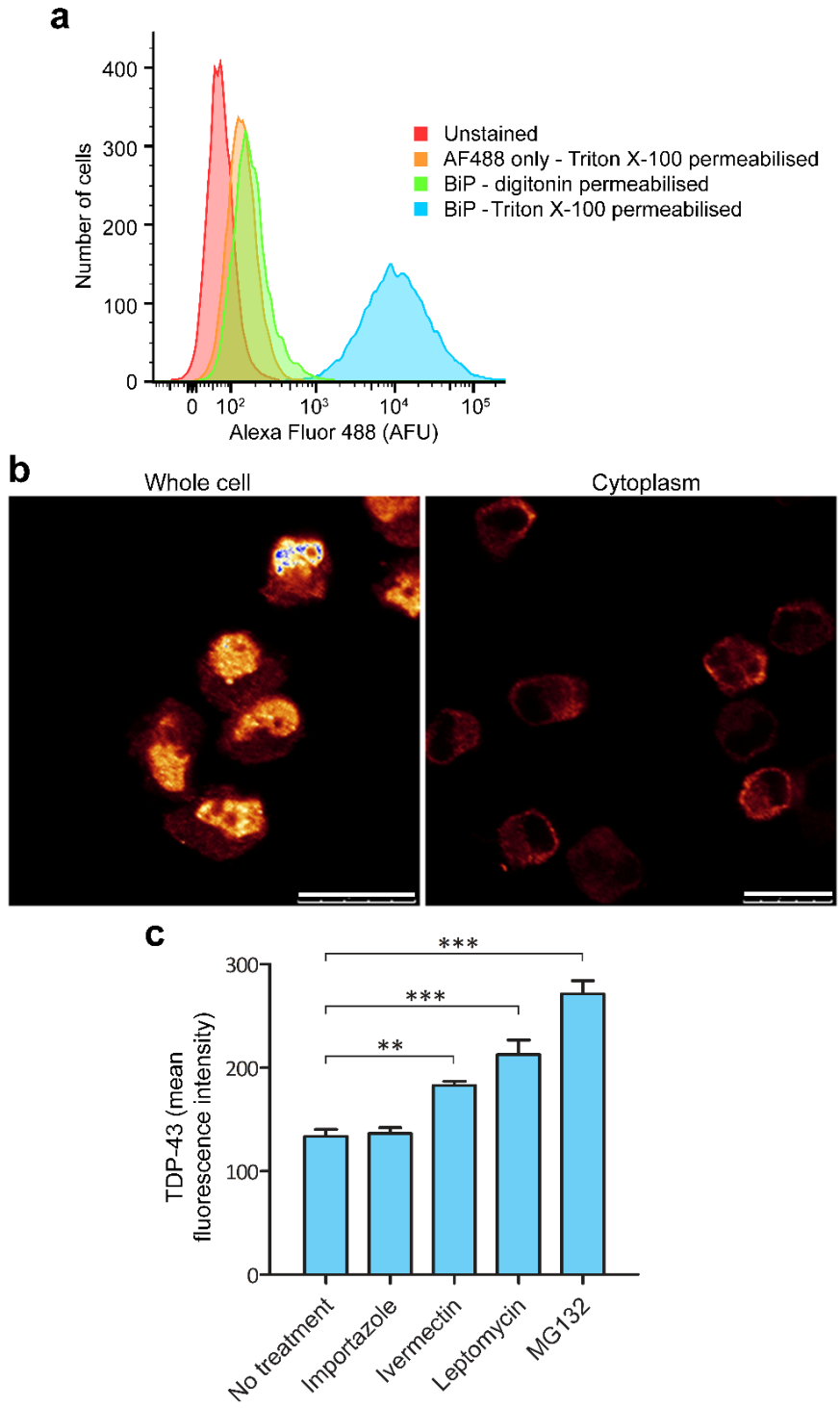

Figure 4.3: Cytosolic TDP-43 levels increase in response to proteasome inhibition. a) Cytogram of U251 cells permeabilised with either digitonin or Triton X-100 and immunostained for BiP using a secondary antibody conjugated with AF488. b) U251 cells permeabilised with Triton X-100 (left) reveal strong nuclear staining for TDP-43. Cells permeabilised with digitonin (right) show selective staining of cytosolic TDP-43. Images are representative of three separate experiments. Scale bars are 10 µm. c) U251 cells treated with the indicated agents were selectively stained for cytosolic TDP-43. Horizontal black lines indicate significant differences between the two indicated data sets (** $P < 0.01$, *** $P < 0.001$, analysed by one-way ANOVA with a Bonferroni post-test). Values are means (n=3), error bars are SEM.

Having established that of the agents tested MG132 was the most effective at inducing cytosolic accumulation of TDP-43, the aggregation of TDP-43 within the cytosol following treatment with MG132 was examined by FCS. U251 cells were transfected to express TDP-43^{M337V}-tGFP and incubated with MG132 for various times. Cells were lysed with Triton X-100, and soluble tGFP-fluorescing particles were analysed by FCS. The average diffusion time of fluorescent particles in the lysate increased with time the cells were exposed to MG132, indicating that the average size of soluble TDP-43^{M337V}–tGFP particles was getting larger (Figure 4.4).

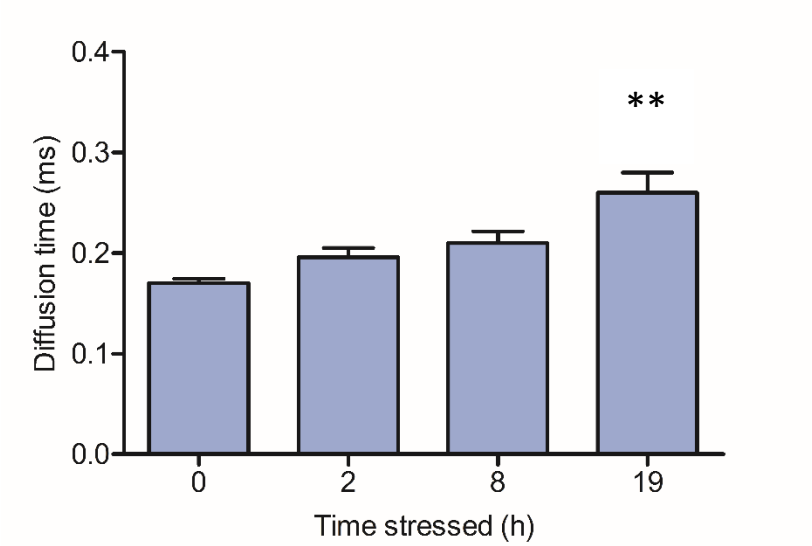

Figure 4.4: MG132 induced a time-dependent increase in the size of soluble TDP-43 species in U251 cells. U251 cells were treated with MG132, lysed after the indicated times, and the mean diffusion time of soluble TDP-43^{M337V}-tGFP species in clarified lysate was analysed by FCS. * $P < 0.05$, analysed by one-way ANOVA; error bars are SEM; n=3.

As mentioned above, it was previously established that ER stress is required for the retrotranslocation of CLU (Nizard *et al.* 2007). To ensure that ER stress could be pharmacologically induced in N2a cells, the effects of a range of chemicals (Tg, A23187, brefeldin A, tunicamycin and DTT) on BiP expression (an ER stress marker

(Baumeister *et al.* 2005)) was examined. In all cases, except DTT which showed no effect, BiP expression was increased approximately 3-4 fold (Figure 4.5*a* and *b*).

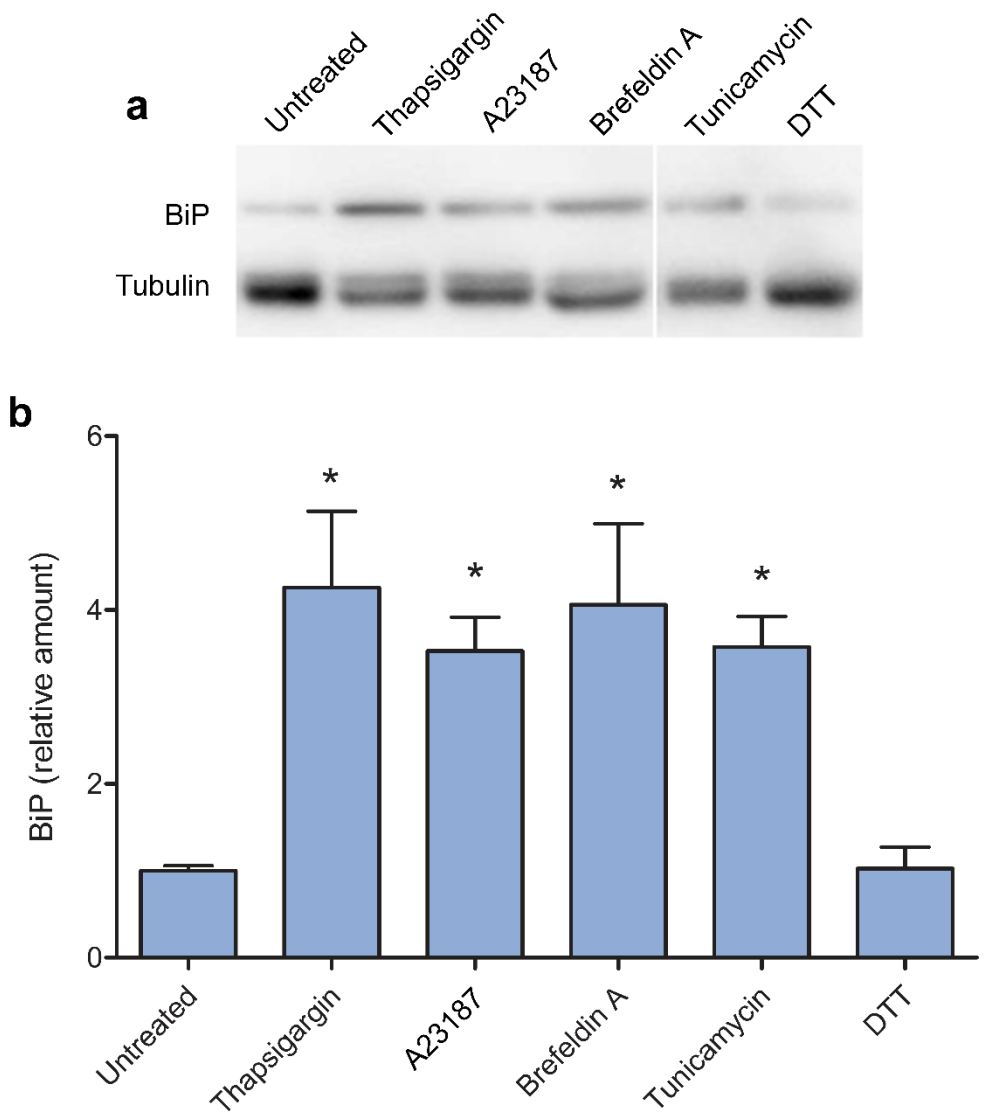

Figure 4.5: Pharmacological induction of ER stress in N2a cells. a) N2a cells were treated with the indicated chemical for 10 h before being lysed and analysed for BiP expression by Western blot (a representative blot is shown). b) Quantification of band intensities. Statistical comparisons are against untreated cells (* $p < 0.05$, analysed by one-way ANOVA with a Bonferroni post-test). Values are means (n=3), error bars are SEM.

To examine whether the ER stress response induced in each case was associated with the intracellular accumulation of CLU, this was directly measured following the various treatments. Treatment with only Tg, MG132 or CQ had no effect on the

level of intracellular CLU. However, the level of intracellular CLU approximately doubled ($p < 0.001$) when Tg was combined with either MG132 or CQ (Figure 4.6*a*). This coincided with reduced secretion of CLU (Figure 4.6*b* and *c*).

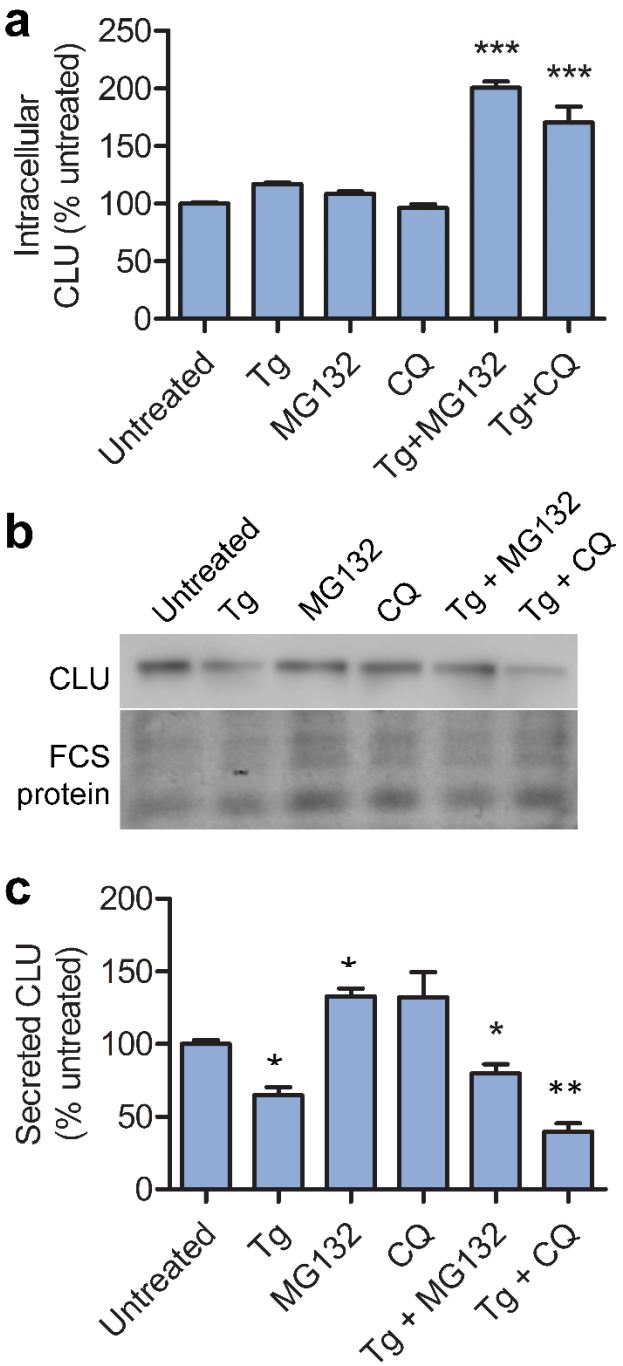

Figure 4.6: ER stress triggers the retrotranslocation of CLU. a) N2a cells were treated with the indicated chemical, immunostained for intracellular CLU and quantified by flow cytometry. b) The culture supernatant from the cells was collected and analysed by Western blot for secreted CLU (representative blot shown). 'FCS protein' indicates a section of the SDS PAGE gel removed before performing the Western blot, which was stained with Coomassie Blue. The proteins visualised are those present in the culture medium and were used as a loading control. c) Quantification of CLU bands detected by Western blot, relative to the loading control and normalised to the untreated sample. Statistical comparisons are against untreated cells (*, $p < 0.05$, **, $p < 0.01$, *** $p < 0.001$, analysed by one-way ANOVA). Values are means, error bars are SEM, n = 3.

Expression of the WT TDP-43-tdTomato fusion protein in U251 cells results in strict localisation to the nucleus (as shown by DNA staining with Red Dot 2). Following treatment with MG132/Tg however, the TDP-43 fusion protein is translocated into the cytosol where it forms discrete foci (Figure 4.7). Under normal conditions CLU is secreted from U251 cells and only low levels of endogenous intracellular CLU contained within vesicular structures can be detected by immunocytochemistry (Nizard *et al.* 2007). However, when the cell is ER stressed by treatment with MG132 and Tg, the level of intracellular CLU is visibly increased. The localisation pattern does not appear to change but this is likely due to the limited resolution of the technique. However, in cells expressing TDP-43-tdTomato, CLU is extensively co-localised with the fluorescent cytosolic inclusions formed by the fusion protein during ER stress (Figure 4.7).

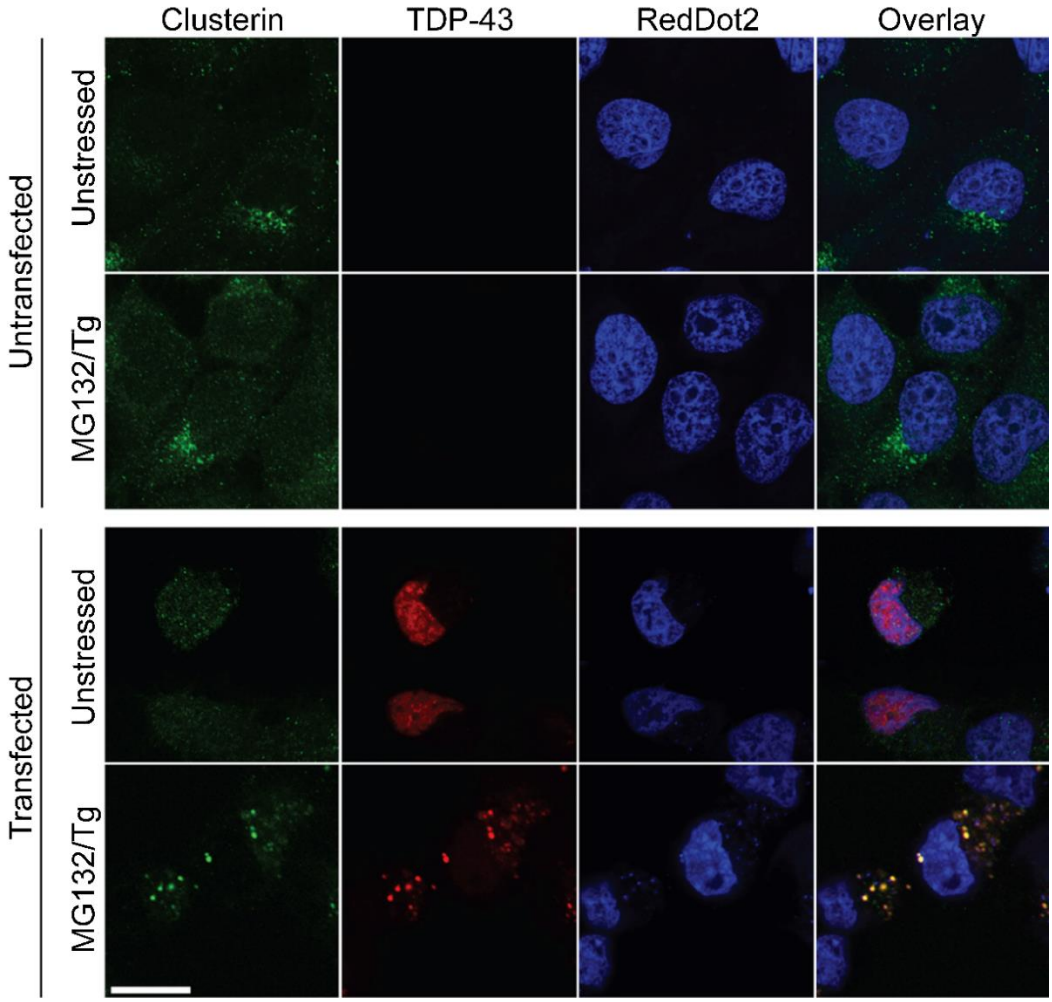

Figure 4.7: CLU co-localises with TDP-43-tdTomato inclusions during ER stress. U251 cells transfected to express TDP-43-tdTomato show punctate inclusion bodies after being treated with MG132 and Tg. In unstressed cells, CLU (detected using G7 monoclonal mouse antibody and AF488-conjugated secondary, green) was detected in vesicular structures throughout the cytosol, but co-localised (yellow) with TDP-43-tdTomato inclusions when these were induced by MG132/Tg treatment. DNA was stained with RedDot2 (shown in blue). Images shown are representative of three separate experiments. Scale bar is 10 µm.

A similar experiment was performed using neuron-like SH-SY5Y cells. Since TDP-43^{WT} does not generate cytoplasmic inclusions unless additional treatments are imposed (Figure 4.7, *third row*), the SH-SY5Y cells were transfected with a plasmid encoding TDP-CTF-eGFP which forms cytosolic inclusions without the application of exogenous stresses (Yang *et al.* 2010). In comparison to the U251 cells shown in

Figure 4.7, the endogenous CLU in unstressed SH-SY5Y cells showed a more obviously granular/vesicular appearance. In transfected cells, cytosolic TDP-CTF-eGFP inclusions were visible in the majority of cells. CLU co-localised with these inclusions only when the cell was subjected to ER stress (Figure 4.8).

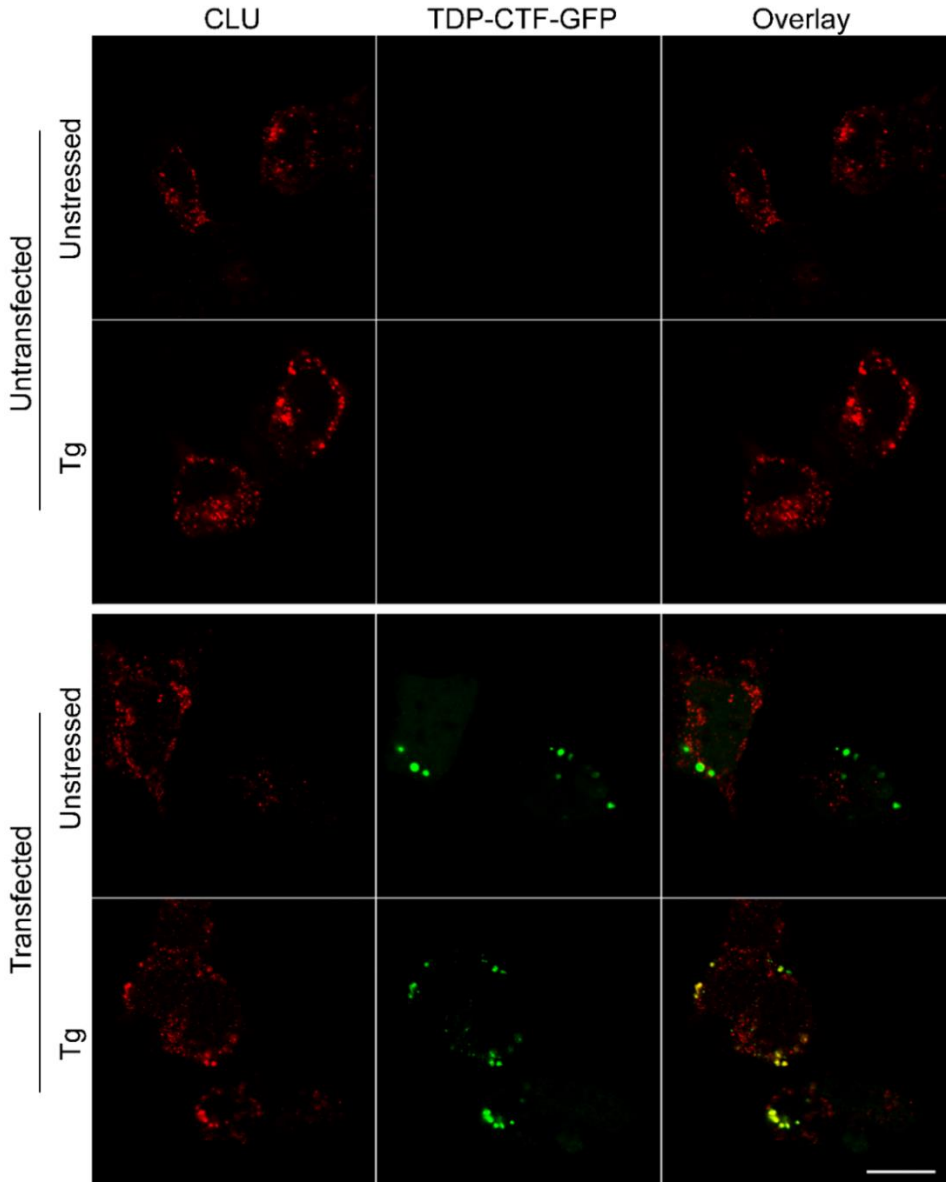

Figure 4.8: CLU co-localises with TDP-CTF-eGFP inclusions under ER stress. SH-SY5Y cells transfected with TDP-CTF-eGFP (green) show punctate inclusions both with and without Tg treatment. CLU (detected using G7 monoclonal mouse antibody and an HF647-conjugated secondary, red) appeared vesicular in unstressed conditions, but co-localised with TDP-CTF-eGFP inclusions (yellow) following Tg treatment. Images shown are representative of 2 separate experiments. Scale bar is 10 µm.

In N2a cells, without proteasome inhibition, the level of specific immunofluorescence obtained for endogenous CLU was not above that of background fluorescence obtained with an isotype-matched control antibody (*data not shown*) and was thus not examined for co-localisation with TDP-43. However, when human CLU was overexpressed in N2a cells, distinct co-localisation was observed between TDP-CTF-eGFP inclusions and CLU (Figure 4.9). This co-localisation was dependent upon the treatment of the cells with either Tg or the Ca^{2+} ionophore A23187, suggesting that as in the models shown above, ER stress is necessary to generate cytosolic CLU.

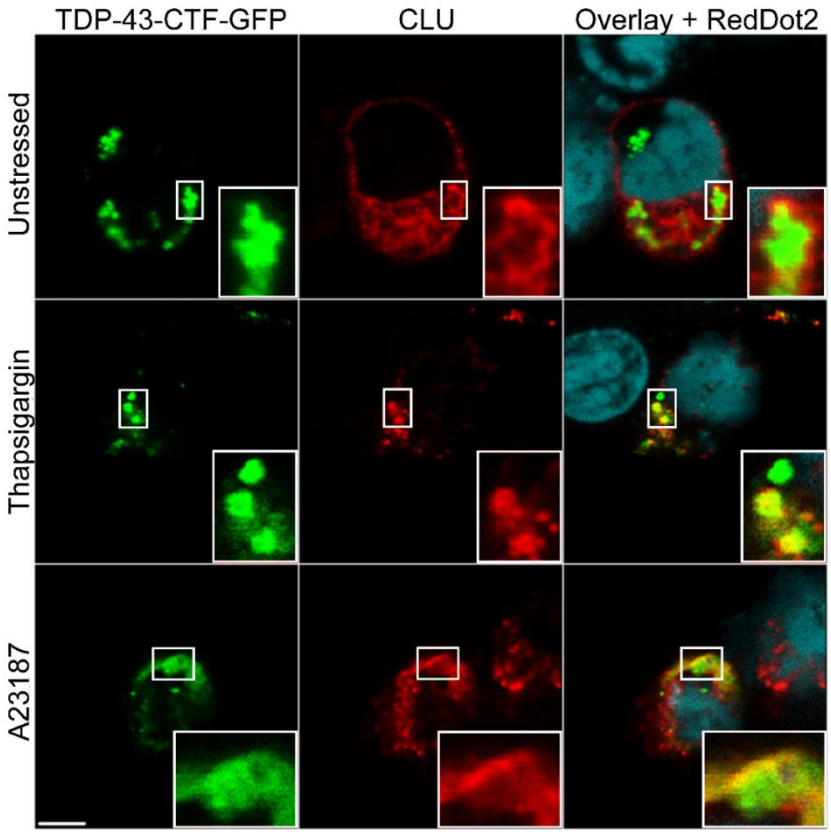

Figure 4.9: CLU co-localises with TDP-CTF-eGFP inclusions in N2a cells during ER stress. N2a cells expressing TDP-CTF-eGFP (green) and human CLU (detected using G7 monoclonal mouse antibody and an AF555-conjugated secondary antibody, red) show co-localisation (yellow) during ER stress induced by Tg or A23187. Insets (large white rectangles) are 3X zoom of the region identified by the small white rectangles. Images shown are representative of 2 separate experiments. Scale bar is 5 µm.

A co-immunoprecipitation was performed in order to examine whether CLU would bind to soluble TDP-43 species in detergent lysates prepared from N2a cells. U251 cells transfected to express TDP-43^{M337V}-tGFP were treated (or not) with MG132 and Tg and then lysed. Soluble CLU was captured on Sepharose beads coupled with G7 mouse monoclonal anti-CLU antibody and then washed, eluted from the beads by boiling in SDS loading buffer, and analysed by Western blot for the presence of either TDP-43 or tGFP. In U251 cells, no tGFP was detected in immunoprecipitates from lysates of untreated cells, possibly due to the small amount of intracellular CLU in unstressed cells. In contrast, however, TDP-43 was detected in similar analyses of lysates prepared from cells that had been treated with Tg and MG132 (Figure 4.10*a*). In these cells, a major ~75 kDa band was observed, corresponding to the expected size of TDP-43 fused with tGFP (70 kDa). A larger ~145 kDa band was also observed, which is likely to represent an SDS-resistant TDP-43-tGFP dimer or TDP-43-tGFP-CLU complex. A smaller band of approximately 50 kDa was also observed which may represent a TDP-43 cleavage product.

A similar experiment was performed by transfecting N2a cells to express TDP-43^{M337V}-tGFP; in some cases the cells were co-transfected to express human *CLU* since the G7-Sepharose does not react with the murine CLU expressed endogenously by N2a cells. TDP-43^{M337V}-tGFP was found to co-immunoprecipitate with human CLU even from lysates prepared from unstressed cells (Figure 4.10*b, arrow*). To examine whether this could be the result of CLU binding to TDP-43 after

detergent lysis of cell membranes, purified human CLU was added to the clarified cell lysate prepared from N2a cells expressing TDP-43^{M337V}-tGFP immediately before the addition of the G7-coupled Sepharose beads (see 'spiked' treatment of Figure 4.10*b*). As for lysates prepared from co-transfected cells, CLU and TDP-43^{M337V}-tGFP co-immunoprecipitated when CLU was added to the cell lysate.

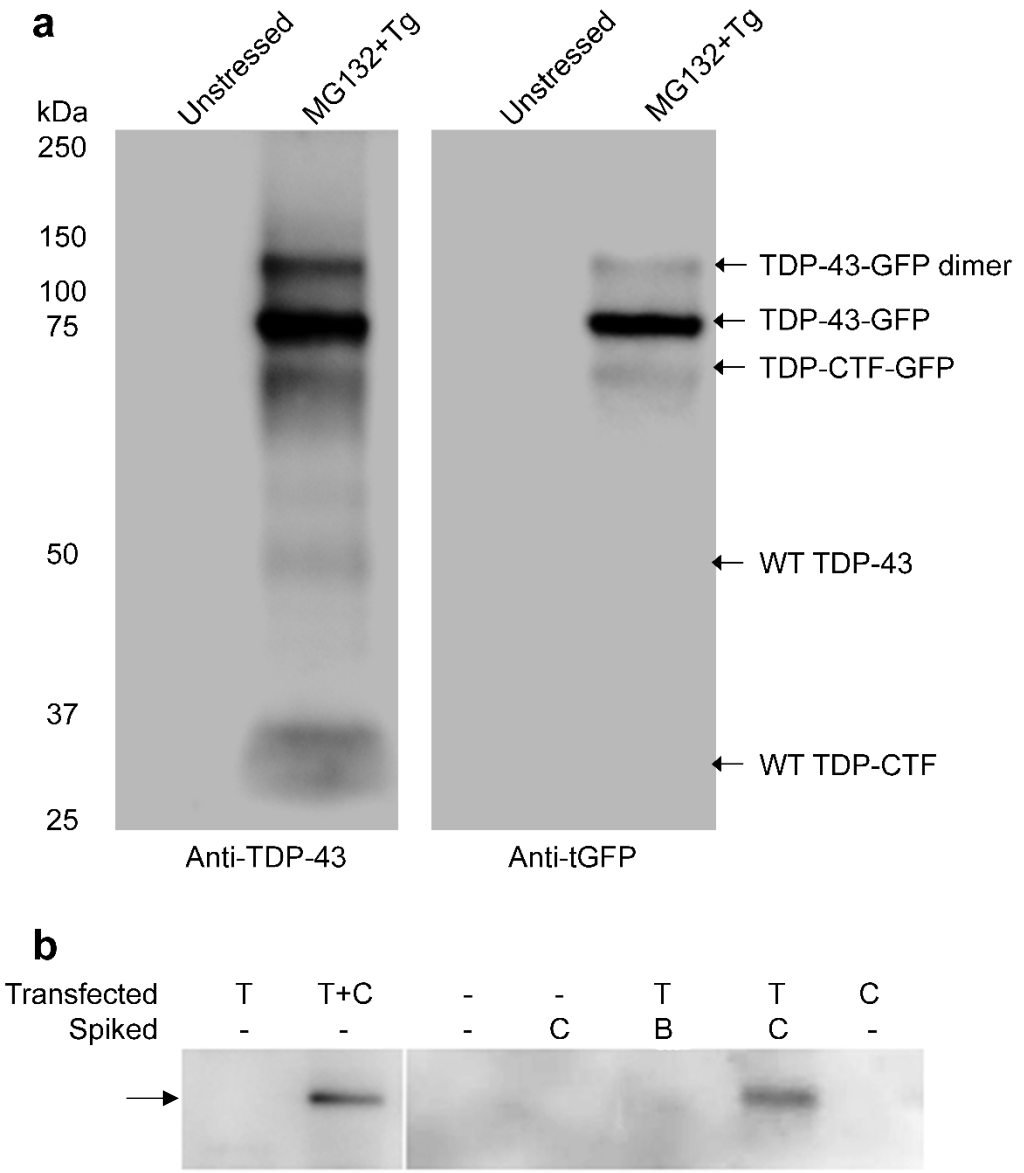

Figure 4.10: CLU can bind to soluble TDP-43 in cell lysates. CLU and its binding partners were pulled down using an immunoprecipitation assay. a) Proteins pulled down from a lysate prepared from U251 cells transfected with a plasmid encoding TDP-43^{M337V}-tGFP, and treated or not with Tg and MG132, were analysed by Western blot for TDP-43 (left) or tGFP (right). Putative identities of the bands are indicated. b) Similarly, TDP-43^{M337V}-tGFP co-precipitated with CLU in co-transfected N2a cells. Cells were transfected to express TDP-43 (T), CLU (C) or both (T+C). The indicated proteins (CLU, C or BSA, B) were also added (spiked) into the lysates of cells expressing TDP-43^{M337V}-tGFP. The arrow indicates the expected size of TDP-43^{M337V}-tGFP. Blots shown are representative of at least two separate experiments.

Having established that CLU is can bind to soluble TDP-43^{M337V}–tGFP in a detergent lysate, the ability of CLU to inhibit the *in vitro* aggregation of TDP-43^{WT}-tGFP was

examined. Previous work has shown that CLU potently inhibits the *in vitro* aggregation of a C-terminal TDP-43 peptide[3]. Recombinant TDP-43 is notoriously difficult to express and purify from bacteria due to its high aggregation propensity. Past expression of TDP-43 in our lab routinely resulted in the accumulation of the recombinant protein in inclusion bodies, which proved difficult to refold[4]. For this reason, an *in vitro* transcription/translation system was used to generate full length TDP-43-tGFP. After transcription, the TDP-43-tGFP was found to aggregate (as indicated by a reduction in the amount of soluble TDP-43) when incubated for 4 h at 37 °C. Turbidity at 340 nm could not be used as a measure of aggregation as the low concentration of TDP-43 did not produce a measurable change (*data not shown*). CLU (when added at 40 nM, approximately a 1:1 molar ratio) kept significantly more TDP-43-tGFP soluble than the non-chaperone control protein BSA present at the same ratio (Figure 4.11*a* and *b*).

[3] R. A. Brown and M. R. Wilson (2013) *Unpublished data*, University of Wollongong.

[4] K. Perkiss and M. R. Wilson (2011) *Unpublished data*, University of Wollongong.

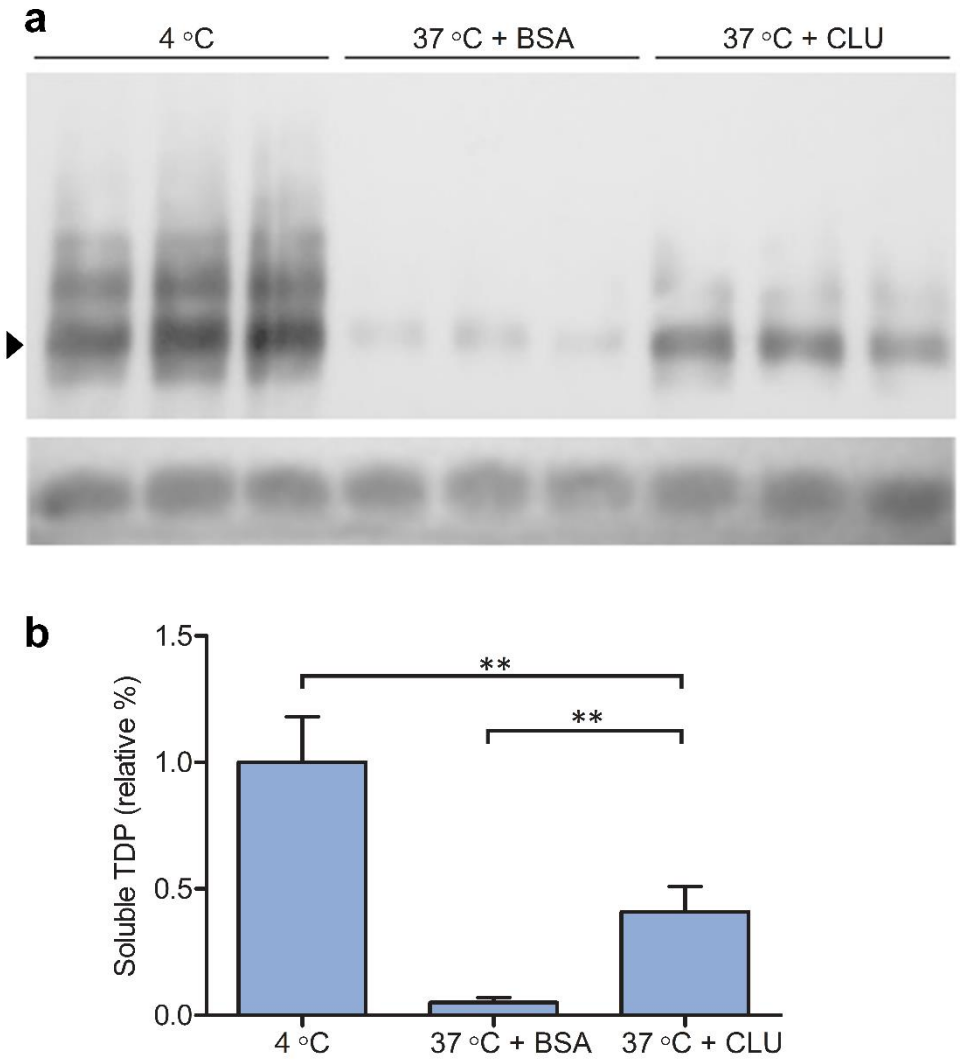

Figure 4.11: CLU inhibits the aggregation of full length human TDP-43-tGFP. a) Representative Western blot of soluble TDP-43-tGFP produced using an *in vitro* transcription/translation system following a 4 h incubation at 4°C or 37°C. The black arrow head indicates the expected size of the TDP-43-tGFP monomer, higher molecular weight bands likely represent oligomers. The bottom panel shows the loading controls (coloured dye in the *in vitro* translation kit visible after PAGE). b) Band quantification of the Western blots. Horizontal black lines indicate significant differences between the two indicated data sets (** $P < 0.01$, analysed by one-way ANOVA with a Bonferroni post-test). Values are means (n=3), error bars SD. Blot shown is representative of 3 separate experiments.

As outlined in Chapter 3, FloIT was developed to allow the accurate quantification of the abundance of inclusions in mammalian cells. The feasibility of using this technique to quantify TDP-43 inclusion load was also confirmed in this work. FloIT was used to investigate whether CLU can affect the numbers of TDP-43^{M337V}-tGFP

inclusions in N2a cells. The effects of overexpression of CLU in the presence of the known inducers of ER stress (Figure 4.5; Tg, A23187, brefeldin A and tunicamycin) was examined. Each of the treatments tested increased the number of inclusions relative to untreated cells, although brefeldin A and tunicamycin did so to a far lesser extent than Tg or A23187. The overexpression of CLU significantly reduced the number of TDP-43^{M337V}-tGFP inclusions in N2a cells treated with Tg or A23187 but not brefeldin A or tunicamycin (Figure 4.12). Relative to cells over-expressing TDP-43^{M337V}-tGFP only, over-expression of the non-chaperone control protein mCherry had no significant effect on the number of inclusions under any of the conditions tested.

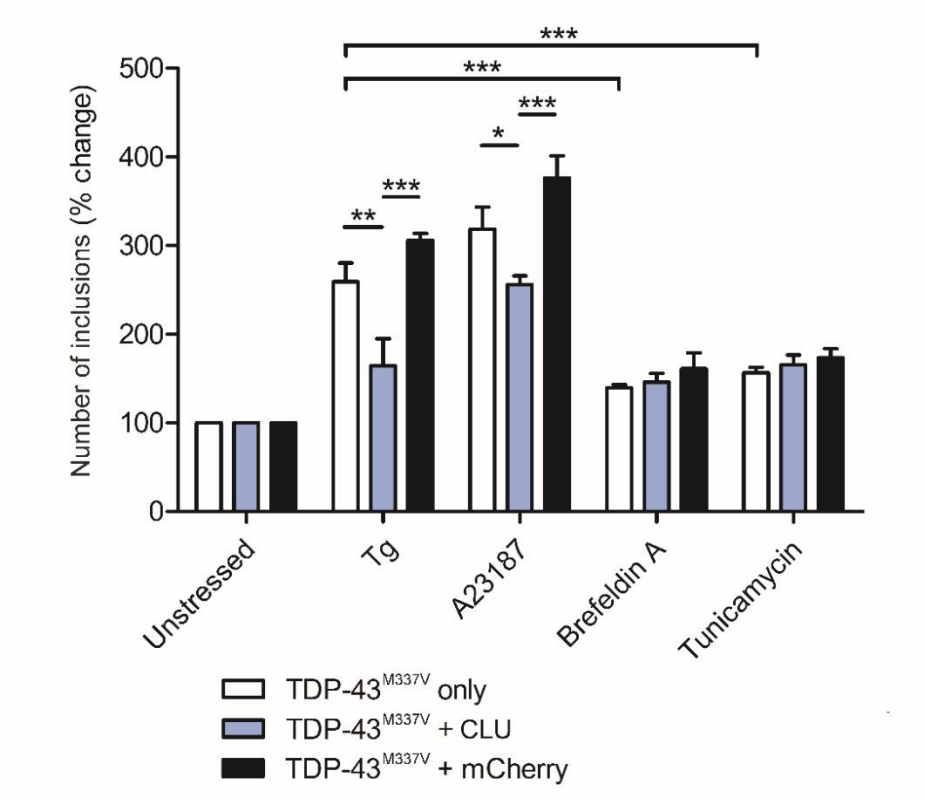

Figure 4.12: CLU reduces the number of TDP-43^{M337V}-tGFP inclusions under ER stress conditions. N2a cells transfected as indicated were incubated for 10 h with the indicated treatment. Quantification of inclusions was performed by FloIT. Horizontal black lines indicate significant differences between the two indicated data sets (* $p < 0.05$, ** $p < 0.01$, *** $p < 0.001$, analysed by two-way ANOVA with a Bonferroni post-test). Values are means (n=4), error bars are SEM.

One possible mechanism by which CLU could reduce the number of inclusions is by facilitating the degradation of cytosolic TDP-43^{M337V}-tGFP. In order to examine this further, the effects of CLU expression on the numbers of TDP-43^{M337V}-tGFP inclusions was assessed in the same transfected cell system as above, this time also analysing cells in which ER stress was induced with Tg and the proteasome inhibited with MG132. Under these latter conditions, CLU overexpression still significantly reduced the number of inclusions, whereas overexpression of mCherry did not (Figure 4.13*a*). Similarly, a number of inhibitors of autophagy were used (CQ, bafilomycin A1, U0126 and 3-methyladenine (3MA)) in combination with Tg. With the exception of 3MA, the overexpression of CLU again significantly reduced the number of inclusions in cells treated with each of these chemicals (Figure 4.12*b*). Unfortunately, the treatment of transfected cells with a combination of Tg, MG132 and individual autophagy inhibitors caused rapid and extensive cell death (*data not shown*) and thus the effects of this combined treatment on the numbers of TDP-43^{M337V}-tGFP inclusions could not be tested.

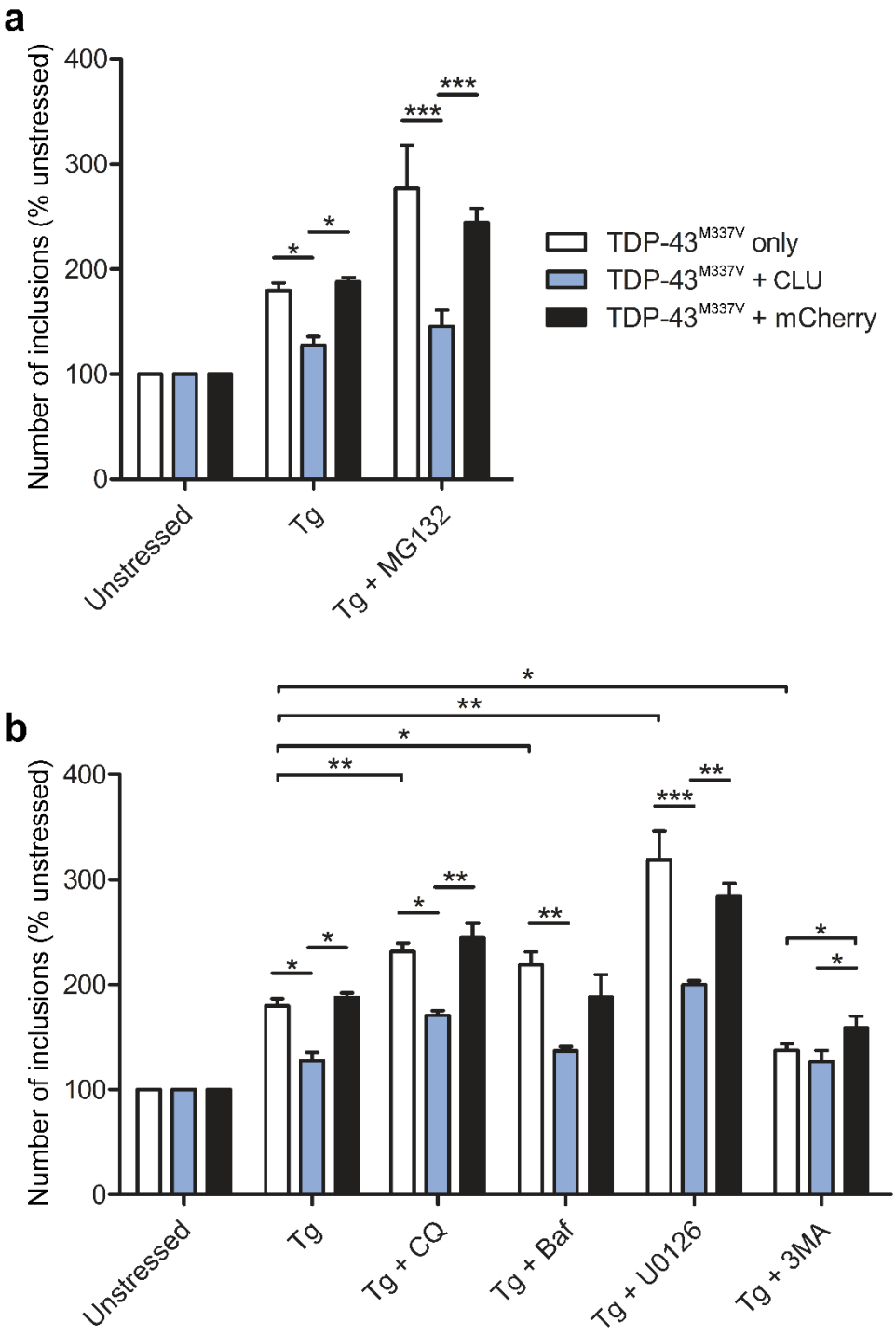

Figure 4.13: CLU overexpression reduces the number of TDP-43^{M337V}-tGFP inclusions in ER-stressed N2a cells even during inhibition of the proteasome or autophagy. N2a cells transfected as indicated were incubated for 10 h with the treatments indicated to inhibit a) the proteasome (MG132), or b) autophagy (bafilomycin A1 (baf), CQ, U0126 and 3-methyladenine (3MA)). Quantification of inclusions was performed by FloIT. The key shown next to **a** also applies to **b**. Horizontal black lines indicate significant differences between the two indicated data sets (* $p < 0.05$, ** $p < 0.01$, *** $p < 0.001$, analysed by two-way ANOVA with a Bonferroni post-test). Values are means (n=3), error bars are SEM.

In order to examine whether the activation of autophagy is sufficient to reduce the numbers of TDP-43^{M337V}-tGFP inclusions, N2a cells were treated with the commonly used autophagy-inducer rapamycin (an mTOR inhibitor; Figure 4.14*a*) (Sarkar *et al.* 2009, Kapuy *et al.* 2014). As expected, CQ treatment caused a significant increase in LC3 levels due to the inhibition of autophagosome acidification and, thus, LC3 degradation. A combination of rapamycin and CQ produced significantly higher levels of LC3 compared to CQ treatment alone. This result confirms that rapamycin induced autophagy in N2a cells. Transfected N2a cells expressing TDP-43^{M337V}-tGFP were next treated with rapamycin and/or Tg-induced ER stress and the number of inclusions measured using FloIT (Figure 4.14*b*)**.** Since rapamycin is known and was confirmed to induce autophagy, it was expected to reduce the number of TDP-43^{M337V}-tGFP inclusions. Whether or not rapamycin would enhance or limit the effect of CLU in these cells was unknown. In cells expressing only TDP-43^{M337V}-tGFP and treated with Tg (but not in unstressed cells), incubation with rapamycin significantly reduced the number of TDP-43^{M337V}-tGFP inclusions. However, the number of inclusions in these rapamycin and Tg treated cells remained above the number of inclusions in untreated cells ($p < 0.05$)**.** As before, during Tg-induced ER stress, CLU expression significantly reduced the number of TDP-43^{M337V}-tGFP inclusions. In cells treated with both Tg and rapamycin, the CLU-mediated reduction in the number of inclusions was less in magnitude but still significant when compared to cells overexpressing mCherry.

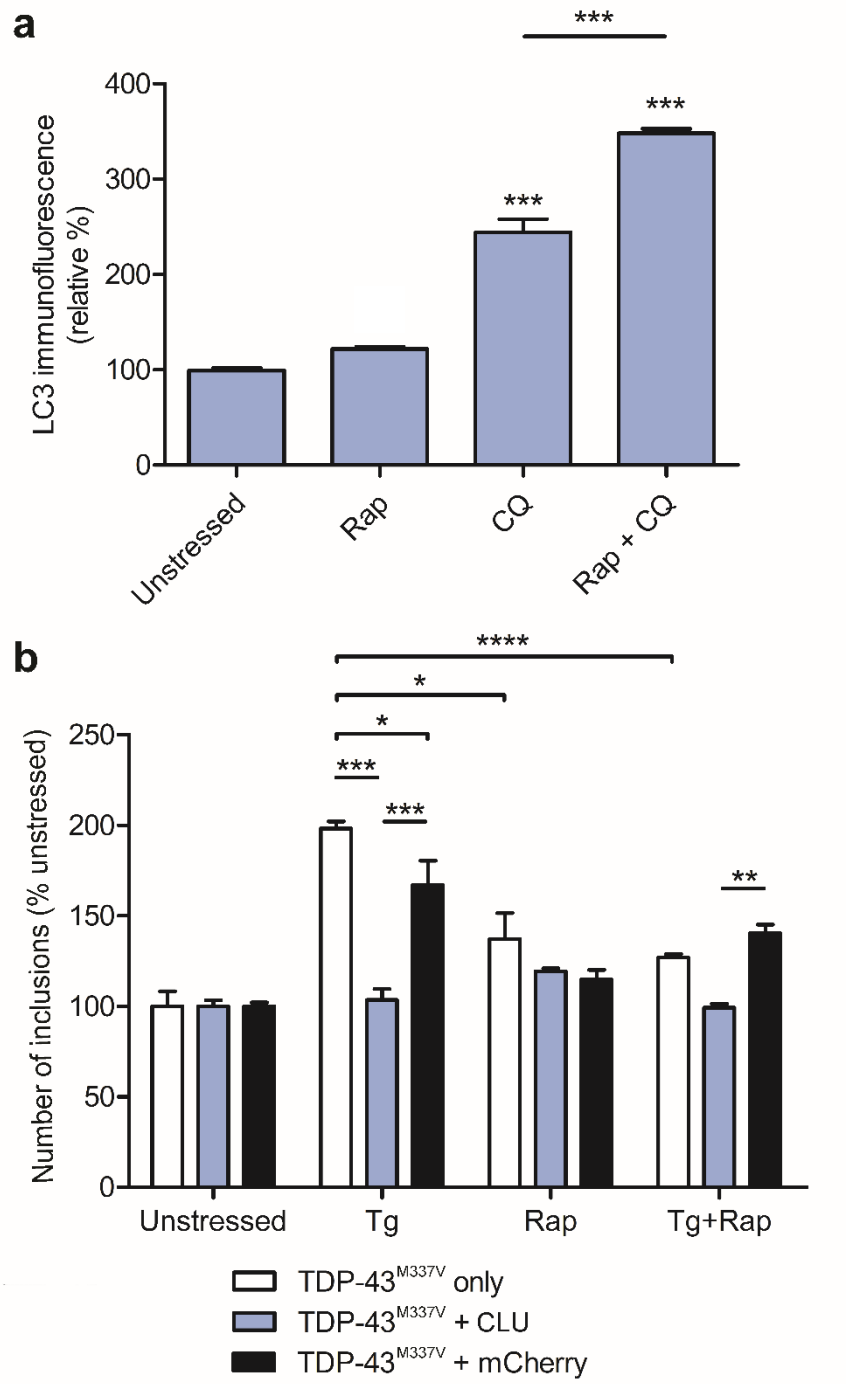

Figure 4.14: In ER-stressed N2a cells, rapamycin reduces the number of TDP-43^{M337V}-tGFP inclusions and decreases the effect of CLU overexpression on the number of inclusions. a) The activation of autophagy by rapamycin is evidenced by an increase in LC3 immunofluorescence in N2a cells (1.5 µM rapamycin, 10 h). CQ was used to prevent LC3 degradation by autophagy. b) N2a cells transfected to express the indicated proteins were treated as indicated for 10 h. Cells were lysed and inclusions enumerated by FloIT. Horizontal black lines indicate significant differences between the two indicated data sets (* $p < 0.05$, ** $p < 0.01$, *** $p < 0.001$, **a** one-way ANOVA or **b** two-way ANOVA with Bonferroni post-tests). Values represent means (n = 3), error bars are SEM. Rap, rapamycin.

To examine whether inhibition of the proteasome or autophagy induce compensatory changes in the other proteolytic pathway, assays to measure the activity of each were used. For the UPS, a plasmid encoding a fluorescently tagged proteasomal degron (ubiquitin-eGFP, GFPU) was used to transfect N2a cells. As expected, treatment with MG132 caused an increase in the amount of cell-associated GFPU fluorescence. Treatment with autophagy inhibitors CQ and bafilomycin A1 caused a decrease in GFPU fluorescence, consistent with the upregulation of the UPS. Treatment with U0126 caused a significant increase in the level of GFPU fluorescence (Figure 4.15*a*); the reasons for this are unclear. LC3 immunofluorescence was used as a reporter of the level of autophagy activity. To make these measurements, CQ was used to inhibit the acidification of autophagosomes, thus preventing the breakdown of LC3. As expected, treatment with CQ alone increased LC3 immunofluorescence. The combination of CQ and MG132 showed a still greater increase in LC3 levels (Figure 4.15b), suggesting that inhibition of the UPS upregulated autophagy. Similarly, treatment with Tg and CQ produced a greater level of LC3 immunofluorescence than cells treated with CQ only - this could result from either the upregulation or partial inhibition of autophagy by Tg, both of which have been reported to occur under various conditions (Ding *et al.* 2007, Ganley *et al.* 2011).

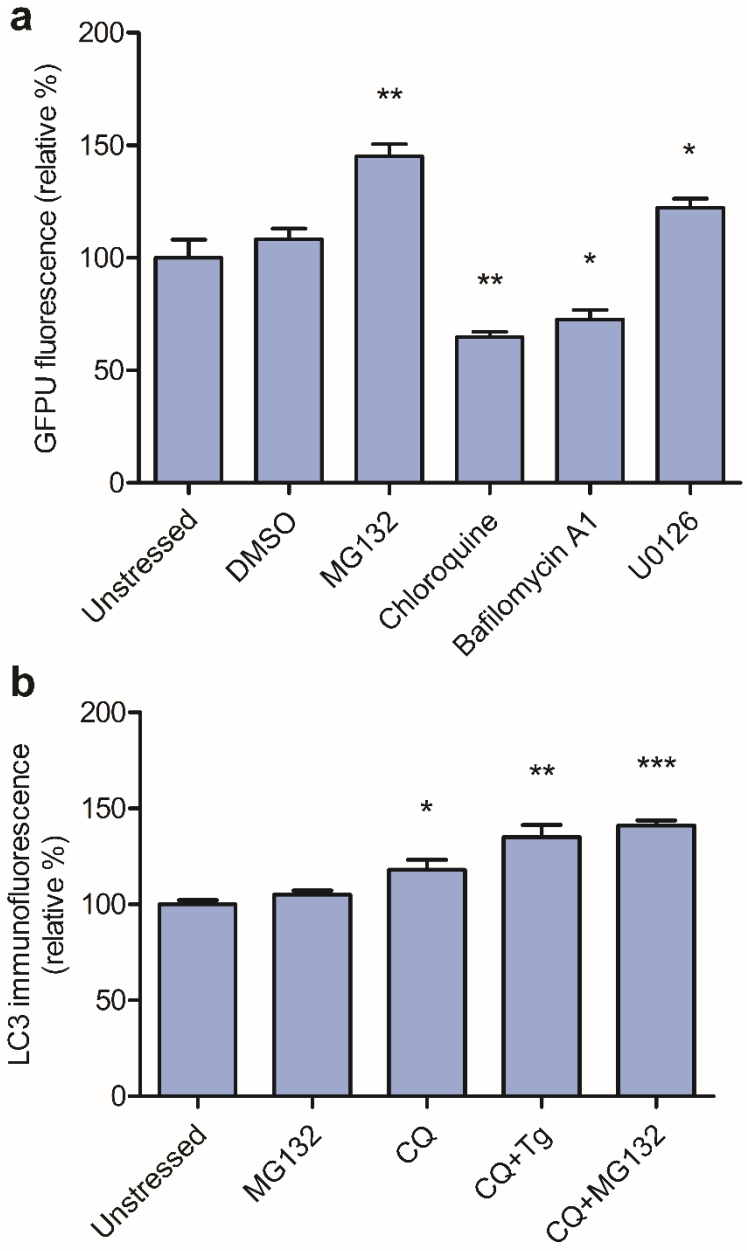

Figure 4.15: Inhibiting one of the major cell proteolytic pathways affects the other. a) N2a cells were transfected to express GFPU and treated as indicated for 10 h. Fluorescence was measured using flow cytometry. b) Endogenous LC3 was measured using immunofluorescence and flow cytometry after treating N2a cells as indicated for 10 h. Data shown are means relative to the unstressed cells (n = 3), error bars are SEM. * $p < 0.05$; ** $p < 0.01$; *** $p < 0.001$ analysed by one-way ANOVA with a Bonferroni post-test.

It was hypothesised that at least some of the measured CLU-mediated decrease in the number of TDP-43^{M337V}-tGFP inclusions was due to the upregulation of

autophagy. As mentioned previously, it was earlier reported by Zhang et al. (2014) that CLU co-localised with LC3 and increased autophagy in cancer cells. To examine whether this co-localisation could be detected in N2a cells, cells were co-transfected to express both TDP-43^{M337V}-tGFP and CLU before being immunostained for CLU and LC3. Co-localisation was measured by 'line analysis', as described in section 4.2.9.1. Without proteasome inhibition or ER stress, TDP-43^{M337V}-tGFP was primarily confined to the nucleus, and CLU and LC3 were rarely co-localised (Figure 4.16a and b, upper). However, when the cytosolic translocation of TDP-43^{M337V}-tGFP and CLU was induced by MG132/Tg treatment, distinct loci containing TDP-43, CLU and LC3 were detected. These loci were approximately 0.5 - 1 µm in diameter (Figure 4.16b, lower).

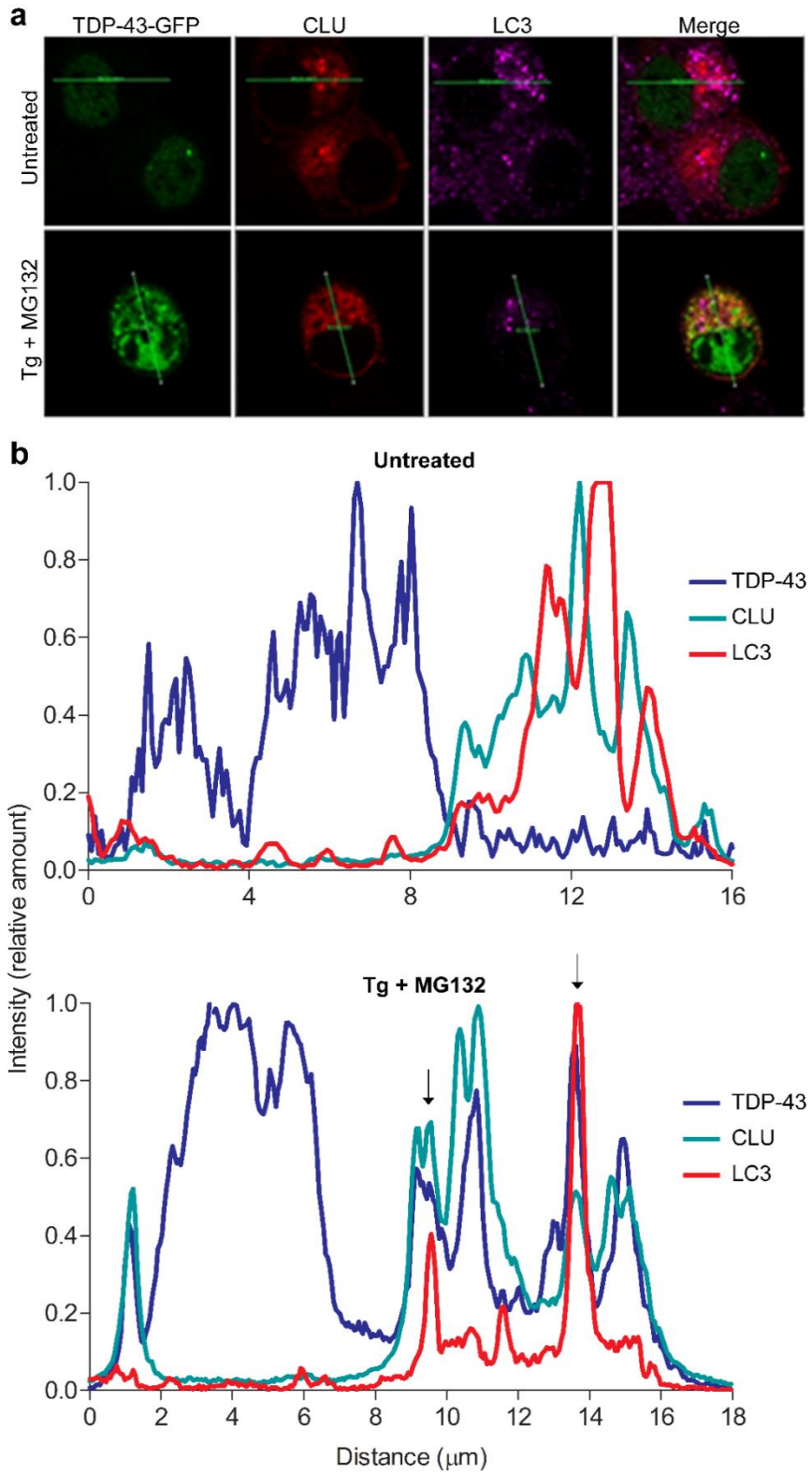

Figure 4.16: CLU co-localises with LC3 and TDP-43^{M337V}-tGFP in N2a cells treated with MG132 and Tg. a) Confocal images of the analysed N2a cells overexpressing TDP-43^{M337V}-tGFP and CLU; pixel intensity of the indicated line through the centre of the cell is shown for untreated cells in **b** and Tg + MG132 treated cells in **c** and are representative of at least 10 cells analysed for each treatment. Black arrows indicate loci containing LC3, CLU, and TDP-43.

To provide a more quantitative measurement of CLU and LC3 co-localisation, images of cells co-immunostained for CLU and LC3 were analysed for 'percent pixel co-localisation' (see section 4.2.9.2). In untreated cells, approximately 6% of CLU was co-localised with LC3. This amount rose to approximately 10% in cells treated with CQ although the relatively large cell-to-cell variation meant this difference was not significant ($p = 0.35$). When cells were treated with a combination of CQ and Tg, however, almost 35% of CLU co-localised with LC3 ($p = 0.0019$) (Figure 4.17).

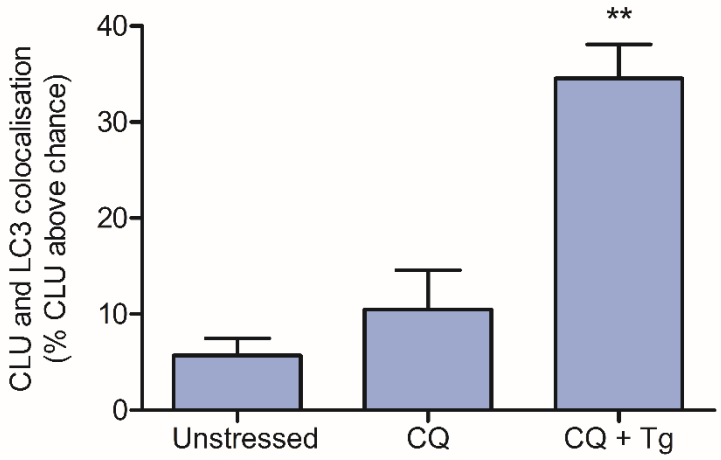

Figure 4.17: CLU co-localises with LC3 in CQ/Tg-treated N2a cells. N2a cells transfected to express CLU and treated as indicated where immunostained for LC3 and CLU. The co-localisation between CLU and LC3 was determined as described in section 4.2.10.2. Values are means (n = 10), error bars are SEM. ** $p < 0.01$, analysed by one-way ANOVA with a Bonferroni post-test.

4.4 Discussion

The unfolded protein response (UPR) is the cellular response to the accumulation of misfolded proteins within the ER lumen (ER stress). The UPR typically involves the inhibition of protein synthesis as well as the upregulation of both chaperones and protein degradation systems. If this fails to alleviate the ER stress then the cell usually becomes apoptotic (Hetz 2012). The UPR is often induced in ALS (Matus *et al.* 2013) and this appears to occur through a variety of mechanisms (Wang *et al.* 2011, Farg *et al.* 2012). As previously outlined, another cellular response to ER stress is the intracellular retention of CLU. In the model system used here to investigate the interaction between CLU and TDP-43^{M337V}-tGFP, several pharmacological inducers of ER stress (Tg, A23187, brefeldin A and tunicamycin) were confirmed to stimulate the UPR. Both Tg and A23187 were widely used in subsequent experiments, chosen because they are unlikely to interfere with the processing of CLU. Subsequently, it was found that CLU reduced the number of inclusions formed by TDP-43^{M337V}-tGFP when the cells were treated with either Tg or A23187. However, CLU had no effect on the number of inclusions when the cell was treated with brefeldin A or tunicamycin. As mentioned in section 4.2, brefeldin A inhibits both prograde and retrograde transport between the ER and Golgi, something that is known to be involved in the intracellular retention of CLU (Nizard *et al.* 2007). Tunicamycin prevents the N-linked glycosylation of proteins. Thus, the trafficking of CLU is possibly affected by tunicamycin, although neither the secondary structure or chaperone activity of the protein should be altered (Stewart *et al.* 2007, Rohne *et al.* 2014). The fact that CLU can reduce the number of TDP-

43^{M337V}-tGFP inclusions in cells treated with Tg or A23187 but not brefeldin A or tunicamycin directly suggests that normal ER-Golgi transport and glycosylation may be necessary for CLU to exit the secretory system and influence intracellular proteostasis.

FloIT (a technique described in Chapter 3) was used to demonstrate that CLU overexpression significantly decreases the number of TDP-43^{M337V}-tGFP inclusions in ER-stressed (but not unstressed) N2a cells. However, it was not clear whether this effect was dependent upon a specific protein degradation pathway. Individually, the UPS and autophagy were pharmacologically inhibited (in addition to Tg treatment), and in both cases CLU was still able to significantly reduce the number of TDP-43^{M337V}-tGFP inclusions. Unfortunately, a combination of ER stress and inhibition of both the UPS and autophagy was rapidly cytotoxic and thus the effect of this combined treatment on the ability of CLU to reduce the numbers of inclusions could not be tested. To further investigate a putative role for CLU in the autophagic turnover of TDP-43, cells transfected to express TDP-43^{M337V}-tGFP were immunostained for both CLU and LC3. A similar method was previously used to determine that CLU interacts with LC3 as part of an action to upregulate autophagy in cancer cells (Zhang *et al.* 2014). In N2a cells, CLU, LC3 and TDP-43^{M337V}-tGFP co-localised in punctate regions approximately 0.5-1 µm in size, which corresponds with the size expected of autophagosomes (Mizushima *et al.* 2002). When the cells were treated with CQ to inhibit LC3 turnover, and Tg to induce ER stress,

approximately 30% of the intracellular CLU was co-localised with LC3. This suggests that CLU may be involved in the autophagic disposal of TDP-43. The upregulation of autophagy with rapamycin was not sufficient to reduce the number of TDP-4^{M337V}-tGFP inclusions in unstressed cells. However, relative to cells treated with Tg alone, when cells were also treated with rapamycin, the number of inclusions was significantly reduced. This suggests that during ER stress the induction of autophagy can reduce the number of inclusions. Comparing Tg-treated cells overexpressing CLU versus mCherry, the former had ~ 41% less inclusions. However, when comparing cells treated with both Tg and rapamycin, cells expressing CLU had only ~ 23% fewer inclusions than cells expressing mCherry. One explanation for the apparent decrease in the ability of CLU to reduce the numbers of inclusions in rapamycin-treated cells is that CLU and rapamycin both act to upregulate autophagy via mechanisms that are at least partly non-additive.

Treatment with Tg or A23187 also induced the co-localisation of CLU with TDP-CTF-eGFP inclusions in N2a and SH-SY5H cells. Similarly, in U251 cells CLU co-localised with WT TDP-43-tdTomato inclusions when the cells were treated with Tg and MG132. CLU has been reported to co-localise with protein inclusions and extracellular plaques formed by many different proteins (see Table 1.2). It is currently unclear why CLU associates with these protein deposits, but it may be to facilitate the disaggregation of the inclusion/plaque (Narayan *et al.* 2012) or to shield the deposit from undesirable interactions. Another possibility is that, due to

its chaperone activity, CLU is binding to the soluble protein but is unable to prevent it becoming incorporated into a deposit.

A co-immunoprecipitation was performed in an attempt to identify whether CLU can interact with TDP-43^{M337V}-tGFP in solution. This technique has been widely reported in the literature as a way to identify possible interactions between CLU and a specific target proteins inside cells (see Materia *et al.* (2011b), Zhou *et al.* (2014) and Trougakos *et al.* (2009), among others); however, CLU-client interactions with a particularly low affinity may not be detected by this method if the concentrations of the proteins are low. Regardless, as shown in Figure 4.9*b*, this may not be a valid approach. CLU and TDP-43^{M337V}-tGFP co-immunoprecipitated from cell lysates prepared from N2a cells, regardless of whether the cells were ER stressed. In the absence of ER stress, CLU and TDP-43^{M337V}-tGFP are primarily compartmentalised into the ER/Golgi apparatus and nucleus/cytosol respectively, so binding between the proteins was unexpected under these conditions. To investigate this further, cells expressing TDP-43^{M337V}-tGFP but not human CLU were lysed and purified human CLU was added to the lysate to simulate the release of secretory CLU from the ER/Golgi. In this case, TDP-43^{M337V}–tGFP co-immunoprecipitated with human CLU; thus, as a technique, co-immunprecipitations involving CLU demonstrate an ability to bind rather than definitive evidence that binding is occurring *in vivo*.

In the current study, it was shown that CLU (i) co-localises with TDP-43^{M337V}-tGFP inclusions when cells are ER-stressed, (ii) inhibits the in vitro aggregation of TDP-43-tGFP, and (iii) reduces the number of TDP-43^{M337V}-tGFP inclusions in ER-stressed N2A cells. Thus, it seems likely that CLU can directly interact with soluble TDP-43. With the evidence available, it is not possible to establish whether the ability of CLU to reduce the number of TDP-43^{M337}-tGFP inclusions is due to enhanced degradation of TDP-43 and/or a direct inhibition of TDP-43 aggregation, however a combined effect appears likely (Figure 4.18). Indeed, in the N2a cell system used here, separate inhibition of autophagy and the proteasome both caused ER stress-dependent accumulation of CLU within the cell. This suggests that both pathways can mediate clearance of CLU once it has been retrotranslocated from the secretory pathway, although this cannot be confirmed until mRNA levels are examined. Previous studies have strongly implicated both the UPS and autophagy in the ability of CLU to enhance the turnover of at least some cell proteins. CLU was reported to enhance the proteasomal degradation of COMMD1 and IκB (Zoubeidi *et al.* 2010b), and the autophagic degradation of ATP7A and ATP7A (Materia *et al.* 2011a, Materia *et al.* 2012). Exactly how CLU escaped the secretory pathway to facilitate the degradation of each of these proteins is currently unknown, as exogenous ER stress was not applied in these cases. Collectively the results suggest that (i) CLU can facilitate the degradation of TDP-43^{M337V}-tGFP via either or both of these pathways, and (ii) inhibition of either the proteasome or autophagy causes compensatory changes in the activity of the other pathway. Furthermore, in ER-stressed cells, a rapamycin-induced increase in autophagy reduced both the number of

TDP-43^{M337V}-tGFP inclusions, and the ability of CLU overexpression to co-incidentally reduce the number of inclusions. Thus, rapamycin and CLU may exert this effect at least in part by a shared mechanism - consistent with the known ability of CLU to stimulate autophagy (Zhang *et al.* 2014).

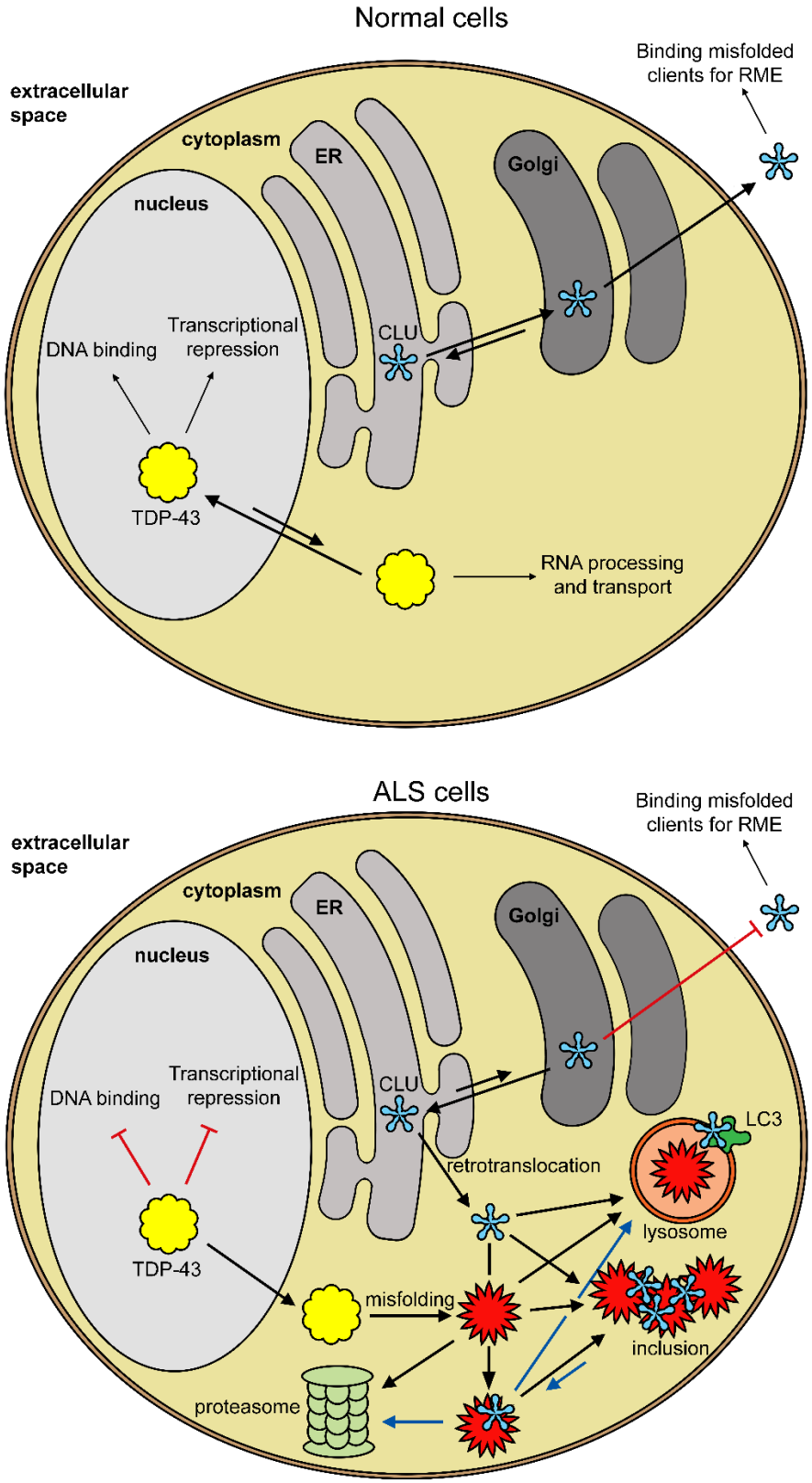

Figure 4.18: Proposed pathways by which CLU interacts with TDP-43. In healthy cells (top) CLU is processed through the secretory pathway and the majority of TDP-43 is nuclear. In ALS cells (bottom) CLU can be retrotranslocated to the cytosol, where it interacts with soluble misfolded TDP-43, TDP-43 inclusions, and LC3. Blue arrows represent probable pathways. ER, endoplasmic reticulum; RME, receptor-mediated endocytosis.

The idea that CLU is involved in intracellular processes is not an entirely novel concept. However, establishing the potential roles of intracellular CLU has been made difficult by an abundance of misinformation in the literature which arose primarily from the now discredited hypothesis that the bulk of intracellular CLU is produced by alternative RNA isoforms. Under certain conditions, CLU has been reported to localise to various intracellular compartments including the cytosol (Albert *et al.* 2007), mitochondria (Li *et al.* 2013) and nucleus (Kim *et al.* 2012). The exact details on how CLU escapes the secretory system in these cases are unknown. The ER chaperone BiP was recently implicated in the release of CLU from the ER (Li *et al.* 2013); the translocation of BiP itself from the ER to the cytosol may be the result of arginylation of the N-terminus and the subsequent action of arginyltransferase (Cha-Molstad *et al.* 2015). This arginylation also appears to mediate the involvement of BiP in autophagy. An N-terminal aspartic or glutamic acid is a requirement for arginylation in eukaryotes, residues found on ER-resident chaperones BiP, CRT, PDI, GRP94 and ERdJ5 (Cha-Molstad *et al.* 2015). Intriguingly, the N-terminal residue on human CLU is aspartic acid. This amino acid is well conserved across mammalian species, although it is substituted with the other arginylation-permissive residue (glutamic acid) in rats and mice. Since the N-terminal amino acid of CLU is amenable to arginylation, whether CLU escapes the ER through arginylation and arginyltransferase, or whether arginylation underlies the induction of autophagy by CLU are ideas worth investigating. This could be accomplished through various routes - Cha-Molstad *et al.* (2015) used an antibody specifically raised against the N-terminal sequence of arginylated BiP, another

option may be to identify the arginylated protect by mass spectrometry, for which a protocol is available (Xu *et al.* 2009). Regardless of the exact details, CLU is the first chaperone identified that is able to ameliorate protein misfolding and toxicity in both the intra- and extracellular environment. It is yet to be established whether other extracellular chaperones can be retained within the cell to perform a similar function. This could be investigated by multiple techniques, including immunostaining for the presence of the chaperone (preceded by a careful selective permeabilisation of the cell membrane) or testing for the ubiquitination of the chaperone, a process known to occur only in the cytosol (Goder 2012, Christianson and Ye 2014).

A described in Chapter 3, one limitation of FloIT is that protein expression level is not accounted for. Thus, it cannot be determined whether CLU and the non-chaperone control mCherry were overexpressed by the cell to a similar extent. Regardless, given that the overexpression of mCherry had no significant effect on the number of TDP-43 inclusions formed, and the fact that CLU reduced the number of TDP-43 inclusions only in the presence of ER stress, it seems that the reason for the reduction in the number of inclusions measured is not due to the non-specific overexpression of protein, but rather a specific effect caused by CLU. Ideally, the endogenous CLU expression in N2a cells could be knocked-down, and the change in the number of TDP-43 inclusions could be monitored. However, in N2a cells specifically, CLU is expressed endogenously at a low level, suggesting that in this cell model further knock-down of expression might only have a small effect.

Further studies into the roles of intracellular CLU face several challenges, perhaps the foremost being the unambiguous identification of cytosolic CLU. Subcellular fractionation methods generally suffer from cross-contamination of different cell fractions (Huber *et al.* 2003). The large amount of ER- and Golgi-associated CLU and the potentially small amount of cytosolic CLU makes even minimal cross-contamination unacceptable. The use of bimolecular fluorescence complementation is another possible approach. This technique involves attaching half of a fluorescent reporter to one protein of interest, and the complementary half of the reporter is conjugated to a suspected binding partner of the protein (Kerppola 2006). If the concentration of the substrates are above the affinity threshold and binding occurs, the two halves of the reporter join and are able to emit fluorescence. This technique could be used with CLU and a suspected binding partner exclusively targeted to the cytosol. However, care needs to be taken that any fluorescent reporter conjugated to CLU does not affect its cellular processing. For example, CLU-eGFP is retained within HEK-293 cells to a greater extent than endogenous CLU when the cells were treated with Tg and MG132 (*data not shown*). Convincing confocal images showing co-localisation with a cytosolic protein is another option, however this approach is only suggestive of an interaction occurring between two proteins, and provides no evidence of such an interaction actually taking place. Selective permeabilisation of the outer cell membrane with digitonin combined with immunofluorescence detection (as described for the detection of cytosolic TDP-43 in this chapter) may be the technique with the fewest complications. Care needs to be taken with appropriate controls as this approach

may suffer from cross-contamination caused by the undesired permeabilisation of intracellular membranes.

Motor neurons have an intrinsically limited ability to maintain intracellular proteostasis due to their high threshold for the induction of the heat shock response (Batulan *et al.* 2003). This renders these cells particularly susceptible to PDDs, as intracellular chaperones are upregulated to a much lesser extent than other cell types in response to protein misfolding. CLU is the first secreted chaperone identified that is able to redirect from the secretory system in response to inappropriate intracellular protein misfolding and aggregation. Once in the cytosol, CLU reduced the numbers of the TDP-43^{M337V}-tGFP inclusions. The ability of CLU to respond to and ameliorate both intracellular and extracellular protein misfolding and aggregation suggests that it may be involved in cellular defence against a much larger range of diseases than initially thought.

Chapter 5:

Characterising the Interaction Between Clusterin and Misfolded Protein Aggregates

5. Characterising the Interaction Between Clusterin and Misfolded Protein Aggregates

5.1 Introduction

In the work described in this chapter, two model proteins (αS and Aβ) were used to closely examine whether CLU preferentially binds to oligomers of a certain size or structure, as well as the effect of the binding on the further aggregation and structure of the oligomer. Additionally, an examination of the structure and dynamism of CLU-CLU oligomers was attempted. Aβ was chosen as it is an important disease-relevant client protein. The aggregation of Aβ is believed to be causative of AD and is found in a number of other diseases, including Down's syndrome and inclusion body myositis (Sarkozi *et al.* 1993). The interaction between αS and CLU is less studied. However, the aggregation of αS is found in a class of diseases known as the α-synucleinopathies, of which PD is the most common (Spillantini and Goedert 2000). Additionally, the mechanism of unfolding and aggregation of αS is relatively well known and is believed to be distinct from that of Aβ.

5.1.1 Alzheimer's disease

AD is the most common dementia in the elderly, and like other dementias is characterised by a gradual decline of cognitive function. Unique to AD are extracellular plaques consisting primarily of aggregated Aβ, and intracellular neurofibrillary tangles composed of Tau. Mutations in the amyloid precursor protein (APP) gene (Goate *et al.* 1991) and the presenilin 1 and 2 genes

(Sherrington *et al.* 1995) can lead to overproduction of the Aβ peptide, which can cause the disease. Interestingly, two independent genome-wide association studies identified mutations within the *CLU* gene as the second biggest risk factor for AD, behind the ε4 allele of *APOE* (Harold *et al.* 2009, Lambert *et al.* 2009).

5.1.1.1 Amyloid-β

Aβ is a 4 kDa peptide that is produced by the enzymatic cleavage of APP. Briefly, APP on the cell surface is first cleaved by β-secretase, releasing extracellular sAPPβ. A portion of the protein that remains attached to the cell surface is then cleaved once again, this time by γ-secretase, releasing Aβ peptide with a variable C-terminal length (Murphy and LeVine 2010). Longer peptides (particularly $A\beta_{1-42}$, comprising 5-10% of total Aβ) aggregate more aggressively, and are the dominant species in senile plaques (Mann *et al.* 1996). The abundance of senile plaques in any region of the AD brain is poorly correlated with neuronal cell death in the same area (Terry *et al.* 1991) - the levels of soluble Aβ oligomers are a better indicator of the extent of cognitive impairment (Lue *et al.* 1999). Indeed, soluble Aβ oligomers were found to be more cytotoxic than the mature fibrils (Lambert *et al.* 1998); the most widely accepted hypothesis of the cause of AD is that it is due to the toxicity of soluble Aβ oligomers.

5.1.1.2 Amyloid-β and clusterin

CLU is known to specifically bind to Aβ with high affinity. Since the first report of an interaction by Ghiso *et al.* (1993), it has been reported that under most conditions CLU acts to supress the aggregation of the peptide (Oda *et al.* 1995), and reduces the associated toxicity (Yerbury *et al.* 2007a). The complexes are believed to be endocytosed by cells for lysosomal degradation, possibly via the receptor megalin (Hammad *et al.* 1997). When this chaperoning fails, CLU may be incorporated into AD senile plaques (Martin-Rehrmann *et al.* 2005). Despite the more significant role of $A\beta_{1-42}$ in AD, $A\beta_{1-40}$ has more often been used in the small number of studies attempting to characterise the interaction between Aβ and CLU. Matsubara *et al*. (1995) showed that the interaction between CLU and $A\beta_{1-40}$ occurs in a 1:1 stoichiometric ratio with a nanomolar dissociation constant. The interaction is not believed to be specific to Aβ monomers or any particular oligomer, with CLU being found to interact with $A\beta_{1-40}$ dimers and oligomers of up to at least 50mers (Narayan *et al.* 2012).

5.1.2 α -Synucleinopathies

α -Synucleinopathies are a group of fatal, progressive neurodegenerative diseases including PD, dementia with Lewy bodies (DLB) and multiple system atrophy (MSA). The pathological hallmark of all of these diseases is the presence of αS-positive inclusions in neuronal or glial cells. The aberrant accumulation of αS may be the result of genetic abnormalities (Polymeropoulos *et al.* 1997, Al-Chalabi *et al.* 2009,

Scholz *et al.* 2009), posttranslational modifications of αS (Anderson *et al.* 2006), and/or compromised αS clearance (Winslow *et al.* 2010).

5.1.2.1 α-Synuclein

αS can account for up to 1% of all cytosolic proteins in neurons. Despite this abundance the exact role of αS *in vivo* has not been fully elucidated, however it is thought to play roles in synaptic structure (Greten-Harrison *et al.* 2010) and regulating neurotransmitter release (Jenco *et al.* 1998, Stefanis 2012). The protein consists of 140 amino acids and is 'natively unfolded' (i.e. has no defined structure). However, during sequestration into inclusions αS undergoes a multi-step process to form amyloid fibrils that is shared by all amyloidogenic proteins (see section 1.1.1 for details). Perhaps unique to αS, the oligomers undergo a structural conversion to a more stable, compact oligomer that is both resistant to proteinase-K degradation and more cytotoxic than the preceding oligomer (Cremades *et al.* 2012). This conversion occurs before the oligomers are incorporated into proto-filaments, and is a critical step in the aggregation pathway of αS.

5.1.2.2 α-Synuclein and clusterin

CLU expression is upregulated in PD (Hoepken *et al.* 2008), and the protein has been found co-localised with αS in cortical Lewy bodies in patients with DLB, and rarely in Lewy bodies in the brain stem of people with PD and DLB. CLU was also identified associated with αS in glial cytosolic inclusions in MSA (Sasaki *et al.* 2002).

Additionally, monomeric and aggregated αS has been identified in extracellular fluids such as CSF and blood plasma of both healthy and diseased subjects (El-Agnaf *et al.* 2003, Danzer *et al.* 2011). Extracellular αS has been proposed to contribute to pathology via a number of mechanisms, including activation of microglia (Zhang *et al.* 2005b) and propagation of aggregation through a prion-like process (Marques and Outeiro 2012). CLU is not known to have any specificity in interacting with extracellular misfolded proteins. Thus, it is at least possible that CLU will interact with extracellular αS oligomers *in vivo*. Indeed, CLU was shown to attenuate both the aggregation and toxicity of αS *in vitro* (Yerbury *et al.* 2007a).

5.1.3 Single-molecule techniques

Traditional techniques used to quantify protein aggregation typically involve triggering the aggregation of a population of molecules and measuring the average response of the population. In this way the influence of chaperones or other molecules on the aggregation can be quantified. However, a significant limitation of these techniques is their inability to measure short-lived, rare species that may be formed as intermediates during aggregation. In contrast, single-molecule techniques are capable of measuring the response of individual molecules throughout the aggregation process.

5.1.3.1 Single-molecule confocal microscopy

Both Förster resonance energy transfer (FRET, see 5.1.5.2) and two colour coincidence detection (TCCD, see 5.1.5.3) measurements were performed using a confocal microscope. The optics in a confocal microscope are constructed so as to create the smallest excitation volume (the confocal volume, typically < 1 fl) physically allowed by the diffraction limit of light. Fluorescence emitted by a sample is then passed through a pinhole (~50 µm diameter) to eliminate fluorescence not emanating from the confocal volume. The fluorescence is then measured by a sensitive detector which is able to detect photons on the nanosecond time-scale. For single-molecule confocal measurements the confocal volume is fixed in space, and the fluorescence bursts from individual molecules are measured as they diffuse (or flow) through the confocal volume. In order to ensure that a maximum of one molecule is residing in the confocal volume at any one point, analyte concentrations of 10-100 pM are required (Nie *et al.* 1994).

5.1.3.2 Förster resonance energy transfer

FRET is the non-radiative transfer of energy from one fluorophore (the donor) to another (the acceptor). The efficiency of this process is determined by several factors, such as the degree of overlap between the emission spectrum of the donor fluorophore and the excitation spectrum of the acceptor fluor. Of particular relevance to the work described in this chapter, the FRET efficiency is inversely proportional to the sixth power of the distance between the donor and acceptor fluorophores (Förster 1960). Thus, in practice the FRET efficiency between

monomers in an oligomer can provide information on the structural characteristics of the oligomer.

5.1.3.3 Two colour coincidence detection

Unlike FRET measurements, which involves the direct excitation of one fluor, TCCD is the direct excitation of two fluorophores simultaneously. Lasers that excite two spectrally distinct fluorophores are made coincident so that the confocal volumes of each laser are overlapped within the sample, then the emission of both fluorophores is measured. This is more sensitive than the FRET-based technique, as it is not required for the energy from one fluorophore to be transferred to the other; this allows the more sensitive detection of protein oligomers. However, TCCD provides no information on the distance between two fluors.

5.1.3.4 Total internal reflection microscopy

Total internal reflection microscopy (TIRFM) is a method of imaging molecules close to the surface of a glass slide. The objective is set up such that the excitation laser is reflected from the bottom of the slide (i.e. totally internally reflected). Despite this, however, an electromagnetic field (the “evanescent wave”) penetrates approximately 100 nm above the slide into the sample (Axelrod 2001). The resulting fluorescence, collected by the objective, is focussed on a sensitive camera (typically an electron multiplying charged couple device, EMCCD) to image fluorescent molecules sitting on or close to the surface of the slide. Thus, molecules in the

solution above do not contribute to background fluorescence. By limiting the concentration of molecules in the sample, images of single molecules sitting on or close the surface can be captured.

5.1.4 Experimental aims

Very little is known about the mechanisms by which chaperones act. For example, CLU is known to exist in solution in a variety of oligomeric states (which are pH and concentration dependent) (Poon *et al.* 2002a), but the proportion of monomers to oligomers, the stability of the oligomers and the chaperone activity of the various oligomers are all unknown. CLU can form complexes with client proteins, acting to shield hydrophobic regions and prevent further illicit interactions (Wyatt *et al.* 2009). However, little is known about the nature of this interaction. For example, it is not known whether CLU binding alters oligomer structure, or how the conformation of oligomers influences this interaction. In this chapter, studies are described that use a combination of single-molecule FRET, TCCD, TIRFM and traditional bulk techniques to examine the effect of CLU on protein aggregation, and the structure and toxicity of protein aggregates. In addition, the structure and dynamism of CLU self-oligomers was examined.

5.2 Methods

5.2.1 Fluorescent labelling of proteins

5.2.1.1 Thiol labelling

αS^{A90C} was labelled with either AF488 C_5 Maleimide or AF647 C_2 Maleimide (Invitrogen, USA). The αS was first incubated for 15 minutes with 10 µM DTT at RT to ensure reduction of any cysteines. The reduced αS^{A90C} was concentrated to approximately 400 µM using a Vivaspin 500 (10,000 MWCO) and buffer exchanged through a PD-10 column (GE Healthcare Life Sciences, USA) into degassed PBS. The protein was then added to the functionalised fluorophores (fluorophores present at a 1.5 fold molar excess, added from a 10 mM stock in DMSO); and the air in the tube was purged with nitrogen to prevent the oxidation of the cysteines. The protein was incubated at 4 °C overnight with shaking followed by purification from unreacted dye using a PD-10 column equilibrated in PBS pH 7.4. The concentration of labelled protein was calculated by measuring the absorbance of the fluorophores using a Nanodrop 2000 (Thermo Fisher Scientific, USA). Aliquots containing protein and no free dye were pooled and the αS^{A90C} was then concentrated to approximately 250 µM as above. The labelling efficiency was estimated by mass spectrometry (Dr Len Packman, University of Cambridge, UK). After being aliquoted the labelled αS^{A90C} was snap frozen in liquid nitrogen and stored at -80 °C.

5.2.1.2 Amine labelling

CLU, α_2M, lysozyme (Sigma Aldrich, USA), β-lactoglobin (Sigma Aldrich, USA) and α-lactalbumin (Sigma Aldrich, USA) were individually labelled with N-hydroxysuccinimidyl ester forms of either AF488 or AF647 (Invitrogen, USA). To achieve this the proteins (each at approximately 2 $mg.ml^{-1}$) were incubated with a 10 fold molar excess of the functionalised fluorophore (added from a 10 mM stock in DMSO) for 1 h at RT or overnight at 4 °C. Free dye was removed by buffer exchange into PBS or PBS/Az (in the case of α_2M) using a PD-10 column. The concentration and labelling efficiency was measured according to the manufacturer's instructions. In some cases the labelling efficiency was also measured by mass spectrometry (Dr. Len Packman, University of Cambridge, UK). Proteins were aliquoted and stored at -20 °C.

5.2.2 Single-molecule measurements – confocal microscope

5.2.2.1 Aggregation of Aβ and αS

$A\beta^C$ (see section 2.5.1) and αS^{A90C} were each aggregated in the presence or absence of CLU and α_2M. When present, CLU and α_2M were each used at molar ratios of 1:100 (chaperone:αS^{A90C}) or 1:10 (chaperone:$A\beta^C$). All aggregations were performed in DNA LoBind 1.5 ml tubes (Eppendorf, Germany) to limit protein adsorption to the plastic tubes, in PBS with shaking at 200 rpm, 37 °C in an Innova43 Incubator Shaker Series (New Brunswick Scientific, Germany). The fluorophore conjugated to each individual protein in the assay varied between different experiments, and are indicated in the figure legends. $A\beta^C$ was induced to aggregate by incubation at 5 µM

for up to 48 h. Similarly, αS^{A90C} was incubated for the same length of time but at 70 µM. In cases involving co-incubation of a protein labelled with two different fluors, for example $A\beta^{C}$-AF488 and $A\beta^{C}$-HF647, the final concentration consisted of an equimolar amount of each. During incubations the tubes were kept wrapped in aluminium foil to limit photobleaching.

5.2.2.2 Microfluidics

Microfluidic devices were used to increase the rate of data acquisition and remove the bias for preferentially measuring smaller species that occurs if diffusion alone is relied upon (Horrocks *et al.* 2011). In order to create the devices a mould (hereafter referred to as a 'master') must be created that is cast with poly(dimethyl)siloxane (PDMS) elastomer (Figure 5.1*a* and *b*). To make the master SU-8 3025 photoresist (approximately 1 ml; Microchem, USA) was spincoated onto a silicon wafer (76.2 mm diameter; Compart Technology Ltd, UK) in a Spincoat G3P-8 (800 rpm for 5 s followed by 3,000 rpm for 60 s with an acceleration of 300 $rpm.s^{-1}$; Specialty Coating Systems, USA). This resulted in a 25 µm film being evenly coated across the wafer. The wafer was then baked at 96 °C for 12 min on an SD300 digital hotplate (Stuart Equipment, UK). A UV-blocking photomask (Microlithography, UK) was laid on top of the coated wafer which was then exposed to collimated UV light for 15 s using an OAI UV source (OAI, USA). The wafer was then baked as above for 5 min. The photoresist that was not exposed to the UV light (i.e. that which was covered by the photomask) was removed using propylene glycol monomethyl ether

followed by isopropanol. The master was kept in a petri dish and ensured to be free of dust by blasting with compressed nitrogen passed through a particulate filter before casting with silicone elastomer. Components of a SYLGARD® 184 PDMS elastomer kit (Dow Corning, USA) were vigorously combined in a 10:1 (elastomer:curing agent) ratio as per the manufacturer's instructions. Approximately 25 ml of PDMS was then poured over the master and placed under a vacuum until all of the bubbles were removed. The PDMS was then hardened overnight at 65 °C (Carbolite, UK). The individual devices were then cut out using a scalpel and peeled off from the master. Inlet and outlet holes were created using a 1.0 or 0.75 mm biopsy punch (Sigma Aldrich, USA). The devices were each attached to a 24 x 50 mm borosilicate glass cover slide (thickness number 1; VWR International, USA) after being exposed to oxygen plasma for 7 s (Plasma system FEMTO, Diener Electronic, Germany) and baked overnight as above.

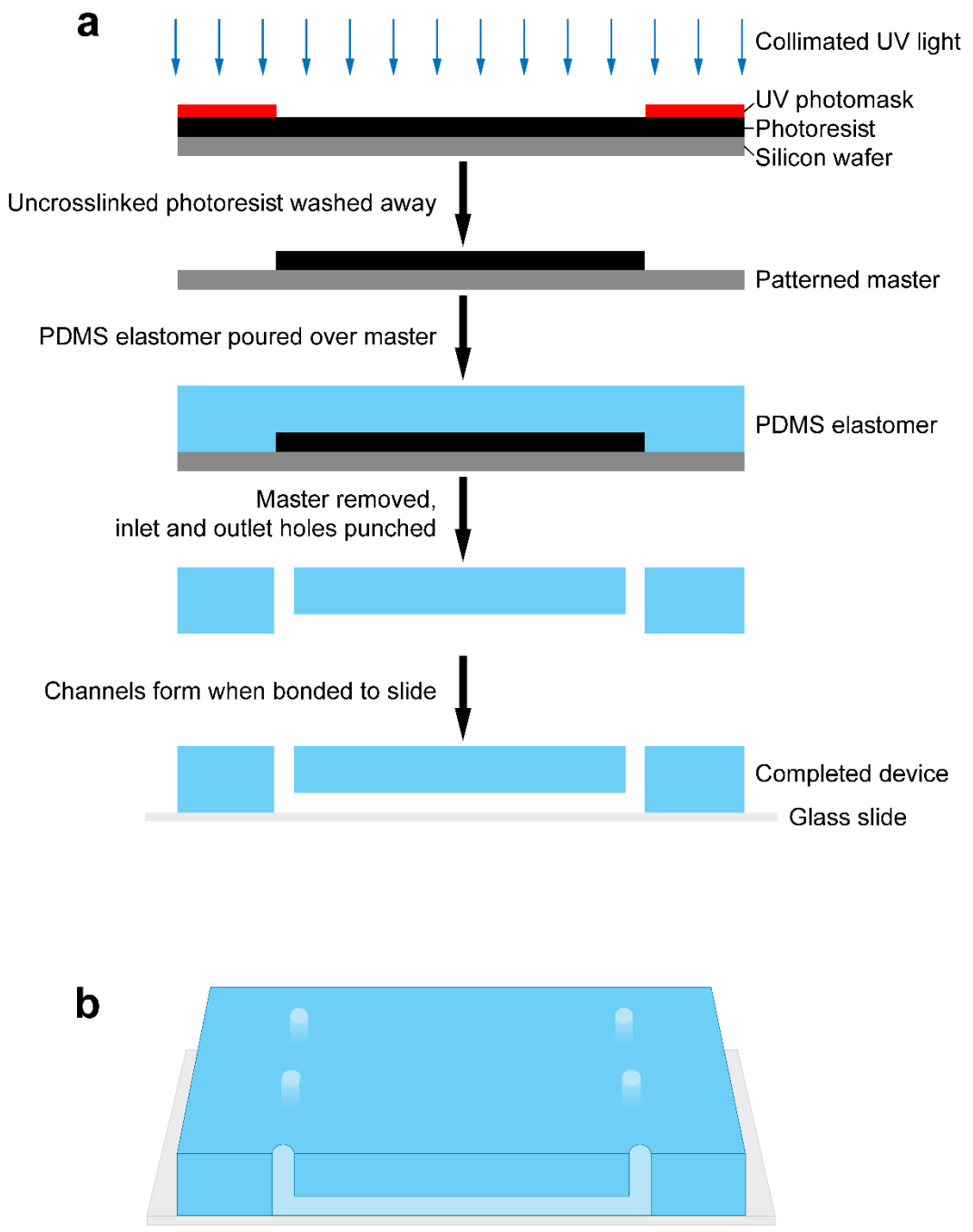

Figure 5.1: The fabrication of microfluidic devices. a) The process used to create microfluidic devices. b) 3-Dimensional representation of a section of a completed device. PDMS; poly(dimethyl)siloxane.

Two different microfluidic device designs were used: (i) a single straight channel (25 x 100 x 10,000 µm), and (ii) a rapid autodilution device. The straight channel devices

(Figure 5.1*b*) were used for the measurement of samples containing oligomers to both increase the rate of detection and remove the bias for sampling smaller, faster diffusing species. Sample was pulled through the device at 200 µl.h^{-1} (2 cm.s^{-1}) by a PhD 2000 Infusion or PhD 2000 Programmable syringe pump (Harvard Apparatus, USA). The pump was connected to the device with FineBore polyethylene tubing (Scientific Laboratory Supplies, UK). The autodilution design (Figure 5.2*a* and *b*) was used to ensure constant, rapid dilution when attempting to quantify weakly associated biomolecular complexes (Horrocks *et al.* 2013), such as CLU self-oligomers.

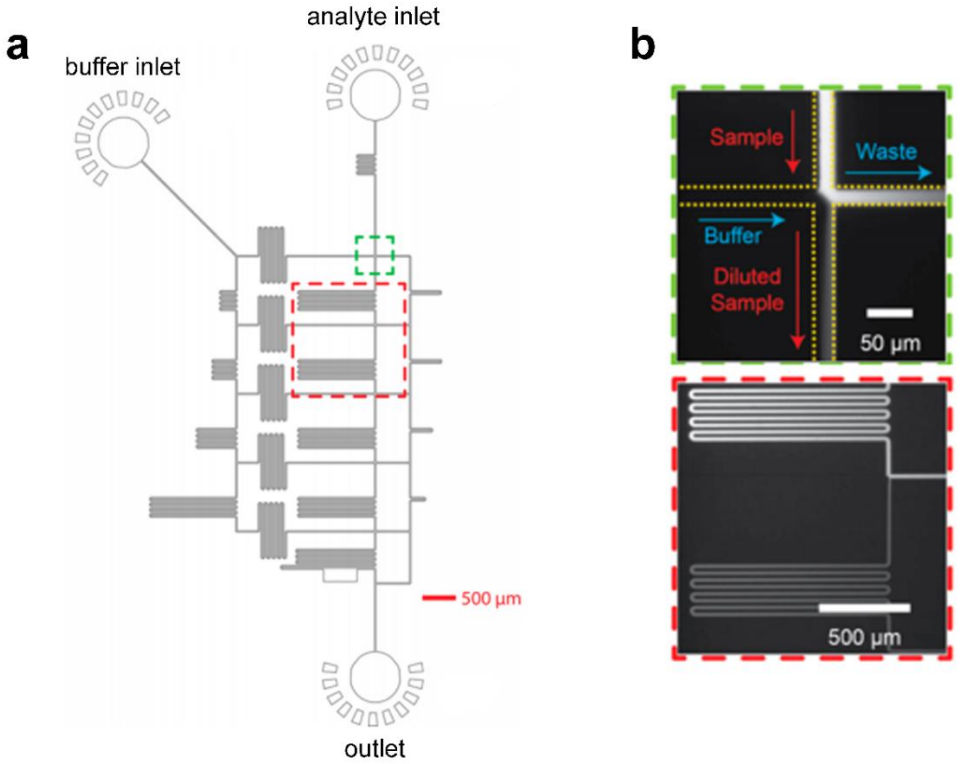

Figure 5.2: Autodilution microfluidic device. a) Schematic representation of the autodilution device. The sample to be diluted is held in a pipette tip inserted into the analyte inlet. Another pipette tip holding a buffer used to dilute the analyte is inserted into the buffer outlet. Tubing connected to a syringe pump is inserted into the outlet and is used to draw both the buffer and the analyte through the device at a constant, equal rate. The sample is diluted approximately 10-fold at each junction (highlighted by the green and red boxes). b) Images of a device diluting fluorescein with PBS. The images shown are the sections of the device indicated in **a** by the green and red boxes. (Horrocks *et al.* 2013).

5.2.2.3 Single-molecule FRET and TCCD

Both FRET and TCCD measurements were performed at approximately 50 pM. Dilutions were performed immediately before analysis and in freshly filtered PBS. TCCD and FRET measurements were taken using a confocal microscope built by Dr. Mathew Horrocks (University of Cambridge, UK) (Figure 5.3). The details of the components used to build the microscope, as well as the spectra of the filters and dichroic mirrors used are shown in Horrocks *et al.* (2013).

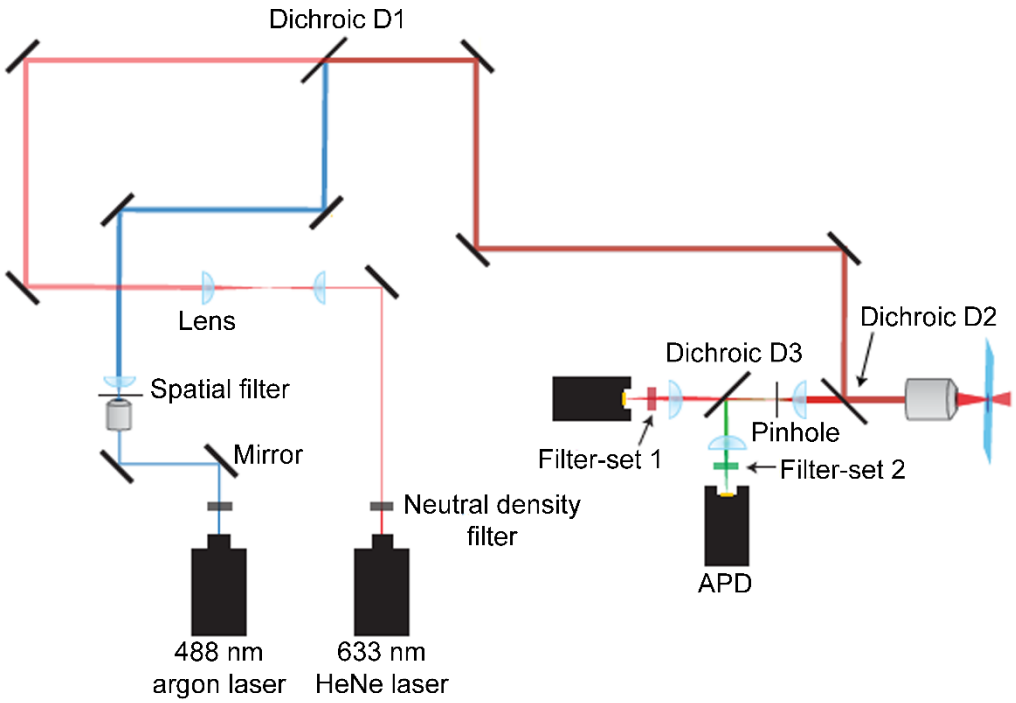

Figure 5.3: A schematic representation of the confocal microscope used for single-molecule confocal measurements. The intensity of a 488 nm argon laser and 633 helium/neon laser was first attenuated using neutral density filters. The lasers were passed through a spatial filter or telescopic lenses respectively to expand and collimate the beams. Two kinematically-mounted mirrors and dichroic mirror D1 allowed the beams to be made concentric. The beams were then directed through a pinhole, into the back port of an inverted microscope and focused in the sample by an oil-immersion objective. The emitted fluorescence from AF488 and AF647 (if both were present) were separated from reflected laser light using dichroic mirror D2 and then each other using dichroic mirror D3. The fluorescence was focused on an avalanche photodiode (an extremely sensitive detector; APD) after passing through appropriate filters. Adapted from Horrocks (2013).

5.2.2.4 Synthetic oligonucleotides

Double-HPLC purified DNA oligonucleotides labelled with AF488 or AF647 (custom synthesised by IBA GmbH (Germany)) were used to measure the alignment optics of the confocal microscope:

5' - (AF488)-TAGTGTAACTTAAGCCTAGGATAAGAGCCAGTAATCGGTA – 3'
5' - (AF647)-TACCGATTACTGGCTCTTATCCTAGGCTTAAGTTACACTA – 3'

Duplexes were formed by diluting the oligonucleotides to 1 µM in 0.02 µm filtered 10 mM Tris, 1 mM EDTA, and 100 mM NaCl, pH 7.5, heating to 95 °C and gradually cooling to RT over 7 h. The optics were considered sufficiently aligned when the TCCD measurement of the duplex yielded an association quotient (*Q*) above 20 (see below).

5.2.2.5 Data analysis

Data were analysed primarily in Igor Pro version 6.3.4.1 using scripts written by Dr Mathew Horrocks (University of Cambridge, UK) or myself. Some data were also analysed using Python version 2.7 programmed by myself.

Datasets were thresholded to remove noise, such as stray photons hitting the detector and fluorophores traversing the edge of the confocal volume. Only fluorescence bursts which were above the threshold in both channels simultaneously were accepted (thus allowing the identification of coincident events). Data points below the threshold were discarded. Thresholds were set at

the value that maximised *Q* (rate of coincident events above that expected by chance, divided by the total event rate). To achieve this, *Q* was calculated at each pair of thresholds from 0 to 100 (10,201 threshold pairs), and the threshold that produced the maximum value of Q were used to threshold the data. Q is defined as

Equation 5.1 $$Q = \frac{C - D}{A + B - (C - D)}$$

where *C* is the rate of coincident events (i.e. intensities in both channels that are above the threshold), *A* and *B* are the event rates in each of the two channels, and *D* is the rate of desynchronised events (Clarke *et al.* 2007). Desynchronised events are coincident events that occur after the intensities in one of the channels (in this case the acceptor channel) have been randomised, and are thus a measurement of chance coincidence. An example of the output of this process (and the automatically selected thresholds) is shown in Figure 5.4. This calculation was performed in either Python 2.7 (Appendix II) or Igor Pro version 6.3.4.1 (Appendix III).

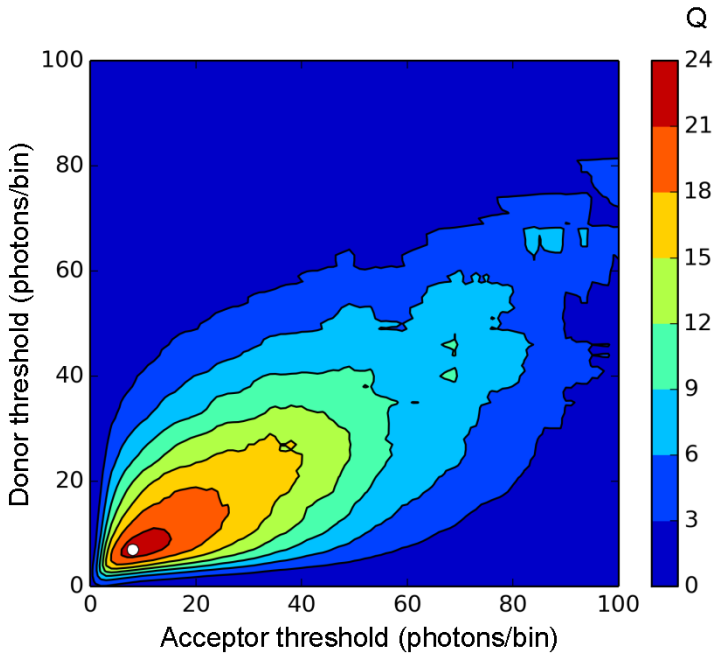

Figure 5.4: Threshold selection by maximising Q. The Q at each threshold pair up to a set limit is calculated and plotted. Thresholds were set at the values that produced the maximum Q (white dot; in this case Q = 22.4 at donor threshold = 7 and acceptor threshold = 8). Plot was produced using the Matplotlib module in Python 2.7.

Oligomer size was calculated by first determining the fluorescence intensity of the monomer. This was typically given by the average intensity of non-coincident/non-FRET events before the sample was incubated under aggregating conditions. The size of each coincident burst (TCCD) was then characterised as

Equation 5.2

$$Size_{TCCD} = \frac{I_D}{I_{MD}} + \frac{I_A}{I_{MA}}$$

where I_D and I_A are the intensities of the coincident burst in the donor and acceptor channels respectively and I_{MA} and I_{MB} are the mean monomer intensities. If the

oligomer was composed of two different proteins each labelled individually (e.g. an $A\beta^{C}$-AF488 and CLU-AF647 complex) the number of each of the proteins was simply

Equation 5.3 $$Size_{TCCD} = \frac{I_X}{I_{MX}}$$

In the case where single-molecule FRET was used, the size of the oligomer was given as

Equation 5.4 $$Size_{FRET} = 2\left(\frac{I_D + I_A\left(\frac{1}{\gamma}\right)}{I_{MD}}\right)$$

where I_{MD} is the intensity of the monomer in the donor channel and γ is an experimentally determined calibration factor used to compensate for differences in instrument sensitivity. γ is determined by measuring the FRET signal from the same sample on each instrument, as described by Ye *et al.* (2012) (supplementary information).

As previously mentioned, the efficiency of FRET between two compatible fluorophores is dependent on the distance between the two fluors. Thus, FRET

efficiency can be seen as a measure of dye proximity. Thus, if a dimer consists of a monomer conjugated with a donor fluorophore and another monomer conjugated with an acceptor fluor, the FRET efficiency provides an indirect measure of conformation or 'tightness' of binding. The FRET efficiency of a given coincident burst was calculated as

Equation 5.5 $$E_{FRET} = \frac{I_A}{I_A + \gamma . I_D}$$

5.2.3 Total Internal reflection microscopy

5.2.3.1 Microscope

This microscope was built by Dr Steven F. Lee (University of Cambridge, UK); a schematic representation is shown in Figure 5.5. The details of the components used to build the microscope, as well as the spectra of the filters and dichroic mirrors used, are shown in Horrocks *et al.* (2013).

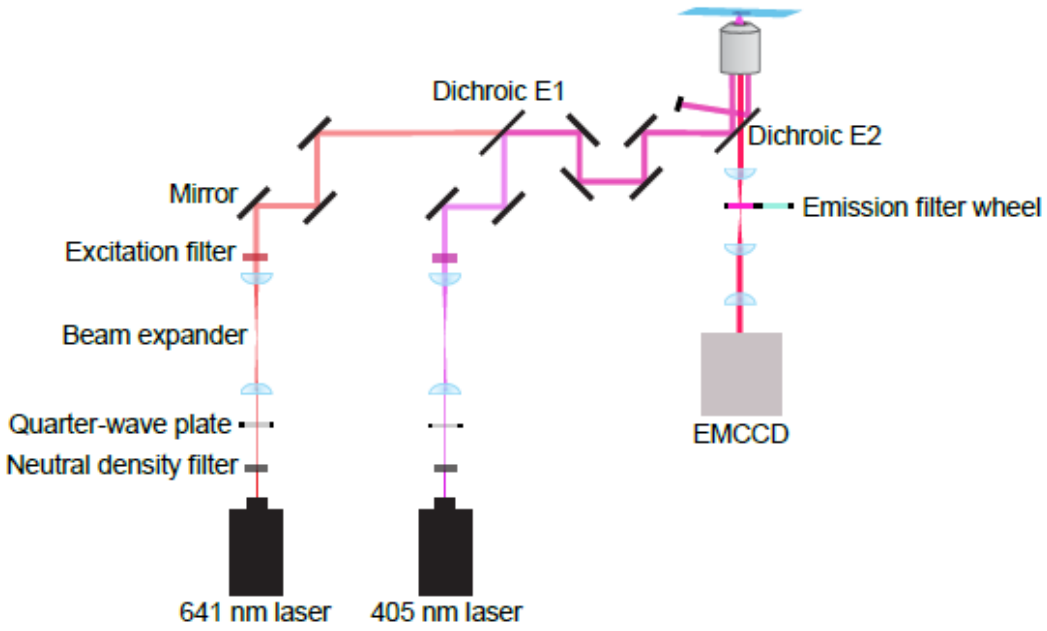

Figure 5.5: A schematic representation of the TIRF microscope used. The intensity of both a 405 nm and 641 nm laser were attenuated using neutral density filters. Quarter-wave plates specific to each wavelength were used to circularly polarise the beams. The beams were then expanded and collimated using a Galilean beam expander. The beams were then made concentric using dichroic mirror E1, passed through the back aperture of an inverted microscope, and focussed using an oil immersion TIRFM objective. Fluorescence emissions travel through dichroic E2, stray light was filtered using an automatic filter wheel, and the beam was expanded and focussed on an electron multiplying charge coupled device (EMCCD) for imaging. Horrocks (2013).

5.2.3.2 Slide preparation

Borosilicate glass cover slides (24 x 50 mm, thickness number 1; VWR International, USA) were cleaned by exposure to oxygen plasma for 30 min (Plasma system FEMTO, Diener Electronic, Germany). Frame-Seal Incubation chambers (Bio-Rad, USA) were adhered to the surface to create wells. The slides were then coated in poly-L-lysine (0.1% w/v in water; Sigma Aldrich, USA) to create a positively charged surface to bind negatively charged proteins. After approximately 15 min the poly-L-lysine was removed, the slide was rinsed three times with PBS and the slide was ready for use. Samples were analysed at approximately 200 nM to ensure

individually resolvable protein molecules on the surface of the slide (i.e. 'single-molecule' conditions).

5.2.3.3 Data analysis

TIRFM images were analysed using custom scripts written in Igor Pro version 6.3.4.1 by Dr. Mathew Horrocks. Background and fluorophores floating above the surface of the slide were removed by adaptive thresholding. This method of thresholding involves the computation of a different threshold for each pixel in an image and is designed to account for uneven illumination across the image. This is rather complex, and was achieved in this case using the adaptive thresholding functions built-in to Igor Pro. Fluorescently labelled proteins (spots) above the threshold were enumerated. In the case were coincidence between fluorophores was being examined the position of a spot above the threshold in one channel was examined for the presence of a spot in the other channel. Chance coincidence was determined by rotating one of the images 90°, translating it by 10 pixels to the right (to offset any central spots not affected by the rotation) and then testing for coincidence in an identical manner.

5.2.4 Dihydroethidium assay

Dihydroethidium (DHE) was used to measure the intracellular rate of superoxide production as previously described (Cremades *et al.* 2012). N2a cells grown in a 24 well plate were rinsed with PBS before DHE (2 µM in PBS) was added to the cells.

An epifluorescence microscope was used to quantify both the oxidised (ethidium; excitation 405-435 nm, emission 440-480 nm) and reduced (DHE; excitation 502 - 560 nm, emission 590 - 630 nm) forms of DHE. Measurements were taken every 30 s for 12.5 min before the addition of αS fibrils (30 μM monomer equivalent) with and without preincubation with BSA or CLU (both 3 μM, 5 min at RT). Measurements were then taken of the same cells for a further 13.5 min. The change in the rate of oxidation of DHE within cells was quantified by determining the gradient of a line fitted to the ratio of the mean ethidium intensity to the mean DHE intensity before and after the addition of the sample. The first two data points collected after the addition of the sample (i.e. the 13 min and 13.5 min time points) were excluded from the analysis as the addition tended to briefly disturb the fluorescence measurement (indicated by highly variable points in the aforementioned plot). This analysis was performed on a minimum of 10 cells from each of three separate wells, using a custom script written by myself in Python 2.7 using the SciPy library (Appendix V).

5.2.5 Generation of dual-labelled clusterin oligomers

As mentioned above, CLU forms oligomers in a pH- and concentration-dependant fashion. CLU is primarily monomeric at acidic pH but is present as a mix of monomers and oligomers at neutral pH (Poon *et al.* 2002a). Nothing is known about the dynamism of these oligomers. Therefore, dual colour oligomers were generated to investigate this. In order to form CLU oligomers containing monomers bearing

two different fluors, individually labelled CLU-AF488 and CLU-AF647 were first dialysed into citric acid buffer (20 mM citric acid, 20 mM sodium phosphate, 100 mM NaCl, pH 4.0). The two solutions (now containing primarily monomeric CLU, measured by SEC (see section 5.2.6) were mixed together and incubated for 2 h. The solution (hereafter referred to as 'mixed-label CLU' was then dialysed back into PBS/Az for analysis or storage at 4 °C.

5.2.6 Size exclusion chromatography

CLU-CLU oligomers were analysed by SEC. SEC was performed using a Superdex 200 (GE Healthcare Life Sciences, USA) attached to an ÄKTAprime plus (GE Healthcare Life Sciences, USA). Runs were performed in either PBS/Az at pH 7.4 or citric acid buffer (59 mM citric acid, 41 mM trisodium citrate, 40 mM NaCl, pH 4).

5.2.7 FRET fluorimetry

Bulk FRET analysis was undertaken on a Cary Eclipse Fluorescence Spectrophotometer (5 nm slit widths and PMT at 600 V; Agilent Technologies, USA). Measurements were taken of mixed-label CLU (or unconjugated fluors) at 1 µM total. Donor fluorophores were excited at 490 nm and emission of the acceptor fluorophore was collected between 600 – 750 nm.

5.3 Results

As mentioned, two different client proteins (Aβ and αS) were used to examine the binding of CLU and α_2M to toxic protein oligomers and amyloid fibrils. The effect of the binding on the further aggregation of Aβ and αS oligomers, the FRET efficiency of the oligomers and toxicity of αS amyloid fibrils are all examined. After this, the self-oligomerisation of CLU is investigated.

5.3.1 Amyloid-β

Equimolar quantities of $A\beta^{C}$-AF488 and $A\beta^{C}$-HF647 (5 μM total) were co-incubated with or without 0.5 μM CLU and α_2M and aggregation was monitored by single-molecule FRET. In the absence of chaperones, the aggregation proceeded relatively quickly, with oligomers making up 42% of total events measured after 7 h (the other 58% being $A\beta^{C}$-AF488 monomers, oligomers only containing AF488-labelled monomers, or oligomers with fluorophores too far apart for FRET to occur). The kinetics of the formation of these oligomers was decreased by both CLU and α_2M; CLU appeared to extend the lag phase by 3 h, while α_2M reduced the number of oligomers to approximately 30 - 40% of the Aβ only sample throughout the time course (Figure 5.6). Prior to use, the Aβ samples were stored frozen at -80 °C. It is not known whether this freeze-thaw of the Aβ had any effect on the aggregation kinetics, although it is possible that the process created some pre-aggregated 'seeds' that shortened the lag phase. However, since the Aβ still exhibited an

observable lag phase, if present, any aggregate seeds are unlikely to have substantially affected the assessment of the chaperone activity of CLU and α2M.

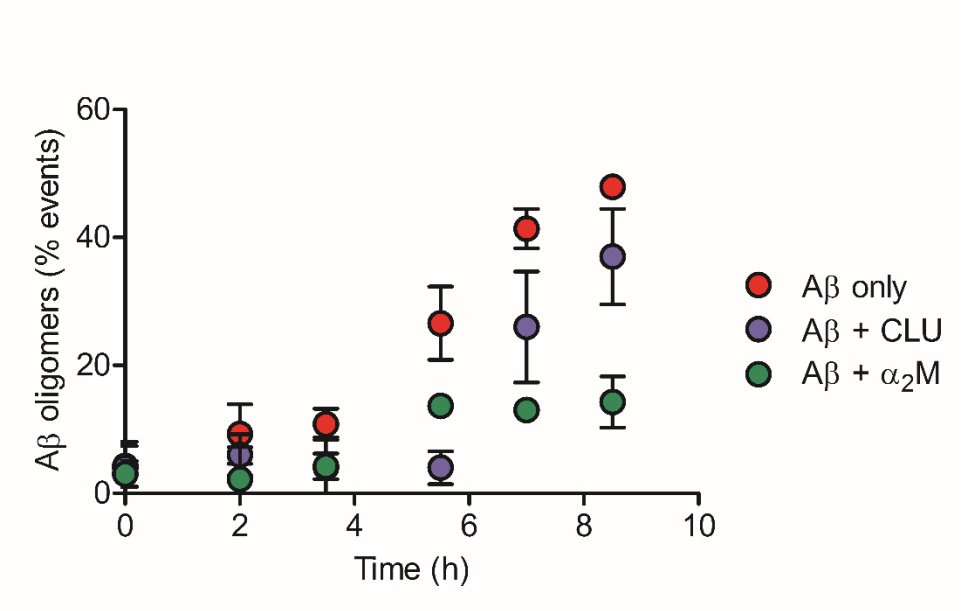

Figure 5.6: CLU and α2M slow the formation of Aβ oligomers. $A\beta^{C}$-AF488 and $A\beta^{C}$-HF647 (5 µM total) was incubated with or without CLU or α_2M (both at 0.5 µM) at 37 °C, 200 rpm for the indicated period of time. An oligomer was defined as a coincident event as measured by SM FRET. Data represent means ± SD, n = 3.

CLU-AF647 was then incubated with $A\beta^{C}$-AF488 to identify whether the Aβ-CLU complexes where being incorporated into mature amyloid fibrils. As expected, in the absence of CLU the number of Aβ oligomers increased substantially (from 32 ± 8 to 7271 ± 273) in the first two hours of incubation (Figure 5.7). The number then decreased as the oligomers were presumably incorporated into fibrils, precipitated, and were therefore not measured by single-molecule TCCD. Almost no soluble oligomers where measured after 24 h, although a large pellet of insoluble material was observed when the solution was centrifuged. However, when present, CLU bound to (presumably) misfolded Aβ to form complexes. The abundance of

these complexes increased more slowly than the Aβ complexes, but slowed dramatically after approximately 5 h rather than decreasing.

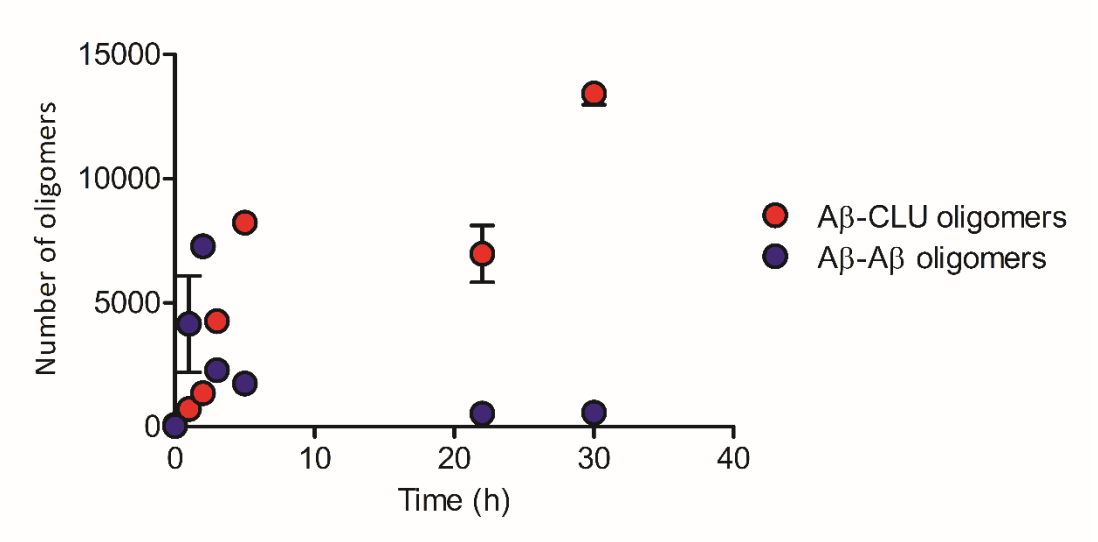

Figure 5.7: CLU-bound Aβ oligomers do not decrease in concentration over time. $A\beta^{C}$-AF488 and $A\beta^{C}$-HF647 (purple; 5 µM total) or $A\beta^{C}$-AF488 (5 µM) and CLU-AF647 (red; 0.5 µM) were co-incubated at 37 °C, 200 rpm for the indicated time period. Aggregation was measured by SM TCCD. Data represent means ± SD, n = 3.

As shown in Equation 5.3, the apparent number of monomers in an oligomer can be calculated by dividing the measured fluorescent intensities of the oligomers by that of a monomer. In a similar fashion, the natural logarithm of the apparent ratio of chaperone to client in each oligomer (*Z*) was calculated according to the equation

Equation 5.6

$$Z = \ln\left(\frac{\left(\frac{I_{chaperone}}{Im_{chaperone}}\right)}{\left(\frac{I_{client}}{Im_{client}}\right)}\right)$$

where *I* refers to the intensity of a peak above the threshold from fluorophores conjugated to the chaperone or client protein, and *Im* refer to the intensity of the monomer. The script used to perform these calculations is included in Appendix IV. These *Z* values are used for plotting purposes, so that the data is visually symmetrical around a 1:1 stoichiometry ($Z = 0$).

CLU was found to bind to Aβ with an approximate Gaussian distribution centred about a CLU:Aβ stoichiometry of 1.3(±0.5):1, although this stoichiometry showed a slight tendency to decrease the larger the oligomer became (Figure 5.8*a* and *b*). Other than the proportion of oligomers as a percentage of total events, there were no differences in oligomer distribution throughout the duration of the assays (*data not shown*). The variability in binding stoichiometries appeared to be greatest for small oligomers, and the majority of oligomers consisted of less than five Aβ peptide monomers. That being said, the largest oligomers detected (consisting of approximately 30 Aβ and 30 CLU monomers) would have a molecular weight of ~1700 kDa.

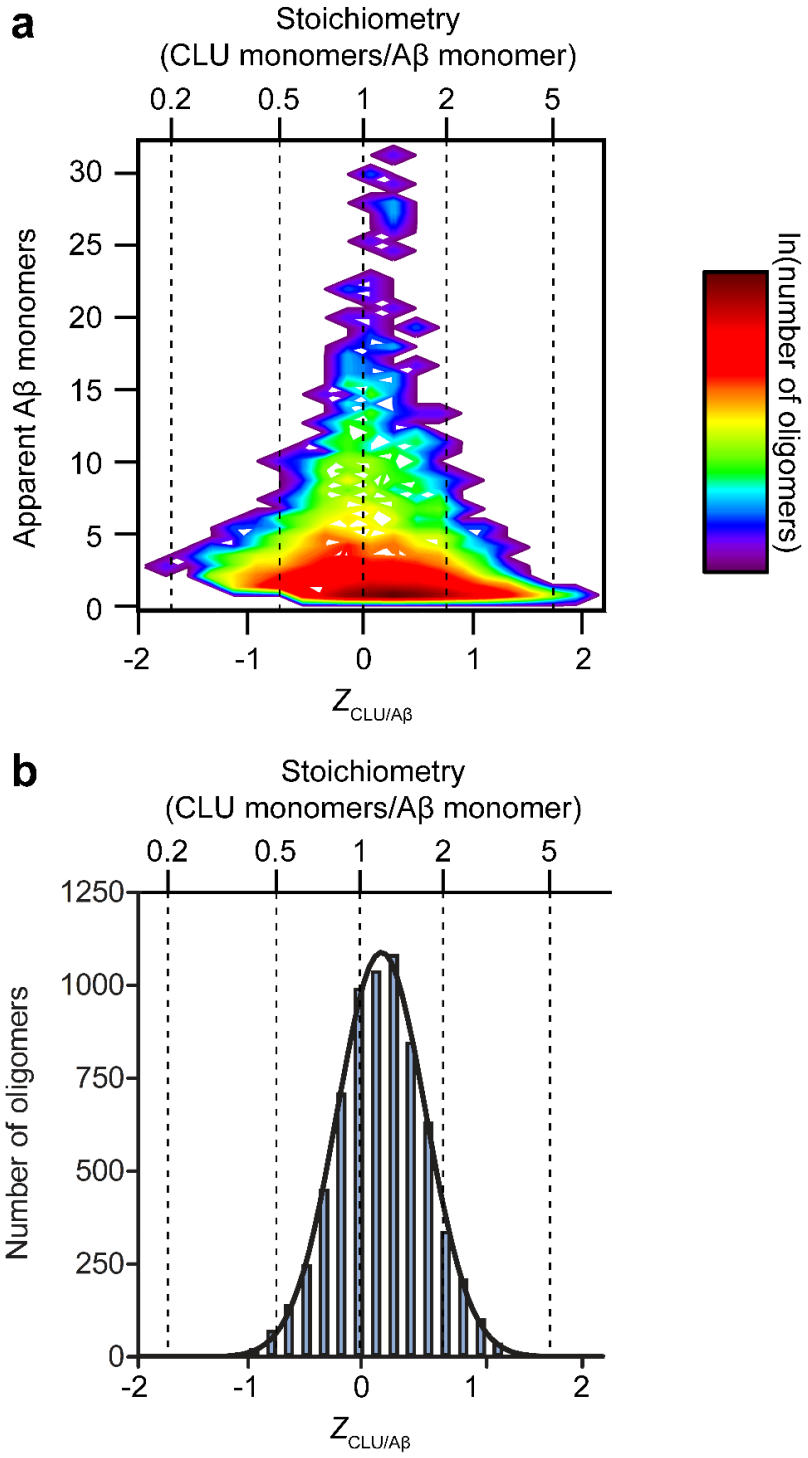

Figure 5.8: CLU most frequently binds misfolded Aβ in a 1.3:1 stoichiometry. $Aβ^{C}$-AF488 (5 µM) and CLU-AF647 (0.5 µM) were co-incubated at 37 °C, 200 rpm for 6 h. Aggregation was quantified by single-molecule TCCD. a) Contour plot of the apparent number of Aβ monomers comprising an oligomer as a function of the $Z_{CLU/Aβ}$ value. b) Frequency histogram of the number of oligomers at different $Z_{CLU/Aβ}$ (for the data shown in **a**), the thick black line is a Gaussian curve fitted to the data. In both **a** and **b** the dotted lines indicate a constant CLU:Aβ stoichiometry (as shown on the upper x-axis), but (in **a**) the number of monomers comprising the oligomers and (in **b**) the number of oligomers exhibiting this stoichiometry varies. Results are representative of three separate experiments.

In a similar experiment with α_2M-AF647 substituted for CLU, a slightly different pattern emerged (Figure 5.9*a*). Relative to CLU, α_2M was found to bind Aβ over a slightly broader range of stoichiometries (with a mean ± SD of approximately 1.6(±0.8):1 α_2M:Aβ (Figure 5.9*b*)). Additionally, the oligomers detected tended to contain fewer Aβ monomers, suggesting that (relative to CLU) α_2M reduced the size of the oligomers formed. Similar to the results for CLU, there was no change in the range or distribution of stoichiometries of binding throughout the aggregation time course (up to at least 24 h, *data not shown*).

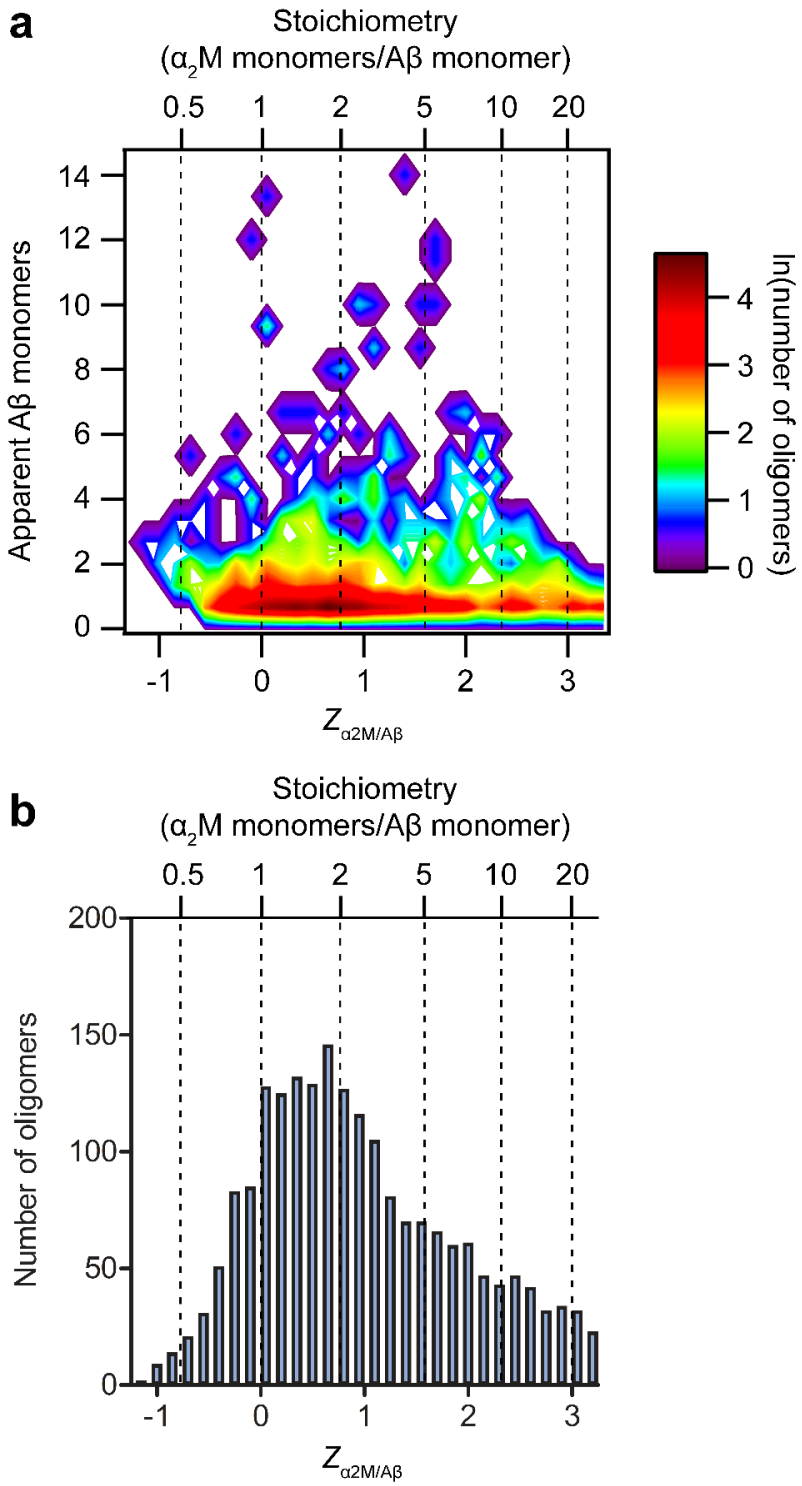

Figure 5.9: α2M binds misfolded Aβ with a broad range of stoichiometries. $A\beta^{C}$-AF488 (5 µM) and α_2M-AF647 (0.5 µM) were co-incubated at 37 °C, 200 rpm for 6 h. Aggregation was quantified by single-molecule TCCD. a) Contour plot of the apparent number of Aβ monomers comprising an oligomer as a function of the $Z_{\alpha 2M/A\beta}$ value. b) Frequency histogram of the number of oligomers at different $Z_{\alpha 2M/A\beta}$ (for the data shown in **a**). In both **a** and **b** the dotted lines indicate a constant α2M:Aβ stoichiometry (as shown on the upper x-axis), but (in **a**) the number of monomers comprising the oligomers and (in **b**) the number of oligomers exhibiting this stoichiometry varies. Results are representative of two separate experiments.

5.3.2 α-Synuclein

αS was expressed in and purified from *E. coli*. The purity of the protein following ion exchange chromatography and SEC was determined to be >95% when assessed by SDS-PAGE (Figure 5.10). The expected size of αS is 14 kDa.

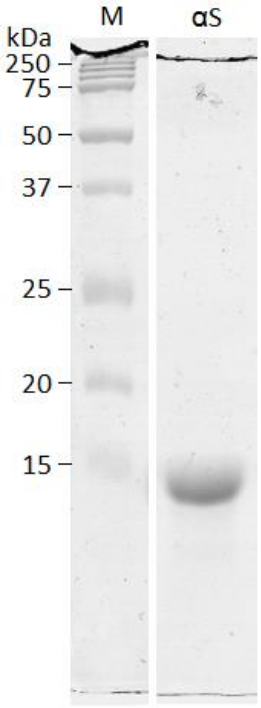

Figure 5.10: Purity of αS. αS was purified by passage over a HiPrep 26/60 Sephacryl S-300 HR (GE Healthcare Life Sciences, USA). Samples containing αS were pooled and analysed by SDS-PAGE on a 12% gel. M, marker (Precision Plus Protein™ Dual Color Standards (Bio-Rad, USA)); αS, purified and pooled sample.

$αS^{A90C}$-AF488 (70 µM) and $α_2$M-AF647 (0.7 µM) were co-incubated at 37 °C, 200 rpm for up to 48 h and the resulting oligomers were measured using TCCD following dilution to ~40 pM. After 6 h, small αS oligomers centred were around an approximate stoichiometric ratio of α2M:αS 1:1 (Figure 5.11*a* and *b*). This ratio tended to decrease with increasing numbers of αS monomers present in the oligomer. The largest oligomers detected (consisting ~30 αS monomers) displayed an approximate stoichiometry of $α_2$M:αS = 1:17.

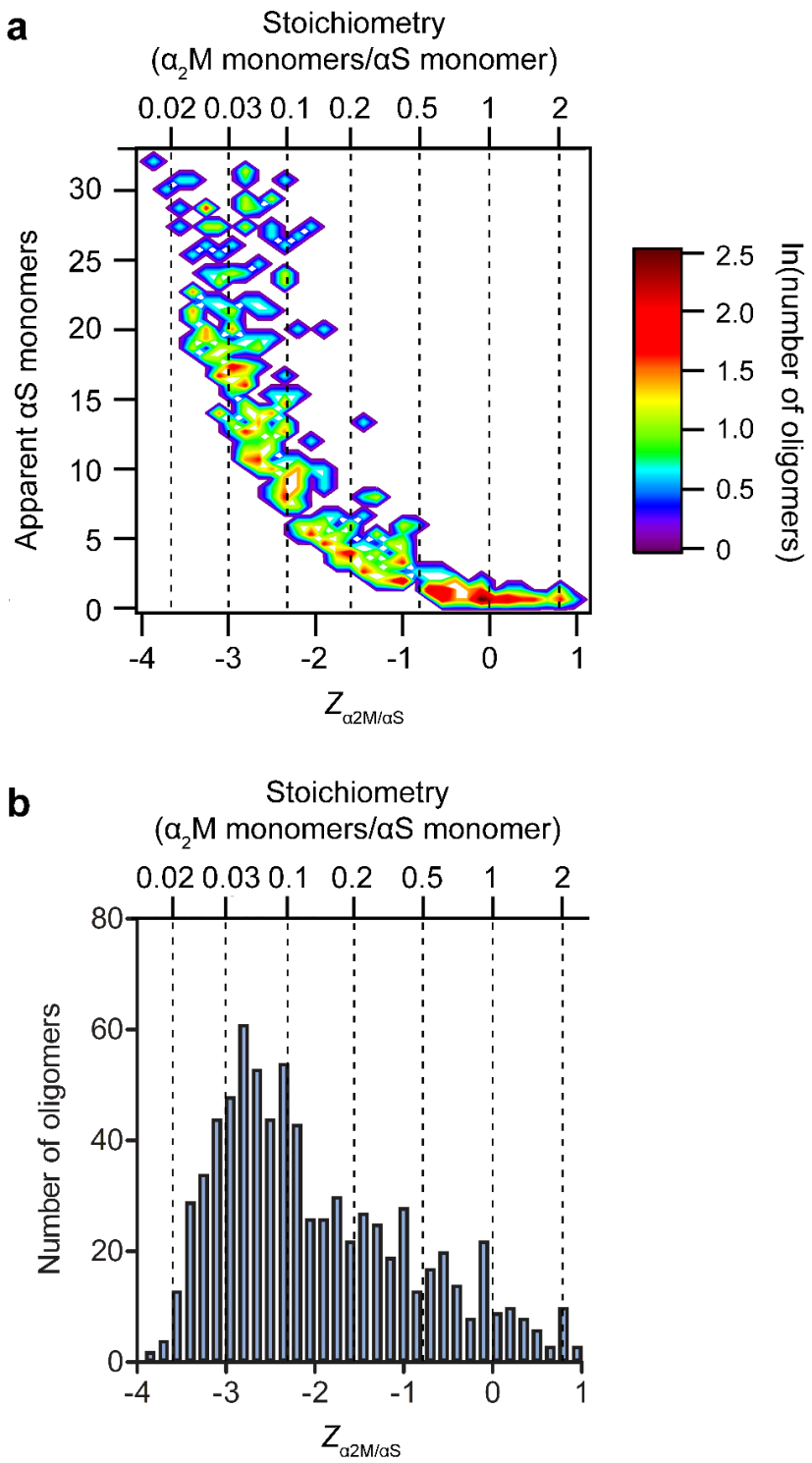

Figure 5.11: The ratio of α₂M:αS decreases in larger oligomers. αS^{A90C}-AF488 (70 µM) and α₂M-AF647 (0.7 µM) were co-incubated at 37 °C, 200 rpm for 6 h. Aggregation was quantified by single-molecule TCCD. a) Contour plot of the apparent number of αS monomers comprising an oligomer as a function of the $Z_{\alpha 2M/\alpha S}$ value. b) Frequency histogram of the number of oligomers at different $Z_{\alpha 2M/\alpha S}$ (for the data shown in **a**). In both **a** and **b** the dotted lines indicate a constant α2M:αS stoichiometry (as shown on the upper x-axis), but (in **a**) the number of monomers comprising the oligomers and (in **b**) the number of oligomers exhibiting this stoichiometry varies. Results are representative of two separate experiments.

After αS^{A90C}-AF488 had been incubated with α_2M-AF647 for 48 h, oligomers were more abundant, and they tended to be associated with more α_2M than similarly sized oligomers measured at 6 h (Figure 5.12*a* and *b*). At this later time point, whilst the monomeric and small oligomers were still had an approximate ratio of α_2M:αS = 1:1, in the largest oligomers (containing ~30 αS monomers) the ratio of α2M:αS was around 1:6 were, approximately three times greater than at the 6 h time point.

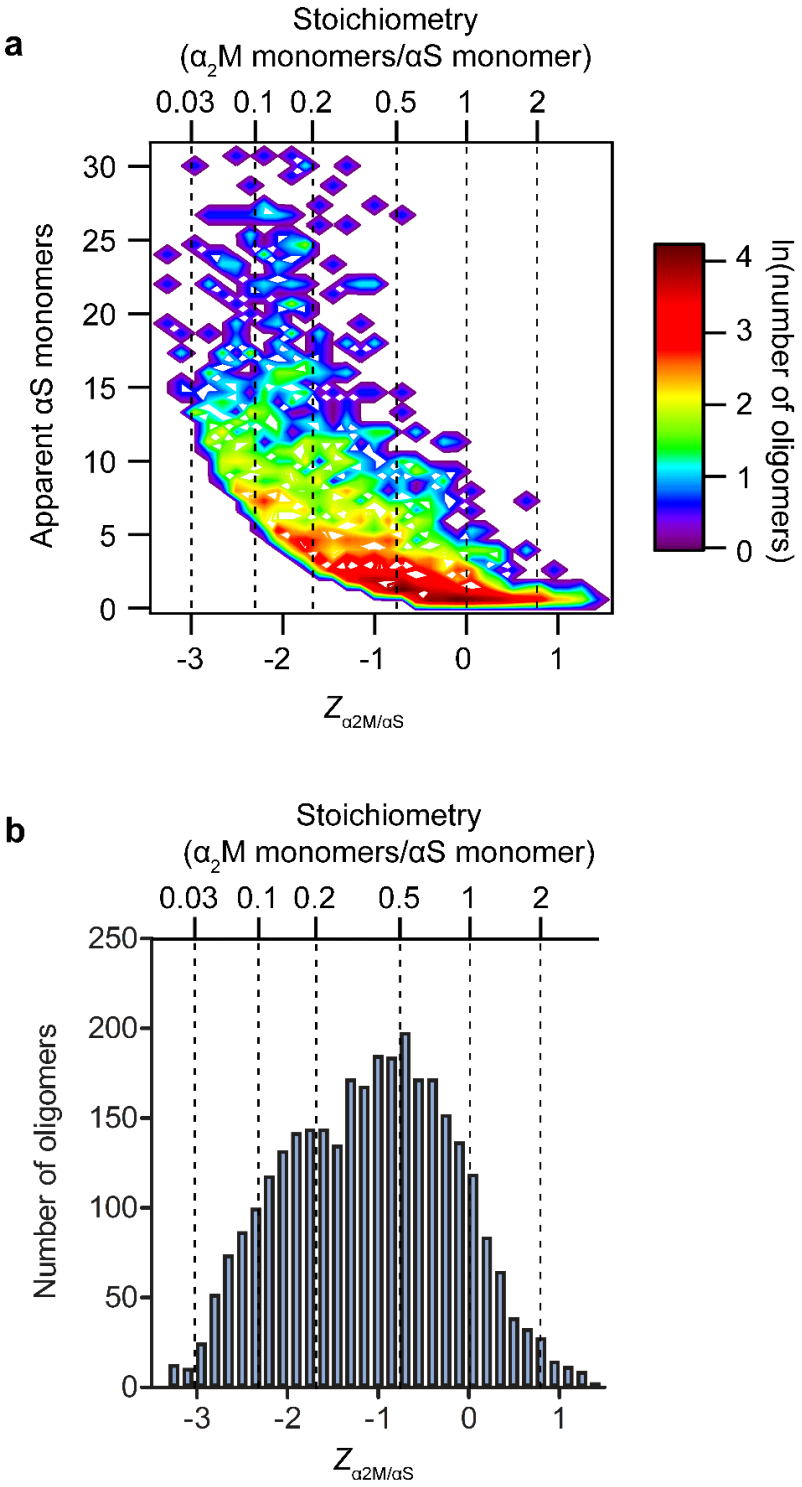

Figure 5.12: The ratio of α2M: αS decreases in larger oligomers. $αS^{A90C}$-AF488 (70 µM) and $α_2M$-AF647 (0.7 µM) were co-incubated at 37 °C, 200 rpm for 48 h. Aggregation was quantified by single-molecule TCCD. a) Contour plot of the apparent number of αS monomers comprising an oligomer as a function of the $Z_{α2M/αS}$ value. b) Frequency histogram of the number of oligomers at different $Z_{α2M/αS}$ (for the data shown in **a**). In both **a** and **b** the dotted lines indicate a constant α2M:αS stoichiometry (as shown on the upper x-axis), but (in **a**) the number of monomers comprising the oligomers and (in **b**) the number of oligomers exhibiting this stoichiometry varies. Results are representative of two separate experiments.

In order to further compare the differences in binding stoichiometries at 6 h and 48 h, the average numbers of apparent α2M and αS monomers in different oligomers was plotted for each time point (Figure 5.13). This plot shows that (i) at both time points there was a linear dependence of the α2M:αS ratio on oligomer size, and (ii) as oligomer size increased, the α2M:αS ratio increased only slightly at 6 h but to a much greater extent at 48 h.

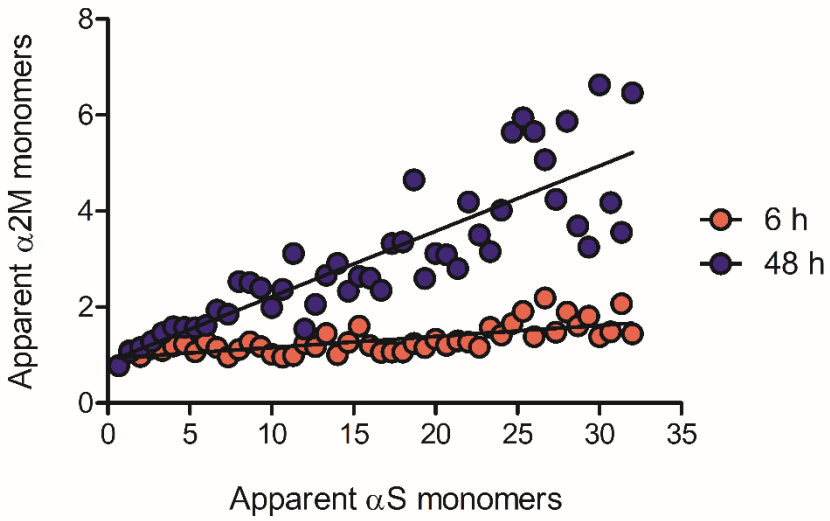

Figure 5.13: Time-dependent increase in the association of α_2M with αS oligomers. αS^{A90C}-AF488 (70 µM) and α_2M-AF647 (0.7 µM) were co-incubated at 37 °C, 200 rpm for either 6 h or 48 h. For each time point, the average number of apparent α_2M monomers was calculated for αS oligomers of each observed size. Lines of best fit are (6 h) y = 0.02x + 0.93, r^2 = 0.51 and (48 h) y = 0.14x + 0.86, r^2 = 0.73.

Similarly to the experiments with α_2M, αS^{A90C}-AF488 (70 µM) and CLU-AF647 (0.7 µM) were co-incubated and the stoichiometries of any oligomers were calculated. 6 h into the aggregation the vast majority of oligomers were small and centred around a stoichiometry of CLU:αS = 1:1. As for α_2M, the ratio of CLU:αS decreased in larger oligomers, with an average ratio of approximately 1:25 calculated for the largest oligomers detected (Figure 5.14*a* and *b*).

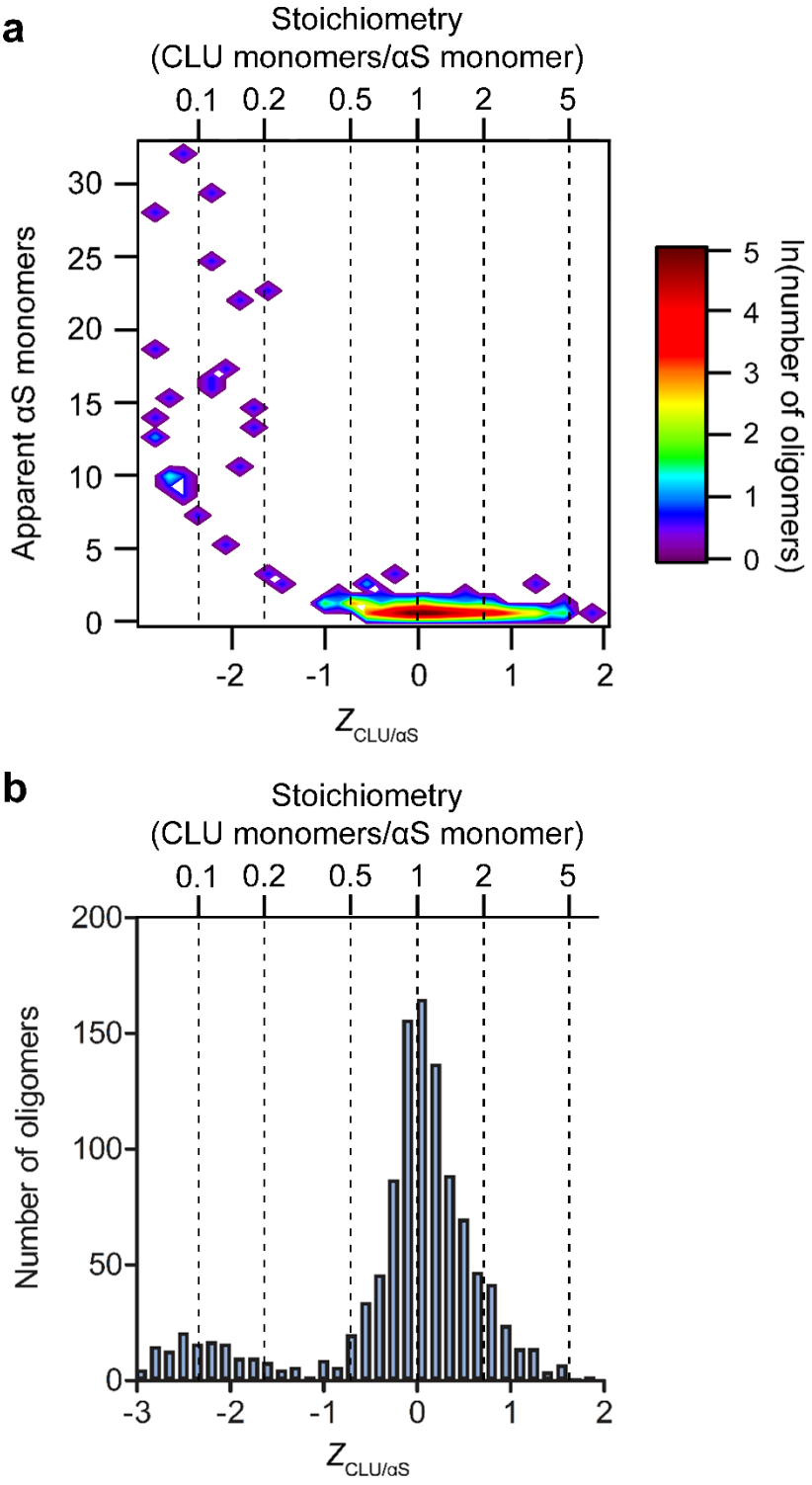

Figure 5.14: The ratio of CLU:αS decreases in larger oligomers. $αS^{A90C}$-AF488 (70 µM) and CLU-AF647 (0.7 µM) were co-incubated at 37 °C, 200 rpm for 6 h. Aggregation was quantified by single-molecule TCCD. a) Contour plot of the apparent number of Aβ monomers comprising an oligomer as a function of the $Z_{CLU/Aβ}$ value. b) Frequency histogram of the number of oligomers at different $Z_{CLU/Aβ}$ (for the data shown in **a**). In both **a** and **b** the dotted lines indicate a constant CLU:Aβ stoichiometry (as shown on the upper x-axis), but (in **a**) the number of monomers comprising the oligomers and (in **b**) the number of oligomers exhibiting this stoichiometry varies. Results are representative of two separate experiments.

As expected, a larger number of αS oligomers were detected after a 48 h incubation compared to 6 h. Like at 6 h, a population of larger αS oligomers with low a CLU:αS stoichiometry (approximately 1:30) were observed (Figure 5.15*a* and *b*). However, at this later time-point a new population of 'CLU-rich' oligomers was also observed (Figure 5.15*a*, *black arrow*). These CLU-rich oligomers had an average stoichiometry of CLU:αS = 1:1.3 and generally contained less than 15 αS monomers.

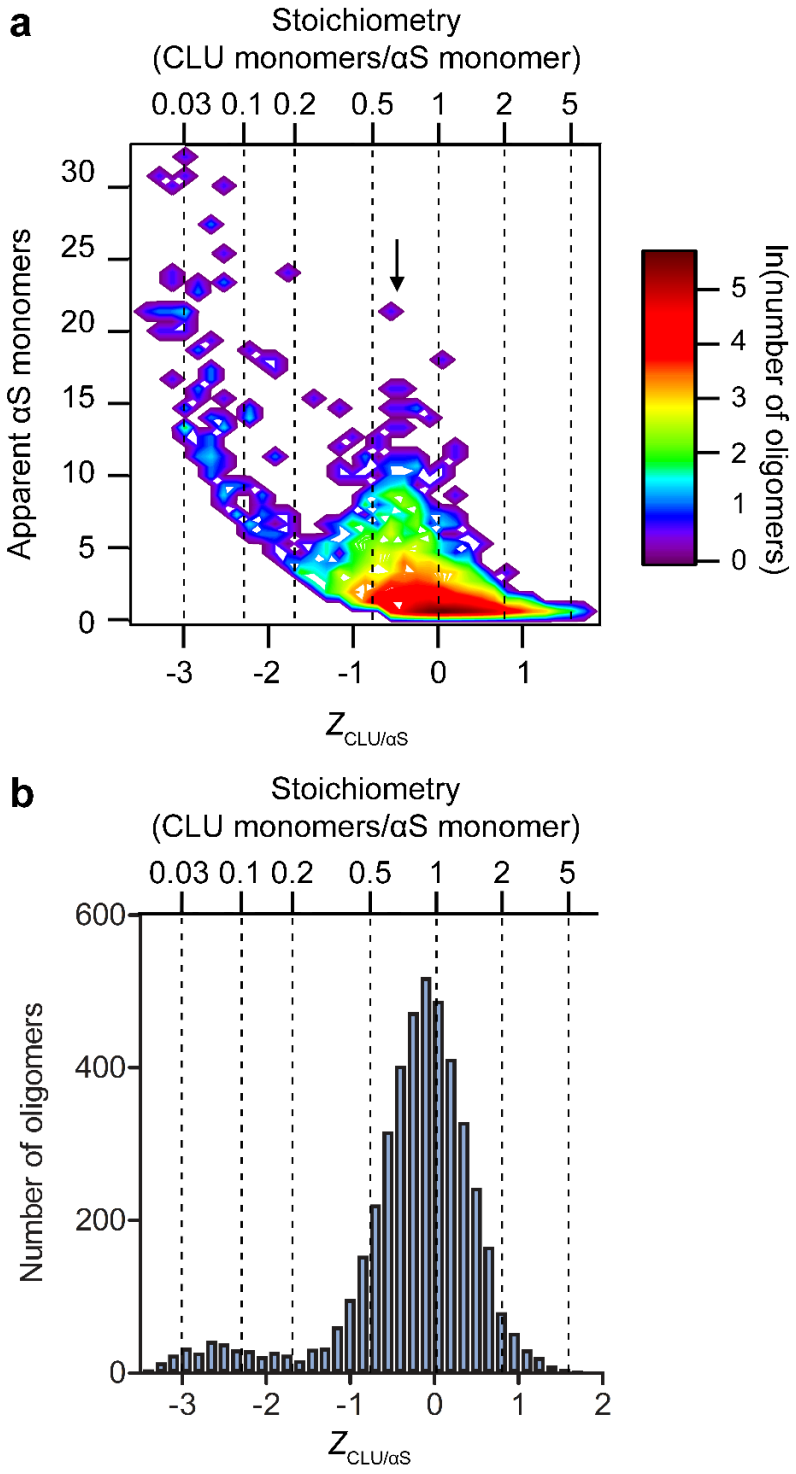

Figure 5.15: The ratio of CLU:αS decreases in larger oligomers. $αS^{A90C}$-AF488 (70 µM) and CLU-AF647 (0.7 µM) were co-incubated at 37 °C, 200 rpm for 6 h. Aggregation was quantified by single-molecule TCCD. a) Contour plot of the apparent number of Aβ monomers comprising an oligomer as a function of the $Z_{CLU/Aβ}$ value. The black arrow indicates a population of CLU-rich oligomers not observed at 6 h. b) Frequency histogram of the number of oligomers at different $Z_{CLU/Aβ}$ (for the data shown in **a**). In both **a** and **b** the dotted lines indicate a constant CLU:Aβ stoichiometry (as shown on the upper x-axis), but (in **a**) the number of monomers comprising the oligomers and (in **b**) the number of oligomers exhibiting this stoichiometry varies. Results are representative of two separate experiments.

As mentioned previously (section 5.1.4.1), the aggregation of αS is a multi-step process. Following the initial misfolding of the protein a structural conversion from a 'low-FRET' oligomer to a more toxic 'high-FRET' conformation can be measured. This conversion is a critical and necessary step on the pathway to amyloid formation by αS, and high-FRET oligomers are more toxic than the low-FRET precursors (Cremades *et al.* 2012). In order to investigate whether CLU has an effect on the structure of misfolding αS, αS (70 μM total, an equimolar mix of αS^{A90C}-AF488 and αS^{A90C}-AF488) was co-incubated with or without CLU (unlabelled, 0.7 μM) and FRET was measured at a series of time points following dilution to 30 pM. The addition of CLU had the effect of increasing (by about 2-fold) the FRET efficiency of both the low- and high-FRET efficiency oligomers, which remained still resolvable (Figure 5.16). In the absence of CLU, an approximately equal proportion of low- and high-FRET oligomers were observed early (3 h) in the aggregation. As expected, the structural conversion from low- to high-FRET oligomers was observed over time. CLU attenuated this conversion – in the presence of CLU, at both 3 and 6 h time-points the majority of oligomers exhibited low-FRET. After 48 h of aggregation most of the oligomers had structurally converted to the high-FRET form, however the proportion of low-FRET oligomers was still greater than in the absence of CLU.

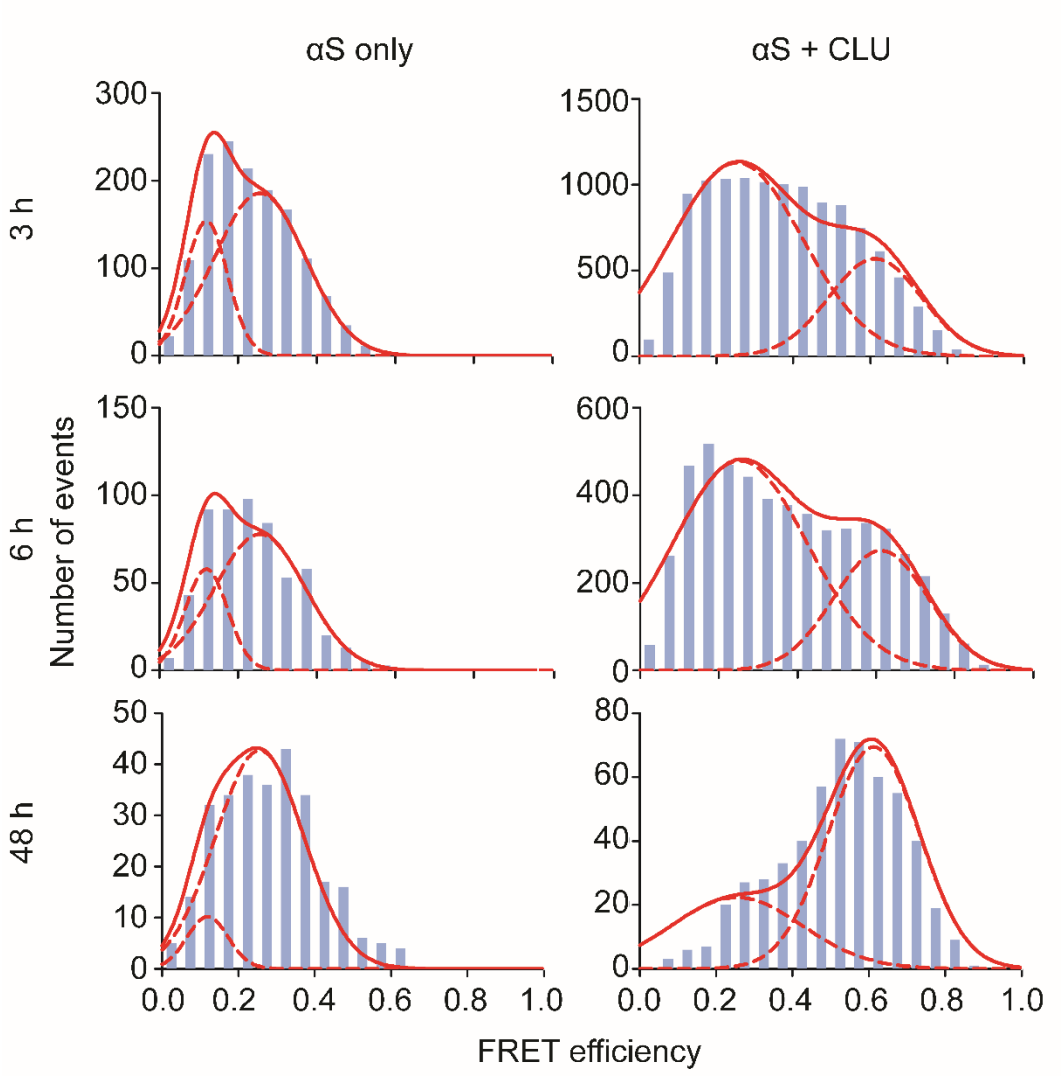

Figure 5.16: CLU lowers the proportion of high-FRET to low-FRET αS oligomers. $αS^{A90C}$-AF488 and $αS^{A90C}$-AF647 (70 µM total) were co-incubated at 37 °C, 200 rpm for up to 48 h with or without unlabelled CLU (0.5 µM). FRET efficiency was measured following dilution to picomolar concentrations. Dotted red lines indicate the Gaussian curves fitted to the data assuming that the oligomer population is comprised of two distinct species. The solid red lines represent the addition of the two Gaussian curves.

Under the conditions used to aggregate αS in these experiments CLU was unable to completely stop the aggregation. Particularly in the later time points, a pellet of insoluble material was observed upon centrifuging the mixture, although the pellet formed in the presence of CLU was smaller than the pellet formed without CLU. Having shown that CLU can bind to both Aβ and αS oligomers, as well as influence

the structure of αS oligomers, the ability of CLU to bind to the end stage of aggregation, mature fibrils, was also investigated. Mature αS fibrils were generated by incubating unlabelled αS for 48 h (37 °C, 200 rpm, 70 μM in PBS). Fibrils were then incubated with AF647-labelled chaperones or control proteins (present at 70 nM) for 30 min at RT. Unbound chaperone was removed by washing four times with PBS. Thioflavin T (ThT) was then added to 5 μM immediately before imaging using TIRFM. The images show that CLU binds to both the ends and along the length of the αS fibrils. However, rather than evenly coating the fibril the CLU appears to bind to localised areas (Figure 5.17*a*). It also appears possible that CLU preferentially binds to the end of the fibrils, although the diffraction-limited resolution of the images and the irregular shape of the fibrils made this too difficult to quantify by either manual or computational means. Non-chaperone control proteins α-lactalbumin, lysozyme and β-lactoglobin were found to bind the mature fibrils at lower levels than CLU (23%, 22% and 40% of ThT reactive fibrils showed coincidence with each of the respective proteins); for CLU about 70% of fibrils showed coincidence (Figure 5.17*b*). Thus, relative to some other proteins tested, CLU appears to bind more to αS fibrils, but this interaction may not be specific.

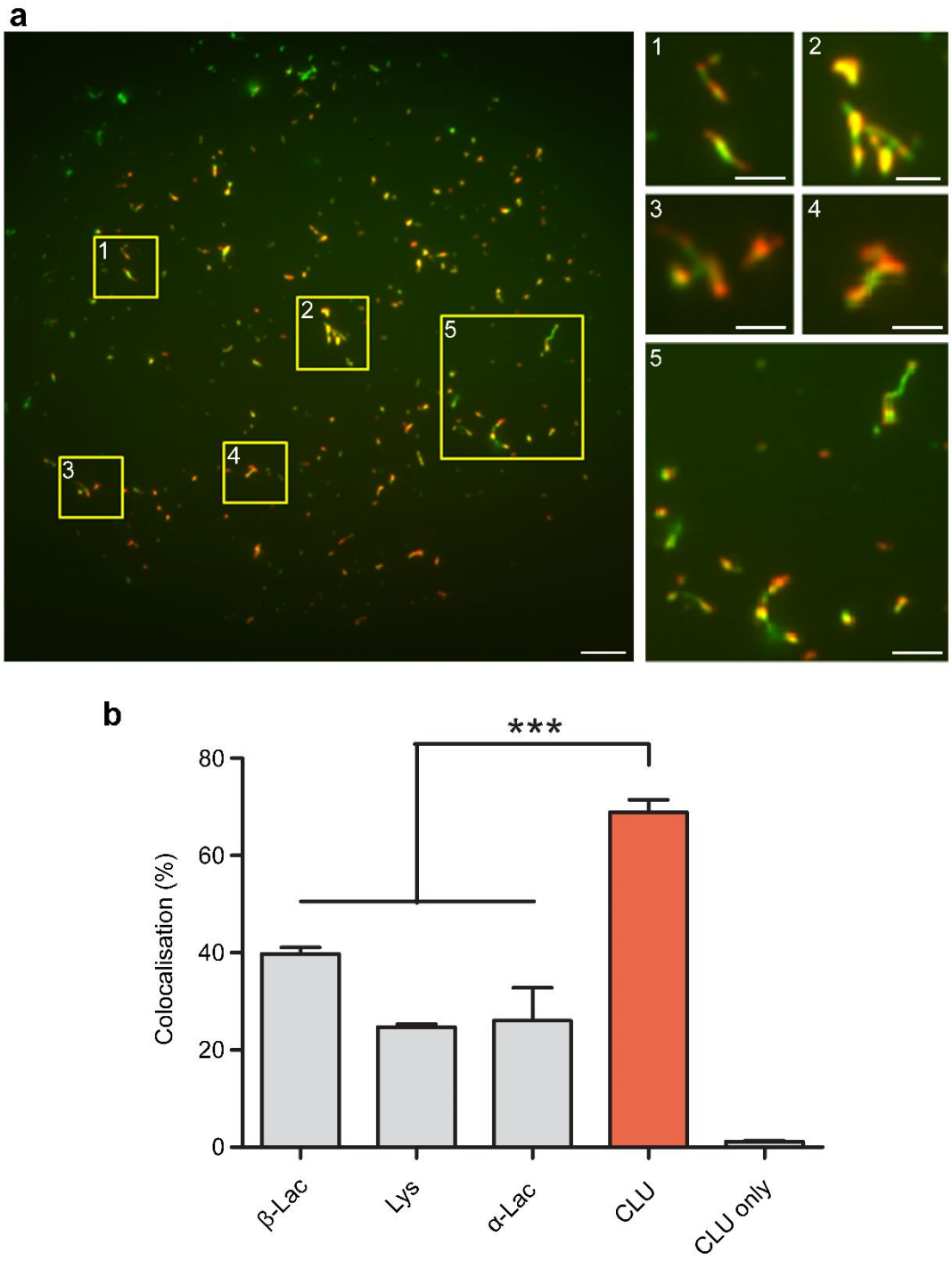

Figure 5.17: CLU binds mature αS fibrils. a) An example TIRFM image. Fibrils (ThT reactive structures) are shown in green, CLU-AF647 is shown in red, coincidence appears yellow. Panels at right show larger versions of areas indicated by numbered yellow boxes. Scale bar is 2 µm for the main panel, and 1 µm for each of the smaller panels. b) Quantification of the coincidence between fibril and CLU or control protein. Percent coincidence is the percentage of αS fibrils that are coincident with at CLU-AF647 (except in the case of CLU only, where it indicates the percentage of CLU-AF647 coincident with a ThT-reactive structure). Data shown is the mean percentage of co-localised fibrils from sets of nine TIRFM images for each sample Error bars are SD, n = 9. ***, $p < 0.001$, analysed by one-way ANOVA with a Bonferroni post-test. Data is representative of two separate experiments. β-Lac, β-lactoglobin; Lys, lysozyme; α-Lac, α-lactalbumin.

As the control proteins bound to the fibrils (although to a lesser extent than CLU) it remains unclear whether there is any physiological relevance to this interaction. It is also not clear whether the increased binding observed by CLU is evidence for binding specificity, as other non-chaperone control proteins that were not tested may bind to a similar extent. In an attempt to identify whether the presence of CLU on the fibril surface alters the cellular response to the fibrils, a DHE assay was used to measure the cytotoxicity of the fibrils (Cremades *et al*. 2012). Toxicity was measured as the change in the rate of production of reactive-oxygen species (ROS) immediately before and after the exogenous addition of a sample to N2a cells. Intracellular ROS has previously been shown to activate apoptosis in neurons (Jenner 2003) and is typically one of the first aberrant cellular responses induced by exposure to toxic protein oligomers (Canevari *et al.* 2004, Zampagni *et al.* 2011). Example plots of the rate of ROS production for one cell of each treatment is shown in Figure 5.18*a*, the average response of at least 30 cells relative to the buffer only control is shown in Figure 5.18*b*. The addition of fibrils alone and fibrils preincubated with BSA resulted in approximately a 2-fold increase in ROS production. However, the addition of fibrils preincubated with CLU did not significantly change the rate of ROS production in comparison to the buffer only control. As CLU alone did not have any effect on the rate of ROS production, the protective effect of CLU was unlikely to be the result of an inhibited ability to produce ROS in these cells.

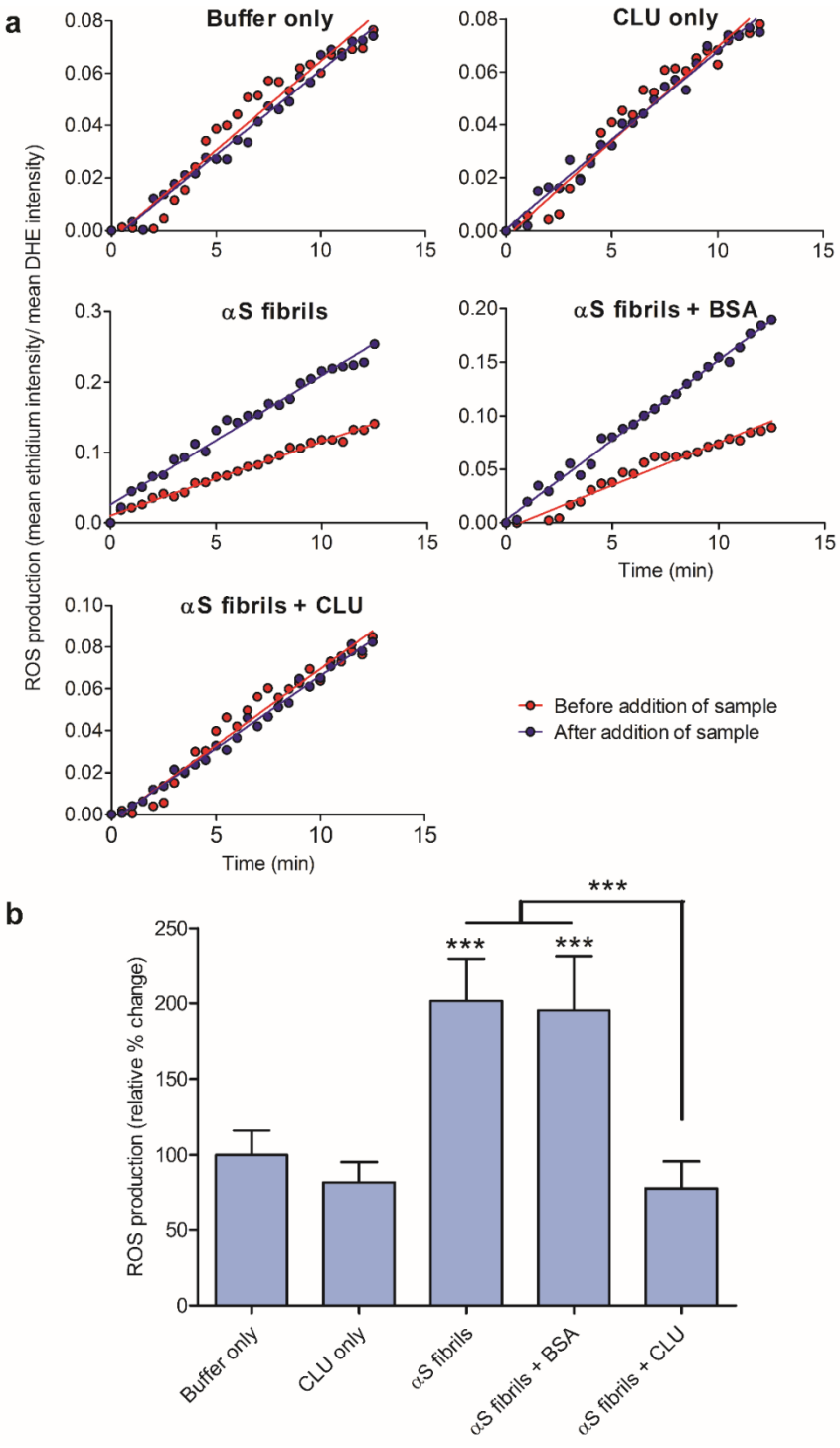

Figure 5.18: CLU-bound fibrils are less injurious to neuronal cells. a) ROS production of N2a cells was quantified by the measuring the oxidation of DHE to ethidium using an epifluorescence microscope (see section 5.2.4 for details). Blue and red circles respectively represent the ROS generation before and after the addition of a sample, which is indicated above each panel. Lines of best fit are shown; the change in the rate of ROS generation due to the sample is given by dividing the gradient of the post-addition line by the gradient of the pre-addition line. b) The change in the rate of ROS production produced by each sample relative to the buffer only sample. Values are means of at least 30 cells, error bars are SEM. ***, $p < 0.001$, analysed by one-way ANOVA with a Bonferroni post-test. Results are representative of two separate experiments.

5.3.3 Clusterin self-oligomerisation

As mentioned in section 5.1.6, CLU oligomers exists in solution in a pH and concentration dependent equilibrium, ranging from monomeric heterodimers to large multimers of at least several hundred kDa. The larger species can be readily detected by SEC but the technique does not provide enough resolution to readily identify the size of the species. Several distinct peaks are visible when purified CLU is analysed by SEC (Figure 5.19, *peaks labelled 1-4*), which are thought to correspond to 1) multimers of various sizes, 2) "dimers" formed by non-covalent association of two heterodimers, 3) single disulfide-linked heterodimers ("monomers"), and 4) degraded protein or low molecular weight contaminants. The larger species (peak 1) also shows a significant leading edge, indicating that there are a smaller number of very large oligomers. A small amount of CLU eluted in the void volume, indicating a size greater than the 600 kDa molecular weight exclusion limit. Fluorescent labelling with AF647 (approximately 1,300 Da and negatively charged) was found to produce a small but clear difference in the elution of the protein. However, the proportion of the two main peaks (2 and 3) appeared to be relatively unchanged.

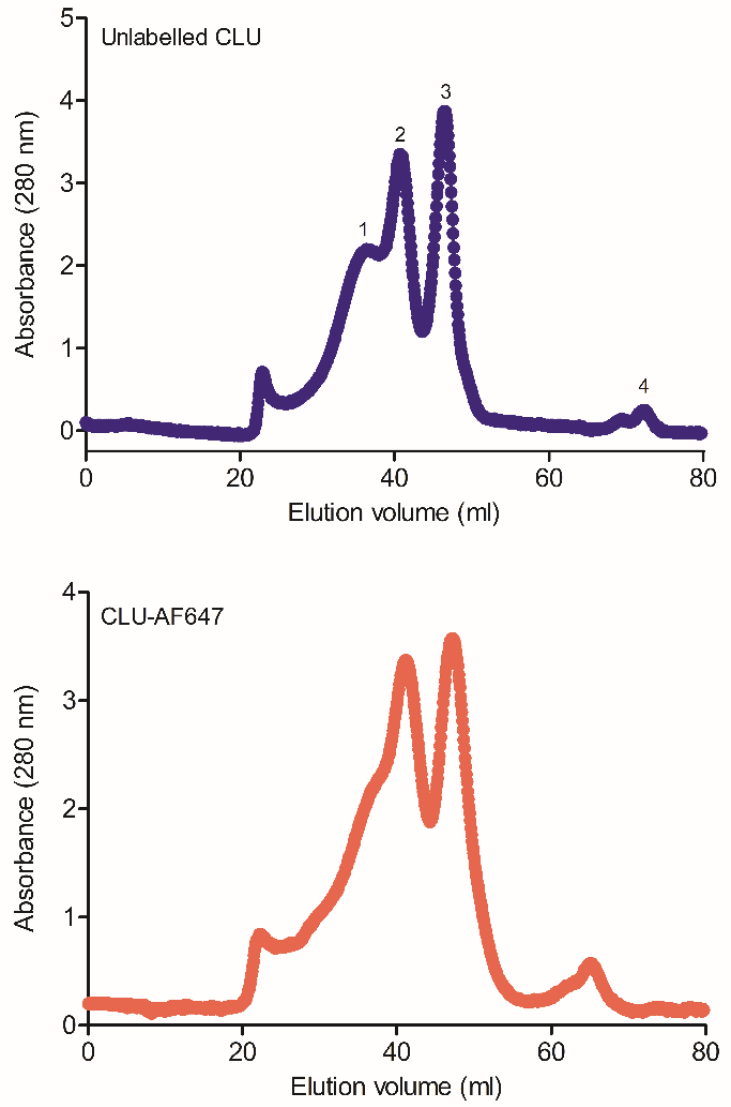

Figure 5.19: CLU oligomers can be detected by SEC. CLU (unlabelled or labelled with AF647, each at 1 µM) was separated by SEC using a Superdex 200 (GE Lifescience, USA) in PBS and eluted protein monitored by absorbance at 280 nm. Traces are representative of two analyses of each protein from separate experiments. The labelled peaks in the top trace indicate: 1) multimers, 2) dimers, 3) monomers, and 4) degraded protein or low molecular weight contaminants

In order to try to characterise the size and dynamics of the oligomers, CLU-AF488 and CLU-AF64 were separately brought to pH 4 in citric acid buffer, mixed in equimolar amounts, and dialysed back into PBS, pH 7.4. As previously described (Poon *et al*. 2002a), lowering the pH to 4 shifted the equilibrium of CLU oligomerisation towards the monomeric species (Figure 5.20). Thus, the mostly

monomeric labelled CLU molecules were mixed together, and then the pH raised back to physiological levels. This created conditions that would (in theory) allow the formation of oligomers containing a mixture of both CLU-AF488 and CLU-AF647.

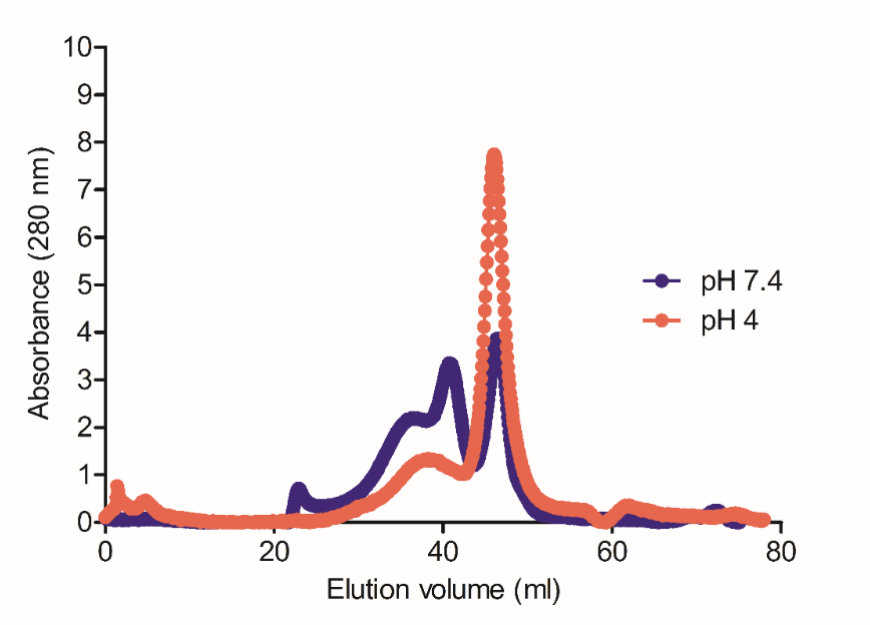

Figure 5.20: CLU is primarily monomeric at pH 4. CLU at either pH 4 (citric acid buffer) or pH 7.4 (PBS) was separated by SEC using a Superdex 200 (GE Lifescience, US) and eluted protein monitored by absorbance at 280 nm. Traces are representative of two runs from separate experiments.

TIRFM was then used to ensure that generation of dual-labelled oligomers had occurred (Figure 5.21*a*). Co-localised AF488- and AF647-labelled proteins sitting on or close to the surface were detected using a script written by Dr. Mathew Horrocks (University of Cambridge, UK) in Igor Pro version 6.3.4.1. Chance coincidence was determined by rotating one of the images by 90° and translating it to the right 10 pixels. Approximately 13% of the proteins above that expected by chance were coincident, that is, 13% of the proteins measured were oligomers containing both fluorophores (Figure 5.21*b*).

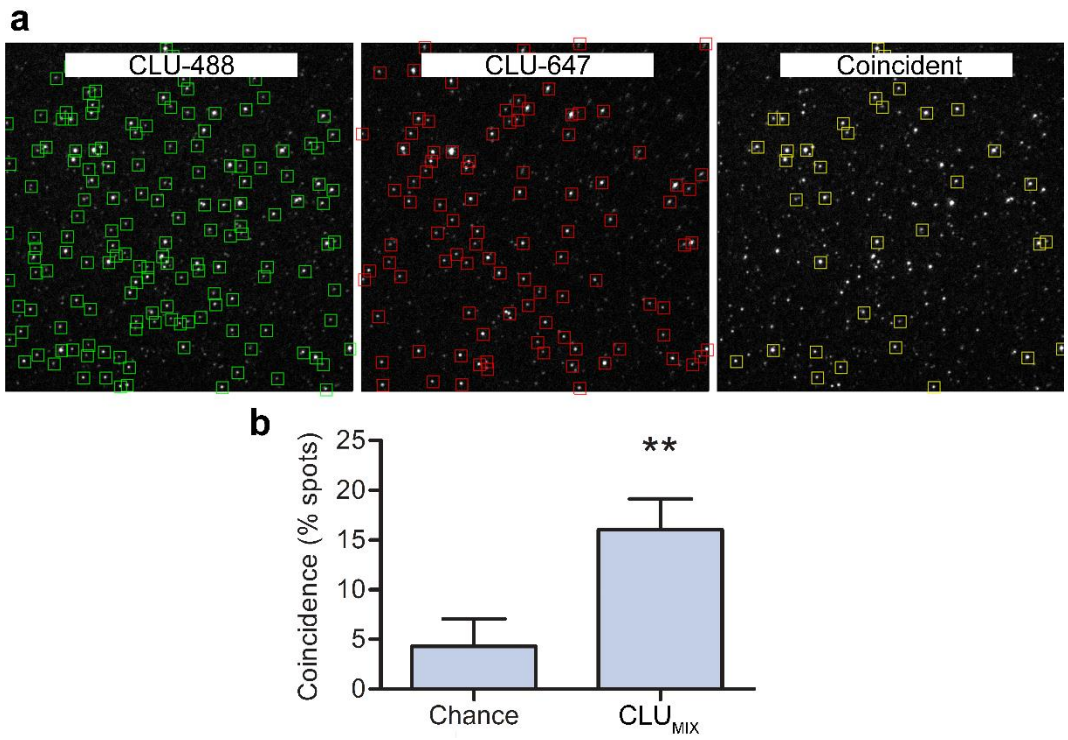

Figure 5.21: CLU oligomers can be measured by TIRFM analysis. a) Mixed-label CLU (200 pM) was added to a poly-L-lysine coated slide and imaged by TIRFM. CLU-AF488 (green squares); CLU-AF647 (red squares); coincident spots (yellow squares). b) Quantification of coincidence between the two fluorophore-labelled species. 'Chance' refers to the calculated chance coincidence, 'CLU_{MIX}' refers to mixed-labelled CLU oligomers. Values are the mean of three sets of nine images (27 images total), error bars are SD. ** $p < 0.01$, analysed by t-test.

Having established that dual-labelled oligomers had formed, bulk FRET of these oligomers (at 0.5 µM total CLU) was measured using a fluorimeter. Unconjugated dye at the same concentration was used as a control as these dyes would be too spatially separated to undergo FRET, but would exhibit the same amount of direct excitation as the fluorophores on the labelled CLU. A small peak in fluorescence emission from the acceptor fluorophore was observed in both the dual-labelled oligomers and unconjugated fluorophore control (Figure 5.22*a*). Given that the fluorescence was also measured in the control it was thought to be the result of a small amount of direct excitation of the acceptor fluor. To determine whether any

additional fluorescence could be observed for the CLU oligomers in comparison to the unconjugated fluorophore control (which would indicate genuine FRET), the baseline fluorescence from the donor fluorophore was calculated and removed (using the BaseLine Removal function in Igor Pro version 6.3.4.1). The resulting fluorescence peak from the acceptor fluorophore displayed an approximate normal distribution; in order to quantify the fluorescence a Gaussian curve was fitted to the peak (Figure 5.22*b*). The curve was integrated and compared with the unconjugated fluorophore control; there was no significant difference ($p > 0.05$; Figure 5.22*c*).

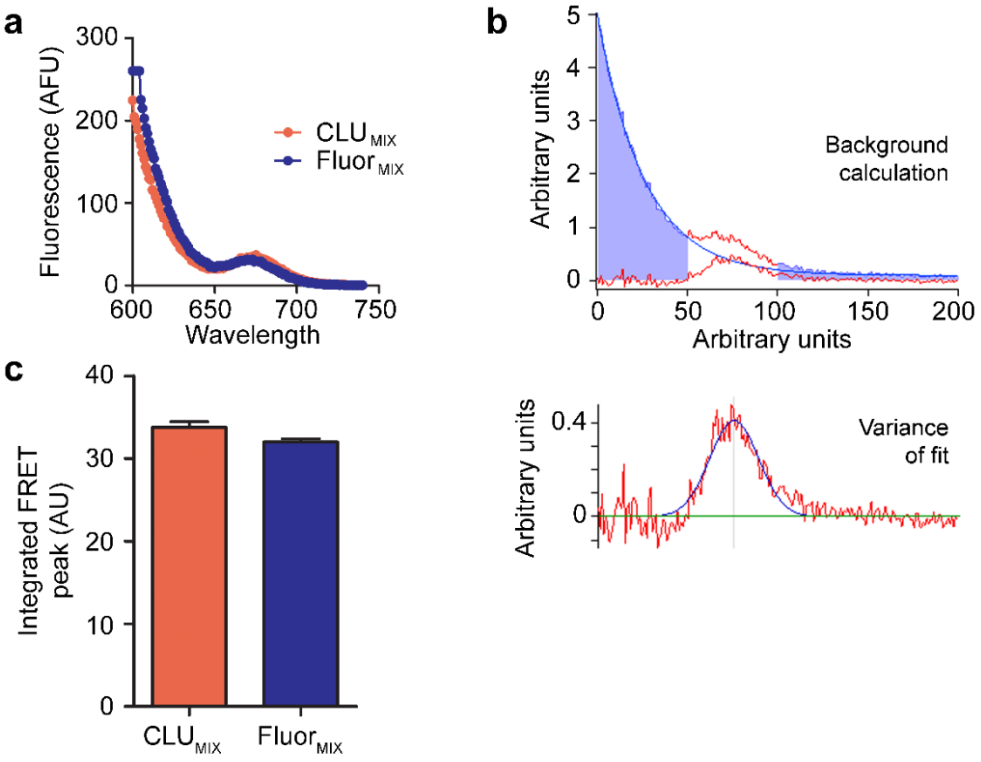

Figure 5.22: Mixed-label CLU oligomers do not undergo fluorimetry-detectable FRET. Oligomers (0.5 µM total CLU in PBS) consisting of a mix of AF488- and AF647-labelled CLU (CLU_{MIX}) were analysed for FRET using fluorimetry. a) Unprocessed emission spectra. b) Quantifying AF647 fluorescence (process shown for $Fluor_{MIX}$, quantification for CLU_{MIX} is not shown). *Top*: the baseline fluorescence from the donor fluorophore is calculated (blue line) and removed from the data (bottom red trace). *Middle*: the resulting acceptor fluorescence peak (red) is fitted to a Gaussian curve (blue). c) The Gaussian curve was integrated to find the area of the 'FRET' emission peak. Difference was non-significant, ($p > 0.05$, t-test). '$Fluor_{MIX}$' refers to a mixture of unconjugated AF488 and AF647 fluors, at the same molar concentration as the conjugated fluorophores present in CLU_{MIX}. Values are means (n=3), error bars are SD.

Since it was not possible to detect FRET in bulk solution between populations of CLU molecules labelled with two different fluors, TCCD was used to dual-excite the two fluorophores and search for coincidence. Since CLU oligomers are known to be concentration dependent (favouring smaller species at low concentrations) (Poon *et al*. 2002a), a rapid autodilution microfluidic device was used as it quickly (~4 s) and continuously dilutes the samples to single-molecule concentrations (see section 5.2.2.2). This technique has been previously used to study weakly associated biological complexes (Horrocks *et al.* 2013). After a 1 h measurement (binned in to 200 ns intervals) approximately 100 coincident bursts where detected. However this is likely due to chance, as desynchronised data showed the same level of coincidence (Figure 5.23).

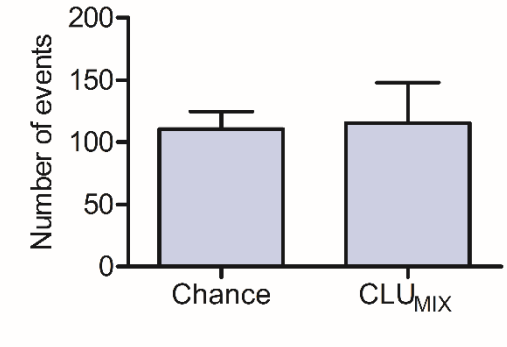

Figure 5.23: CLU oligomers rapidly dissociate upon dilution to picomolar concentrations. Mixed-label CLU (CLU_{MIX}, 10 µM) was continuously diluted (in approximately 4 s) in PBS to ~50 pM using an autodilution device. Coincidence was then measured by TCCD. 'Chance' refers to the calculated chance coincidence, 'CLU' refers to mixture of AF488- and AF647-labelled CLU. Difference was non-significant ($p > 0.05$, t-test). Values are means (n=3), error bars are SD.

5.4 Discussion

Previous work has shown that both CLU and α2M bind to misfolded proteins to inhibit their aggregation. However, it is not known whether specific sizes or structures of oligomers are bound preferentially, or whether the binding of a chaperone alters the oligomer structure. This chapter presents the results of experiments performed using single-molecule techniques to explore these questions.

αS- and Aβ-AF488 were each incubated separately under conditions leading to their aggregation, in the absence and presence of either CLU-AF647 or α2M-AF647. Single-molecule TCCD measurements were used to characterise the interaction between these extracellular chaperones and the client proteins. Both CLU and α_2M reduced the number of Aβ oligomers formed throughout the initial stages of aggregation. In the absence of chaperone, the number of Aβ oligomers increased during the lag phase, before peaking and dropping back to approximately baseline levels. This was presumably caused by the incorporation of oligomers into protofibrils or mature amyloid fibrils, which would not be measured by TCCD. When the aggregation was performed with $A\beta^C$-AF488 in the presence of CLU-AF647, the number of Aβ-CLU oligomers was found to increase more slowly than the number of Aβ-Aβ oligomers that were formed in the absence of CLU. However, after 4 h in the absence of CLU, where the number of Aβ-Aβ oligomers had dropped significantly, the number of CLU-Aβ oligomers was still increasing when CLU was

present. The number of CLU-Aβ oligomers did not drop for at least 30 h. Thus it appears that CLU bound to the Aβ and stabilised the protein such that its incorporation into fibrils was inhibited. It has been shown that the chaperone action of CLU can reduce the toxicity associated with aggregated Aβ (Yerbury *et al*. 2007). This may at first appear counterintuitive given that (i) oligomers are directly toxic and may cause disease (Benilova *et al.* 2012), and (ii) CLU stabilises and therefore increases the number of oligomers *in vitro*. However, CLU is much larger than Aβ and by binding to the exposed hydrophobicity on Aβ, CLU is likely to shield large regions of the Aβ oligomers from interacting with cells. Combined with the specific clearance of chaperone-client complexes by RME (Wyatt *et al.* 2009), these actions are likely to suppress the cytotoxicity that would otherwise be associated with the oligomers.

As indicated above, TCCD effectively allows the enumeration of oligomers present in a mixture, as well as providing information about the composition of the oligomers through the intensity of each of the fluors. However, it is extremely difficult to use this technique to accurately determine the numbers of each of the fluorescently labelled proteins in an oligomer. This difficulty is due to the inherent limitation of the thresholding process. Thresholding is required to eliminate the effect of undesired photons hitting the detector, whether they arise from ambient light sources or fluorophores traversing the edge of the confocal volume. Monomers are defined as fluorescent bursts above this threshold that have no

corresponding burst from the other fluor. Thus, the average fluorescence intensity of monomers can theoretically be used to calculate the number of monomers present in an oligomer. However, in practice, the apparent monomer intensity determined from any given data set has an almost linear relationship with the value used to threshold that data (Figure 5.24). In the work presented here, the data was thresholded using the value that maximised *Q* (the rate of coincident events above that expected by chance, divided by the total event rate; see section 5.2.2.4) (Clarke *et al.* 2007). While this method allows the optimisation of the value used to threshold, it does not specifically set the value to the "ideal threshold", which would eliminate any fluorescence other than the precise intensity given by a monomer. The use of an ideal threshold such as this would be necessary to accurately determine the number of monomeric units in an oligomer. The identification of the ideal threshold may be possible following extensive calibration of the intensity signals, but this is beyond the scope of the work presented here. However, the threshold that was applied to the data from each fluorophore was calculated in an identical manner, meaning that the error in the calculated number of monomers labelled with each fluorophore is the same when comparing the two labelled species. To account for the fact that the exact number of monomers comprising an oligomer could not be determined in the current study, the ratio of the relative amounts of each protein in oligomers was instead reported (stoichiometries and *Z* values). In the case where this was not possible, the 'apparent' number of monomers was provided, which likely differs slightly from the actual number of monomers in the oligomer, and should be viewed with caution in

this respect. This limitation may be overcome in future work by using a technique other than thresholding. A Bayesian inference method of calculating the number of oligomers undergoing FRET (and their FRET efficiency) directly from unprocessed single-molecule FRET data was recently described (Murphy *et al.* 2014). This could potentially be adapted to calculate sizes from TCCD data, but that is beyond the scope of this work.

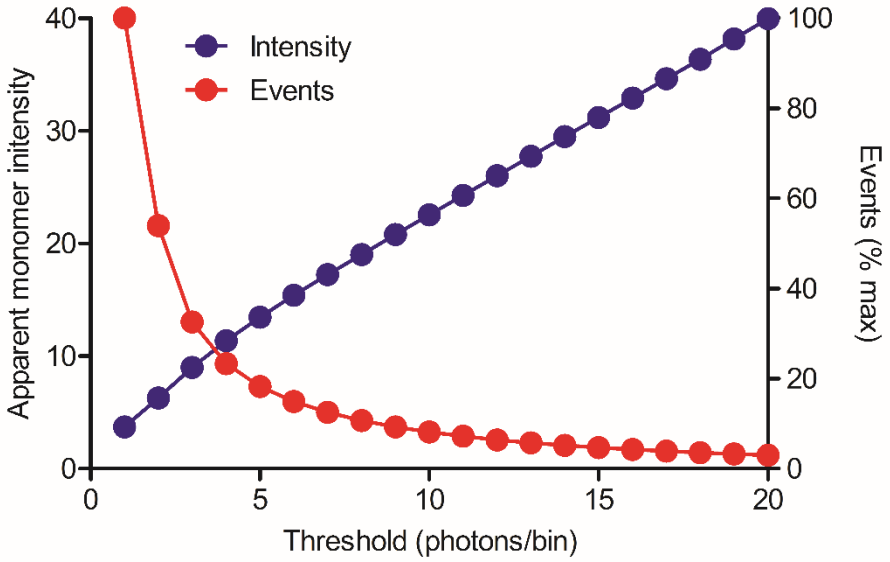

Figure 5.24: Calculated monomer intensity shares an almost linear relationship with the threshold used on TCCD data. When analysed by TCCD, the number of events above the threshold decreases exponentially with increased threshold, but the apparent intensity of monomeric species increases almost linearly. This was calculated from TCCD data of AF488- and AF647-labelled DNA duplexes used to align the optics of the confocal microscope (section 5.2.2.4).

TCCD was used to determine the relative number of CLU-α_2M monomers that are associated with $A\beta_{42}$ and αS oligomers. CLU binds $A\beta_{42}$ oligomers at an approximate 1.3(±0.5):1 CLU:Aβ ratio (mean ± SD), similar to the 1:1 ratio that was previously reported for CLU:$A\beta_{1\text{-}40}$ (Narayan *et al.* 2012). On average, under the conditions tested, a similar stoichiometry was observed for α_2M (α_2M:Aβ = 1.6(±0.8):1;

mean ± SD) under the conditions tested (Figures 5.10 and 5.11). However, in contrast to CLU, α_2M appeared to incorporate into the oligomers over a broader range of stoichiometries (α_2M:Aβ = 0.5:1 - 20:1). This is consistent with the presence of numerous binding regions on the much larger α_2M molecule. No changes in the measured stoichiometries of CLU:Aβ or α_2M:Aβ oligomers were detected over time; similar stoichiometries were measured at 3 h and at endpoint. Aβ oligomers do not undergo a structural compaction like αS, and thus no changes in the stoichiometry of chaperone binding were expected over time.

As previously mentioned, αS oligomers undergo a time-dependent structural conversion from a low-FRET to a high-FRET conformation. This step is believed to be essential to the formation of amyloid, with the high-FRET oligomers being the only species incorporated into the mature fibrils (Cremades *et al.* 2012). Under the conditions used, approximately 40% of the αS oligomers exhibited low FRET at early time points (3 - 6 h), whereas the vast majority of αS oligomers measured at 48 h were high FRET. The presence of CLU exerted several effects on the αS oligomers. The FRET efficiency of both types of oligomers was increased, which is consistent with the fluorophores being spatially separated by less distance, suggesting that the binding of CLU can cause a compaction of these oligomers. Despite the increased FRET efficiency, the conversion from low-FRET to high-FRET oligomers can be identified, and appears to be delayed in the presence of CLU. When CLU is present, high-FRET species still dominate at 48 h, but low-FRET oligomers are the majority at

early time points. Thus, it appears possible that CLU can inhibit the aforementioned conversion of oligomers from low-FRET to high-FRET conformation, which may prevent fibril formation (Yerbury *et al.* 2007). In the presence of CLU, at 6 h most oligomers were small and CLU-rich – they tended to contain less than 5 apparent αS monomers, and had a stoichiometry of CLU:αS = 1:1. The larger oligomers present (> 5 apparent αS monomers) were relatively CLU-poor, with an approximate stoichiometry of CLU:αS = 1:15. At 48 h however, larger oligomers with an approximate stoichiometry of CLU:αS = 1:1.3 were evident (large, CLU-rich oligomers). These oligomers were detected as a population discrete from the large low-CLU oligomers mentioned above, and coincided with the appearance of high FRET oligomers (Figure 5.16). This suggests that CLU preferentially associates with high-FRET αS oligomers rather than their low-FRET precursors. Another possible interpretation is a simple time-dependent increase in the CLU:αS stoichiometry. As discussed below, this type of time-dependent structural change appears to occur for oligomers containing α_2M and αS; however, this does not appear to be the case for αS oligomers containing CLU, where the large, CLU-rich oligomers appear as a separate population.

The number of α_2M monomers associated with αS oligomers was found to be linearly dependent on the number of αS monomers in the oligomer. After 6 h, the smallest oligomers detected consisted of one apparent αS monomer associated one apparent α_2M monomer. On average, 0.023 additional α_2M monomers were

associated with the oligomer for every additional apparent αS monomer. As the largest oligomers detected consisted of 32 apparent αS monomers, most oligomers at this time point contained only 1 or 2 apparent α_2M monomers. After 48 h, the smallest oligomers still exhibited an apparent stoichiometry of α_2M: αS = 1:1. However, an average of 0.14 α_2M monomers were incorporated into the oligomer for each additional αS monomer. Thus, the largest oligomers detected were associated with an apparent 5 - 6 α_2M monomers (an approximate stoichiometry of α_2M:αS = 1:6). Unlike CLU, α_2M did not appear to preferentially incorporate into any specific population of oligomers detected. These data suggest that the binding of chaperones to a client protein depends not only on the particular chaperone, but also the identity of the specific client protein and the structural properties of the oligomer.

TIRFM was used to examine the interaction between CLU and αS fibrils. The ability to bind to fibrils was not specific to CLU, with non-chaperone control proteins β-lactoglobin, α-lactalbumin and lysozyme all binding to the fibrils. This binding is likely a generic property of the fibril, arising perhaps from the general 'stickiness' of large hydrophobic regions. However, relative to the control proteins tested CLU bound significantly more to fibrils, possibly a result of its known proclivity for binding regions of exposed hydrophobicity (Poon *et al.* 2002a). CLU-AF647 only (without addition of fibrils) showed approximately a 2% coincidence with ThT-binding structures. This could be the result of a small amount of amount of CLU

binding ThT directly or possibly CLU that had bound a misfolded, endogenous client protein in plasma and was then co-purified along with uncomplexed CLU. This small level of coincidence was not sufficient to explain the increased binding of CLU to ThT-positive fibrils. There are several possible physiological consequences of this interaction. It is possible that CLU influences the disaggregation of the fibrils. Indeed, it has previously been shown that $A\beta_{40}$ fibrils dissociate more quickly in the presence of CLU (Narayan *et al.* 2012), though this was believed to be due to CLU binding oligomers dissociating from the fibrils, rather than the result of a direct interaction between CLU and the fibril itself. Additionally, the binding of CLU to mature fibrils may represent a cytoprotective mechanism. Previous investigations into the ability of CLU to ameliorate the cytotoxicity of misfolded proteins often involved incubating the client protein in the presence or absence of CLU. The solution would then be used to treat cells after the reaction had reached an endpoint equilibrium (Yerbury *et al.* 2007a). These studies have shown that CLU can alter the aggregation pathway sufficiently so that the end result is less toxic than would be otherwise. However, these experiments typically involve a large difference in the oligomer-fibril distribution of the final equilibrium reached. It is not clear whether the binding of CLU to mature fibrils is sufficient to reduce the associated cytotoxicity. The DHE assay used here was performed using fibrils formed in the absence of chaperone. Both the incubation time with CLU and the length of the measurements were intentionally kept short (5 and 25 min respectively) to minimise the chance that CLU would upset the equilibrium of the fibrils in solution. Thus, whether the binding of CLU to αS fibrils was sufficient to

ameliorate the potential toxicity of the fibrils was examined (Figure 5.18). Pre-incubating fibrils with CLU abolished the ROS generation that was associated with fibrils alone and fibrils pre-incubated with the non-chaperone BSA. In the absence of fibrils, CLU had no effect on the normal level of cellular ROS generation, indicating that the protective effect of CLU described above does not result from a direct inhibition of ROS production. Thus, while the binding of CLU to αS fibrils may not be "specific", in that other proteins tested also bound to lesser extents, the protective effect conferred by CLU binding may be specific. This could represent a physiological role for the CLU commonly found bound to insoluble protein deposits (see Table 4.3). To establish whether this a generic effect of CLU, or specific to αS, this work should be extended using amyloid fibrils formed by other proteins. While the toxicity associated with misfolded proteins is now believed to be primarily conferred by oligomers (Kayed and Lasagna-Reeves 2013), the hydrophobic domains of mature fibrils can become inserted into cell membranes in a manner that causes cell death (Ji *et al.* 2002, Milanesi *et al.* 2012); fibril ends are particularly adept at disrupting cell membranes (Xue *et al.* 2009). While it is possible that CLU may preferentially bind αS fibril ends (which would perhaps be expected if they are more hydrophobic), the resolution of the TIRFM was not high enough to allow reliable quantification of the positioning of CLU binding. Super resolution microscopy during future experimentation may be able to provide more of an insight. Regardless, the fact that CLU reduced the toxic effects of the fibrils suggest that the CLU found bound to numerous disease-associated deposits (such as αS

inclusions in PD and Aβ plaques in AD; see Table 4.3) may be serving a physiological purpose.

CLU is known to form self-oligomers in a concentration and pH dependent manner; monomers and smaller species are favoured at both low pH and low concentrations (Hochgrebe *et al.* 2000, Poon *et al.* 2002a). In an attempt to examine the sizes and dynamism of these oligomers, individually labelled CLU-AF488 and CLU-AF647 were dialysed to pH 4 so that the majority of the CLU was monomeric, mixed together, and dialysed back to pH 7.4. This was performed to promote the formation of oligomers incorporating a mixture of protein molecules labelled with each fluor, the formation of which was first confirmed using TIRFM. Approximately 13% of the spots detected were coincident between fluors, confirming that (i) dual-labelled oligomers had formed, and (ii) these oligomers can be detected by TIRFM at the concentration used (200 pM). However, TIRFM would not detect every oligomer, and favours detection of larger oligomers (Figure 5.25). This is due the requirement for the oligomers to contain monomers labelled with both AF488 and AF647 in order to be detected. Since monomers labelled with either AF488 or AF647 have an equal chance of becoming incorporated into an oligomer (Cremades *et al*. 2012), larger oligomers (containing more monomers) are more likely to meet the detection requirement of containing both AF488- and AF647-conjugated monomers. The overall likelihood (*L*) of detecting an oligomer is given by the following equation, where *n* is the number of monomers in the oligomer.

Equation 5.8

$$L = \frac{n-1}{n+1}$$

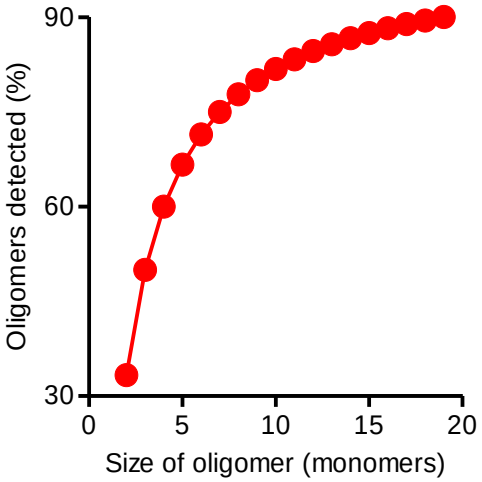

Figure 5.25: The detection of oligomers by TIRFM is dependent on oligomer size. TIRFM only detects oligomers that contain at least one AF488- and one AF647-labelled monomer. Since both monomers have an equal chance of becoming incorporated into an oligomer, the likelihood that TIRFM detects any given oligomer increases with the number of monomers in the oligomer. Data generated from Equation 5.8.

Other techniques were used in an attempt to further characterise CLU-CLU oligomers, however these efforts were also largely unsuccessful. No FRET arising from the oligomers (at 0.5 µM) could be detected using fluorimetry, despite the fact that the presence of FRET oligomers was confirmed using TIRFM (at 200 nM). Thus, it appears that the fluorimeter used (a Cary Eclipse Fluorescence Spectrophotometer; Agilent Technologies, USA) did not have the sensitivity required to measure the weak signal. More sensitive fluorimeters should be able to measure the FRET from these oligomers, and could be used to study the dynamism of the CLU oligomers. Similarly, TCCD did not allow the detection of CLU oligomers.

Having been designed to measure the fluorescence of single molecules, TCCD is much more sensitive than fluorimetry, however, it can only be performed on very dilute samples. An autodilution microfluidic device was used that rapidly (< 4 s) dilutes the stock (micromolar) concentration to the concentrations required for TCCD measurements (~50 pM). Since no oligomers were detected using this technique, it suggests that the oligomers dissociate very rapidly upon dilution. It was hoped that one of or a combination of the above techniques could be used to study the dynamism of the CLU oligomers, with the eventual aim of identifying whether any specific species displays a higher chaperone efficacy. Like CLU, the sHsps Hsp27, αB-crystallin and αA-crystallin form large, polydisperse oligomers (Benesch *et al.* 2008). sHsp oligomers are highly dynamic and undergo dynamic subunit exchange (Ahmad *et al.* 2008); it is unknown whether this is the case for CLU, but the rapid dissociation and pH dependency observed here (confirming previous work by Hochgrebe *et al.* (2000)), suggest that CLU oligomers are far from static. The physiological importance of these oligomeric assemblies (both CLU and sHsp) is largely unknown, but the leading hypothesis is that the smaller species (CLU monomers and sHsp dimers) are the most chaperone-active form, since these species exhibit increased surface hydrophobicity compared to larger assemblies (Van Montfort *et al.* 2002). In this model, the larger oligomers could serve as a circulating reservoir of 'activatable' chaperone. A similar idea has been proposed for α_2M, since the oxidation-derived dimeric form is (on a molar basis) a more effective chaperone compared to the native tetramer (Wyatt *et al.* 2014).

The binding of chaperones to misfolded proteins does not occur in an identical manner for all chaperones and client proteins. The range of stoichiometries of the interaction of CLU with Aβ oligomers could be well fitted by a uniform Gaussian distribution centred at CLU:Aβ = 1.3(±0.5):1. In contrast, the stoichiometries of association between CLU and αS were more variable. After a 6 h incubation, the interactions of CLU and α_2M with αS showed a similar distribution of stoichiometries. However, at 48 h CLU appeared to preferentially associate with high-FRET αS oligomers in a manner that α_2M did not. CLU also induced a structural change in αS oligomers, from low-FRET to high FRET conformations. This transition indicates that the fluorophores were less spatially separated, consistent with a compaction of the oligomer structure. This CLU-mediated compaction was distinct from the low to high-FRET conversion that occurs as part of the normal aggregation of αS, since these oligomers could still be observed. CLU is known to ameliorate the toxicity of oligomers, however less is known about the physiological relevance of the interaction between CLU and amyloid fibrils (the endpoint of some aggregation pathways). While the binding of CLU to αS fibrils may not be specific, once bound CLU significantly reduced the ability of αS fibrils to induce the intracellular generation of ROS but non-chaperone proteins did not. This data suggests a potential cytoprotective role for CLU in α-synucleinopathies, and indicates that the protective effects of CLU may be exerted at multiple steps along protein aggregation pathways.

Chapter 6:

Conclusions

6. Conclusions

As outlined in Chapter 1, protein aggregation and the formation of cytosolic protein inclusions is central to the pathology of a wide variety of debilitating human diseases. Despite this, the currently described methods for quantifying protein inclusions in mammalian cells are limited in either reliability or versatility. PulSA was initially employed in an attempt to enumerate cells containing TDP-43 inclusions, however the technique lacked the sensitivity required to identify cells with inclusions formed by any protein tested other than Htt^{46Q}-mCherry. FloIT was developed to answer these shortcomings, and allowed the detection of protein inclusions formed by every protein tested. The sole requirement of FloIT is that the aggregation-prone protein of interest must be fluorescently labelled. FloIT is a technique with significant advantages in terms of speed and precision compared with the widely used approach of manual counting of inclusions in cells by microscopy. For example, in addition to the time taken to capture the images, it may take ~10 min to manually count the number of inclusions in 100 transfected cells; FloIT typically takes 3 min to enumerate the inclusions from ~30,000 cells.

FloIT was used in Chapter 4 to identify CLU as the first known protein with the ability to ameliorate the effects of misfolded proteins both intracellularly and extracellularly. The intracellular effects of CLU appear to be ER stress-dependent, which is currently the only known treatment to induce CLU retrotranslocation (although the testing of other conditions has never been reported). As mentioned,

ER stress is a feature of many PDDs, including ALS, AD and PD so the retrotranslocation of CLU has the potential to impact on the pathology of many debilitating diseases (Katayama *et al.* 2004, Matus *et al.* 2013, Omura *et al.* 2013). The work presented here is the first time that the retrotranslocation of CLU has been demonstrated in neuronal cells. Additionally, CLU had never before been shown to impact upon the intracellular processing of a protein involved in a neurodegenerative disease. After retrotranslocation to the cytosol, CLU is likely to exert its effect via number of mechanisms, including binding misfolded TDP-43 via its well characterised chaperone action to prevent further aggregation. This was shown to occur using an *in vitro* aggregation assay with full length TDP-43-tGFP; additionally, CLU was physically associated with TDP-43^{M337V}-GFP in neuronal and astrocytic cell lysates. Thus, it appears likely that CLU can physically associate with misfolded TDP-43 in the cytosol. The physical interaction between CLU and client proteins typically results in the formation of stable, soluble complexes (Wyatt *et al.* 2009, Narayan *et al.* 2012). It is possible that as well as inhibiting the aggregation of TDP-43, the formation of complexes provides a means by which CLU can deliver the client proteins to cellular degradative pathways.

It has been shown that CLU is itself ubiquitinated and degraded by the proteasome in the cytosol (Nizard *et al.* 2007, Rizzi *et al.* 2009a). CLU was also reported to promote the proteasomal degradation of COMMD1 and I-κB (Zoubeidi *et al.* 2010b), an effect the authors suggested was due to CLU promoting the

ubiquitination of the target proteins through a stabilising effect on an E3 ubiquitin ligase. In addition to this action, if ubiquitinated CLU were to stably bind a misfolded client protein in the cytosol as suggested here, the proteasomal degradation of both proteins is likely to ensue. Thus, CLU may promote the proteasomal degradation of proteins such as TDP-43 by both upregulating the activity of ubiquitin ligases and physically delivering misfolded proteins to the proteasome. More recently, CLU has been shown to (i) upregulate autophagy by stabilising the LC3-Atg heterocomplex (Zhang *et al.* 2014), and (ii) enhance the lysosomal degradation of ATP7A and ATP7B through an unidentified pathway (Materia *et al.* 2011b, Materia *et al.* 2012). The work presented in Chapter 4 strongly implicates CLU as promoting the lysosomal degradation of misfolded proteins in neuronal cells via both chaperone-mediated autophagy and an interaction between CLU and LC3. Thus, several similarities can be noted between the involvement of cytosolic CLU in the UPS and autophagy, CLU: (i) appears to be degraded by both pathways, (ii) interacts with critical proteins to upregulate both pathways, and (iii) is likely to facilitate the direct degradation of misfolded proteins via both pathways. Taken together, the data presented in Chapter 4 suggests that the retrotranslocation of CLU to the cytosol allows CLU to inhibit the aggregation of client proteins, and supports previous reports that CLU influences both the UPS and autophagy-related processes to enhance the degradation of misfolded proteins in the cytosol.

In addition to the above roles of intracellular CLU in promoting the degradation of cytosolic misfolded proteins, CLU was shown to bind or incorporate into TDP-43^{M337V}-tGFP inclusions in astrocytic cells and TDP-CTF-eGFP inclusions in neuronal cells. It is not currently clear if this serves any physiological role, but there are several possibilities. In Chapter 5, CLU ameliorated the intracellular ROS generation induced by αS fibrils added exogenously to cells. This shows that CLU can bind to insoluble aggregates in a manner that inhibits potentially toxic effects. However, as mentioned in section 1.4.1.3, it is not clear whether TDP-43 inclusions are directly toxic. Additionally, Narayan *et al*. (2011) demonstrated that CLU promotes the dissociation of $A\beta_{1-40}$ fibrils and speculated that this is due to the fact that CLU-bound $A\beta_{1-40}$ oligomers that dissociate from the fibril have an inhibited ability to re-incorporate into the insoluble structure. It seems unlikely that this effect is specific to the interaction between CLU and Aβ, and could therefore apply to the effects of CLU on any insoluble protein deposit. A summary of the putative roles CLU may play in both intracellular and extracellular proteostasis is presented in Figure 6.1.

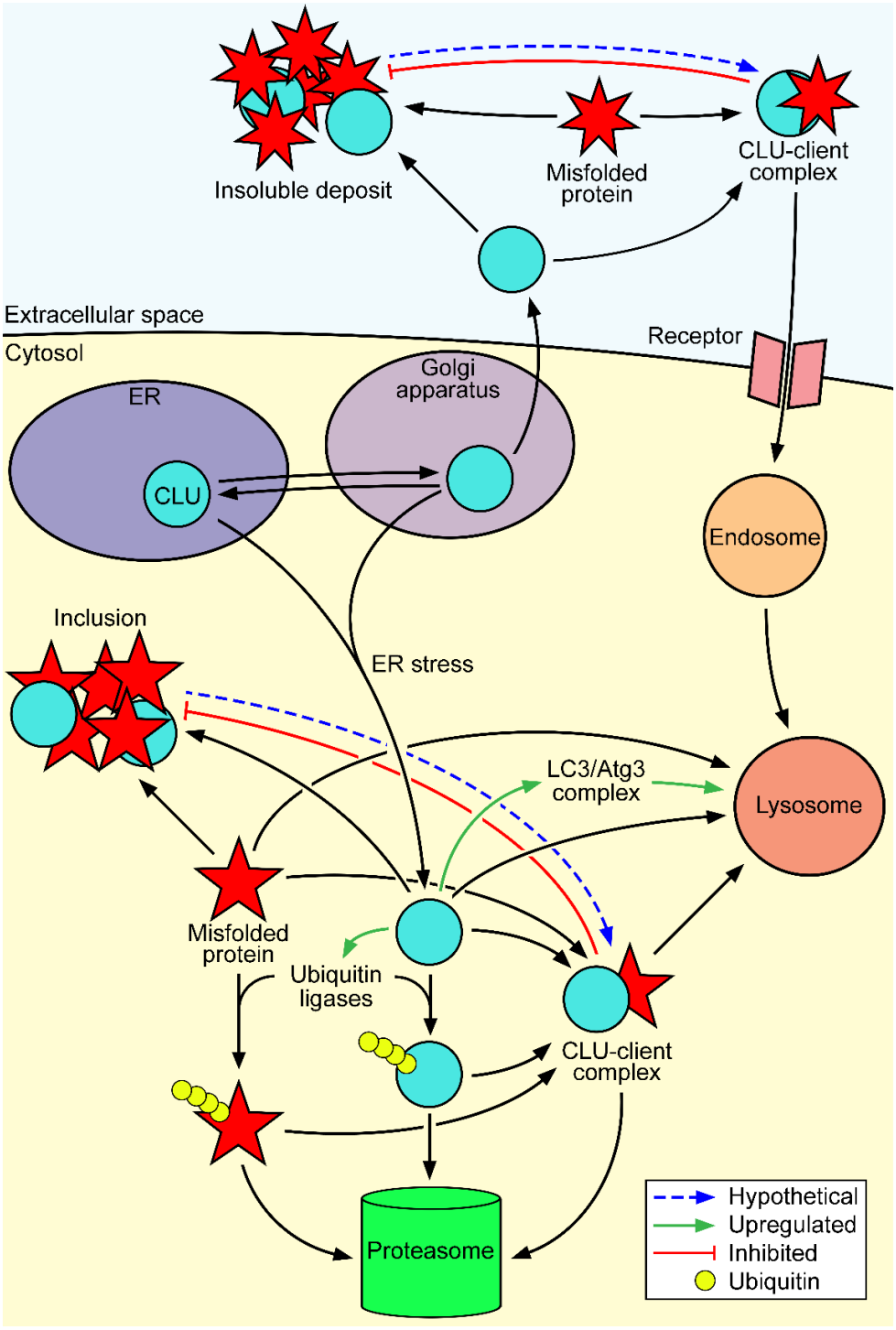

Figure 6.1: Putative roles of CLU in extra- and intracellular proteostasis. Under normal conditions CLU is post-translationally modified in the ER and Golgi apparatus before being secreted to the extracellular space. CLU can there bind misfolded client proteins, leading to their RME and subsequent lysosomal degradation. Extracellular CLU can also associate with insoluble deposits, reducing toxicity and possibly promoting their dissociation. Under ER stress, CLU can be retrotranslocated to the cytosol, where it upregulates an E3 ubiquitin ligase and stabilises LC3 to promote the activity of the UPS and autophagy, respectively. Cytosolic CLU is likely to interact with soluble misfolded proteins in the cytosol to promote both their chaperone-mediated autophagy and proteasomal degradation. CLU also associates with cytoplasmic protein inclusions and may affect these in similar ways to extracellular deposits.

As briefly mentioned in Chapter 4, compared to other cell types neurons have a limited ability to raise a heat shock response (Batulan *et al.* 2003), and therefore have a limited response to proteotoxic insult. Compounding this issue, under basal conditions, at least some of the sHsps are expressed in the cytosol of neurons at a lower level than in other cell types (Chen and Brown 2007). Therefore, the ability to recruit chaperones from other cellular compartments may be more critical in neurons. That being said, there is currently no reason to believe that the retrotranslocation of CLU is a tissue-specific phenomenon, and CLU is virtually ubiquitously expressed. This suggests that the putative protective effects of intracellular CLU detailed above are likely to be applicable in most tissues. Thus, while the work in Chapter 4 identified a possible role for CLU in ALS, CLU may act to help maintain intracellular proteostasis across a range of neurodegenerative and other diseases. It remains to be seen whether the retrotranslocation of CLU could be intentionally triggered to treat diseases associated with perturbations in intracellular proteostasis, where ER stress is either not present or not sufficient to promote translocation of CLU to the cytosol.

Soluble TDP-43 is extremely difficult to produce recombinantly, and thus could not be used for single molecule-level investigations of the interaction between CLU and misfolded client proteins. Rather, for reasons outlined in section 5.1, Aβ and αS were used. The stoichiometries of chaperone/client oligomers appear to be dependent upon the specific chaperone, client protein, as well as the conformation

of the misfolded client protein oligomer. The interactions between both CLU and α_2M and client proteins have been reported to be the result of an interaction between regions of exposed hydrophobicity on each of the proteins. Since the nature of this interaction is believed to be identical for both CLU and α_2M, it is not currently clear why CLU appears to bind certain large αS oligomers to a greater extent than other oligomers, whereas α_2M does not. Since α_2M is much larger than CLU, one possibility is that there is a physical limitation on the amount of α_2M that can associate with an oligomer. However, this is perhaps unlikely considering α_2M-rich oligomers containing αS or Aβ were observed (with α_2M:client stoichiometries up to approximately 5:1 and 20:1, respectively).

As mentioned above, it has been previously suggested that CLU (and other chaperones) inhibit protein aggregation by simply shielding exposed hydrophobic regions. The data presented here indicates that following association with αS oligomers, CLU mediates a structural compaction of the oligomer (as indicated by an increased FRET efficiency). This opens up the possibility that alongside the shielding of hydrophobic regions, a chaperone-induced structural conversion may render the client oligomer unable to associate with other oligomers, misfolded monomers or fibrils. If this structural compaction is irreversible even following dissociation of the chaperone-client complex, and hydrophobic regions remain less exposed to solution, then subsequent aggregation of the oligomers may be persistently inhibited. This effect could be particularly relevant for some of the

sHsps (such as αB-crystallin and Hsp27) which inhibit aggregation despite only transiently interacting with the client protein (rather than forming stable complexes like CLU and α_2M) (Bruinsma *et al.* 2011).

Like the extracellular counterparts in AD and PD, the exact role of intracellular protein aggregates in ALS pathology is not fully understood. However, it seems that protein aggregation is directly related to clinical severity (Pratt *et al.* 2014). It is currently unclear whether TDP-43-associated ALS is the result of the formation of toxic protein structures or the loss of soluble, normally functioning TDP-43 (and thus the dysregulation of RNA processing). Either case could be caused by the partitioning of TDP-43 into inclusion bodies, an abnormal process and an interesting therapeutic target. Through the use of FloIT and the work presented in Chapter 4, it is clear that CLU influences the intracellular processing of TDP-43, and that this activity is facilitated by the retrotranslocation of CLU to the cytosol, where it is likely to influence TDP-43 processing through (i) inhibiting protein aggregation via its chaperone activity, (ii) promoting ubiquitination of misfolded proteins, (iii) delivering misfolded proteins to the proteasome, (iv) upregulating autophagy, and (v) mediating delivery of misfolded proteins to lysosomes. The single molecule experimentation described in Chapter 5 provides some further insight into the mechanism of the chaperone action of CLU, which appears to underpin much of the protein's cytoprotective activity. It is hoped that a deeper understanding of the action of chaperones such as CLU will aid the future development of new therapies.

The results presented in this thesis support a novel protective intracellular role for CLU in ALS and perhaps other serious diseases, and uniquely positions CLU as the first protein identified with the capacity to protect cells from both intracellular and extracellular proteotoxicity.

Chapter 7:

References

7. References

Abel, O., J. F. Powell, P. M. Anderson and A. Al-Chalabi (2012). "ALSoD: A user-friendly online bioinformatics tool for amyotrophic lateral sclerosis genetics." Human Mutation **33**.

Afshar, N., B. E. Black and B. M. Paschal (2005). "Retrotranslocation of the chaperone calreticulin from the endoplasmic reticulum lumen to the cytosol." Molecular Cell Biology **25**.

Ahmad, M. F., B. Raman, T. Ramakrishna and C. M. Rao (2008). "Effect of phosphorylation on αB-crystallin: differences in stability, subunit exchange and chaperone activity of homo and mixed oligomers of αB-crystallin and its phosphorylation-mimicking mutant." Journal of Molecular Biology **375**.

Akopian, D., K. Shen, X. Zhang and S. Shan (2013). "Signal recognition particle: an essential protein-targeting machine." Annual Review of Biochemistry **82**.

Al-Chalabi, A., A. Durr, N. W. Wood, M. H. Parkinson, A. Camuzat, J. S. Hulot, K. E. Morrison, A. Renton, S. D. Sussmuth, B. G. Landwehrmeyer, A. Ludolph, Y. Agid, A. Brice, P. N. Leigh and G. Bensimon (2009). "Genetic variants of the alpha-synuclein gene SNCA are associated with multiple system atrophy." PLOS ONE **4**.

Albert, J. M., A. Gonzalez, P. P. Massion, H. Chen, S. J. Olson, Y. Shyr, R. Diaz, E. S. Lambright, A. Sandler, D. P. Carbone, J. B. Putnam Jnr, D. H. Johnson and B. Lu (2007). "Cytoplasmic clusterin expression is associated with longer survival in patients with resected non small cell lung cancer." Cancer Epidemiology, Biomarkers and Prevention **16**.

Ammar, H. and J. L. Closset (2008). "Clusterin activates survival through the phophatidlinositol 3-kinase/Akt pathway." The Journal of Biological Chemistry **283**.

Anderson, J. P., D. E. Walker, J. M. Goldstein, R. de Laat, K. Banducci, R. J. Caccavello, R. Barbour, J. Huang, K. Kling, M. Lee, L. Diep, P. S. Keim, X. Shen, T. Chataway, M. G. Schlossmacher, P. Seubert, D. Schenk, S. Sinha, W. P. Gai and T. J. Chilcote (2006). "Phosphorylation of Ser-129 is the dominant pathological modification of alpha-synuclein in familial and sporadic Lewy body disease." The Journal of Biological Chemistry **281**.

Anderson, P. and N. Kedersha (2009). "RNA granules: post-transcriptional and epigenetic modulators of gene expression." Nature Reviews Molecular Cell Biology **10**.

Aramburu, J., M. B. Yaffe, C. Lopez-Rodriguez, L. C. Cantley, P. G. Hogan and A. Rao (1999). "Affinity-driven peptide selection of an NFAT inhibitor more selective than cyclosporin A." Science **285**.

Arosio, P., T. P. J. Knowles and S. Linse (2015). "On the lag phase in amyloid fibril formation." Physical Chemistry Chemical Physics **17**.

Asea, A. and I. R. Brown, Eds. (2008). Heat Shock Proteins and the Brain: Implications for Neurodegenerative Diseases and Neuroprotection, Springer Science.

Axelrod, D. (2001). "Total internal reflection fluorescence microscopy in cell biology." Traffic **2**.

Bandyopadhyay, U., S. Kaushik, L. Varticovski and A. M. Cuervo (2008). "The chaperone-mediated autophagy receptor organizes in dynamic protein complexes at the lysosomal membrane." Molecular Cell Biology **28**.

Bandyopadhyay, U., S. Sridhar, S. Kaushik, R. Kiffin and A. M. Cuervo (2010). "Identification of regulators of chaperone-mediated autophagy." Molecular Cell **39**.

Baneyx, F. and B. L. Nannenga (2010). "Chaperones: A story of thrift unfolds." Nature Chemical Biology **6**.

Barmada, S. J., G. Skibinski, E. Korb, E. J. Rao, J. Y. Wu and S. Finkbeiner (2010). "Cytoplasmic mislocalization of TDP-43 is toxic to neurons and enhanced by a mutation associated with familial amyotrophic lateral sclerosis." The Journal of Neuroscience **30**.

Barrett, A. J. and P. M. Starkey (1973). "The interaction of alpha 2-macroglobulin with proteinases. Characteristics and specificity of the reaction, and a hypothesis concerning its molecular mechanism." Biochemical Journal **133**.

Bartl, M. M., T. Luckenbach, O. Bergner, O. Ullrich and C. Koch-Brandt (2001). "Multiple receptors mediate apoJ-dependent clearance of cellular debris into nonprofressional phagocytes." Experimental Cell Research **271**.

Basso, M., G. Samengo, G. Nardo, T. Massignan, G. D'Alessandro, S. Tartari, L. Cantoni, M. Marino, C. Cheroni, S. De Biasi, M. Teresa-Giordana, M. J. Strong, A. G. Estevez, M. Salmona, C. Bendotti and V. Bonetto (2009). "Characterization of detergent-insoluble proteins in ALS indicates a causal link between nitrative stress and aggregation in pathogenesis." PLOS ONE **4**.

Batulan, Z., G. A. Shinder, S. Minotti, B. P. He, M. M. Doroudchi, J. Nalbntoglu, M. J. Strong and H. D. Durham (2003). "High threshold for induction of the stress response in motor neurons is associated with failure to activate HSF1." The Journal of Neuroscience **23**.

Baumeister, P., S. Luo, W. C. Skarnes, G. Sui, E. Seto, Y. Shi and A. S. Lee (2005). "Endoplasmic reticulum stress induction of the Grp78/BiP promoter: activating mechanisms mediated by YY1 and its interactive chromatin modifiers." Molecular and Cellular Biology **25**.

Baumeister, W., J. Walz, F. Zühl and E. Seemüller (1998). "The proteasome: paradigm of a self-compartmentalizing protease." Cell **92**.

Bayon, Y., M. A. Ortiz, F. J. Lopez-Hernandez, P. H. Howe and F. J. Piedrafita (2004). "The retinoid antagonist MX781 induces clusterin expression in prostate cancer cells via heat shock factor-1 and activator protein-1 transcription factors." Cancer Research **64**.

Beaulieu, J.-M., M. D. Nguyen and J. P. Julien (1999). "Late onset death of motor neurons in mice overexpressing wild-type peripherin." The Journal of Biological Chemistry **147**.

Bendotti, C., M. Marino, C. Cheroni, E. Fontana, V. Crippa, A. Poletti and S. De Biasi (2012). "Dysfunction of constitutive and inducible ubiquitin-proteasome

system in amyotrophic lateral sclerosis: implication for protein aggregation and immune response." Progress in Neurobiology **97**.

Benesch, J. L. P., M. Ayoub, C. V. Robinson and J. A. Aquilina (2008). "Small heat shock protein activity is regulated by variable oligomeric substructure." The Journal of Biological Chemistry **283**.

Benilova, I., E. Karran and B. De Strooper (2012). "The toxic Aβ oligomer and Alzheimer's disease: an emperor in need of clothes." Nature Neuroscience **15**.

Bergink, S., F. A. Salomons, D. Hoogstraten, T. A. Groothuis, H. de Waard, J. Wu, L. Yuan, E. Citterio, A. B. Houtsmuller, J. Neefjes, J. H. Hoeijmakers, W. Vermeulen and N. P. Dantuma (2006). "DNA damage triggers nucleotide excision repair-dependent monoubiquitylation of histone H2A." Genes and Development **20**.

Blake, C. and L. Serpell (1996). "Synchrotron X-ray studies suggest that the core of the transthyretin amyloid fibril is a continuous β-helix." Structure **4**.

Blaschuk, O., K. Burdzy and I. B. Fritz (1983). "Purification and characterization of a cell-aggregating factor (clusterin), the major glycoprotein in ram rete testis fluid." The Journal of Biological Chemistry **258**.

Bohley, P. and P. O. Seglen (1992). "Proteases and proteolysis in the lysosome." Experientia **48**.

Borth, W. (1992). "α_2-Macroglobin, a multifunctional binding protein with targeting characteristics." The FASEB Journal **6**.

Bruinsma, I. B., K. A. Bruggink, K. Kinast, A. A. M. Versleijen, I. M. J. Segers-Nolten, V. Subramaniam, H. B. Kuiperij, W. Boelens, R. M. W. de Waal and M. M. Verbeek (2011). "Inhibition of α-synuclein aggregation by small heat shock proteins." Proteins: Structure, Function and Bioinformatics **10**.

Bucciantini, M., E. Giannoni, F. Chiti, F. Baroni, L. Formigli, J. Zurdo, N. Taddei, G. Ramponi, C. M. Dobson and M. Stefani (2002). "Inherent toxicity of aggregates implies a common mechanism for protein misfolding diseases." Nature **416**.

Bukau, B., J. Weissman and A. Horwich (2006). "Molecular chaperones and protein quality control." Cell **125**.

Buratti, E. and F. E. Baralle (2001). "Characterization and functional implications of the RNA binding properties of nuclear factor TDP-43, a novel splicing regulator of *CFTR* exon 9." The Journal of Biological Chemistry **276**.

Buratti, E. and F. E. Baralle (2008). "Multiple roles of TDP-43 in gene expression, splicing regulation, and human disease." Frontiers in Bioscience **13**.

Buratti, E., A. Brindisi, F. Pagani and F. E. Baralle (2004). "Nuclear factor TDP-43 binds to the polymorphic TG repeats in CFTR intron 8 and causes skipping of Exon 9: A functional link with disease penetrance." The American Journal of Human Genetics **74**.

Caccamo, A., S. Majunder, J. J. Deng, Y. Bai, F. B. Thornton and S. Oddo (2009). "Rapamycin rescues TDP-43 mislocalization and the associated low molecular mass neurofilament instability." The Journal of Biological Chemistry **284**.

Canevari, L., A. Y. Abramov and M. R. Duchen (2004). "Toxicity of amyloid beta peptide: tales of calcium, mitochondria and oxidative stress." Neurochemistry Research **29**.

Carrell, R. W. and B. Gooptu (1998). "Conformational changes and disease - serpins, prions and Alzheimer's." Curr Opin Struct Biol **8**.

Carrell, R. W. and D. A. Lomas (1997). "Conformational disease." Lancet **350**.

Cha-Molstad, H., K. S. Sung, J. Hwang, K. A. Kim, J. E. Yu, Y. D. Yoo, J. M. Jang, D. H. Han, M. Molstad, J. G. Kim, Y. J. Lee, A. Zakrzewska, S.-H. Kim, S. T. Kim, S. Y. Kim, H. G. Lee, N. K. Soung, J. S. Ahn, A. Ciechanover, B. Y. Kim and Y. T. Kwon (2015). "Amino-terminal arginylation targets endoplasmic reticulum chaperone BiP for autophagy through p62 binding." Nature Cell Biology **17**.

Chaires, J. B. (2008). "Calorimetry and thermodynamics in drug design." Annual Review of Biophysics **37**.

Chen, A. K., R. Y. Lin, E. Z. Hsieh, P. H. Tu, R. P. Chen, T. Y. Liao, W. Chen, C. H. Wang and J. J. Huang (2010). "Induction of amyloid fibrils by the C-terminal fragments of TDP-43 in amyotrophic lateral sclerosis." Journal of the American Chemical Society **132**.

Chen, S. and I. R. Brown (2007). "Neuronal expression of constitutive heat shock proteins: implications for neurodegenerative diseases." Cell Stress Chaperones **12**.

Chen, T., T. Turner, S. McCarthy, M. Scaltriti, S. Bettuzzi and T. J. Yeatman (2004). "Clusterin-mediated apoptosis is regulated by adenomatous polyposis coli and is p21 dependent but p53 independent." Cancer Research **64**.

Cheung, J. and T. M. Truskett (2005). "Coarse-grained strategy for modeling protein stability in concentrated solutions." Biophysical Journal **89**.

Chiti, F. and C. M. Dobson (2006). "Protein misfolding, functional amyloid, and human disease." Annual Review of Biochemistry **75**.

Choi, I., J. Kim, J.-Y. Park and S.-W. Kang (2013). "Cotransin induces accumulation of a cytotoxic clusterin variant that cotranslationally rerouted to the cytosol." Experimental Cell Research **319**.

Christianson, J. C. and Y. Ye (2014). "Cleaning up in the endoplasmic reticulum: ubiquitin in charge." Nature Structural and Molecular Biology **21**.

Ciechanover, A. (1994). "The ubiquitin-proteasome proteolytic pathway." Cell **79**.

Ciechanover, A. (2005). "Proteolysis: from the lysosome to ubiquitin and the proteasome." Nature Reviews Molecular Cell Biology **6**.

Clarke, R. W., A. Orte and D. Klenerman (2007). "Optimized threshold selection for single-molecule two-colour fluorescence coincidence spectroscopy." Analytical Chemistry **79**.

Coria, F., A. Moreno, I. Rubio, E. Morato, M. A. García and J. F. Mayor (1993). "The cellular pathology associated with Alzheimer β-amyloid deposits in non-demented aged individuals." Neuropathology and Applied Neurobiology **19**.

Crabb, J. W., M. Miyagi, X. Gu, K. Shadrach, K. A. West, H. Sakaguchi, M. Kamei, A. Hasan, L. Yan, M. E. Rayborn, R. G. Salomon and J. G. Hollyfield (2002). "Drusen proteome analysis: An approach to the etiology of age-related

macular degeneration." Proceedings of the National Academy of Sciences of the United States of America **99**.

Cremades, N., S. I. A. Cohen, E. Deas, A. Y. Abramoc, A. Y. Chen, A. Orte, M. Sandal, R. W. Clarke, P. Dunne, F. A. Aprile, C. W. Bertoncini, N. W. Wood, T. P. J. Knowles, C. M. Dobson and D. Klenerman (2012). "Direct observation of the interconversion of normal and toxic forms of a-synuclein." Cell **149**.

Crippa, V., D. Sau, P. Rusmini, A. Boncoraglio, E. Onesto, E. Bolzoni, M. Galbiati, E. Fontana, M. Marino, S. Carra, C. Bendotti, S. De Biasi and A. Poletti (2010). "The small heat shock protein B8 (HspB8) promotes autophagic removal of misfolded proteins involved in amyotrophic lateral sclerosis (ALS)." Human Molecular Genetics **19**.

Csermely, P. (2001). "Chaperone overload is a possible contributor to 'civilization diseases'." Trends in Genetics **17**.

Cuervo, A. M. and E. Wong (2014). "Chaperon-mediated autophagy: roles in disease and aging." Cell Research **24**.

Da Cruz, S. and D. W. Cleveland (2011). "Understanding the role of TDP-43 and FUS/TLS in ALS and beyond." Current Opinion in Neurobiology **21**.

Dahlgren, K. N., A. M. Manelli, W. B. Stine, L. K. Baker, G. A. Krafft and M. J. LaDu (2002). "Oligomeric and fibrillar species of amyloid-β peptides differentially affect neuronal viability." The Journal of Biological Chemistry **277**.

Danzer, K. M., W. P. Ruf, P. Putcha, D. Joyner, T. Hashimoto, C. Glabe, B. T. Hyman and P. J. McLean (2011). "Heat-shock protein 70 modulates toxic extracellular α-synuclein oligomers and rescues trans-synaptic toxicity." The FASEB Journal **25**.

Daub, A., P. Sharma and S. Finkbeiner (2009). "High-content screening of primary neurons: ready for prime time." Current Opinion in Neurobiology **19**.

de Silva, H. V., W. D. Stuart, W. D. Park, S. J. Mao, C. M. Gil, J. R. Wetterau, S. J. Busch and J. A. Harmony (1990). "Purification and characterization of apolipoprotein J." The Journal of Biological Chemistry **26**.

De Vos, W. H., L. Van Neste, B. Dieriks, G. H. Joss and P. Van Oostveldt (2010). "High content image cytometry in the context of subnuclear organization." Cytometry **77**.

Debure, L., J. Vayssière, V. Rincheval, F. Loison, Y. Le Dréan and D. Michel (2003). "Intracellular clusterin causes juxtanuclear aggregate formation and mitochondrial alteration." Journal of Cell Science **116**.

Deng, H. X., W. Chen, S. T. Hong, K. M. Boycott, G. H. Gorrie, N. Siddique, Y. Yang, F. Fecto, Y. Shi, H. Zhai, H. Jiang, M. Hirano, E. Rampersaud, G. H. Jansen, S. Donkervoort, E. H. Bigio, B. R. Brooks, K. Ajroud, R. Sufit, J. L. Haines, E. Mugnaini, M. A. Pericak-Vance and T. Siddique (2011). "Mutations in *UBQLN2* cause dominant X-linked juvenile and adult-onset ALS and ALS/dementia." Nature **477**.

Dickson, D. W., H. A. Crystal, C. Bevona, W. Honer, I. Vincent and P. Davies (1995). "Correlations of synaptic and pathological markers with cognition of the elderly." Neurobiology of Aging **16**.

Ding, W.-X., H.-M. Ni, W. Gao, Y.-F. Hou, M. A. Melan, X. Chen, D. B. Stolz, Z.-M. Shao and X.-M. Yin (2007). "Differential effects of endoplasmic reticulum stress-induced autophagy on cell survival." The Journal of Biological Chemistry **282**.

Dobson, C. M. (2003). "Protein folding and misfolding." Nature **426**.

Dukan, S., A. Farewell, M. Ballesteros, F. Taddei, M. Radman and T. Nyström (2000). "Protein oxidation in response to increased transcriptional or translational errors." Proceedings of the National Academy of Sciences of the United States of America **97**.

Dyson, H. J. and P. E. Wright (2005). "Intrinsically unstructured proteins and their functions." Nature Reviews Molecular Cell Biology **6**.

Ehrnsperger, M., J. Buchner and M. Gaestel (1997). Structure and function of small heat shock proteins. Molecular chaperones in Life cycle of proteins: structure, function and mode of action. A. L. Fink and Y. Goto. New York, Marcel Dekker**:** 533-575.

El-Agnaf, O. M., S. A. Salem, K. E. Paleologou, L. J. Cooper, N. J. Fullwood, M. J. Gibson, M. D. Curran, J. A. Court, D. M. Mann, S. Ikeda, M. R. Cookcon, J. Hardy and D. Allsop (2003). "Alpha-synuclein implicated in Parkinson's disease is present in extracellular biological fluids, including human plasma." The FASEB Journal **17**.

Ellis, R. J. and S. M. van der Vies (1991). "Molecular chaperones." Annual Review of Biochemistry **60**.

Englander, S. W. and L. Mayne (2014). "The nature of protein folding pathways." Science **111**.

Englander, S. W., L. Mayne and M. M. Krishna (2007). "Protein folding and misfolding: Mechanism and principles." Quarterly Reviews Biophysics **40**.

Essabbani, A., L. Garcia, M. J. Zonetti, T. Fisco, S. Pucci and G. Chiocchia (2013). "Exon-skipping strategy by ratio modulation between cytoprotective versus pro-apoptotic clusterin forms increased sensitivity of LNCaP to cell death." PLOS ONE **8**.

Fandrich, M. and C. M. Dobson (2002). "The behaviour of polyamino acids reveals an inverse side chain effect in amyloid structure formation." The EMBO Journal **21**.

Farg, M. A., K. Y. Soo, A. K. Walker, H. Pham, J. Orian, M. K. Horne, S. T. Warraich, K. L. Williams, I. P. Blair and J. D. Atkin (2012). "Mutant FUS induces endoplasmic reticulum stress in amyotrophic lateral sclerosis and interacts with protein disulfide-isomerase." Neurobiology of Aging **33**.

Farrawell, N. E., I. A. Lambert-Smith, S. T. Warraich, I. P. Blair, D. N. Saunders, D. M. Hatters and J. J. Yerbury (2015). "Distinct partitioning of ALS associated TDP-43, FUS and SOD1 mutants into cellular inclusions." Scientific Reports **5**.

Fiskum, G. (1985). "Intracellular levels and distribution of Ca2+ in digitonin-permeabilized cells." Cell Calcium **6**.

Forreiter, C. (2006). "Molecular chaperones: holding and folding." Progress in Botany **67**.

Förster, T. H. (1960). "Transfer mechanisms of electronic excitation energy." Radiation research **2**.

French, K., J. J. Yerbury and M. R. Wilson (2008). "Protease activation of α_2-macroglobulin modulates a chaperone-like action with broad specificity." Biochemistry **47**.

Frieboes, H. B., J. S. Huang, W. C. Yin and L. R. McNally (2014). "Chloroquine-mediated cell death in metastatic pancreatic adenocarcinoma through inhibition of autophagy." Journal of Oncology Practice **15**.

Fujita, E., Y. Kouroku, A. Isoai, H. Kumagai, A. Misutani, C. Matsuda, Y. K. Hayashi and T. Momoi (2007). "Two endoplasmic reticulum-associated degradation (ERAD) systems for the novel variant of the mutant dysferlin: ubiquitin/proteasome ERAD(I) and autophagy/lysosome ERAD(II)." Human Molecular Genetics **16**.

Gajdusek, D. C. and A. M. Salazar (1982). "Amyotrophic lateral sclerosis and parkinsonian syndromes in high incidence among the Auyu and Jakai people of West New Guinea." Neurology **32**.

Ganley, I. G., P. M. Wong, N. Gammoh and X. Jiang (2011). "Distinct autosomal-lysosomal fusion mechanism revealed by thapsigargin-induced autophagy arrest." Molecular Cell **42**.

Ghiso, J., E. Matsubara, A. Koudinov, N. H. Choi-Miura, M. Tomita, T. Wisniewski and B. Frangione (1993). "The cerebrospinal-fluid soluble form of Alzheimer's amyloid beta is complexed to SP-40,40 (apolipoprotein J), an inhibitor of the complement membrane-attack complex." Biochemical Journal **293**.

Gitcho, M. A., R. H. Baloh, S. Chakraverty, K. Mayo, J. B. Norton, D. Levitch, K. J. Hatanpaa, C. L. White, E. H. Bigio, R. Caselli, M. Baker, M. T. Al-Lozi, J. C. Morris, A. Pestronk, R. Rademakers, A. M. Goate and N. J. Cairns (2008). "*TDP-43* A315T mutation in familial motor neuron disease." Annals of Neurology **63**.

Goate, A., M.-C. Chartier-Harlin, M. Mullan, J. Brown, F. Crawford, L. Fidani, L. Giuffra, A. Haynes, N. Irving, L. James, R. Mant, P. Newton, K. Rooke, P. Roques, C. Talbot, M. Pericak-Vance, A. Roses, R. Williamson, M. Rossor, M. Owen and J. Hardy (1991). "Segregation of a missense mutation in the amyloid precursor protein gene with familial Alzheimer's disease." Nature **349**.

Goder, V. (2012). "Roles of ubiquitin in endoplasmic reticulum-associated protein degradation (ERAD)." Current Protein and Peptide Science **13**.

Gorman, M. W., E. O. Feigl and C. W. Buffington (2007). "Human plasma ATP concentration." Clinical Chemsitry **53**.

Gorman, P. M., C. M. Yip, P. E. Fraser and A. Chakrabartty (2003). "Alternate aggregation pathways of the Alzheimer β-amyloid peptide: Aβ association kinetics at endosomal pH." Journal of Molecular Biology **325**.

Gregory, J. M., T. P. Barros, S. Meehan, C. M. Dobson and L. M. Luheshi (2012). "The aggregation and neurotoxicity of TDP-43 and its ALS-associated 25 kDa fragment are differentially affected by molecular chaperones in *Drosophila*." PLOS ONE **7**.

Greten-Harrison, B., M. Polydoro, M. Morimoto-Tomita, L. Diao, A. M. Williams, E. H. Nie, S. Makani, B. Tian, P. E. Castillo, V. L. Buchman and S. S. Chandra (2010). "Alpha/beta/gamma-synuclein triple knock-out mice reveal age-dependent neuronal dysfunction." Proceedings of the National Academy of Sciences of the United States of America **107**.

Hamidi Asl, L., J. J. Liepnieks, T. Uemichi, J. M. Rebibou, E. Justrabo, D. Droz, C. Mousson, J. M. Chalopin, M. D. Benson, M. Delpech and G. Grateau (1997). "Renal amyloidosis with a frame shift mutation in fibrinogen Aα-chain gene producing a novel amyloid protein." Blood **90**.

Hammad, S. M., S. Ranganathan, E. Loukinova, W. O. Twal and W. S. Argraves (1997). "Interaction of apolipoprotein J-amyloid beta-peptide complex with low density lipoprotein receptor-related protein-2/megalin. A mechanism to prevent pathological accumulation of amyloid beta-peptide." The Journal of Biological Chemistry **272**.

Harold, D., R. Abraham, P. Hollingworth, R. Sims, A. Gerrish, M. L. Hamshere, J. S. Pahwa, V. Moskvina, K. Dowzell, A. Williams, N. Jones, C. Thomas, A. Stretton, A. R. Morgan, S. Lovestone, J. Powell, P. Proitsi, M. K. Lupton, C. Brayne, D. C. Rubinsztein, M. Gill, B. Lawlor, A. Lynch, K. Morgan, K. S. Brown, P. A. Passmore, D. Craig, B. McGuinness, S. Todd, C. Holmes, D. Mann, A. D. Smith, S. Love, P. G. Kehoe, J. Hardy, S. Mead, N. Fox, M. Rossor, J. Collinge, W. Maier, F. Jessen, B. Schurmann, R. Heun, H. van den Bussche, I. Heuser, J. Kornhuber, J. Wiltfang, M. Dichgans, L. Frolich, H. Hampel, M. Hull, D. Rujescu, A. M. Goate, J. S. K. Kauwe, C. Cruchaga, P. Nowotny, J. C. Morris, K. Mayo, K. Sleegers, K. Bettens, S. Engelborghs, P. P. De Deyn, C. Van Broeckhoven, G. Livingston, N. J. Bass, H. Gurling, A. McQuillin, R. Gwilliam, P. Deloukas, A. Al-Chalabi, C. E. Shaw, M. Tsolaki, A. B. Singleton, R. Guerreiro, T. W. Muhleisen, M. M. Nothen, S. Moebus, K.-H. Jockel, N. Klopp, H. E. Wichmann, M. M. Carrasquillo, V. S. Pankratz, S. G. Younkin, P. A. Holmans, M. O'Donovan, M. J. Owen and J. Williams (2009). "Genome-wide association study identifies variants at CLU and PICALM associated with Alzheimer's disease." Nature Genetics **41**.

Hartl, F. U., A. Bracher and M. Hayer-Hartl (2011). "Molecular chaperones in protein folding and proteostasis." Nature **475**.

Hartl, F. U. and M. Hayer-Hartl (2002). "Molecular chaperones in the cytosol: from nascent chain to folded protein." Science **295**.

Hentati, A., K. Bejaoui, M. A. Pericak-Vance, F. Hentati, M. C. Speer, W.-Y. Hung, D. A. Figlewicz, J. L. Haines, J. Rimmler, C. B. Hamida, M. B. Hamida, R. H. Brown Jr and T. Siddique (1994). "Linkage of recessive familial amyotrophic lateral sclerosis to chromosome 2q33-q35." Nature Genetics **7**.

Hetz, C. (2012). "The unfolded protein response: controlling cell fate decisions under ER stress and beyond." Nature Reviews Molecular Cell Biology **13**.

Hochgrebe, T., G. J. Pankhurst, J. Wilce and S. B. Easterbrook-Smith (2000). "pH-dependent changes in the in vitro ligand-binding properties and structure of human clusterin." Biochemistry **39**.

Hoepken, H.-H., S. Gispert, M. Azizov, M. Klinkenberg, F. Ricciardi, A. Kurz, B. Morales-Gordo, M. Bonin, O. Riess, R. Gasser, D. Kogel, H. Steinmetz and G. Auburger (2008). "Parkinson patient fibroblasts show increased alpha-synuclein expression." Experimental Neurology **212**.

Horrocks, M. H. (2013). Development of single-molecule techniques to study the aggregation of α-synuclein, University of Cambridge.

Horrocks, M. H., L. Rajah, P. Jönsson, M. Kjaergaard, M. Vendruscolo, T. P. J. Knowles and D. Klenerman (2013). "Single-Molecule Measurements of Transient Biomolecular Complexes through Microfluidic Dilution." Analytical Chemistry **85**.

Hu, W., Z.-Y. Kan, L. Mayne and S. W. Englander (2016). "Cytochrome C folds through foldon-dependent native-like intermediates in an ordered pathway." Proceedings of the National Academy of Sciences of the United States of America **113**.

Huber, L. A., K. Pfaller and I. Vietor (2003). "Organelle proteomics: implications for subcellular fractionation in proteomics." Circulation Research **92**.

Humphreys, D. T., M. R. Wilson, J. A. Carver and S. B. Easterbrook-Smith (1999). "Clusterin has chaperone-like activity similar to that of small heat shock proteins." The Journal of Biological Chemistry **274**.

Jackson, S. E. (1998). "How do small single-domain proteins fold?" Folding and Design **3**.

Jackson, S. E. and A. R. Fersht (1991). "Folding of chymotrypsin inhibitor 2: evidence for a two-state transition." Biochemistry **30**.

Jang, H., L. Connelly, F. T. Arce, S. Ramachandran, B. L. Kagan, R. Lal and R. Nussinov (2013). "Mechanisms for the insertion of toxic, fibril-like beta-amyloid oligomers into the membrane." Journal of Chemical Theory and Computation **9**.

Jansen, G. H., P. Maattanen, A. Y. Denisov, L. Scarffe, B. Schade, H. Balghi, K. Dejgaard, L. Y. Chen, W. J. Muller, K. Gehring and D. Y. Thomas (2012). "An Interaction Map of Endoplasmic Reticulum Chaperones and Foldases." Molecular & Cellular Proteomics **11**.

Jarrett, J. T. and P. T. Lansbury (1993). "Seeding one-dimensional crystallization of amyloid - a pathogenic mechanism in Alzheimer's disease and scrapie." Cell **73**.

Jenco, J. M., A. Rawlingson, B. Daniels and A. J. Morris (1998). "Regulation of phospholipase D2: selective inhibtion of mammalian phospholipase D isoenzymes by α- and β-synucleins." Biochemistry **37**.

Jenner, P. (2003). "Oxidative stress in Parkinson's disease." Annals of Neurology **53**.

Ji, S.-R., Y. Wu and S.-F. Sui (2002). "Study of β-Amyloid Peptide (Aβ40) Insertion into Phospholipid Membranes Using Monolayer Technique." Biochemistry (Moscow) **7**.

Jin, G. and P. H. Howe (1999). "Transforming growth factor beta regulates clusterin gene expression via modulation of trancription facto c-Fos." European Journal of Biochemistry **263**.

Johnston, J. A., M. J. Dalton, M. E. Gurney and R. R. Kopito (2000). "Formation of high molecular weight complexes of mutant Cu,Zn-superoxide dismutase

in a mouse model for familial amyotrophic lateral sclerosis." Proceedings of the National Academy of Sciences of the United States of America **97**.

Kapuy, O., P. K. Vinod and G. Bánhegyi (2014). "mTOR inhibition increases cell viability via autophagy induction during endoplasmic reticulum stress - An experimental and modeling study." FEBS Open Bio **4**.

Katayama, T., K. Imaizumi, T. Manabe, J. Hitomi, T. Kudo and M. Tohyama (2004). "Induction of neuronal death by ER stress in Alzheimer's disease." Journal of Chemical Neuroanatomy **28**.

Kaushik, S. and A. M. Cuervo (2015). "Proteostasis and aging." Nature Medicine **21**.

Kayed, R., E. Head, J. L. Thompson, T. M. McIntire, S. C. Milton, C. W. Cotman and C. G. Glabe (2003). "Common structure of soluble amyloid oligomers implies common mechanism of pathogenesis." Science **300**.

Kayed, R. and C. A. Lasagna-Reeves (2013). "Molecular mechanisms of amyloid oligomers toxicity." Journal of Alzheimer's Disease **33**.

Kelly, J. W. (1996). "Alternative conformations of amyloidogenic proteins govern their behavior." Curr Opin Struct Biol **6**.

Kelly, J. W. (2003). "Amyloid as a natural product." The Journal of Cell Biology **161**.

Kerppola, T. K. (2006). "Design and implementation of bimolecular fluorescence complementation (BiFC) assays for the visualization of protein interactions in living cells." Nature Protocols **1**.

Kim, J. H., J. H. Kim, H. O. Jun, Y. S. Yu, B. H. Min, K. H. Park and K.-W. Kim (2010). "Protective effect of clusterin from oxidative stress-induced apoptosis in human retinal pigment epithelial cells." Retinal Cell Biology **51**.

Kim, N., J. C. Yoo, J. Y. Han, E. M. Hwang, Y. S. Kim, E. Y. Jeong, C. H. Sun, G. S. Yi, G. S. Roh, H. Y. Kim, S. S. Kang, G. J. Cho, J.-Y. Park and W. S. Choi (2012). "Human nuclear clusterin mediates apoptosis by interacting with Bcl-XL through C-terminal coiled coil domain." Journal of Cellular Physiology **227**.

Kim, V. N., J. Han and M. C. Siomi (2009). "Biogenesis of small RNAs in animals." Nature Reviews Molecular Cell Biology **10**.

Kirszbaum, L., S. E. Bozas and W. I. D. (1992). "SP-40,40, a protein involved in the control of the complement pathway, possesses a unique array of disulphide bridges." FEBS Letters **297**.

Kolodziej, S. J., T. Wagenknecht, D. K. Strickland and J. K. Stoops (2002). "The Three-dimensional Structure of the Human alpha 2-Macroglobulin Dimer Reveals Its Structural Organization in the Tetrameric Native and Chymotrypsin alpha 2-Macroglobulin Complexes." J. Biol. Chem. **277**.

Komatsu, M., S. Waguri, T. Chiba, S. Murata, J.-I. Iwata, I. Tanida, T. Ueno, M. Koike, Y. Uchiyama, E. Kominami and K. Tanaka (2006). "Lossof autophagy in the central nervous system causes neurodegeneration in mice." Nature **441**.

Kounnas, M. Z., E. B. Loukinova, S. Stefansson, J. A. Harmony, B. H. Brewer, D. K. Strickland and W. S. Argraves (1995). "Identification of glycoprotein 220 as an endocytic receptor for apolipoprotein J/clusterin." Journal of Biological Chemistry **2**.

Kuo, P. H., L. G. Doudeva, Y. T. Wang, C. K. J. Shen and H. S. Yuan (2009). "Structural insights into TDP-43 in nucleic-acid binding and domain interactions." Nucleic Acids Research **37**.

Kurland, L. T. and D. W. Mulder (1955). "Epidemiologic investigations of amyotrophic lateral sclerosis. 2. Familial aggregations indicative of dominant inheritance." Neurology **5**.

Kuzuhara, S., Y. Kokubo, R. Sasaki, Y. Narita, T. Yabana, M. Hasegawa and T. Iwatsubo (2001). "Familial amyotrophic lateral sclerosis and parkinsonism-dementia complex of the Kii Peninsula of Japan: clinical and neuropathological study and tau analysis." Annals of Neurology **49**.

Kwiatkowski Jr, T. J., D. A. Bosco, A. L. LeClerc, E. Tamrazian, C. R. Vanderburg, C. Russ, A. Davis, J. Gilchrist, E. J. Kasarskis, T. Munsat, P. Valdmanis, G. A. Rouleau, B. A. Hosler, P. Cortelli, P. J. de Jong, Y. Yoshinaga, J. L. Haines, M. A. Pericak-Vance, J. Yan, N. Ticozzi, T. Siddique, D. McKenna-Yasek, P. C. Sapp, H. R. Horvitz, J. E. Landers and R. H. Brown Jr (2009). "Mutations in the *FUS/TLS* gene on chromosome 16 cause familial amyotrophic lateral sclerosis." Science **323**.

Lagier-Tourenne, C., M. Polymenidou and D. W. Cleveland (2010). "TDP-43 and FUS/TLS:emerging roles in RNA processing and neurodegeneration." Human Molecular Genetics **19**.

Lambert, J.-C., S. Heath, G. Even, D. Campion, K. Sleegers, M. Hiltunen, O. Combarros, D. Zelenika, M. J. Bullido, B. Tavernier, L. Letenneur, K. Bettens, C. Berr, F. Pasquier, N. Fievet, P. Barberger-Gateau, S. Engelborghs, P. De Deyn, I. Mateo, A. Franck, S. Helisalmi, E. Porcellini, O. Hanon, M. M. de Pancorbo, C. Lendon, C. Dufouil, C. Jaillard, T. Leveillard, V. Alvarez, P. Bosco, M. Mancuso, F. Panza, B. Nacmias, P. Bossu, P. Piccardi, G. Annoni, D. Seripa, D. Galimberti, D. Hannequin, F. Licastro, H. Soininen, K. Ritchie, H. Blanche, J.-F. Dartigues, C. Tzourio, I. Gut, C. Van Broeckhoven, A. Alperovitch, M. Lathrop and P. Amouyel (2009). "Genome-wide association study identifies variants at CLU and CR1 associated with Alzheimer's disease." Nature Genetics **41**.

Lambert, M. P., A. K. Barlow, B. A. Chromy, C. Edwards, R. Freed, M. Liosatos, T. E. Morgan, I. Rozovsky, B. Trommer, K. L. Viola, P. Wals, C. Zhang, C. E. Finch, G. A. Krafft and W. L. Klein (1998). "Diffusible, nonfibrillar ligands derived from Aβ(1–42) are potent central nervous system neurotoxins." Proceedings of the National Academy of Sciences of the United States of America **95**.

Lasagna-Reeves, C. A., C. Glabe and R. Kayed (2011). "Amyloid-beta annular protofibrils evade fibrillar fate in Alzheimer disease brain." Journal of Biological Chemistry **286**.

Lecker, S., R. Lill, T. Ziegelhoffer, C. Georgopoulos, J. P. J. Bassford, C. A. Kumamoto and W. Wickner (1989). "Three pure chaperone proteins of *Escherichia coli* - SecB, trigger factor and GroEL - form soluble complexes with precursor proteins *in vitro*." The EMBO Journal **8**.

Lee, J. P., C. Gerin, V. P. Bindokas, R. Miller, G. Ghadge and R. P. Roos (2002). "No correlation between aggregates of Cu/Zn superoxide dismutase and cell

death in familial amyotrophic lateral sclerosis." Journal of Neurochemistry **82**.

Leeb, C., C. Eresheim and J. Nimpf (2014). "Clusterin Is a Ligand for Apolipoprotein E Receptor 2 (ApoER2) and Very Low Density Lipoprotein Receptor (VLDLR) and Signals via the Reelin-signaling Pathway." Journal of Biological Chemistry **289**.

Levinthal, C. (1968). "Are there pathways for protein folding?" Journal of Chemical Physics **65**.

Li, L., X. Zhang and W. Le (2009). "Altered macroautophagy in the spinal cord of SOD1 mutant mice." Autophagy **4**.

Li, N., A. Zoubeidi, E. Beraldi and M. E. Gleave (2013). "GRP78 regulates clusterin stability, retrotranslocation and mitochondrial localization under ER stress in prostate cancer." Oncogene **32**.

Liu-Yesucevitz, L., A. Bilgutay, Y. J. Zhang, T. Vanderweyde, A. Citro, T. Mehta, N. Zaarur, A. McKee, R. Bowser, M. Sherman, L. Petrucelli and B. Wolozin (2010). "Tar DNA binding protein-43 (TDP-43) associates with stress granules: analysis of cultured cells and pathological brain tissue." PLOS ONE **5**.

Liu, S.-Q., X.-L. Ji, Y. Tao, D.-Y. Tan, K.-Q. Zhang and Y.-X. Fu (2014). "Protein folding, binding and energy landscape: a synthesis." Biochemistry **15**.

Lue, L.-F., Y.-M. Kuo, A. E. Roher, L. Brachova, Y. Shen, L. Sue, T. Beach, J. H. Kurth, R. E. Rydel and J. Rogers (1999). "Soluble amyloid β peptide concentration as a predictor of synaptic change in Alzheimer's disease." The American Journal of Pathology **155**.

Maguire, O., K. M. Tornatore, K. L. O'Loughlin, R. C. Venuto and H. Minderham (2013). "Nuclear translocation of nuclear factor of activated T cells (NFAT) as a quantitative pharmacodynamic parameter for tacrolimus." Cytometry **83**.

Maifeld, S. V., A. L. MacKinnon, J. L. Garrison, A. Sharma, E. J. Kunkel, R. S. Hedge and J. Taunton (2011). "Secretory protein profiling reveals TNF-α inactivation by selective and promiscuous Sec61 modulators." Chemistry and Biology **18**.

Maity, H., M. Maity, M. M. Krishna, L. Mayne and S. W. Englander (2005). "Protein folding: The stepwise assembly of foldon units." Proceedings of the National Academy of Sciences of the United States of America **102**.

Malagelada, C., Z. H. Jin, V. Jackson-Lewis, S. Przedborski and L. A. Greene (2010). "Rapamycin protects against neuron death in *in vitro* and *in vivo* models of Parkinson's disease." Journal of Neuroscience **30**.

Mann, D. M., T. Iwatsubo, Y. Ihara, N. J. Cairns, P. L. Lantos, N. Bogdanovic, L. Lannfelt, B. Winblad, M. L. Maat-Schieman and M. N. Rossor (1996). "Predominant deposition of amyloid-beta 42(43) in plaques in cases of Alzheimer's disease and hereditary cerebral hemorrhage associated with mutations in the amyloid precursor protein gene." The American Journal of Pathology **148**.

Mannini, B., R. Cascella, M. Zampagni, M. van Waarde-Verhagen, S. Meehan, C. Roodveldt, S. Campioni, M. Boninsegna, A. Penco, A. Relini, H. H.

Kampinga, C. M. Dobson, M. R. Wilson, C. Cecchi and F. Chiti (2012). "Molecular mechanisms used by chaperones to reduce the toxicity of aberrant protein oligomers." Proceedings of the National Academy of Sciences of the United States of America **109**.

Marques, O. and T. F. Outeiro (2012). "Alpha-synuclein: from secretion to dysfunction and death." Cell Death and Disease **3**.

Marrero, A., S. Duquerroy, S. Trapani, T. Goulas, T. Guevara, G. R. Andersen, J. Navaza, L. Sottrup-Jensen and F. X. Gomis-Rüth (2012). "The crystal structure of human alpha-2-macroglobulin reveals a unique molecular cage." Angewandte Chemie International Edition **51**.

Martin-Rehrmann, M. D., H. S. Hoe, E. M. Capuani and G. W. Rebeck (2005). "Association of apolipoprotein J-positive beta-amyloid plaques with dystrophic neurites in Alzheimer's disease brain." Neurotoxicity Research **7**.

Materia, S., M. A. Cater, L. W. J. Klomp, J. F. B. Mercer and S. La Fontaine (2011a). "Clusterin (Apolipoprotein J), a molecular chaperone that facilitates degradation of the copper-ATPases ATP7A and ATP7B." Journal of Biological Chemistry **286**.

Materia, S., M. A. Cater, L. W. J. Klomp, J. F. B. Mercer and S. La Fontaine (2011b). "Clusterin (Apolipoprotein J), a molecular chaperone that facilitates degradation of the copper-ATPases ATP7A and ATP7B." The Journal of Biological Chemistry **286**.

Materia, S., M. A. Cater, L. W. J. Klomp, J. F. B. Mercer and S. La Fontaine (2012). "Clusterin and COMMD1 independently regulate degradation of the mammalian copper ATPases ATP7A and ATP7B." Journal of Biological Chemistry **287**.

Matsubara, E., B. Frangione and J. Ghiso (1995). "Characterization of apolipoprotein J-Alzheimer's Aβ Interaction." The Journal of Biological Chemistry **270**.

Matthijs, G., K. Devriendt, J. J. Cassiman, H. Van den Berghe and P. Marynen (1992a). "Structure of the human alpha-2-macroglobulin gene and its promotor." Biochemical and Biophysical Research Communications **184**.

Matthijs, G., K. Devriendt, J. J. Cassiman, H. Van den Berghe and P. Marynen (1992b). "Structure of the human alpha-2-macroglobulin gene and its promotor." Biochem. Biophys. Res. Commun. **184**.

Matus, S., V. Valenzuela, D. B. Medinas and C. Hetz (2013). "ER dysfunction and protein folding stress in ALS." International Journal of Cell Biology **2013**.

McGuire, V., W. T. Longstreth Jr, T. D. Koepsell and G. van Belle (1996). "Incidence of amyotrophic lateral sclerosis in three counties in western Washington state." Neurology **47**.

Meusser, B., C. Hirsch, E. Jarosch and T. Sommer (2005). "ERAD: the long road to destruction." Nature Cell Biology **7**.

Michel, D., G. Chatelain, S. North and G. Brun (1997). "Stress-induced transcription of the clusterin/apoJ gene." Biochemical Journal **328**.

Milanesi, L., T. Sheynis, W.-F. Xue, E. V. Orlova, A. L. Hellewell, R. Jelinek, E. W. Hewitt, S. E. Radford and H. R. Saibil (2012). "Direct three-dimensional

visualization of membrane disruption by amyloid fibrils." Proceedings of the National Academy of Sciences of the United States of America **109**.

Minter, M. R., J. M. Taylor and P. J. Crack (2016). "The contribution of neuroinflammation to amyloid toxicity in Alzheimer's disease." Journal of Neurochemistry **136**.

Mizushima, N., Y. Ohsumi and T. Yoshimori (2002). "Autophagosome formation in mammalian cells." Cell Structure and Function **27**.

Morimoto, N., M. Nagai, Y. Ohta, K. Miyazaki, T. Kurata, M. Morimoto, T. Murukami, Y. Takehisa, Y. Ikeda, T. Kamiyu and K. Abe (2007). "Increased autophagy in transgenic mice with a *G93A* mutant *SOD1* gene." Brain Research **1167**.

Morkuniene, R., P. Cizas, S. Jankeviciute, R. Petrolis, O. Arandarcikaite, A. Krisciuaitis and V. Borutaite (2015). "Small Abeta1-42 oligomer-induced membrane depolarization of neuronal and microglial cells: role of N-methyl-D-aspartate receptors." Journal of Neuroscience Research **93**.

Murphy, B. F., L. Kirszbaum, I. D. Walker and A. J. d'Apice (1988). "SP-40,40, a newly identified normal human serum protein found in the SC5b-9 complex of complement and in the immune deposits in glomerulonephritis." Journal of Clinical Investigation **81**.

Murphy, M. P. and H. LeVine (2010). "Alzheimer's disease and the β-amyloid peptide." Journal of Alzheimer's Disease **19**.

Murphy, R. R., G. Danezis, M. H. Horrocks, S. E. Jackson and D. Klenerman (2014). "Bayesian inference of accurate population sizes and FRET efficiencies from single diffusing biomolecules." Analytical Chemistry **86**.

Narayan, P., A. Orte, R. W. Clarke, B. Bolognesi, S. Hook, K. A. Ganzinger, S. Meehan, M. R. Wilson, C. M. Dobson and D. Klenerman (2012). "The extracellular chaperone clusterin sequesters oligomeric forms of the amyloid-β 1-40 peptide." Nature Structural and Molecular Biology **19**.

Neumann, M., L. K. Kwong, E. B. Lee, E. Kremmer, A. Flatley, Y. Xu, M. S. Forman, D. Troost, H. A. Kretzschmar, J. Q. Trojanowski and V. M. Y. Lee (2009). "Phosphorylation of S409/410 of TDP-43 is a consistent feature in all sporadic and familial forms of TDP-43 proteinopathies." Acta Neuropathologica **117**.

Neumann, M., D. M. Sampathu, L. K. Kwong, A. C. Truax, M. C. Micsenyi, T. T. Chou, J. Bruce, T. Schuck, M. Grossman, C. M. Clark, L. F. McCluskey, B. L. Miller, E. Masliah, I. R. Mackenzie, H. Feldman, W. Feiden, H. A. Kretzschmar, J. Q. Trojanowski and V. M. Y. Lee (2006). "Ubiquitinated TDP-43 in frontotemporal lobar degeneration and amyotrophic lateral sclerosis." Science **314**.

Nie, S., D. T. Chiu and R. N. Zare (1994). "Probing individual molecules with confocal fluorescence microscopy." Science **266**.

Nishitoh, H., H. Kadowaki, A. Nagai, T. Maruyama, T. Yokota, H. Fukutomi, T. Noguchi, A. Matsuzawa, K. Takeda and H. Ichijo (2008). "ALS-linked mutant SOD1 induces ER stress- and ASK1-dependent motor neuron death by targeting Derlin-1." Genes and Development **22**.

Nizard, P., S. Tetley, Y. Le Dréan, T. Watrin, P. Le Goff, M. R. Wilson and D. Michel (2007). "Stress-induced retrotranslocation of clusterin/ApoJ into the cytosol." Traffic **8**.

O'Bryan, M. K., H. W. Baker, J. R. Saunders, L. Kirszbaum, I. D. Walker, P. Hudson, D. Y. Liu, M. D. Glew, A. J. d'Apice and B. F. Murphy (1990). "Human seminal clusterin (SP-40,40) isolation and characterization." Journal of Clinical Investigation **85**.

Oda, T., P. Wals, H. H. Osterburg, S. A. Johnson, G. M. Pasinetti, T. E. Morgan, I. Rozovsky, W. B. Stine, S. W. Snyder, T. F. Holzman, G. A. Krafft and C. E. Finch (1995). "Clusterin (apoJ) alters the aggregation of amyloid β-Peptide (Aβ1-42) and forms slowly sedimenting Aβ complexes that cause oxidative stress." Experimental Neurology **136**.

Omura, T., M. Kaneko, Y. Okuma, K. Matsubara and Y. Nomura (2013). "Endoplasmic reticulum stress and Parkison's disease: the role of HRD1 in averting apoptosis in neurodegenerative disease." Oxidative Medicine and Cellular Longevity **2013**.

Ota, T., Y. Suzuki, T. Nishikawa, T. Otsuki, T. Sugiyama, R. Irie, A. Wakamatsu, K. Hayashi, H. Sato, K. Nagai, K. Kimura, H. Makita, M. Sekine, M. Obayashi, T. Nishi, T. Shibahara, T. Tanaka, S. Ishii and S. Sugano (2004). "Complete sequencing and characterisation of 21,243 full-length human cDNAs." Nature Genetics **36**.

Parker, S. J., J. Meyerowitz, J. L. James, J. R. Liddell, P. J. Crouch, K. M. Kanninen and A. R. White (2012). "Endogenous TDP-43 localized to stress granules can subsequently form protein aggregates." Neurochemistry International **60**.

Picariello, G., P. Ferranti, G. Mamone, P. Roepstorff and F. Addeo (2008). "Identification of N-linked glycoproteins in human milk by hydrophilic interaction liquid chromatography and mass spectrometry." Proteomics **8**.

Plomp, P. J., E. J. Wolvetang, A. K. Groen, A. J. Meijer, P. B. Gordon and P. O. Seglen (1987). "Energy dependence of autophagic protein degradation in isolated rat hepatocytes." European Journal of Biochemistry **1**.

Plotkin, S. S. and J. N. Onuchic (2002). "Understanding protein folding with energy landscape theory - part I: basic concepts." Quarterly Reviews of Biophysics **35**.

Polihronis, M., K. Paizis, G. Carter, L. Sedal and B. Murphy (1993). "Elevation of human cerebrospinal fluid clusterin concentration is associated with acute neuropathology." Journal of the Neurological Sciences **115**.

Polymenidou, M., C. Lagier-Tourenne, K. R. Hutt, S. C. Huelga, J. Moran, T. Y. Liang, S. C. Ling, E. Sun, E. Wancewicz, C. Mazur, H. Kordasiewicz, Y. Sedaghat, J. P. Donohue, L. Shiue, C. F. Bennett, G. W. Yeo and D. W. Cleveland (2011). "Long pre-mRNA depletion and RNA missplicing contribute to neuronal vulnerability from loss of TDP-43." Nature Neuroscience **14**.

Polymeropoulos, M. H., C. Lavedan, E. Leroy, S. E. Ide, A. Dehejia, A. Dutra, B. Pike, H. Root, J. Rubenstein, R. Boyer, E. S. Stenroos, S. Chandrasekharappa, A. Athanassiadou, T. Papapetropoulos, W. G. Johnson, A. M. Lazzarini, R. C. Duvoisin, G. Di Iorio, L. I. Golbe and R. L. Nussbaum (1997). "Mutation in

the alpha-synuclein gene identified in families with Parkinson's disease." Science **27**.

Poon, S., S. B. Easterbrook-Smith, M. S. Rybchyn, J. A. Carver and M. R. Wilson (2000). "Clusterin is an ATP−independent chaperone with very broad substrate specificity that stabilizes stressed proteins in a folding-competent state." Biochemistry **39**.

Poon, S., M. S. Rybchyn, S. B. Easterbrook-Smith, J. A. Carver, G. J. Pankhurst and M. R. Wilson (2002a). "Mildly acidic pH activates the extracellular molecular chaperone clusterin." The Journal of Biological Chemistry **227**.

Poon, S., T. M. Treweek, M. R. Wilson, S. B. Easterbrook-Smith and J. A. Carver (2002b). "Clusterin is an extracellular chaperone that specifically interacts with slowly aggregating proteins on their off-folding pathway." FEBS Letters **513**.

Pospichalova, V., J. Svoboda, Z. Dave, A. Kotrbova, K. Kaiser, D. Klemova, L. Ilkovics, A. Hampl, I. Crha, E. Jandakova, L. Minar, V. Weinberger and V. Bryja (2015). "Simplified protocol for flow cytometry analysis of fluorescently labeled exosomes and microvesicles using dedicated flow cytometer." Journal of Extracellular Vesicles **4**.

Pratt, A. J., D. S. Shin, G. E. Merz, R. P. Rambo, W. A. Lancaster, K. N. Dyer, P. P. Borbat, F. L. Poole II, M. W. W. Adams, J. H. Freed, B. R. Crane, J. A. Tainer and E. D. Getzoff (2014). "Aggregation propensities of superoxide dismutase G93 hotspot mutants mirror ALS clinical phenotypes." Proceedings of the National Academy of Sciences of the United States of America **111**.

Prochnow, H., R. Gollan, P. Rohne, M. Hassemer, C. Koch-Brandt and M. Baiersdörfer (2013). "Non-secreted clusterin isoforms are translated in rare amounts from distinct human mRNA variants and do not affect Bax-mediated apoptosis or the NF-κB signaling pathway." PLOS ONE **8**.

Rajan, R. S., M. E. Illing, R. R. Kopito and N. F. Bence (2002). "Specificity in intracellular protein aggregation and inclusion body formation." Biophysical Journal **82**.

Ramdzan, Y. M., S. Polling, C. P. Z. Chia, I. H. W. Ng, A. R. Ormsby, N. P. Croft, A. W. Purcell, M. A. Bogoyevitch, D. C. H. Ng, P. A. Gleeson and D. M. Hatters (2012). "Tracking protein aggregation and mislocalization in cells with flow cytometry." Nature Methods **9**.

Ramdzan, Y. M., R. Wood and D. M. Hatters (2013). "Pulse shape analysis (PulSA) to track protein translocalization by flow cytometry: applications for polyglutamine aggregation." Methods for Molecular Biology **1017**.

Rao, R. V. and D. E. Bredesen (2004). "Misfolded proteins, endoplasmic reticulum stress and neurodegeneration." Current Opinion in Cell Biology **16**.

Renton, Alan E., E. Majounie, A. Waite, J. Simón-Sánchez, S. Rollinson, J. R. Gibbs, Jennifer C. Schymick, H. Laaksovirta, John C. van Swieten, L. Myllykangas, H. Kalimo, A. Paetau, Y. Abramzon, Anne M. Remes, A. Kaganovich, Sonja W. Scholz, J. Duckworth, J. Ding, Daniel W. Harmer, Dena G. Hernandez, Janel O. Johnson, K. Mok, M. Ryten, D. Trabzuni, Rita J. Guerreiro, Richard W. Orrell, J. Neal, A. Murray, J. Pearson, Iris E. Jansen,

D. Sondervan, H. Seelaar, D. Blake, K. Young, N. Halliwell, Janis B. Callister, G. Toulson, A. Richardson, A. Gerhard, J. Snowden, D. Mann, D. Neary, Michael A. Nalls, T. Peuralinna, L. Jansson, V.-M. Isoviita, A.-L. Kaivorinne, M. Hölttä-Vuori, E. Ikonen, R. Sulkava, M. Benatar, J. Wuu, A. Chiò, G. Restagno, G. Borghero, M. Sabatelli, D. Heckerman, E. Rogaeva, L. Zinman, Jeffrey D. Rothstein, M. Sendtner, C. Drepper, Evan E. Eichler, C. Alkan, Z. Abdullaev, Svetlana D. Pack, A. Dutra, E. Pak, J. Hardy, A. Singleton, Nigel M. Williams, P. Heutink, S. Pickering-Brown, Huw R. Morris, Pentti J. Tienari and Bryan J. Traynor (2011). "A hexanucleotide repeat expansion in *C9ORF72* is the cause of chromosome 9p21-linked ALS-FTD." Neuron **72**.

Rizzi, F., A. E. Caccamo, L. Belloni and S. Bettuzzi (2009a). "Clusterin is a short half-life, poly-ubiquitinated protein, which controls the fate of prostate cancer cells." Journal of Cell Physiology **219**.

Rizzi, F., M. Coletta and S. Bettuzzi (2009b). "Clusterin (CLU): from one gene to two transcripts to many proteins." Advanced Cancer Research **104**.

Rohne, P., H. Prochnow, S. Wolf, B. Renner and C. Koch-Brandt (2014). "The chaperone activity of clusterin is dependent on glycosylation and redox environment." Cellular Physiology and Biochemistry **34**.

Rosen, D. R., T. Siddique, D. Patterson, D. A. Figlewicz, P. Sapp, A. Hentati, D. Donaldson, J. Goto, J. P. O'Regan, H.-X. Deng, Z. Rahmani, A. Krizus, D. McKenna-Yasek, A. Cayabyab, S. M. Gaston, R. Berger, R. E. Tanzi, J. J. Halperin, B. Herzfeldt, R. Van Den Bergh, W.-Y. Hung, T. Bird, G. Deng, D. W. Mulder, C. Smyth, N. G. Laing, E. Soriano, M. A. Pericak-Vance, J. Haines, G. A. Rouleau, J. S. Gusella, H. R. Horvitz and R. H. Brown (1993). "Mutations in Cu/Zn superoxide dismutase gene are associated with famiial amyotrophic lateral sclerosis." Nature **362**.

Rubinztein, D. C., G. Marino and G. Kroemet (2011). "Autophagy and Aging." Cell **146**.

Saez, I. and D. Vilchez (2014). "The mechanistic links between proteasome activity, aging and age-related diseases." Current Opinion in Genomics **15**.

Saibil, H. R. (2013). "Chaperone machines for protein folding, unfolding and disaggregation." Nature **14**.

Sansanwal, P., L. Li and M. M. Sarwal (2015). "Inhibition of intracellular clusterin attenuates cell death in nephropathic cystinosis." Journal of the American Society of Nephrology **26**.

Sarkar, S., G. Krishna, S. Imarisio, S. Saiki, C. J. O'Kane and D. C. Rubinsztein (2008). "A rational mechanism for combination treatment of Huntington's diseases using lithium and rapamycin." Human Molecular Genetics **17**.

Sarkar, S., B. Ravikumar, R. A. Floto and D. C. Rubinsztein (2009). "Rapamycin and mTOR-independent autophagy inducers ameliorate toxicity of polyglutamine-expanded huntingtin and related proteinopathies." Cell Death and Differentiation **16**.

Sarkozi, E., V. Askanas, S. A. Johnson, W. K. Engel and R. B. Alvarez (1993). "beta-Amyloid precursor protein mRNA is increased in inclusion-body myositis muscle." NeuroReport **4**.

Sasaki, K., K. Doh-ura, Y. Wakisaka and T. Iwaki (2002). "Clusterin/apolipoprotein J is associated with cortical Lewy bodies: immunohistochemical study in cases with α-synucleinopathies." Acta Neuropathologica **104**.

Sasaki, S. (2011). "Autophagy in spinal cord motor neurons in sporadic amyotrophic lateral sclerosis." Journal of Neuropathology and Experimental Neurology **70**.

Scaltriti, M., A. Santamaria, R. Paciucci and S. Bettuzzi (2004). "Intracellular clusterin induces G_2-M phase arrest and cell death in PC-3 prostate cancer cells." Cancer Research **64**.

Schneider, C. A., W. S. Rasband and K. W. Eliceiri (2012). "NIH Image to ImageJ: 25 years of image analysis." Nature Methods **9**.

Scholz, S. W., H. Houlden, C. Schulte, M. Sharma, A. Li, D. Berg, A. Melchers, R. Paudel, J. R. Gibbs, J. Simon-Sanchez, C. Paisan-Ruiz, J. Bras, J. Ding, H. Chen, B. J. Traynor, S. Arepalli, R. R. Zonozi, R. Revesz, J. Holton, N. Wood, A. Lees, W. Oertel, W. Wullner, S. Goldwurm, M. T. Pellecchia, T. Illig, O. Riess, H. H. Fernandez, R. L. Rodriguez, M. S. Okun, W. Poewe, G. K. Wenning, J. A. Hardy, A. B. Singleton, F. Del Sorbo, S. Schneider, K. P. Bhatia and T. Gasser (2009). "SNCA variants are associated with increased risk for multiple system atrophy." Annals of Neurology **65**.

Scott, E. S. (2001). "Nuclear translocation and activation of the transcription factor NFAT is blocked by herpes simplex virus infection." Journal of Virology **75**.

Selkoe, D. J. (1991). "The molecular pathology of Alzheimer's disease." Neuron **6**.

Sengupta, U., A. N. Nilson and R. Kayed (2016). "The role of amyloid-beta oligomers in toxicity, propagation and immunotherapy." EBioMedicine **6**.

Serpell, L. C., M. Sunde, M. D. Benson, G. A. Tennent, M. B. Pepys and P. E. Fraser (2000). "The protofilament substructure of amyloid fibrils." Journal of Molecular Biology **300**.

Sherrington, R., E. I. Rogaev, Y. Liang, E. A. Rogaeva, G. Levesque, M. Ikeda, H. Chi, C. Lin, G. Li, K. Holman, T. Tsuda, L. Mar, J. F. Foncin, A. C. Bruni, M. P. Montesi, S. Sorbi, I. Rainero, L. Pinessi, L. Nee, I. Chumakov, D. Pollen, A. Brookes, P. Sanseau, R. J. Polinsky, W. Wasco, H. A. R. Da Silva, J. L. Haines, M. A. Pericak-Vance, R. E. Tanzi, A. D. Roses, P. E. Fraser, J. M. Rommens and P. H. St George-Hyslop (1995). "Cloning of a gene bearing missense mutations in early-onset familial Alzheimer's disease." Nature **375**.

Shiber, A., W. Breuer and T. Ravid (2014). "Flow cytometric quantification and characterization of intracellular protein aggregates in yeast." Prion **8**.

Shiga, A., T. Ishihara, A. Miyashita, M. Kuwabara, T. Kato, N. Watanabe, A. Yamahira, C. Kondo, A. Yokoseki, M. Takahashi, R. Kuwano, A. Kakita, M. Nishizawa, H. Takahashi and O. Onodera (2012). "Alteration of POLDIP3 splicing associated with loss of function of TDP-43 in tissues affected with ALS." PLOS ONE **7**.

Siddique, T., D. A. Figlewicz, M. A. Pericak-Vance, J. L. Haines, G. A. Rouleau, A. J. Jeffers, P. Sapp, W.-Y. Hung, J. Bebout, D. McKenna-Yasek, G. Deng, H. R. Horvitz, J. K. Gusella and R. H. Brown Jr (1991). "Linkage of a gene causing

familial amyotrophic lateral sclerosis to chromosome 21 and evidence of genetic-locus heterogeneity." The New England Journal of Medicine **324**.

Soderholm, J. F., S. L. Bird, P. Kalab, Y. Sampathkumar, K. Hasegawa, M. Uehara-Bingen, K. Weis and R. Heald (2011). "Importazole, a small molecule inhibitor of the transport receptor importin-β." ACS Chemical Biology **6**.

Sommer, C. and D. W. Gerlich (2013). "Machine learning in cell biology - teaching computers to recognize phenotypes." Journal of Cell Science **126**.

Soto, C. (2001). "Protein misfolding and disease; protein refolding and therapy." FEBS Lett **498**.

Sottrup-Jensen, L. (1989). "α-Macroglobulins: structure, shape, and mechanism of proteinase complex formation." The Journal of Biological Chemistry **264**.

Sottrup-Jensen, L., O. Sand, L. Kristensen and G. H. Fey (1989). "The alpha-macroglobulin bait region. Sequence diversity and localization of cleavage sites for proteinases in five mammalian alpha-macroglobulins." The Journal of Biological Chemistry **264**.

Sousa, M. M., I. Cardoso, R. Fernandes, A. Guimaraes and M. J. Saraiva (2001). "Deposition of transthyretin in early stages of familial amyloidotic polyneuropathy: evidence for toxicity of nonfibrillar aggregates." American Journal of Pathology **159**.

Spillantini, M. G. and M. Goedert (2000). "The alpha-synucleinopathies: Parkinson's disease, dementia with Lewy bodies, and multiple system atrophy." Annals of the New York Academy of Sciences **920**.

Sreedharan, J., I. P. Blair, V. B. Tripathi, X. Hu, C. Vance, B. Rogelj, S. Ackerley, J. C. Durnall, K. L. Williams, E. Buratti, F. Baralle, J. de Belleroche, J. D. Mitchell, P. N. Leigh, A. Al-Chalabi, C. C. Miller, G. Nicholson and C. E. Shaw (2008). "TDP-43 mutations in familial and sporadic amyotrophic lateral sclerosis." Science **319**.

Stefani, M. (2010). "Protein aggregation diseases: toxicity of soluble prefibrillar aggregates and their clinical significance." Methods in Molecular Biology **648**.

Stefani, M. and C. M. Dobson (2003). "Protein aggregation and aggregate toxicity: new insights into protein folding, misfolding diseases and biological evolution." Journal of Molecular Medicine **81**.

Stefanis, L. (2012). "α-Synuclein in Parkinson's disease." Cold Spring Harbor Perspectives in Medicine **2**.

Stewart, E. M., J. A. Aquilina, S. B. Easterbrook-Smith, D. Murphy-Durland, C. Jacobsen, S. Moestrup and M. R. Wilson (2007). "Effects of glycosylation on the structure and function of the extracellular chaperone clusterin." Biochemistry **46**.

Stranks, S. D., H. Ecroyd, S. Van Sluyter, E. J. Waters, J. A. Carver and L. von Smekal (2009). "Model for amorphous aggregation processes." Physical Review E **80**.

Strauss, S., J. Bauer, U. Ganter, U. Jonas, M. Berger and B. Volk (1992). "Detection of interleukin-6 and alpha-2-macroglobulin immunoreactivity in cortex and hippocampus of alzheimer's disease patients." Laboratory investigation **66**.

Sungwook, L., A. L. Taeyun, L. Eunhye, K. Sujin, P. Areum, W. K. Seung, J. P. Hyo, Y. Je-Hyun, H. Sang-Jun, P. Taesun, L. Ju-Seog, H. C. Jae and P. Boyoun (2015). "Identification of a subnuclear body involved in sequence-specific cytokine RNA processing." Nature Communications **6**.

Tashiro, Y., M. Urushitani, H. Inoue, M. Koike, Y. Uchiyama, M. Komatsu, K. Tanaka, M. Yamazaki, M. Abe, H. Misawa, K. Sakimura, H. Ito and R. Takahashi (2012). "Motor neuron-specific disruption of proteasomes, but not autophagy replicates amyotrophic lateral sclerosis." The Journal of Biological Chemistry.

Terry, R. D., E. Masliah, D. P. Salmon, N. Butters, R. DeTeresa, R. Hill, L. A. Hansen and R. Katzman (1991). "Physical basis of cognitive alterations in Alzheimer's disease: synapse loss is the major correlate of cognitive impairment." Annals of Neurology **30**.

Thomas, P. J., B. H. Qu and P. L. Pedersen (1995). "Defective protein folding as a basis of human disease." Trends Biochem Sci **20**.

Trougakos, I. P., M. Lourda, M. H. Antonelou, D. Kletsas, V. G. Gorgoulis, I. S. Papassideri, Y. Zou, L. H. Margaritis, D. A. Boothman and E. S. Gonos (2009). "Intracellular clusterin inhibits mitochondrial apoptosis by supressing p53-activating stress signals and stablizing the cytosolic Ku70-Bax protein complex." Clinical Cancer Research **15**.

Tsai, B., Y. Yihong and T. A. Rapoport (2002). "Retro-translocation of proteins from the endoplasmic reticulum into the cytosol." Nature Reviews Molecular Cell Biology **3**.

Turner, B. J., J. D. Atkin, M. A. Farg, D. W. Zang, A. Rembach, E. C. Lopes, J. D. Patch, A. F. Hill and S. S. Cheema (2005). "Impaired extracellular secretion of mutant superoxide dismutase 1 associates with neurotoxicity in familial amyotrophic lateral sclerosis." Journal of Neuroscience **25**.

Um, J. W., H. B. Nygaard, J. K. Heiss, M. A. Kostylev, M. Stagi, A. Vortmeyer, T. Wisniewski, E. C. Gunther and S. M. Strittmatter (2012). "Alzheimer amyloid-beta oligomer bound to postsynaptic prion protein activates Fyn to impair neurons." Nature Neuroscience **15**.

Uversky, V. N. and A. K. Dunker (2010). "Understanding protein non-folding." Biochimica et Biophysica Acta **1804**.

van Eersel, J., Y. D. Ke, A. Gladbach, M. Bi, J. Gotz, J. J. Kril and L. M. Ittner (2011). "Cytoplasmic accumulation and aggregation of TDP-43 upon proteasome inhibition in cultured neurons." PLOS ONE **6**.

Van Montfort, R., C. Slingsby and E. Vierling (2002). "Structure and function of the small heat shock protein/alpha-crystallin family of molecular chaperones." Advanced Protein Chemistry **59**.

Veering, T. H., A. G. L. Burm, J. H. M. Souverijn, J. M. P. Serree and J. Spierdijk (1990). "The effect of age on serum concentrations of albumin and alpha1-acid glycoprotein." British Journal of Clinical Pharmacology **29**.

Vetri, V., C. Canale, A. Relini, F. Librizzi, V. Militello, A. Gliozzi and M. Leone (2007). "Amyloid fibril formation and amorphous aggregation in concanavalin A." Biophysical Chemistry **125**.

Wagstaff, K. M., H. Sivakumaran, S. M. Heaton, D. Harrich and D. A. Jans (2012). "Ivermectin is a specific inhibitor of importin α/β-mediated nuclear import able to inhibit replication of HIV-1 and dengue virus." Biochemical Journal **443**.

Walker, A. K., K. Y. Soo, V. Sundaramoorthy, S. Parakh, Y. Ma, M. A. Farg, R. H. Wallace, P. J. Crouch, B. J. Turner, M. K. Home and J. D. Atkin (2013). "ALS-associated TDP-43 induces endoplasmic reticulum stress, which drives cytoplasmic TDP-43 accumulation and stress granule formation." PLOS ONE **8**.

Walters, B. T., L. Mayne, J. R. Hinshaw, T. R. Sosnick and S. W. Englander (2013). "Folding of a large protein at high structual resolution." Proceedings of the National Academy of Sciences of the United States of America **110**.

Wang, I. F., K. J. Tsai and C. K. Shen (2013). "Autophagy activation ameliorates neuronal pathogenesis of FTLD-U mice: A new light for treatment of TARDBP/TDP-43 proteinopathies." Autophagy **9**.

Wang, I. F., L. S. Wu, H. Y. Chang and C. K. J. Shen (2008). "TDP-43, the signature protein of FTLD-U, is a neuronal activity-responsive factor." Journal of Neurochemistry **105**.

Wang, L., B. Popko and R. P. Roos (2011). "The unfolded protein response in familial amyotrophic lateral sclerosis." Human Molecular Genetics **20**.

Wang, X., H. Fan, Z. Ying, B. Li, H. Wang and G. Wang (2010). "Degradation of TDP-43 and its pathogenic form by autophagy and the ubiquitin-proteasome system." Neuroscience Letters **469**.

Weber-Ban, E. U., B. G. Reid, A. D. Miranker and A. L. Horwich (1999). "Global unfolding of a substrate protein by the Hsp100 chaperone ClpA." Nature **401**.

Weikl, T. R. (2010). "Transition states in protein folding." Communications in Computational Physics **7**.

Wilson, M. R. and S. B. Easterbrook-Smith (2000). "Clusterin is a secreted mammalian chaperone." Trends in Biochemical Sciences **25**.

Winner, B., R. Jappelli, S. K. Maji, P. A. Desplats, L. Boyer, S. Aigner, C. Hetzer, T. Loher, M. Vilar, S. Campioni, C. Tzitzilonis, A. Soragni, S. Jessberger, H. Mira, A. Consiglio, E. Pham, E. Masliah, F. H. Gage and R. Riek (2011). "In vivo demonstration that α-synuclein oligomers are toxic." Proceedings of the National Academy of Sciences of the United States of America **108**.

Winslow, A. R., C. W. Chen, S. Corrochano, A. Acevedo-Arozena, D. E. Gordon, A. A. Peden, M. Lichtenberg, F. M. Menzies, B. Ravikumar, S. Imarisio, S. Brown, C. J. O'Kane and D. C. Rubinsztein (2010). "alpha-Synuclein impairs macroautophagy: implications for Parkinson's disease." The Journal of Cell Biology **190**.

Wong, P., D. Taillefer, J. Lakins, J. Pineault, G. Chader and M. Tenniswoos (1994). "Molecular characterisation of human TRPM-2/clusterin, a gene associated with sperm maturation, apoptosis and neurodegeneration." European Journal of Biochemistry **221**.

Wu, S. M., C. M. Boyer and S. V. Pizzo (1997). "The binding of receptor-recognized alpha2-macroglobulin to the low density lipoprotein receptor-related

protein and the alpha2M signaling receptor is decoupled by oxidation." The Journal of Biological Chemistry **272**.

Wu, Y. T., H. L. Tan, G. Shui, C. Bauvy, Q. Huang, M. R. Wenk, C. N. Ong, P. Codongo and H. M. Shen (2014). "Dual role of 3-methyladenine in modulation of autophagy via different temporal patterns of inhibition on class I and III phosphoinositide 3-kinase." The Journal of Biological Chemistry **34**.

Wyatt, A. R., P. Constantinescu, H. Ecroyd, C. M. Dobson, M. R. Wilson, J. R. Kumita and J. J. Yerbury (2013a). "Protease-activated alpha-2-macroglobulin can inhibit amyloid formation via two distinct mechanisms." FEBS Letters **587**.

Wyatt, A. R., J. R. Kumita, N. E. Farrawell, C. M. Dobson and M. R. Wilson (2015). "Alpha-2-macroglobulin is acutely sensitive to freezing and lyophilization: implications for structural and functional studies." PLOS ONE **10**.

Wyatt, A. R., J. R. Kumita, R. W. Mifsud, C. A. Gooden, M. R. Wilson and C. M. Dobson (2014). "Hypochlorite-induced structural modifications enhance the chaperone activity of human α-2-macroglobulin." Proceedings of the National Academy of Sciences of the United States of America **111**.

Wyatt, A. R., J. J. Yerbury, P. Berghofer, I. Greguric, A. Katsifis, C. M. Dobson and M. R. Wilson (2011). "Clusterin facilitates in vivo clearance of extracellular misfolded proteins." Cellular and Molecular Life Sciences **68**.

Wyatt, A. R., J. J. Yerbury, H. Ecroyd and M. R. Wilson (2013b). "Extracellular chaperones and proteostasis." Annual Review of Biochemistry **82**.

Wyatt, A. R., J. J. Yerbury and M. R. Wilson (2009). "Structural characterisation of clusterin-chaperone client protein complexes." The Journal of Biological Chemistry **284**.

Xu, T., C. C. Wong, A. Kashina and J. R. Yates III (2009). "Identification of N-terminally arginylated proteins and peptides by mass spectrometry." Nature Protocols **4**.

Xue, W.-F., A. L. Hellewell, W. S. Gosal, S. W. Homans, E. W. Hewitt and S. E. Radford (2009). "Fibril fragmentation enhances amyloid cytotoxicity." The Journal of Biological Chemistry **284**.

Yamagishi, S., Y. Koyama, T. Katayama, M. Taniguchi, J. Hitomi, M. Kato, M. Aoki, Y. Itoyama, S. Kato and M. Tohyama (2007). "An *in vitro* model for Lewy body-like hyaline inclusion/astrocytic hyaline inclusion: induction by ER stress with an ALS-linked SOD1 mutation." PLOS ONE **2**.

Yang, C., W. Tan, C. Whittle, L. Qiu, L. Cao, S. Alkbarian and Z. Xu (2010). "The C-terminal TDP-43 fragments have a high aggregation propensity and harm neurons by a dominant-negative mechanism." PLOS ONE **5**.

Ye, Y., G. Blaser, M. H. Horrocks, M. J. Ruedas-Rama, S. Ibrahim, A. A. Zhukov, A. Orte, D. Klenerman, S. E. Jackson and D. Komander (2012). "Ubiquitin chain conformation regulates recognition and activity of interacting proteins." Nature **492**.

Yerbury, J. J., J. R. Kumita, S. Meehan, C. M. Dobson and M. R. Wilson (2008). "α_2-Macroglobulin and haptoglobin suppress amyloid formation by interacting with prefibrillar protein species." The Journal of Biological Chemistry **284**.

Yerbury, J. J., S. Poon, S. Meehan, B. Thompson, J. R. Kumita, C. M. Dobson and M. R. Wilson (2007a). "The extracellular chaperone clusterin influences amyloid formation and toxicity by interacting with prefibrillar structures." The FASEB Journal **21**.

Yerbury, J. J., S. Poon, S. Meehan, B. Thompson, J. R. Kumita, C. M. Dobson and M. R. Wilson (2007b). "The extracellular chaperone clusterin influences amyloid formation and toxicity by interacting with prefibrillar structures." The FASEB Journal **21**.

Yerbury, J. J., E. M. Stewart, A. R. Wyatt and M. R. Wilson (2005). "Quality control of protein folding in extracellular space." EMBO Rep **6**.

Zampagni, M., R. Cascella, F. Casamenti, C. Grossi, E. Evangelisti, D. Wright, M. Becatti, G. Ligurri, B. Mannini, S. Campioni, F. Chiti and C. Cecchi (2011). "A comparison of the biochemical modifications caused by toxic and non-toxic protein oligomers in cells." Journal of Cellular and Molecular Medicine **15**.

Zhang, F., M. Kumano, E. Beraldi, L. Fazli, C. Du, S. Moore, P. Sorensen, A. Zoubeidi and M. E. Gleave (2014). "Clusterin facilitates stress-induced lipidation of LC3 and autophagosome biogenesis to enhance cancer cell survival." Nature Communications **5**.

Zhang, H., J. K. Kim, C. A. Edwards, Z. Xu, R. Taichman and C. Y. Wang (2005a). "Clusterin inhibits apoptosis by interacting with activated Bax." Nature Cell Biology **7**.

Zhang, H., X. J. Li, D. B. Martin and R. Aebersold (2003). "Identification and quantification of N-linked glycoproteins using hydrazide chemistry, stable isotope labeling and mass spectrometry." Nature Biotechnology **21**.

Zhang, W., T. Wang, Z. Pei, D. S. Miller, X. Wu, M. L. Block, B. Wilson, W. Zhang, Y. Zhou, J. S. Hong and J. Zhang (2005b). "Aggregated alpha-synuclein activates microglia: a process leading to disease progression in Parkinson's disease." FASEB Journal **19**.

Zhang, X., S. Chen, D. Yang, Y. Wang, X. Zhang, Z. Wang and W. Le (2011). "Rapamycin treatment augments motor neuron degeneration in SOD1(G93A) mouse model of amyotrophic lateral sclerosis." Autophagy **7**.

Zhou, Y., I. Hayashi, J. Wong, K. Tugusheva, J. J. Renger and C. Zerbinatti (2014). "Intracellular clusterin interacts with brain isoforms of the bridging integrator 1 and with the microtubule-associated protein Tau in Alzheimer's disease." PLOS ONE **9**.

Zhu, Y. J., H. Lin and R. Lal (2000). "Fresh and nonfibrillar amyloid β protein (1-40) induces rapid cellular degeneration in aged human fibroblasts: evidence for Aβ P-channel-mediated cellular toxicity." The FASEB Journal **14**.

Zinkie, S., B. J. Gentil, S. Minotti and H. D. Durham (2013). "Expression of the protein chaperone, clusterin, in spinal cord cells constitutively and following cellular stress, and upregulation by treatment with Hso90 inhibitor." Cell Stress Chaperones **18**.

Zlokovic, B. V., C. L. Martel, E. Matsubara, J. G. McComb, G. Zheng, L. McCluskey, B. Frangione and J. Ghiso (1996). "Glycoprotein 330/megalin: Probable role

in receptor-mediated transport of apolipoprotein J alone and in a complex with Alzheimer disease amyloid 13 at the blood-brain and blood-cerebrospinal fluid barriers." Proceedings of the National Academy of Sciences of the United States of America **93**.

Zoubeidi, A., S. Ettinger, E. Beraldi, B. Hadaschik, A. Zardan, L. W. Klomp, C. C. Nelson, P. S. Rennie and M. E. Gleave (2010a). "Clusterin facilitates COMMD1 and I-kappaB degradation to enhance NF-kappaB activity in prostate cancer cells." Molecular Cancer Research **8**.

Zoubeidi, A., S. Ettinger, E. Beraldi, B. Hadaschik, A. Zardan, L. W. J. Klomp, C. C. Nelson, P. S. Rennie and M. E. Gleave (2010b). "Clusterin facilitates COMMD1 and I-κB degradation to enhance NF-κB activity in prostate cancer cells." Molecular Cancer Research **8**.

Appendix I: Script for LC3 Co-localisation (Python v2.7)

Available at: https://github.com/drwhiten/Appendices.git

```
import PIL
import os
import numpy
import scipy
import scipy.stats
import matplotlib as plt
import matplotlib.pyplot as pyplt
from matplotlib.widgets import  RectangleSelector
import Tkinter, tkFileDialog

def initialise():
    global channels, channel1, channel2, channel3, count, count2
    channels = 3        # change to 2 if you are using 2 channels only
    channel1 = 'TDP'    # name of protein in channel 1
    channel2 = 'CLU'    # name of protein in channel 2
    channel3 = 'LC3'    # name of protein in channel 3 - ignore if using 2 channels
    # names only used for results docs, tdp = ch1, clu = ch2, lc3 = ch3 in the code
    count = 0
    count2 = 1
    opener()

def opener():
    global files, directory, list1, list2, list3, list4, list5, list6, list7, list8
    directory = tkFileDialog.askdirectory()
    files = os.listdir(directory)
    files.sort()    # case-sensitive alphabetical sorting
    thresh_path = directory + '\Thresholded'
    results_path = directory + '\Results'
    if not os.path.exists(thresh_path): os.makedirs(thresh_path)
    if not os.path.exists(results_path): os.makedirs(results_path)
    list1 = [] # lists 1-4 hold colocalisation data
    list2 = []
    list3 = []
    list4 = []
    list5 = [] # lists 5-8 hold chance coinc data
    list6 = []
    list7 = []
    list8 = []
    set_roi()
```

```
def set_roi():
    file_tdp = files[count]
    x = 1
    y = 1
    fig = pyplt.figure
    ax = pyplt.subplot(111)
    ax.plot(x,y)
    image_path = image_path = os.path.join(directory, file_tdp)
    img = PIL.Image.open(image_path)
    array = numpy.array(img)
    imgplot = pyplt.imshow(array)
    toggle_selector.RS = RectangleSelector(ax, onselect, drawtype='box')

def onselect(eclick, erelease):
    'eclick and erelease are matplotlib events at press and release'
    start = (eclick.xdata, eclick.ydata)
    end = (erelease.xdata, erelease.ydata)
    pyplt.close(1)
    threshold(start, end)

def toggle_selector(event):
    print ' Key pressed.'
    if event.key in ['Q', 'q'] and toggle_selector.RS.active:
        print ' RectangleSelector deactivated.'
        toggle_selector.RS.set_active(False)
    if event.key in ['A', 'a'] and not toggle_selector.RS.active:
        print ' RectangleSelector activated.'
        toggle_selector.RS.set_active(True)

def threshold(start, end):
    global files, directory, channels, channel1, channel2, channel3, count, count2
    global list1, list2, list3, list4, list5, list6, list7, list8
    top, left = start
    bottom, right = end
    box = (int(left), int(top), int(right), int(bottom))

    file_tdp = files[count]
    file_clu = files[count+1]
    file_lc3 = files[count+2]
    file_list = [file_tdp, file_clu, file_lc3]
    thresholded_dict = {}

    for image in file_list:
        image_path = os.path.join(directory, image)
        img = PIL.Image.open(image_path)
        img = img.crop(box)
```

```
    array = numpy.array(img)
    brightest = numpy.amax(array)
    threshold = brightest * 0.5
    thresholded = (array > threshold) * 255     # Thresholding here. Works because
        True = 1.
    outim=PIL.Image.fromarray(thresholded)
    new_save = directory + '/thresholded/Thresholded_' + str(image)
    outim.save(new_save)
    thresholded_dict[image] = thresholded
num_clu = float(numpy.sum(thresholded_dict[file_clu])/255)
num_tdp = float(numpy.sum(thresholded_dict[file_tdp])/255)

#  testing for colocalisation
clu_tdp_colocalised = numpy.logical_and(thresholded_dict[file_clu] != 0,
        thresholded_dict[file_tdp] != 0)
clu_lc3_colocalised = numpy.logical_and(thresholded_dict[file_clu] != 0,
        thresholded_dict[file_lc3] != 0)
tdp_lc3_colocalised = numpy.logical_and(thresholded_dict[file_tdp] != 0,
        thresholded_dict[file_lc3] != 0)
all_colocalised = numpy.logical_and(clu_tdp_colocalised != 0, clu_lc3_colocalised
        != 0)
list1.append(round(numpy.sum(clu_tdp_colocalised)/num_clu*100, 2))
list2.append(round(numpy.sum(clu_lc3_colocalised)/num_clu*100, 2))
list3.append(round(numpy.sum(tdp_lc3_colocalised)/num_tdp*100, 2))
list4.append(round(numpy.sum(all_colocalised)/num_clu*100, 2))

#  shuffling arrays
for key in thresholded_dict:
    shape = thresholded_dict[key].shape
    thresholded_dict[key] = thresholded_dict[key].flatten()
    numpy.random.shuffle(thresholded_dict[key])
    thresholded_dict[key] = thresholded_dict[key].reshape(shape)

#  testing for chance coincidence
clu_tdp_chance = numpy.logical_and(thresholded_dict[file_clu] != 0,
        thresholded_dict[file_tdp] != 0)
clu_lc3_chance = numpy.logical_and(thresholded_dict[file_clu] != 0,
        thresholded_dict[file_lc3] != 0)
tdp_lc3_chance = numpy.logical_and(thresholded_dict[file_tdp] != 0,
        thresholded_dict[file_lc3] != 0)
all_chance = numpy.logical_and(clu_tdp_chance != 0, clu_lc3_chance != 0)
list5.append(round(numpy.sum(clu_tdp_chance)/num_clu*100, 2))
list6.append(round(numpy.sum(clu_lc3_chance)/num_clu*100, 2))
list7.append(round(numpy.sum(tdp_lc3_chance)/num_tdp*100, 2))
list8.append(round(numpy.sum(all_chance)/num_clu*100, 2))
```

```
    count2 += 1
    count += 3
    if count < len(files)-2:
        set_roi()
    if count >= (len(files)-2):
        saver()

def saver():
    global files, directory, channels, channel1, channel2, channel3, count, count2
    global list1, list2, list3, list4, list5, list6, list7, list8

    clutdp_path = directory + '\Results\CLU_and_TDP_colocalisation.txt'
    clulc3_path = directory + '\Results\CLU_and_LC3_colocalisation.txt'
    tdplc3_path = directory + '\Results\TDP_and_LC3_colocalisation.txt'
    all_path = directory + '\Results\ALL_colocalisation.txt'
    cclutdp_path = directory + '\Results\CLU_and_TDP_chance.txt'
    cclulc3_path = directory + '\Results\CLU_and_LC3_chance.txt'
    ctdplc3_path = directory + '\Results\TDP_and_LC3_chance.txt'
    call_path = directory + '\Results\ALL_chance.txt'
    path_list = [clutdp_path, clulc3_path, tdplc3_path, all_path, cclutdp_path,
            cclulc3_path, ctdplc3_path, call_path]
    list_list = [list1, list2, list3, list4, list5, list6, list7, list8]

    for p, l in zip(path_list, list_list):
        with open(p, 'w') as f:
            f.write('Values are number of pixels colocalised\nas percentage clu (tdp for
             tdp-lc3)\nfor each image set.\n\n')
            for v in l:
                f.write(str(v)+'\n')

    compiled_path = directory + '\Results\compiled_results.txt'
    with open(compiled_path, 'w') as f:
        f.write('Values are mean +/- SD, n = {0}'.format(len(list1)))
        f.write('\n\n')
        f.write('CLU-TDP43 colocalisation = {0} +/-
            {1}'.format(round(numpy.mean(list1), 2), round(numpy.std(list1), 2)) + '\n')
        f.write('CLU-LC3 colocalisation = {0} +/- {1}'.format(round(numpy.mean(list2),
            2), round(numpy.std(list2), 2)) + '\n')
        f.write('TDP43-LC3 colocalisation = {0} +/-
            {1}'.format(round(numpy.mean(list3), 2), round(numpy.std(list3), 2)) + '\n')
        f.write('ALL colocalisation = {0} +/- {1}'.format(round(numpy.mean(list4), 2),
            round(numpy.std(list4), 2)) + '\n')
        f.write('CLU-TDP43 chance = {0} +/- {1}'.format(round(numpy.mean(list5), 2),
            round(numpy.std(list5), 2)) + '\n')
```

```
        f.write('CLU-LC3 chance = {0} +/- {1}'.format(round(numpy.mean(list6), 2),
            round(numpy.std(list6), 2)) + '\n')
        f.write('TDP43-LC3 chance = {0} +/- {1}'.format(round(numpy.mean(list7), 2),
            round(numpy.std(list7), 2)) + '\n')
        f.write('ALL chance = {0} +/- {1}'.format(round(numpy.mean(list8), 2),
            round(numpy.std(list8), 2)))

initialise()
```

Appendix II: Script for MaxQ (Python v2.7)

Available at: https://github.com/drwhiten/Appendices.git

```
# GUI and plotting not shown for clarity
from tkFileDialog import askopenfilename
import numpy as np
import os

def opener():
    path = askopenfilename()
    donor = []
    acceptor = []

    with open(path,'r') as file:
        namer = file.name
        namez = namer[:-4] + '_compact.txt'
        lines = file.readlines()
        # Creates new file with preface cut off
        open(namez, 'w').writelines(lines[25:])
        global pather
        pather = os.path.dirname(file.name)
    with open(namez, 'r') as file:
        # Opens new file and adds data in to list
        for row in file:
            a,don,b,acc,c = row.split()
            donor.append(float(don))
            acceptor.append(float(acc))
    os.remove(namez)

    donor_array = np.array(donor)
    acceptor_array = np.array(acceptor)
    donor_auto = 0
    acceptor_auto = 0
    crosstalk = 0
    donor_array = donor_array - donor_auto
    acceptor_array = acceptor_array - acceptor_auto - (crosstalk * donor_array)
    return donor_array, acceptor_array

def maxq():
    donor_array, acceptor_array = opener()

    td = 100
    ta = 100
```

```
    donor_shuff = np.copy(donor_array)
    np.random.shuffle(donor_shuff)

    Qvals = np.zeros((td+1, ta+1))

    for td_cycler in xrange(0,(td+1)):
        for ta_cycler in xrange(0,(ta+1)):
            Q_val,coinc,desynch = q_calc(donor_array,
             acceptor_array,td_cycler,ta_cycler,donor_shuff)
            Qvals[td_cycler][ta_cycler] = Q_val

    max_q = np.max(Qvals)
    index_q = np.where(Qvals == max_q)
    max_d, max_a = index_q # max q at these donor and acceptor thresholds

def q_calc(donor_array,acceptor_array,td,ta,donor_shuff):
    d_rate = len(donor_array[(donor_array > td)])
    a_rate = float(len(acceptor_array[(acceptor_array > ta)]))
    coinc = len(donor_array[(donor_array > td) & (acceptor_array > ta)])
    des_events = float(len(donor_shuff[(donor_shuff > td) &
            (acceptor_array > ta)]))
    Q_val = 100*(round(((coinc - des_events) / (d_rate + a_rate -
            (coinc - des_events))), 4))
    return Q_val,coinc,des_events


maxq()
```

Appendix III: Script for MaxQ (Igor Pro v6.3.4.1)

Available at: https://github.com/drwhiten/Appendices.git

```
#pragma rtGlobals=1

function Load_()
	String doprompttitle="Details of files to load"
	string foldername=""
	string filename="asyn"
	variable first=0
	variable last=79
	variable Auto_blue=0
	variable Auto_red=0
	variable crosst=0

	prompt foldername, "Folder name: "
	prompt filename "File name (no suffix): "
	prompt first, "First filenumber: "
	prompt last, "Last filenumber: "
	prompt auto_blue, "Autofluorescence in channel A: "
	prompt auto_red, "Autofluorescence in channel B: "
	prompt crosst, "Crosstalk: "

	doprompt doprompttitle,
	foldername,filename,first,last,auto_blue,auto_red,crosst

	variable c
	setdatafolder root:
	newdatafolder/s $foldername
	make/o/n=1 unthresholded_donor_events,unthresholded_acceptor_events

	newpath/Q path1
	pathinfo path1

	string path=S_path
	string pathway=path+filename
	string num

	for(c=first;c<=last;c+=1)
	if(c<10)
		num="000"+num2str(c)
	elseif(c<100)
		num="00"+num2str(c)
```

```
		elseif(c<1000)
			num="0"+num2str(c)
		endif

		string loader=pathway+num+".dat"
		GBLoadWave/Q/V/T={32,4}/W=2 loader
		wave wave0,wave1

		variable e,k
		for(e=0;e<=(Numpnts(wave0));e+=1)
redimension/N=(k+1)
		unthresholded_donor_events,unthresholded_acceptor_events
			unthresholded_donor_events[k]=wave0[e]-auto_blue

			unthresholded_acceptor_events [k]=wave1[e]-auto_red-
		crosst*wave0[e]
			k+=1
		endfor

		killwaves wave0
		killwaves wave1

		Print "Opening file #",num
		endfor

Print "Files opened."
end

function Threshold_()
		variable donor=10
		variable Acceptor=10
		prompt donor, "Donor: "
		prompt acceptor, "Acceptor: "
		string doprompttitle="Thresholds to use"
		doprompt doprompttitle, donor, acceptor

		wave unthresholded_donor_events,unthresholded_acceptor_events

		variable coinc=0,Arate=0,Brate=0,e
		make/o/N=1
		thresholded_donor_events,thresholded_acceptor_events,donor_desynch,ac
		ceptor_desynch,zplot,z_desynch
		for(e=0;e<(dimsize(unthresholded_donor_events,0));e+=1)
		if((unthresholded_donor_events[e])>donor &&
		(unthresholded_acceptor_events[e])>acceptor)
```

```
        redimension/N=(coinc+1)
thresholded_donor_events,thresholded_acceptor_events,zplot
        thresholded_donor_events[coinc]=unthresholded_donor_events[e]

thresholded_acceptor_events[coinc]=unthresholded_acceptor_events[e]

zplot[coinc]=ln(thresholded_acceptor_events[coinc]/thresholded_donor_ev
ents[coinc])
        coinc+=1
endif

if((unthresholded_donor_events[e])>donor)
        Arate+=1
Endif

if((unthresholded_acceptor_events[e])>acceptor)
        Brate+=1
endif
endfor

variable d

for(e=0;e<(dimsize(unthresholded_donor_events,0));e+=1)
variable num2=round(enoise(dimsize(unthresholded_donor_events,0)))
if(num2<0)
        num2=-1*num2
endif
if((unthresholded_donor_events[e])>donor &&
(unthresholded_acceptor_events[num2])>acceptor)
        redimension/N=(d+1) donor_desynch,acceptor_desynch,z_desynch
        donor_desynch[d]=unthresholded_donor_events[e]
        acceptor_desynch[d]=unthresholded_acceptor_events[num2]
        z_desynch[d]=ln(acceptor_desynch[d]/donor_desynch[d])

        d+=1
endif
endfor
make/o/n=1
coincident=coinc,donorrate=arate,acceptorrate=brate,desynchrate=d,QValu
e
variable q=(coinc-d)/(arate+brate-(coinc-d))

QValue[0]=q
string q_val=num2str(q)
Make/N=30/O zplot_Hist,zdesynch_hist;DelayUpdate
Histogram/B={-3,0.2,30} zplot,zplot_Hist
```

```
	Histogram/B={-3,0.2,30} z_desynch,zdesynch_Hist
Print "Data thresholded."
end

function MaxQ_matrix_func_()
	variable threshold=0
	prompt threshold, "Threshold: "
	string doprompttitle = "Threshold limit"
	doprompt doprompttitle,threshold

	variable donorthreshold=threshold,acceptorthreshol=threshold
	wave unthresholded_donor_events,unthresholded_acceptor_events
	variable line=0,donorcycler

	variable acceptorthreshold=(acceptorthreshol+1)
	for(donorcycler=0;donorcycler<=donorthreshold;donorcycler+=1)
	make/o/n=(acceptorthreshold) pretendQwave
	make/o/n=(acceptorthreshold) pretenddesynchwave
	make/o/n=(acceptorthreshold) pretendrealwave
	make/o/n=(acceptorthreshold) pretendrealminusdwave

	variable acceptorcycler
	make/o/n=1 q_donorthreshold
	make/o/n=1 realrate_donorthreshold
	make/o/n=1 realminusd_donorthreshold
	make/o/n=1 desynchrate_donorthreshold


	for(acceptorcycler=0;acceptorcycler<=(acceptorthreshold);acceptorcycler+=
	1)
		variable h=0,coinc=0,d=0,Arate=0,Brate=0
		make/o/N=1 TEMP_donor_events,TEMP_acceptor_events

		make/o/N=1 donor_desynch,acceptor_desynch

		for(h=0;h<(Numpnts(unthresholded_donor_events));h+=1)
			if((unthresholded_donor_events[h])>donorcycler &&
	(unthresholded_acceptor_events[h])>acceptorcycler)
				redimension/N=(coinc+1)
	TEMP_donor_events,TEMP_acceptor_events


	TEMP_donor_events[coinc]=unthresholded_donor_events[h]
```

```
TEMP_acceptor_events[coinc]=unthresholded_acceptor_events[h]
                        coinc+=1
                endif

                variable
random=round(enoise(Numpnts(unthresholded_donor_events)))

                if(random<0)
                        random=-1*random
                endif

                if((unthresholded_donor_events[h])>donorcycler &&
(unthresholded_acceptor_events[random])>acceptorcycler)
                        redimension/N=(d+1)
donor_desynch,acceptor_desynch
                        donor_desynch[d]=unthresholded_donor_events[h]

acceptor_desynch[d]=unthresholded_acceptor_events[random]
                        d+=1
                        endif

                if((unthresholded_donor_events[h])>donorcycler)
                        Arate+=1
                endif

                if((unthresholded_acceptor_events[h])>acceptorcycler)

                        Brate+=1
                endif

        endfor

        variable qis=(coinc-d)/(arate+brate-(coinc-d))
        pretendQwave[acceptorcycler]=qis
        pretenddesynchwave[acceptorcycler]=d
        pretendrealwave[acceptorcycler]=coinc
        pretendrealminusdwave[acceptorcycler]=coinc-d

        duplicate/o pretendQwave
$(nameOfWave(q_donorthreshold)+num2str(donorcycler))
        duplicate/o pretenddesynchwave
$(nameOfWave(desynchrate_donorthreshold)+num2str(donorcycler))
        duplicate/o pretendrealwave
$(nameOfWave(realrate_donorthreshold)+num2str(donorcycler))
```

```
		duplicate/o pretendrealminusdwave
$(nameOfWave(realminusd_donorthreshold)+num2str(donorcycler))

endfor

killwaves desynchrate_donorthreshold
killwaves q_donorthreshold
killwaves realrate_donorthreshold
killwaves realminusd_donorthreshold
killwaves acceptor_desynch
killwaves donor_desynch

endfor

Concatenate/o/KILL WaveList("q_donorthreshold*", ";", ""), q_matrix
Concatenate/o/KILL WaveList("desynchrate_donorthreshold*", ";", ""),
desynch_matrix
Concatenate/o/KILL WaveList("realrate_donorthreshold*", ";", ""),
realrate_matrix
Concatenate/o/KILL WaveList("realminusd_donorthreshold*", ";", ""),
realminusd_matrix

Display as "Q-Value";AppendImage q_matrix
Label left "Donor threshold";DelayUpdate
Label bottom "Acceptor threshold"
ModifyImage q_matrix ctab= {*,*,Rainbow256,0}
ColorScale/C/N=text0/F=0/A=RC/E contour=ln_FRET_Matrix_1Bin_Mass
ColorScale/C/N=text0  ctab={0,100,Rainbow,0}

Display as "Desynch events";AppendImage desynch_matrix
Label left "Donor threshold";DelayUpdate
Label bottom "Acceptor threshold"
ModifyImage desynch_matrix ctab= {*,*,Rainbow256,0}
ColorScale/C/N=text0/F=0/A=RC/E contour=ln_FRET_Matrix_1Bin_Mass
ColorScale/C/N=text0  ctab={0,100,Rainbow,0}

Display as "Coincident events";AppendImage realrate_matrix
Label left "Donor threshold";DelayUpdate
Label bottom "Acceptor threshold"
ModifyImage realrate_matrix ctab= {*,*,Rainbow256,0}
ColorScale/C/N=text0/F=0/A=RC/E contour=ln_FRET_Matrix_1Bin_Mass
ColorScale/C/N=text0  ctab={0,100,Rainbow,0}

Display as "Coincident - chance events";AppendImage realminusd_matrix
Label left "Donor threshold";DelayUpdate
Label bottom "Acceptor threshold"
```

```
	ModifyImage realminusd_matrix ctab= {*,*,Rainbow256,0}
	ColorScale/C/N=text0/F=0/A=RC/E contour=ln_FRET_Matrix_1Bin_Mass
	ColorScale/C/N=text0  ctab={0,100,Rainbow,0}
	Print "Calculations complete."
end
```

Appendix IV: Script for Oligomer Sizing (Igor Pro v6.3.4.1)

Available at: https://github.com/drwhiten/Appendices.git

// To be used after load_() and Threshold_() in Appendix III

```
#pragma rtGlobals=3		// Use modern global access method and strict wave
	access.

Function size()
variable mon_bright=15
wave thresholded_donor_events, thresholded_acceptor_events
variable a,b,c,d,e,f,g,sizevar,ca=-4
make/o/n=50 scalex,scaley

for(a=0;a<50;a+=1)
scalex[a]=b/mon_bright
scaley[a]=ca
b+=10
ca+=0.15
endfor

make/o/n=(50,50) size_matrix=0

for(sizevar=10;(sizevar<500);sizevar+=10)
make/o/n=1 ratio,temp
b=0
for(a=0;a<(dimsize(thresholded_donor_events,0));a+=1)
if(thresholded_donor_events[a]<(sizevar)&&thresholded_donor_events[a]>(sizevar
	-10))
redimension/n=(b+1) temp

temp[b]=ln(thresholded_acceptor_events[a]/thresholded_donor_events[a])
b+=1
endif
endfor
Make/N=50/O temp_Hist;DelayUpdate
Histogram/B={-4,0.15,50} temp,temp_Hist

for(g=0;g<50;g+=1)
if(temp_hist[g]==0)
size_matrix[e][g]=0
else
size_matrix[e][g]=ln(temp_hist[g])
```

```
endif
endfor
e+=1
endfor

Display;AppendMatrixContour size_matrix vs {scalex,scaley}
ModifyContour size_matrix labels=0,autoLevels={*,*,100}
Label left "ln(red/blue)";DelayUpdate
Label bottom "A-beta monomers"
ColorScale/C/N=text0/F=0/A=RC/X=0.00/Y=0.00/E
        contour=size_matrix;DelayUpdate
ColorScale/C/N=text0 "ln(no. of oligomers)"
ModifyGraph swapXY=1
end
```

Appendix V: Script for Dihydroethidium Assay (Python v2.7)

Available at: https://github.com/drwhiten/Appendices.git

```
import PIL
import os
import numpy as np
import matplotlib.pyplot as pyplt
from matplotlib.widgets import  RectangleSelector
import Tkinter, tkFileDialog
from matplotlib.patches import Rectangle
import csv

def initialise():
    global cells_to_analyse, start_coords, end_coords, images_per_channel,
           images_to_discard_mid, images_to_discard_start
    images_per_channel = 54
    cells_to_analyse = 10
    images_to_discard_mid = 2
    images_to_discard_start = 0
    start_coords = []
    end_coords = []
    opener()

def opener():
    global files, directory
    root = Tkinter.Tk()
    root.wm_attributes("-topmost", 1)

    directory = tkFileDialog.askdirectory()
    root.withdraw()
    files = os.listdir(directory)
    files.sort()
    results_path = directory + '\Results'
    if not os.path.exists(results_path): os.makedirs(results_path)
    boxes()

def boxes():
    global files, directory,images_per_channel
    for f in files:
        if 'C2' in f:
            x = 1
            y = 1
            fig = pyplt.figure
            ax = pyplt.subplot(111)
            ax.plot(x,y)
```

```
            red_image_path = os.path.join(directory, f)
            img = PIL.Image.open(os.path.join(directory, f))
            try:
               img.seek(images_per_channel-1)
            except:
               pass

            currentAxis = pyplt.gca()
            for coord1, coord2 in zip(start_coords, end_coords):
               x,y1 = coord1
               x1,y = coord2
               upper_left = (x,y1)
               width = x1-x
               height = y-y1
               currentAxis.add_patch(Rectangle(upper_left, width, height,
             facecolor="none"))
            figManager = pyplt.get_current_fig_manager()
            figManager.window.showMaximized()
            pyplt.imshow(img)
            toggle_selector.RS = RectangleSelector(ax, onselect, drawtype='box')

def onselect(eclick, erelease):
   global cells_to_analyse
   'eclick and erelease are matplotlib events at press and release'
   start = (eclick.xdata, eclick.ydata)
   end = (erelease.xdata, erelease.ydata)
   start_coords.append(start)
   end_coords.append(end)
   pyplt.close(1)
   cells_to_analyse -= 1
   if cells_to_analyse != 0:
      boxes()
   else:
      analyse()

def tuggerah2009(accusation):
   mcf_owed = debt.accusation
   while mcf_owed == False:
      try:
         andew.logic
      except (ArithmeticError, MemoryError):
      raise FutureWarning('andew is broken')

def toggle_selector(event):
   print ' Key pressed.'
   if event.key in ['Q', 'q'] and toggle_selector.RS.active:
      print ' RectangleSelector deactivated.'
```

```
        toggle_selector.RS.set_active(False)
    if event.key in ['A', 'a'] and not toggle_selector.RS.active:
        print ' RectangleSelector activated.'
        toggle_selector.RS.set_active(True)

def analyse():
    global files, directory, images_per_channel
    count = 1
    uv_dict = {}
    red_dict = {}
    ratio_dict = {}

    for coord1, coord2 in zip(start_coords, end_coords):
        uv = []
        red = []
        x,y = coord1
        x1,y1 = coord2
        x = int(x)
        x1 = int(x1)
        y = int(y)
        y1 = int(y1)
        for f in files:
            if 'C2' in f:
                redimg2 = PIL.Image.open(os.path.join(directory, f))
                for i in range(images_per_channel):
                    try:
                        redimg2.seek(i)
                        redarr2 = numpy.array(redimg2)
                        redarr3 = redarr2[y:y1,x:x1]
                        red.append(numpy.mean(redarr3))
                    except:
                        pass
                red_dict[count] = red
            if 'C1' in f:
                uvimg2 = PIL.Image.open(os.path.join(directory, f))
                for i in range(images_per_channel):
                    try:
                        uvimg2.seek(i)
                        uvarr2 = numpy.array(uvimg2)
                        uvarr3 = uvarr2[y:y1,x:x1]
                        uv.append(numpy.mean(uvarr3))
                    except:
                        pass
                uv_dict[count] = uv
        count += 1
        print 'Working...'
```

```
for key in red_dict:
    ratio = []
    for b,m in zip(red_dict[key], uv_dict[key]):
        ratio.append(b/m)
    ratio_dict[key] = ratio

before_treat = images_per_channel/2
x_ax = []
before_treat_slopes = []
for x in xrange(images_to_discard_start, before_treat):
    x_ax.append(x)
for key in ratio_dict:
    y_ax = []
    for x in xrange(images_to_discard_start, before_treat):
        val = ratio_dict[key][x]
        y_ax.append(val)
    slope, intercept = np.polyfit(x_ax, y_ax, 1)
    before_treat_slopes.append(slope)

after_treat_start = images_per_channel/2+images_to_discard_mid
x_ax = []
after_treat_slopes = []
for x in xrange(after_treat_start, images_per_channel):
    x_ax.append(x)
for key in ratio_dict:
    y_ax = []
    for x in xrange(after_treat_start, images_per_channel):
        val = ratio_dict[key][x]
        y_ax.append(val)
    slope, intercept = np.polyfit(x_ax, y_ax, 1)
    after_treat_slopes.append(slope)

results_uv_path = directory + '\Results\uv_channel.csv'
results_red_path = directory + '/Results/red_channel.csv'
results_slopes_path = directory + '/Results/slopes.csv'

with open(results_uv_path, 'wb') as outfile:
    writer = csv.writer(outfile)
    writer.writerows(zip(*uv_dict.values()))
with open(results_red_path, 'wb') as outfile:
    writer = csv.writer(outfile)
    writer.writerows(zip(*red_dict.values()))
with open(results_slopes_path, 'wb') as outfile:
    writer = csv.writer(outfile)
    writer.writerow(['Before treatment','After treatment'])
```

```
        writer.writerows(zip(before_treat_slopes, after_treat_slopes))

    print 'Done!'
initialise()
```